



**McGill**

**New and Traditional Density Functional Theory  
Methods for Unveiling Mechanisms of Green  
Chemistry Processes**

Hanh Doan Minh Pham (Cindy)

Department of Chemistry

Montréal, Québec, Canada

December 2024

*A thesis submitted to McGill University in partial fulfillment of  
the requirements of the degree of Doctor of Philosophy*

*To my father Ngoc Lien, my mother Minh Nguyet, and my little brother Ngoc Phuc,  
for their endless love and constant support.*

*« Con cam on ba me! Con yeu ca nha! »*



## Abstract

Green chemistry develops processes and products that reduce the use of substances that are harmful for humans and the environment. Computational chemistry can advance green chemistry research by offering tools to model and predict chemical behavior and by facilitating the design of eco-friendly processes and materials. Density functional theory (DFT) is one of the most widely used computational tools in green chemistry that is vital for explaining and predicting reaction pathways, designing catalysts, and assessing environmental impact, all of which advance sustainability in chemical research.

The first part of this thesis (Chapter 2) investigates the mechanism of reversible CO<sub>2</sub> capture – a promising green chemistry technology – by a cyclodextrin-based metal–organic framework called CD-MOF-2, which is synthesized from environmentally benign ingredients. By analysing results of DFT modeling and available experimental data, this study describes the nature and structural characteristics of diverse alcohol adsorption sites in CD-MOF-2, capable of binding CO<sub>2</sub> in the irreversible, reversible, and weak regimes. It explains the role of hydrogen bonding environments in modulating CO<sub>2</sub> binding strength at these sites. These findings provides insights into designing solid materials for CO<sub>2</sub> capture or detection by linking acid-base proton equilibrium and hydrogen bonding to CO<sub>2</sub> binding efficiency.

The second part of the thesis presents a new DFT method for describing excited electronic states, modeling of which is essential for green chemistry research in photochemistry, photovoltaics, and photocatalysts. Many inaccuracies of time-dependent (TD) DFT, which is most often used to model excited states, arise from its non-variational nature. On the other hand, recently developed variational time-*independent* DFT must deal with the problem of excited states collapsing onto the

ground state during their optimization. We present a computational method that solves the collapse problem while keeping theory simple and computations efficient. This is done in two steps.

The first chapter of the development part of the thesis (Chapter 3) presents a method to avoid collapse of molecular orbitals within a single electronic state during the self-consistent field (SCF) optimization. This method, called variable-metric SCF, is applied to describe the electronic ground state. The main idea of the method is to allow nonorthogonal molecular orbitals and then penalize linearly dependent orbitals with a term that is added to the DFT energy functional. Variable-metric SCF method allows to use molecular orbital coefficients as independent variables in a direct, unconstrained minimization. It is shown that variable-metric SCF equations are simple and can be solved efficiently even with a basic preconditioned conjugate gradient algorithm for various molecular and solid-state systems, including challenging narrow gap systems and singlet diradicals.

The second chapter of the development part (Chapter 4) extends variable-metric SCF to multiple electronic states by adding a new term that penalizes overlapping states, not just overlapping molecular orbitals. The resulting variable-metric time-independent DFT method treats both ground and excited states variationally and equally, improving the accuracy of modeling charge-transfer and two-electron excited states of various molecules compared to TDDFT. The variational nature of variable-metric time-independent DFT also allows to greatly simplify the evaluation of atomic forces, which will lead to more efficient non-adiabatic molecular dynamics simulations of green photochemical and photocatalytic processes.

## Résumé

La chimie verte est essentielle au développement de procédés et de matériaux durables qui réduisent l'impact environnemental. La chimie computationnelle renforce ce domaine en fournissant des outils pour modéliser et prédire les comportements chimiques, facilitant ainsi la conception de matériaux et de procédés respectueux de l'environnement. Des techniques telles que la théorie de la fonctionnelle de la densité (DFT) sont cruciales pour optimiser les voies réactionnelles, concevoir des catalyseurs et évaluer les impacts environnementaux, contribuant ainsi à l'innovation et à la durabilité dans la recherche chimique.

La première partie de cette thèse (Chapitre 2) étudie le mécanisme de capture réversible du  $\text{CO}_2$ , une technologie prometteuse de la chimie verte, par un cadre métal organique à base de cyclodextrine appelée CD-MOF-2, qui est synthétisée à partir d'ingrédients inoffensifs pour l'environnement. En analysant les résultats de la modélisation DFT et les données expérimentales disponibles, cette étude décrit la nature et les caractéristiques structurales de divers sites d'adsorption d'alcool dans le CD-MOF-2, capables de lier  $\text{CO}_2$  dans les régimes irréversible, réversible et faible. Elle explique le rôle des liaisons hydrogène dans la modulation de la force de liaison de  $\text{CO}_2$  sur ces sites. Ces résultats permettent d'envisager la conception de matériaux solides pour la capture ou la détection de  $\text{CO}_2$  en reliant l'équilibre acide-base des protons et la liaison hydrogène à l'efficacité de la liaison avec  $\text{CO}_2$ .

La deuxième partie de la thèse présente une nouvelle méthode DFT pour décrire les états électroniques excités, dont la modélisation est essentielle pour la recherche en chimie verte dans les domaines de la photochimie, de la photovoltaïque et des photocatalyseurs. De nombreuses imprécisions de la DFT dépendante du temps (TD), qui est le plus souvent utilisée pour modéliser les

états excités, proviennent de sa nature non variationnelle. D'une autre part, la DFT variationnelle en fonction du temps, récemment développée, doit faire face au problème de l'absence de variation de l'état excité et doit faire face au problème de l'effondrement des états excités sur l'état fondamental au cours de leur optimisation. Nous présentons une méthode de calcul qui résout le problème de l'effondrement tout en conservant une théorie simple et des calculs efficaces, cela se fait en deux étapes.

Le premier chapitre de la partie développement de la thèse (Chapitre 3) présente une méthode pour éviter l'effondrement des orbitales moléculaires dans un état électronique unique pendant l'optimisation du champ autoconsistant (SCF). Cette méthode, appelée SCF à métrique variable, est appliquée pour décrire l'état fondamental électronique. L'idée principale de la méthode est d'autoriser les orbitales moléculaires non orthogonales et de pénaliser les orbitales linéairement dépendantes à l'aide d'un terme ajouté à la fonctionnelle énergétique DFT. La méthode SCF à métrique variable permet d'utiliser les coefficients des orbitales moléculaires comme variables indépendantes dans une minimisation directe et sans contrainte. Il est démontré que les équations SCF à paramètres variables sont simples et peuvent être résolues efficacement, même avec un algorithme de gradient conjugué préconditionné de base, pour divers systèmes moléculaires et à l'état solide, y compris des systèmes difficiles à espace étroit et des diradicals singuliers.

Le deuxième chapitre de la partie développement (Chapitre 4) étend la méthode SCF à paramètres variables à des états électroniques multiples en ajoutant un nouveau terme qui pénalise les états qui se chevauchent, et ce, pas seulement les orbitales moléculaires qui se chevauchent. La méthode DFT indépendante du temps à mesure variable qui en résulte traite les états fondamentaux et les états excités de manière variable et égale, améliorant la précision de la modélisation du transfert de charge et des états excités à deux électrons de diverses molécules par rapport à la

TDDFT. La nature variationnelle de la méthode DFT variable et indépendante du temps permet également de simplifier considérablement l'évaluation des forces atomiques, ce qui conduira à des simulations de dynamique moléculaire non adiabatique plus efficaces des processus photochimiques et photocatalytiques verts.

## Acknowledgements

Going through the PhD path has been a truly life-changing experience for me, and this milestone would not have been possible to reach without the support and guidance I received from many people.

First and foremost, I am deeply grateful and want to extend my heartfelt thanks to my supervisor, Dr. Rustam Z. Khaliullin, for his constant guidance, support, and patience throughout my PhD journey. Starting with little experience in the field, his expertise and dedication have profoundly shaped both my research and academic growth, sparking a deep interest in computational chemistry within me. I greatly appreciate our weekly meetings, where I continually learned from our progress discussions, gaining skills in problem-solving, planning, and forward-thinking. Not to mention for the countless hours he spent reviewing my work, providing insightful feedback, and fostering a stimulating and productive research environment. I also cherish the fun and appreciate the positive and supportive atmosphere he created during our group meetings and activities.

I would like to thank my committee members – Dr. Chao-Jun Li, Dr. Amy Blum, and Dr. Lena Simine – for all the insightful comments, constructive criticism, and suggestions on my research projects. Additionally, I am grateful to Dr. Peter B. Armentrout and Dr. Georgia C. Boles from the University of Utah for providing me with the opportunity to join and work under their guidance during my undergraduate research. Their mentorship was instrumental in setting me on the path of chemistry research and has been a foundational part of my academic journey.

To my family, words cannot fully express how grateful I am for your unwavering love and support. To my parents, Mr. Ngoc Lien and Mrs. Minh Nguyet, thank you for your sacrifices, encouragement, and steadfast belief in me. I am immensely proud and grateful to be your daughter.

To my little brother, Ngoc Phuc, thank you for maturing into such a responsible sibling. Not only have you learned to take care of yourself, but you've also been there for me and our parents. I am thankful for your presence in my life and hope that you, along with Mom and Dad, will continue to be by my side. I love you all dearly. Lastly, I want to thank my aunt, Nga Doan, who has been like a second mother to me.

To my dear colleagues—Dr. Ziling Luo, Dr. Zhenzhe Zhang, and Sylvester Zhang—being the only woman in the lab initially made me feel shy and apprehensive, but your warm and friendly reception quickly made me feel welcome. I deeply appreciate your kindness and understanding. Thank you also to Pengqi Liu, Dr. Kiwon Lee from the Math Department for your emotional support and comfort. A special thank you to my bestie plus sister Phuong Nguyen. Your encouragement and support through all the ups and downs have made this journey far more enjoyable and manageable. I sincerely thank Mrs. Chantal Marotte for her help with the paperwork and the McGill Chemistry Department for the opportunity to study and work here. I also appreciate the technical support from Compute Canada and Calcul Quebec.

To my amazing boyfriend, Benny Cheung, I am incredibly grateful to have found you. You, your family, and your friends have added so much joy and richness to my journey. Ily my dudu.

To those not specifically named in this acknowledgment, your support and impact have not gone unnoticed. You are deeply valued and sincerely appreciated.

# Contribution to Original Knowledge

Original scientific contributions described in this work include:

## **Chapter 2. Unraveling the Origins of Strong and Reversible Chemisorption of Carbon Dioxide in a Green Metal-Organic Framework**

- Examined the nature of CO<sub>2</sub> adsorption sites in CD-MOF-2.
- Performed the analysis of environmental effects on the CO<sub>2</sub> binding strength of CD-MOF-2.
- Explained the origins of the wide range of the adsorption energies measured for CD-MOF-2.

## **Chapter 3. Direct Unconstrained Optimization of Molecular Orbital Coefficients in Density Functional Theory**

- Developed a simple unconstrained optimization approach that can be performed without imposing conventional orthonormality constraints.
- Demonstrated the use of molecular orbital coefficients as independent variables in a direct unconstrained optimization procedure.
- Demonstrated the efficient convergence of the method using a basic preconditioned algorithm, successfully applied it to difficult systems.

## **Chapter 4. Direct Unconstrained Optimization of Excited States in Density Functional Theory**

- Extended the variable-metric approach to excited state optimization.

- Demonstrated the method's ability to prevent variational collapse of excited states to the ground and lower-energy states during optimization.
- Showed that the new approach is robust and produces accurate energies for both standard excitations and more challenging cases, where traditional time-dependent density functional theory struggles.

Research articles that were prepared for publication during course of this thesis.

I. Computational research performed by the author and included in this thesis:

1. **Pham, H. D. M.**; Khaliullin, R. Z. Unraveling the Origins of Strong and Reversible Chemisorption of Carbon Dioxide in a Green Metal-Organic Framework. *J. Phys. Chem. C* **2021**, 125 (44), 24719-24727.
2. **Pham, H. D. M.**; Khaliullin, R. Z. Direct Unconstrained Optimization of Molecular Orbital Coefficients in Density Functional Theory. *J. Chem. Theory Comput.* **2024**, 20, 18, 7936–7947.
3. **Pham, H. D. M.**; Khaliullin, R. Z. Direct Unconstrained Optimization of Excited States in Density Functional Theory (*submitted*)

II. Computational studies of green chemical processes performed exclusively by the thesis author to support experimental studies performed by collaborators:

4. Qiu Z., **Pham, H. D. M.**; Li, J.; Li, C. C.; Castillo-Pazos, D. J.; Khaliullin, R. Z., and Li, C. J. Light-enabled metal-free pinacol coupling by hydrazine. *Chem. Sci.* **2019**, 10, 10937–10943.

5. Luo S.; **Pham, H. D. M.**; Li, C. C., Qiu, Z.; Khaliullin, R. Z., and Li, C. J. Anti-Markovnikov Hydroalkylation of Alkenes via Hydrazones Catalyzed by Ru-PNP Complex. *Org Lett.* **2024**, 26(15), 3004–3009.
6. Juneau, A.; Abdolhosseini, M.; Rocq, C.; **Pham, H. D. M.**; Pascall M.; Khaliullin, R. Z.; Canesi, S.; McCallaa, E., and Mauzerolla, J. Overcoming Challenges in Electrosynthesis Using High-Throughput Electrochemistry: Hypervalent Iodine-Mediated Phenol Dearomatization, a Case Study. *Chem. Electro. Chem.*, **2024**, e202400193.

### III. Computational studies performed in collaboration:

7. Shirani, J.; **Pham, H. D. M.**; Yuan, S.; Tchagang, A. B.; Valdés, J. J., and Bevan, K. B. Machine Learning Based Electronic Structure Predictors in Single-Atom Alloys: A Model Study of CO Kink-Site Adsorption across Transition Metal Substrates *J. Phys. Chem. C.* **2023**, 127, 25, 12055–12067.
8. Zhang, Z.; **Pham, H. D. M.**; Perepichka, D. F., and Khaliullin, R. Z. Highly Stable Two-Dimensional Carbon Allotropes Based on Azulenoid Kekulene. *Nat Commun.* **2024**, 15(1), 1953.

## Contribution of Authors

**Chapter 1.** Introduction has been written by the author.

**Chapter 2.** This work has been completed entirely by the author. The chapter is a copy of a published peer-reviewed article: **Pham, H. D. M.** and Khaliullin, R. Z. Unraveling the Origins of Strong and Reversible Chemisorption of Carbon Dioxide in a Green Metal–Organic Framework. *J. Phys. Chem. C* **2021**, 125 (44), 24719-24727.

**Chapter 3.** This work has been completed entirely by the author. The chapter is a copy of a published peer-reviewed article: **Pham, H. D. M.** and Khaliullin, R. Z. Direct Unconstrained Optimization of Molecular Orbital Coefficients in Density Functional Theory. *J. Chem. Theory Comput.* **2024**, 20, 18, 7936–7947.

**Chapter 4.** This work has been completed entirely by the author. The chapter is a copy of a manuscript prepared for publication: **Pham, H. D. M.**, and Khaliullin, R. Z. Direct Unconstrained Optimization of Excited States in Density Functional Theory, (*submitted*).

**Chapter 5.** A comprehensive overview has been written by the author.

**Chapter 6.** Conclusion has been written by the author.

---

# Contents

---

<b>Preface</b>	<b>i</b>
Abstract . . . . .	i
Résumé . . . . .	iii
Acknowledgements . . . . .	vi
Contribution to Original Knowledge . . . . .	viii
Contribution of Authors . . . . .	xi
Contents . . . . .	xii
List of Figures . . . . .	xix
List of Tables . . . . .	xxiv
List of Abbreviations . . . . .	xxv
<b>1 Introduction</b>	<b>1</b>
1.1 Preface . . . . .	1
1.2 Green Chemistry . . . . .	2
1.2.1 Background . . . . .	2
1.2.2 12 Principles of Green Chemistry . . . . .	4
1.2.3 Green Technologies . . . . .	6

1.2.3.1	Carbon Capture . . . . .	7
1.2.3.2	Photovoltaics . . . . .	14
1.2.3.3	Photocatalysis . . . . .	17
1.3	Computational Methods for Green Chemistry Applications . . . . .	19
1.3.1	Computational Chemistry Introduction . . . . .	19
1.3.2	Computational Chemistry Utility . . . . .	20
1.3.2.1	Carbon Capture . . . . .	20
1.3.2.2	Photovoltaics . . . . .	22
1.3.2.3	Photocatalysis . . . . .	25
1.4	Theoretical Methods for Green Chemistry Applications . . . . .	27
1.4.1	DFT Overview . . . . .	27
1.4.1.1	Electronic Hamiltonian Derivation . . . . .	27
1.4.1.2	Hohenberg-Kohn Theorems . . . . .	30
1.4.1.3	Kohn-Sham Density Functional Theory (KS-DFT) . . . . .	32
1.4.2	Exchange-Correlation (XC) Functionals . . . . .	33
1.4.2.1	Local Density Approximation (LDA) . . . . .	34
1.4.2.2	Generalized Gradient Approximation (GGA) . . . . .	35
1.4.2.3	Hybrid Functionals . . . . .	36
1.4.3	SCF Methods . . . . .	37
1.4.3.1	Diagonalization of the Hermitian Matrix . . . . .	38
1.4.3.2	Unitary Transformation . . . . .	39
1.4.4	DFT for Excited States . . . . .	41
1.4.4.1	TDDFT . . . . .	41

1.4.4.2	$\Delta$ SCF . . . . .	43
1.4.4.3	Orthogonality Constrained DFT (OCDFT) . . . . .	44
1.4.4.4	Maximum Overlap Method (MOM) . . . . .	45
1.4.4.5	Square Gradient Minimization (SGM) . . . . .	46
1.5	References . . . . .	49
<b>2</b>	<b>Unraveling the origins of strong and reversible chemisorption of carbon dioxide in a green metal-organic framework</b>	<b>58</b>
2.1	Preface . . . . .	58
2.2	Abstract . . . . .	59
2.3	Introduction . . . . .	60
2.4	Computational models and methods . . . . .	64
2.5	Results and discussion . . . . .	66
2.5.1	Chemisorption on neutral alcohol groups . . . . .	66
2.5.2	Chemisorption on alkoxide sites . . . . .	69
2.5.3	Effect of the environment on CO <sub>2</sub> adsorption . . . . .	70
2.5.4	Formation of active chemisorption sites . . . . .	75
2.5.5	Analysis of computational and experimental data . . . . .	77
2.6	Conclusions . . . . .	78
2.7	Acknowledgements . . . . .	80
2.8	References . . . . .	81
2.9	Supporting Information . . . . .	85
2.9.1	Enthalpy of Adsorption . . . . .	85

2.9.2	Comparison of the CO <sub>2</sub> Binding Strength Obtained with BLYP and HSE06 Functionals . . . . .	87
2.9.3	Number of CO <sub>2</sub> Molecules Adsorbed Per Unit Cell of CD-MOF-2 . . . . .	88
2.10	References . . . . .	89

### **3 Direct unconstrained optimization of molecular orbital coefficients in density**

	<b>functional theory</b>	<b>90</b>
3.1	Preface . . . . .	90
3.2	Abstract . . . . .	91
3.3	Introduction . . . . .	92
3.4	Methodology . . . . .	94
3.4.1	Theory . . . . .	94
3.4.2	Optimization Algorithm . . . . .	97
3.4.3	Penalty Strength . . . . .	101
3.4.4	Variable-metric Optimization for Open-shell Systems . . . . .	103
3.4.5	Computational Details . . . . .	106
3.5	Data Availability . . . . .	108
3.6	Numerical Results and Discussion . . . . .	109
3.6.1	Preconditioner . . . . .	109
3.6.2	Penalty Strength . . . . .	111
3.6.3	SCF Convergence . . . . .	112
3.6.4	Variable-metric ROKS SCF for Singlet Diradicals . . . . .	114
3.7	Conclusions . . . . .	117

3.8	Acknowledgements . . . . .	117
3.9	References . . . . .	118
3.10	Supporting Information . . . . .	122
3.10.1	Methodology . . . . .	122
3.10.1.1	Description of Unrestricted Kohn Sham (UKS) . . . . .	122
3.10.1.2	Description of Restricted Open-Shell Optimization (ROSO) . . . . .	123
3.10.1.3	Description of Restricted Open-Shell Kohn Sham (ROKS) . . . . .	124
3.10.2	Derivation of the Equations for the Closed-Shell Case . . . . .	127
3.10.2.1	Energy derivatives . . . . .	127
3.10.2.2	Penalty derivatives . . . . .	128
<b>4</b>	<b>Direct unconstrained optimization of excited states in density functional theory</b>	<b>132</b>
4.1	Preface . . . . .	132
4.2	Abstract . . . . .	133
4.3	Introduction . . . . .	134
4.4	Methodology . . . . .	137
4.4.1	Theory . . . . .	137
4.4.2	Optimization Algorithm . . . . .	140
4.4.3	Penalty Strength Adjustment . . . . .	143
4.4.4	Computational Details . . . . .	144
4.5	Results and Discussion . . . . .	145
4.5.1	Penalty Strength Effect . . . . .	145
4.5.2	Accuracy . . . . .	146

4.5.3	Double-electron Excitations . . . . .	148
4.5.4	Charge-transfer Excitations . . . . .	150
4.5.5	SCF Convergence . . . . .	152
4.6	Conclusions . . . . .	153
4.7	Acknowledgements . . . . .	155
4.8	References . . . . .	156
4.9	Supporting Information . . . . .	161
4.9.1	Unrestricted Kohn-Sham Equations for Variable Metric Time-Independent Optimization . . . . .	161
4.9.2	First Derivative of the Intrastate Term . . . . .	161
4.9.3	First Derivative of the Interstate Term . . . . .	162
<b>5</b>	<b>Comprehensive Overview</b>	<b>164</b>
5.1	Facilitate CO <sub>2</sub> Binding in CD-MOF-2 . . . . .	164
5.1.1	Determine Precise Proton Transfer Mechanism . . . . .	165
5.1.2	Analyze the H-bond Network Environment of CO <sub>2</sub> Binding Sites . . . . .	166
5.1.3	Design Water-Stable Engineering Strategies . . . . .	167
5.1.4	Utilize Hybrid Functionals for More Accurate Binding Energies . . . . .	168
5.2	Improve Convergence Rate of VM SCF . . . . .	168
5.2.1	Implement BFGS Algorithm . . . . .	168
5.2.2	Implement Trust Region (TR) Algorithm . . . . .	170
5.2.3	Reduce the Cost of the Preconditioner Inversion . . . . .	172
5.3	Improve Excited-State VM TIDFT Optimization . . . . .	173

5.3.1	Design Better Loss Function . . . . .	173
5.3.2	Implement ROKS Method for Spin-Pure States in VM TIDFT . . . . .	174
5.3.3	Perform Orbital Optimization with the Frozen Hamiltonian . . . . .	175
5.4	References . . . . .	176
<b>6</b>	<b>Conclusion</b>	<b>178</b>
6.1	Summary . . . . .	178

## List of Figures

1.1	12 Principles of Green Chemistry proposed by Anastas and Warner <sup>4</sup> . The figure is reproduced from Harison et al. <sup>7</sup> . . . . .	4
1.2	A comprehensive illustration of carbon capturing, transportation, storage and utilization ecosystem: from source to utilization. The figure is reproduced from Goren et al. <sup>8</sup> . . . . .	7
1.3	Main CO <sub>2</sub> capture technologies. The figure is reproduced from Hekmatmehr et. al. <sup>10</sup>	8
1.4	Pros and cons of different types of carbon dioxide adsorbents. The figure is reproduced from Allangawi et al. <sup>11</sup> . . . . .	9
1.5	A diagram showing the photovoltaic effect. The figure is reproduced from Donev et al. <sup>34</sup> . . . . .	15
1.6	The four main steps in photocatalysis process. The figure is reproduced from Liao et al. <sup>51</sup> . . . . .	18
2.1	(a) Cyclic arrangement of $\gamma$ -cyclodextrin (CD) showing eight $\alpha$ -1,4-linked D-glucopyranosyl residues with the primary alcohol groups colored red. (b) Repeating maltosyl unit of CD with attached rubidium ions. (c) Cubic unit cell of CD-MOF-2 with carbon, oxygen, and rubidium atoms shown with cyan, red, and pink colors, respectively. The primary faces of the six CD tori point inward, whereas the secondary faces are oriented outward. The CD tori are connected via rubidium cations, forming an extended crystal structure <sup>25,26,28</sup> . . . . .	62

2.2	Model reactions for CO <sub>2</sub> adsorption: (a) neutral alcohol groups, (b) alkoxide groups, (c) counterion-bonded groups. Only a single maltosyl unit of $\gamma$ -cyclodextrin is shown for clarity. The proximity of the CO <sub>2</sub> binding sites to the Rb ion in this simplified scheme might not correctly reflect the distance between them in the MOF crystal structure. . . . .	67
2.3	CO <sub>2</sub> adsorption energy calculated for different model reactions at primary (red) and secondary (black) binding sites. Filled shapes represent geometries generated using AIMD, whereas empty shapes represent geometries obtained from the straightforward geometry optimization. The corresponding numerical data is listed in Table 1.1 in Supporting Information. . . . .	68
2.4	Effect of replacing neighbor alcohol groups with hydrogen atoms on CO <sub>2</sub> adsorption energies at primary (red) and secondary (black) binding sites. Filled shapes represent models using AIMD before the adsorption procedure, while the unfilled ones did not. The corresponding numerical data is listed in Table 1.1 . . . . .	71
2.5	Effect of replacing neighbor alcohol groups with hydrogen atoms on the CO <sub>2</sub> binding strength. The adsorption site and nearby alcohol groups are shown as spheres in the wireframe MOF background. The CO <sub>2</sub> carbon atom is green and the hydrogen atoms are yellow. Oxygen atoms of the adsorption site and alkylcarbonic group are shown in purple, whereas oxygen atoms of nearby alcohol groups are shown in red. Blue dash lines represent hydrogen bonds. Values of $\Delta\Delta E_{\text{ads}}^{(i)}$ , defined in Eq. (2.1), are shown as red numbers. The CO <sub>2</sub> adsorption energies before the neighbor replacement are shown in grey fields. . . . .	72

2.6	Effect of replacing neighbor alcohol groups with hydrogen atoms on the CO <sub>2</sub> binding strength for sites that bind CO <sub>2</sub> strongly (green), moderately (yellow) and weakly (red). Color coding and labels are explained in the caption of Figure 2.5. . . .	74
3.1	Variable-metric SCF based on the PCG algorithm. . . . .	104
3.2	An illustrative example of the two Slater determinants that are used to describe a spin-pure singlet diradical state. The relation between the energies of the singlet, mixed, and triplet states is also shown. . . . .	105
3.3	Organic radicals considered in this work: a) 3,5-ditert-butyl-3'-(N-tert-butyl-N-aminoxy)-4-oxybiphenyl (oxybiphenyl), b) $\alpha H$ -undecachlorodiphenylmethyl (PTM), c) biphenyl-3,5-diyl-bis(N-t-butyl nitroxide) (biphenyl), and d) bis-nitronyl nitroxide (BNN). . . . .	107
3.4	Influence of the preconditioner on the rate of convergence of the VM SCF optimization. The list of preconditioners includes: overlap ( $A = 0, D = I$ ), $F + S$ ( $A = D = I$ ), $QFQ + S$ ( $A = Q, D = I$ ), $QFQ + QSQ$ ( $A = D = Q$ ). The dashed line refers to the level of the SCF accuracy typically required in <i>ab initio</i> molecular dynamics (AIMD) simulation. In all three tests, $\epsilon$ was set to 0.85 a.u. for $F + S$ preconditioner.	109
3.5	Influence of the value of $\epsilon$ on the number of VM SCF steps required to reach convergence of $10^{-8}$ a.u. Missing data points indicate the Cholesky inversion of the preconditioner failed. Default settings were used in all three tests. . . . .	111
3.6	Convergence rate of VM approach corresponding to different scaling of penalty strength. . . . .	112

3.7	Deviation from the orthogonality for occupied MOs in the SCF optimization for armchair carbon nanotube for different initial values of the penalty strength $C_p$ . Orbitals re-orthogonalized in the outer loop. . . . .	113
3.8	Comparison of the convergence rate for the VM and OT SCF procedures. Line search steps, one per PCG step, are not included in the iteration count. The dashed line refers to the level of accuracy typically required in <i>ab initio</i> molecular dynamics simulations. . . . .	114
3.9	Comparison of the convergence rate of the VM and OT SCF procedures for singlet diradicals. Line search steps, one per PCG step, are not included in the iteration count. The dashed line refers to the level of accuracy typically required in <i>ab initio</i> molecular dynamics simulations. . . . .	115
3.10	An illustrative example of the two Slater determinants that are used to describe a singlet diradical state. . . . .	125
4.1	Excitation energy for the first two excitations of He atom (PBE/TZVP) and HF molecule (PBE/DZVP) computed with VM TIDFT optimization procedure for the DFO values measured after convergence is reached. The recovered excitation energy is a fraction of the converged excitation energy $E_{\text{conv}}$ obtained with very tight requirement for the orthogonality criterion ( $\mathcal{E}_0 = 10^{-5}$ ). . . . .	146

4.2	Comparison of VM TIDFT excitation energies with those calculated with TDDFT, OCDFT, and wavefunction correlation methods. TDDFT and VM TIDFT results were obtained in this work using CP2K, OCDFT energies were computed using Psi4 in Ref. <sup>44</sup> , and MP2/6-31G* and CCSD/aug-cc-pVTZ results were computed using Gaussian in Ref. <sup>78</sup> . . . . .	150
4.3	PBE/SZV ground-state and excited-state dissociation curves for H <sub>2</sub> computed with VM TIDFT. The energy of the Coulomb interactions is down-shifted by 0.36 Ha to account for sum of the ionization potential (IP) and electron affinity (EA) of the isolated hydrogen atoms. . . . .	151
4.4	Excitation energy for the charge transfer state of HeH <sup>+</sup> as a function of the He–H distance, computed using VM TIDFT and TDDFT at the PBE/DZVP level of theory. For comparison, OCDFT PBE/STO-3G results are also shown <sup>44</sup> . . . . .	152
4.5	Convergence rate for the VM TIDFT procedure for the ground states (GS) and selected excited states (ES). Line search steps, one per PCG step, are not included in the iteration count. The dashed lines show the SCF convergence threshold. . . .	154
5.1	The Cauchy point. The figure is reproduced from Nocedal and Wright <sup>16</sup> . . . . .	171
5.2	The dogleg method. The figure is reproduced from Nocedal and Wright <sup>16</sup> . . . .	172

## List of Tables

2.1	CO <sub>2</sub> adsorption energy calculated for different model reactions (Figure 1.2) . . . . .	86
2.2	Comparison of the CO <sub>2</sub> binding strength (kJ/mol) obtained with BLYP and HSE06 functionals. . . . .	87
2.3	Energy of the proton transfer from the specified adsorption site to a randomly selected hydroxyl counterion. . . . .	87
3.1	Key input parameters that control the PCG optimization of MO coefficients. . . . .	106
3.2	PBE/aug-TZV2P singlet-triplet energy gaps for singlet diradicals computed with the single-determinant UKS and two-determinant ROKS methods. . . . .	116
3.3	Non-default settings used for several test systems. Notation is defined in Table 1. Preconditioner $QFQ + S$ is a shorthand for $A = Q$ and $D = I$ . Preconditioner $F + S$ is a shorthand for $A = D = I$ . . . . .	126
4.1	Input parameters that control the PCG optimization of MO coefficients. . . . .	144
4.2	PBE/QZV3P excitation energies calculated using TDDFT and VM TIDFT. . . . .	148
4.3	First singlet excitation energies calculated using TDDFT, VM TIDFT, OCDFT and high-level quantum mechanics calculations and shown alongside experimental data. . . . .	149

## List of Abbreviations

BFGS	Broyden-Fletcher-Goldfarb-Shanno
BLYP	Becke/Lee-Yang-Parr functional
BO	Born-Oppenheimer
CCDC	Cambridge Crystallographic Data Centre
CD-MOF-2	Cyclodextrine Metal Organic Framework
CG	Conjugate Gradient
CT	Charge Transfer
CV-DFT	Constricted Variational Density Functional Theory
DFT	Density Functional Theory
DIIS	Direct Inversion in The Iterative Subspace
DZVP	Double- $\zeta$ Gaussian basis set with one set of polarization functions
EA	Electron Affinity
GGA	Generalized Gradient Approximation
HOMO	Highest Occupied Molecular Orbital
HF	Hartree-Fock
HK	Hohenberg-Kohn
HSE	Heyd-Scuseria-Ernzerhof
IP	Ionization Potential
KS	Kohn-Sham
LDA	Local Density Approximation
LUMO	Lowest Unoccupied Molecular Orbital

MO	Molecular Orbital
MOF	Metal Organic Framework
NQEs	Nuclear Quantum Effects
OPVs	Organic Photovoltaics
OSCs	Organic Solar Cells
PBE	Perdew-Burke-Ernzerhof functional
PES	Potential Energy Surface
PIMD	Path Integral Molecular Dynamics
PSCs	Perovskite Solar Cells
PV	Photovoltaic
QZV3P	Quadruple- $\zeta$ Gaussian basis set with three sets of polarization functions
SCF	Self-Consistent Field
TDDFT	Time-Dependent Density Functional Theory
TDSE	Time-Dependent Schrödinger Equation
TIDFT	Time-Independent Density Functional Theory
TISE	Time-Independent Schrödinger Equation
TR	Trust Region
TZVP	Triple- $\zeta$ Gaussian basis set with one set of polarization functions
RPMD	Ring Polymer Molecular Dynamics
XC	Exchange-Correlation

# Chapter 1

---

## Introduction

---

### 1.1 Preface

Since the industrial revolution, broad concern for environmental degradation has been rising steadily, gradually making it one of the most pressing issues of our time. Humanized activities such as industrialization, mass production, heavy transportation, and the use of non-degradable chemicals contribute to climate change, air-water-soil pollution, and the staggering loss of biodiversity. Those environmental burdens are destructive not only to natural habitats but also to our ecosystems. Consequently, the imperative to reverse these adverse impacts demands proactive action from individuals, communities, and governments around the globe. By acknowledging the situation and taking action to adopt sustainable practices, we could mitigate the harmful effects and protect the well-being of our shared home.

The methodological developments and applications presented in this thesis are unified by their emphasis on green chemistry applications in the computational modeling of electrons and atoms. This introductory chapter begins with a review of green chemistry, highlighting its significance and application in developing carbon capture materials with potential industrial applications, as

discussed in Chapter 2. It then delves into the theoretical foundations of Kohn-Sham density functional theory (DFT), the most widely used electronic structure theory today, covering various self-consistent field (SCF) orbital optimization techniques. These concepts lay the groundwork for the direct unconstrained optimization methods introduced for DFT ground-state calculations in Chapter 3 and extended to optimizing excited states in Chapter 4.

## 1.2 Green Chemistry

### 1.2.1 Background

Modern science, with its vast potential, offers numerous pathways and promising solutions to address the current environmental challenges. Green chemistry, in particular, plays a key role by integrating scientific advancements to achieve both environmental and economic efficiency in pollution reduction. By definition, green chemistry is defined as the "design of chemical products and processes to reduce or eliminate the use and generation of hazardous substances"<sup>1,2</sup>.

The concept of green chemistry can be traced back to the early 1990s<sup>1-3</sup>. In 1990, the Pollution Prevention Act was passed in the United States, establishing source reduction as the highest priority in solving environmental problems and signaling a shift towards pollution prevention over traditional "command and control" approaches. Building on this momentum, in 1991, the U.S. Environmental Protection Agency (EPA) launched the Green Chemistry Program's first research initiative, focusing on alternative synthetic pathways. The following year, the National Science Foundation partnered with the EPA on the Environmentally Benign Syntheses and Processes program, officially adopting the name "U.S. Green Chemistry Program" in 1993.

A significant milestone was reached in 1995 with the announcement of the U.S. Presidential Green Chemistry Challenge Award to recognize achievements in green chemistry across several sectors such as industry, academia, and government. The first awards were given in 1996, marking the growing adoption of green chemistry principles. In the late 1990s, international expansion spread to Italy, the United Kingdom, and Japan, where major green chemistry initiatives were launched, including research and education programs. In 1999, the inaugural edition of the journal *Green Chemistry*, sponsored by the Royal Society of Chemistry, was published, highlighting the field's increasing recognition.

Further development in green chemistry occurred in the 2000s, with significant advancements in renewable feedstocks, catalysis, and the design of safer chemicals. The 2010s continued this trend, with a heightened emphasis on sustainable chemistry and the circular economy, driving international growth and collaboration. Entering the 2020s, green chemistry has solidified its role as a crucial component of sustainable development, with ongoing research and widespread industrial implementation, reinforcing its importance in addressing global environmental challenges.

With its inception and evolution since then, green chemistry has gained global recognition and adoption, leading to the establishment of numerous governmental initiatives and programs worldwide that significantly influence sustainable design practices. These efforts have promoted the integration of principles in chemical research and industry, cementing green chemistry's crucial role in advancing sustainable development.

## 1.2.2 12 Principles of Green Chemistry

To achieve the primary goal of benefiting human health and the environment, green chemistry is guided by a set of 12 principles developed by Paul Anastas and John Warner in their book "Green Chemistry: Theory and Practice" (1998)<sup>4</sup>. These principles, conveniently summarized into the acronym PRODUCTIVELY<sup>1</sup>, serve as comprehensive guidelines for chemists to create greener chemicals and processes by reducing or eliminating the use and generation of hazardous substances in the design, manufacture, and application of chemicals<sup>5,6</sup>.



Figure 1.1: 12 Principles of Green Chemistry proposed by Anastas and Warner<sup>4</sup>. The figure is reproduced from Harison et al.<sup>7</sup>

Collectively, these guidelines aim to minimize the environmental and health impacts of chemical production and use while enhancing efficiency and reducing costs. Specifically, each principle is detailed as shown in Fig.1.1.

The first principle, **Prevention**, is the prevention of waste. The principle aims to minimize waste by designing chemical processes that do not produce harmful substances, thereby reducing environmental impact and associated costs.

The second principle, **Atom Economy** (AE), or so-called atom efficiency, was introduced by Barry Trost in 1990 to emphasize the efficient use of raw materials to maximize the number of atoms in the final product. AE is calculated by dividing the molecular weight (MW) of the desired product by the total MW of all reactants used in the reaction. A high AE ratio indicates a more efficient reaction.

The third principle, **Less Hazardous Chemical Syntheses**, urges scientists to develop methods that use and produce substances with minimal toxicity to human health and the environment. The fourth principle, **Designing Safer Chemicals**, emphasizes reducing the toxicity of the chemical products themselves. Similarly, the fifth principle, **Safer Solvents and Auxiliaries**, focuses on eliminating the use of hazardous auxiliary substances, such as solvents.

Next, the sixth principle, **Design for Energy Efficiency**, and the seventh principle, **Use of Renewable Feedstocks**, both highlight the need to optimize the energy requirements of chemical processes and to use renewable resources wherever possible.

The eighth principle, **Reduce Derivatives**, refers to avoiding the use of blocking groups, protection/deprotection steps, or temporary modifications of chemical structures during synthesis. This is due to the fact that these steps often require additional reagents and can generate waste, which is contrary to the goals of green chemistry.

The ninth principle, **Catalysis**, promotes the use of catalytic processes to achieve high selectivity and yield in chemical reactions to reduce waste and energy consumption.

**Design for Degradation**, the tenth principle, ensures that chemical products break down into

harmless substances at the end of their use, preventing environmental persistence. This helps reduce the environmental impact of chemical products and processes, making them compatible with natural biodegradation processes.

**Real-time Analysis for Pollution Prevention** calls for the development of analytical methods that enable real-time monitoring and control of processes to prevent pollution before it occurs.

Finally, **Inherently Safer Chemistry for Accident Prevention** focuses on selecting substances and conditions that minimize the potential for chemical accidents, such as releases, explosions, and fires.

Together, the twelve principles of green chemistry form the foundation of this field, integrating sustainability into chemical design and production. To illustrate their practical application, the following sections review selected green technologies in green chemistry. While this review cannot cover all of the developed experiments and technologies, it highlights a few standout examples, particularly those relevant to the carbon capture application discussed in Chapter 2 of this thesis. Collectively, these examples demonstrate the integration of green chemistry principles into innovative solutions that promote sustainable development and environmental protection.

### 1.2.3 Green Technologies

Utilizing advanced technologies and innovative practices promotes a more sustainable and eco-friendly approach to energy and materials. Among the various green chemistry technologies, several stand out for their significant impact and potential for future development, especially carbon capture, photovoltaics, and photocatalysis.

## 1.2.3.1 Carbon Capture

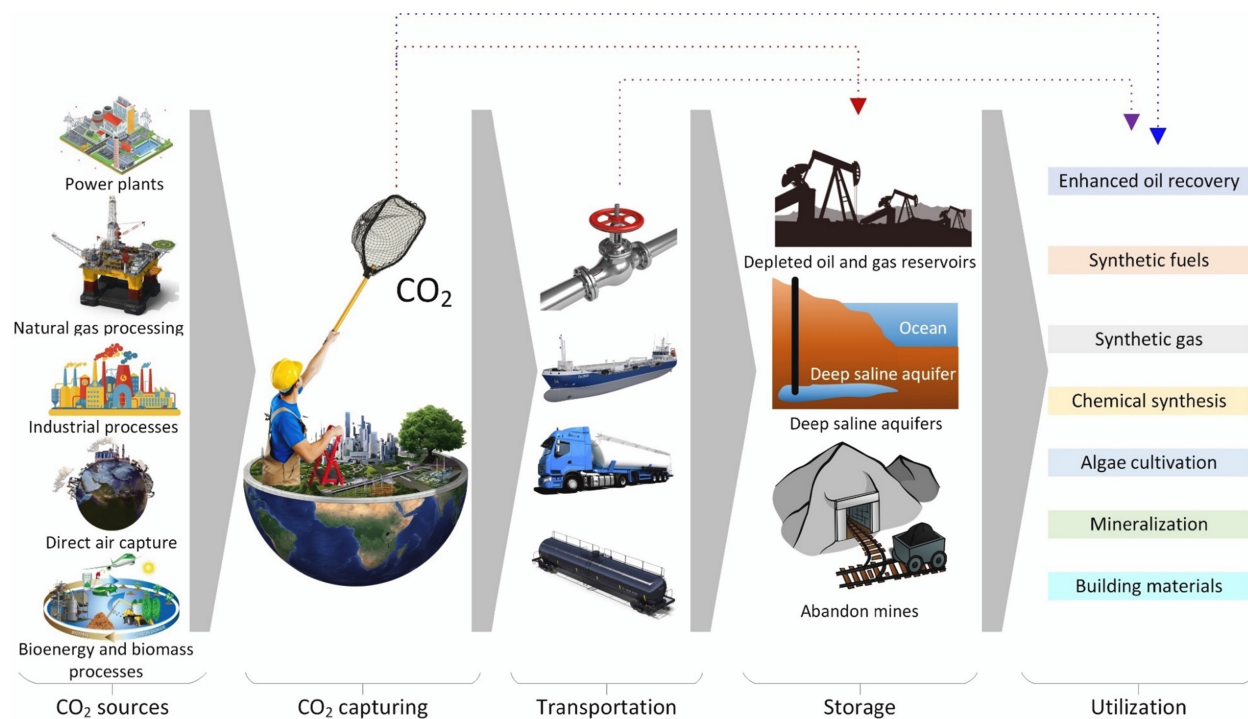


Figure 1.2: A comprehensive illustration of carbon capturing, transportation, storage and utilization ecosystem: from source to utilization. The figure is reproduced from Goren et al.<sup>8</sup>

Carbon capture is a critical and emerging technology aimed at addressing climate change by trapping carbon dioxide (CO<sub>2</sub>) emissions from large sources such as fossil fuel power plants and industrial facilities before they can enter the atmosphere (Fig.1.2). The process involves capturing CO<sub>2</sub> from plenty of sources, including exhaust streams, atmospheric air, oceans, etc., without interrupting the operations of existing systems that create carbon emissions<sup>8</sup>. Once captured, the CO<sub>2</sub> is then transported via pipelines or other methods and then either stored in underground geological formations or utilized in various industrial applications such as synthetic fuels and gas, concrete, ammonium bicarbonate, etc.<sup>9</sup>. The technology contains two approaches: direct capture (pre-combustion, post-combustion, and oxy-combustion) and indirect capture (reforestation,

enhanced weathering, bio-energy with carbon capture, and agricultural practices), each with vast degrees of development and implementation<sup>8</sup>. Throughout these, post-combustion techniques, which use physical and chemical methods to separate and selectively enrich CO<sub>2</sub> from flue gases emitted by combustion equipment, are the most widely adopted on a commercial scale. Fig.1.3 summarizes the main technologies and solvents used for CO<sub>2</sub> separation, including absorption, adsorption, membrane systems, gas hydrate crystallization, and cryogenic separation. While solvents are effectively used in chemical and physical absorption, natural and synthesized porous mediums are used in adsorption through various bed configurations<sup>10</sup>.

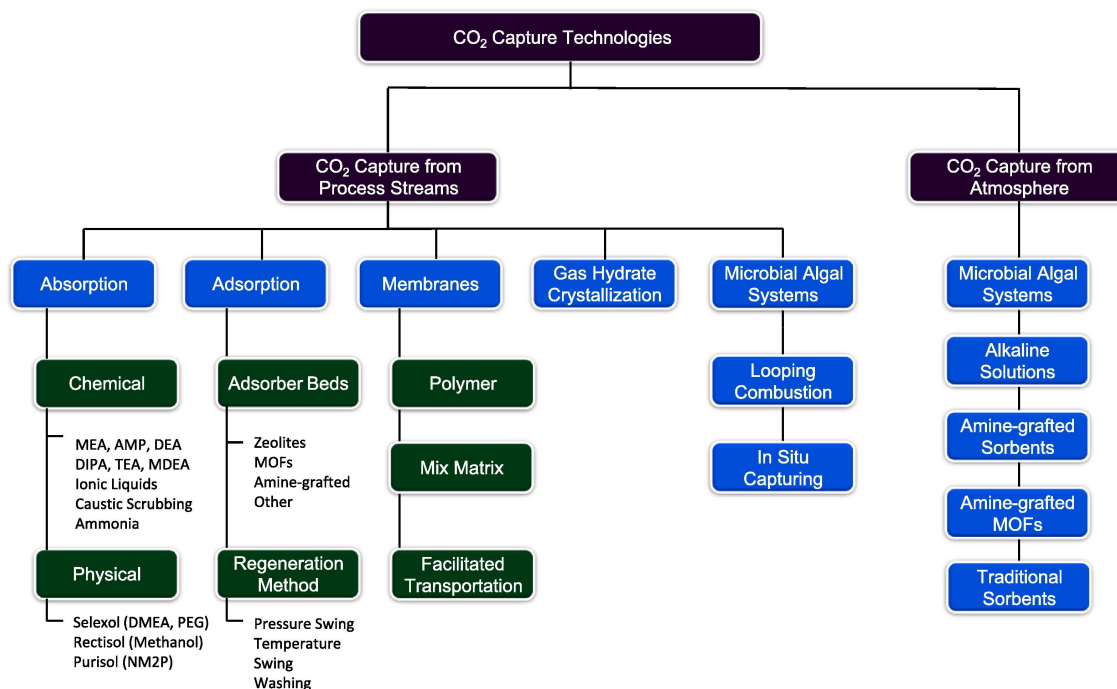


Figure 1.3: Main CO<sub>2</sub> capture technologies. The figure is reproduced from Hekmatmehr et. al.<sup>10</sup>

The design of effective carbon capture materials offers numerous opportunities for capturing and storing carbon more efficiently. Current developments in carbon capture technology focus on enhancing efficiency, scalability, and cost-effectiveness.

Type of Adsorbent	Adsorbents	Advantages	Disadvantages
<i>Chemisorbents</i>	Amine-based sorbents	Low regeneration energy High adsorption capacity in case of high amine and nitrogen content Stable materials Fast adsorption of carbon dioxide Multiuse sorbents	Expensive synthetic material
	Metal oxides and metal oxides-based sorbents	Common for pre-combustion of CO <sub>2</sub> Cost-effective Abundant materials Low toxic substance Durable after various cycles The operation temperature is moderate to high	Require long reaction time Require high energy for regeneration
	Alkali-metal adsorbents	Low regeneration energy Cost-effective Ability to operate at low temperature below 200 °C	Slow operation adsorbents Durable Irreversible adsorbents in the presence of SO <sub>2</sub> and HCl
<i>Physisorbents</i>	Zeolites	High adsorption capacity Porous materials Large surface area High stability	Low selectivity of CO <sub>2</sub> Large decrease in adsorption with slight increase in temperature
	Carbonaceous materials	Excellent thermal stability Tolerance to moisture Cost-effective Low adsorption operating temperature Abundancy Good conductivity Large surface area Suitable pore sizes and volumes	Low for selectivity to CO <sub>2</sub> High thermal sensitivity
	Mesoporous silica materials	Tuneable structure Good thermal and mechanical stability Large surface area Porous structures Low cost	Low adsorption capacity in the absence of functionalities
	MOFs	Uniform and tuneable structures Large surface area Ultrahigh porosity Easy functionalization Chemical and thermal stability	Low adsorption capacity at low pressure Sensitive to moisture Sensitive to mixture of gases Expensive generation procedures

Figure 1.4: Pros and cons of different types of carbon dioxide adsorbents. The figure is reproduced from Allangawi et al.<sup>11</sup>

One commonly used group of sorbents is amine-based solutions, which effectively remove CO<sub>2</sub>

from flue gas through chemical reactions with amines. Primary amines, or monoethanolamine (MEA), are favored for their fast reaction rates and high absorption capacity, followed by secondary, tertiary, hindered amines, and polyamines for their enhanced properties<sup>12</sup>. However, drawbacks such as degradation, corrosion, and high thermal regeneration costs necessitate innovations to overcome these challenges. Blended amines, phase-separating absorbents, and water-lean solvents have been developed to improve capture efficiency and reduce energy consumption<sup>11,12</sup>. Despite these advancements, further research is required to fully address these difficulties.

Another promising candidate for CO<sub>2</sub> absorption is metal oxides, such as calcium oxide (CaO), magnesium oxide (MgO), TiO<sub>2</sub>, and their various combinations. These materials are widely used due to their ability to react with CO<sub>2</sub> to form metal carbonates, enabling a cyclic process where CO<sub>2</sub> can be thermally desorbed and the sorbent regenerated<sup>13,14</sup>. A key advanced carbon capture technology involving metal oxides is high-temperature solid looping, which employs reversible chemical reactions at elevated temperatures for efficient CO<sub>2</sub> capture<sup>15,16</sup>. This includes chemical looping combustion (CLC), where oxygen carriers facilitate CO<sub>2</sub> capture through combustion, reforming, or hydrogen production, and calcium looping (CaL), where CO<sub>2</sub> reacts with CaO to form calcium carbonate, which is then heated to release CO<sub>2</sub> and regenerate CaO. These methods offer flexible and efficient solutions for carbon capture, particularly in industrial applications. Additionally, combining metal oxides with other catalytic components (e.g., Ni, Fe, Cu, etc.) creates dual-function materials (DFMs)<sup>17-19</sup>, which can capture and convert CO<sub>2</sub> to value-added products. While metal oxides are cost-effective, less toxic than zeolites and MOFs, and demonstrate high CO<sub>2</sub> selectivity at elevated temperatures, they face challenges such as rapid saturation and high energy consumption during regeneration<sup>14</sup>.

Lastly, porous materials, such as zeolites, MOFs, and carbon-based materials like activated

carbon and graphene, are gaining significant attention for carbon capture applications.

Zeolites, a class of microporous aluminosilicates, are recognized as benchmark adsorbents for CO<sub>2</sub> capture due to their excellent adsorption kinetics, thermal stability, and molecular sieving capabilities<sup>14,20</sup>. Their performance in pressure swing adsorption (PSA) and vacuum swing adsorption (VSA) is attributed to their efficiency in CO<sub>2</sub> adsorption at low temperatures<sup>21,22</sup>. However, a well-known limitation of zeolites is their reduced CO<sub>2</sub> adsorption capacity at elevated temperatures, which diminishes their selectivity for CO<sub>2</sub> in the presence of other gases. Additionally, their necessity for higher temperatures during regeneration restricts their practical application in large-scale carbon capture processes. Furthermore, zeolites are highly susceptible to degradation upon exposure to water vapor, which adversely affects their performance in humid environments. In response to these challenges, advancements in green technologies have emerged to improve the sustainability and performance of zeolites, aligning with the global shift towards clean energy and environmental preservation. Sustainable zeolite synthesis from waste and renewable materials, along with advancements in green synthesis techniques, has further reinforced their role in carbon capture. Recent innovations in zeolite synthesis include ambient pressure hydrothermal processes, which reduce costs and safety risks, and microwave and ultrasonic-assisted methods, which accelerate synthesis while improving purity<sup>23,24</sup>. Additional methods, such as vacuum-assisted synthesis and radical routes, increase efficiency and reduce dependence on organic templates. The incorporation of seed crystals enhances crystallization speed and product control. Collectively, these green technologies lower energy consumption, minimize waste, and support the sustainability of zeolite production, aligning with environmental goals.

Carbon-based porous materials are highly valued for their extensive surface area, adjustable pore size, and robust thermal and chemical stability, making them essential in applications such

as energy storage, catalysis, and gas separation<sup>13,25</sup>. Several examples include activated carbon, carbon nanotubes, carbon nanofibers, graphene, and carbon aerogels, each with unique properties<sup>26</sup>. Their inherent porosity enables efficient adsorption, particularly advantageous for carbon capture. Activated carbon, available in granular, powdered, fiber-based, and monolithic forms, is produced through physical or chemical activation processes that enhance its porous structure<sup>27</sup>. This versatility makes it an effective and adaptable choice for capturing CO<sub>2</sub> in both environmental and industrial settings. Activated carbon is widely used as a CO<sub>2</sub> collection agent due to its low cost, exceptional thermal stability, wide availability, and minimal susceptibility to moisture. Carbon nanotubes are recognized for their exceptional mechanical strength and electrical conductivity, making them suitable for applications in electronics and composite materials<sup>27</sup>. Graphene aerogels, on the other hand, merge the remarkable properties of graphene with a porous architecture, offering outstanding thermal and electrical conductivity<sup>28</sup>. Similarly, ultra-light carbon aerogels, characterized by a high degree of porosity, are ideal for use in supercapacitors and insulation<sup>28</sup>. In the field of carbon capture, green synthesis methods emphasize sustainable approaches that minimize environmental impact. One significant method is the carbonization of biomass, where natural materials such as wood, algae, or agricultural waste are transformed into porous carbon through controlled pyrolysis<sup>28</sup>. The introduction of heteroatom doping (e.g. nitrogen, sulfur) and multi-atom co-doping significantly enhances the wettability and alkalinity of porous carbon, increasing its CO<sub>2</sub> trapping capacity<sup>29</sup>. Specifically, carbon molecular sieve (CMS) can enhance CO<sub>2</sub> capture by modifying its pores through pyrolysis, partial gasification, and pore shrinkage, as well as surface functionalization and metal impregnation. CMS can also be engineered to achieve a uniform distribution of pore sizes, optimizing its performance<sup>29</sup>. Despite their advantages, carbon-based porous materials have some limitations, such as lower toughness and strength compared to hierarchically structured ceramic and

metal porous materials.

MOFs are advanced hybrid materials with exceptional properties for gas adsorption, including CO<sub>2</sub> capture. These materials feature a porous crystalline structure formed by metal nodes interconnected with organic ligands, resulting in frameworks with highly tunable pore sizes<sup>21</sup>. MOFs distinguish themselves from traditional adsorbents such as zeolites and activated carbon due to their low density, extensive surface areas, high thermal stability, and customizable chemical functionalities. These attributes enhance their effectiveness for CO<sub>2</sub> capture, offering significant advantages over conventional materials. Their adaptability extends to CO<sub>2</sub> separation, delivering outstanding performance even in the presence of water vapor. MOFs can be classified into various types based on their structural properties, such as rigid, dynamic, or surface-functionalized<sup>20</sup>. Recent advances in green technologies for MOF synthesis have focused on enhancing both sustainability and efficiency. This includes electrochemical, sonochemical, mechanical, spray drying, and continuous flow techniques<sup>25</sup>. Electrochemical synthesis offers mild reaction conditions, high yields, and reduced costs, while sonochemical methods enhance crystallinity and CO<sub>2</sub> capture efficiency with simpler processes. Mechanochemical synthesis, involving grinding or ball milling, minimizes solvent use and generates easily removable by-products, whereas spray drying is cost-effective and scalable, reducing energy and purification needs. Continuous flow synthesis allows for rapid, controlled production with reduced solvent consumption and high-quality outcomes. Functionalization strategies, such as incorporating open metal sites, Lewis basic sites, and polar functional groups, have further refined MOFs for CO<sub>2</sub> capture by boosting their adsorption capacities and selectivity<sup>25,30</sup>. The development of isorecticular MOFs<sup>31</sup> and the use of seed crystals have also contributed to improved performance by tailoring the pore sizes and functional groups. Furthermore, the development of MOFs that incorporate carbon-based components offers efficient CO<sub>2</sub> adsorption while promoting

the use of sustainable materials and energy-efficient processes<sup>13</sup>. Despite their promising attributes, MOFs face challenges such as high production costs and their sensitivity to moisture. Ongoing research aims to overcome these hurdles by developing more cost-effective synthesis methods and enhancing operational stability.

Despite the challenges of high costs, significant energy consumption, and the need for extensive CO<sub>2</sub> transport and storage infrastructure<sup>10</sup>, as well as concerns about the long-term safety of CO<sub>2</sub> storage and the limitations of current materials, there are promising opportunities in the field. Integrating carbon capture with renewable energy sources can reduce both costs and the carbon footprint of energy production. Additionally, advancements in storage methods and potential economic incentives offer further motivation for development. By addressing these challenges and leveraging emerging opportunities, carbon capture technology can advance significantly and play a crucial role in climate mitigation efforts.

### **1.2.3.2 Photovoltaics**

Among renewable energy resources such as wind energy, ocean thermal, geothermal plants, and solar energy, solar photovoltaic (PV) stands out as the most promising system in the power production sector for future energy technology. Indeed, they are user-friendly and offer the design flexibility to generate power from 10W to more than 1GW, making their market highly global<sup>32</sup>. Photovoltaics can be simply defined as the direct conversion of sunlight to electricity using thin layers of semiconductor materials, which possess properties intermediate between metals and insulators. When these semiconductors are irradiated with photons, they generate direct current electrical power, measured in watts (W) or kilowatts (kW)<sup>33</sup>. Silicon, the keystone of microelectronics and the information age, is the most widely used semiconductor.

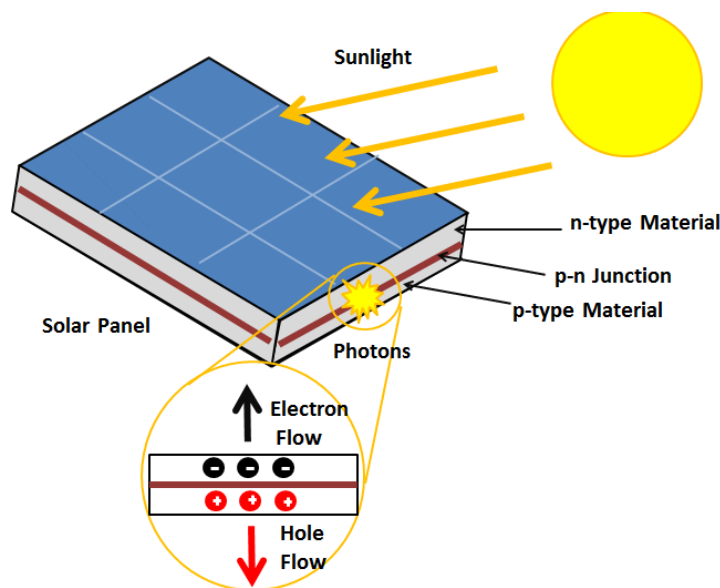


Figure 1.5: A diagram showing the photovoltaic effect. The figure is reproduced from Donev et al.<sup>34</sup>

A photovoltaic cell functions as a "quantum device" by converting photons into electrons through the photovoltaic effect<sup>33</sup>, as shown in Fig.1.5. The core component is usually a silicon wafer, which is treated with a thin layer of another material to create a p-n (positive-negative) junction that enables electric flow. When sunlight hits the semiconductor material, it excites electrons, forming electron-hole pairs. An internal electric field then drives these charges to opposite sides of the cell, where metal conductive plates collect the electrons to produce an electrical current. This process continues as long as light is present, eliminating the need for recharging batteries. Despite being efficient, wafer-based PV cells are material-intensive and costly. In contrast, thin-film PV cell technology reduces the amount of semiconductor material required by depositing thin layers of PV material onto a substrate like glass, plastic, or metal<sup>35</sup>. This option enables the use of a wider variety of materials like cadmium telluride (CdTe), copper indium gallium diselenide (CIGS), and copper zinc tin sulfide (CZTS) rather than single-crystal silicon, amorphous silicon, or polycrystalline

silicon. Thin-film cells are usually lighter and more flexible compared to conventional silicon cells, making them ideal for building-integrated photovoltaics and portable solar panels. While having lower efficiency compared to silicon-based cells, thin-film PVs<sup>35,36</sup> offer advantages in reduced material usage, lower production costs, and scalable manufacturing.

Perovskite solar cells (PSCs)<sup>37-43</sup> have attracted significant interest in the field of photovoltaic materials because of their remarkable power conversion efficiencies, which have surged from 3.8% in 2009 to over 25% recently. This significant advancement is complemented by the ease of accessing components and the potential for low-cost production. Named after the mineral  $\text{CaTiO}_3$ , metal halide perovskites feature a cubic crystal structure and follow the general formula  $\text{ABX}_3$ , where A is an organic cation, B is a metal cation, and X is a halide anion. They are recognized for their strong absorption, tunable bandgaps, and cost-effective production<sup>41</sup>. Traditional perovskites often contain lead, however, leading to environmental concerns. Recent green advancements focus on lead-free alternatives, such as bismuth-based and tin-based perovskites, and lead-free double PV cells<sup>43,44</sup>, while also improving material stability and durability through novel fabrication techniques<sup>45</sup>. Various other materials like organic photovoltaics (OPVs)<sup>42</sup>, which use conjugated polymers and small molecules, or quantum dots<sup>44,46</sup> such as cadmium selenide ( $\text{CdSe}$ ), cadmium sulfide ( $\text{CdS}$ ), and copper indium diselenide ( $\text{CuInSe}_2$ ), are noted for their lightweight properties and tunable bandgaps. Additionally, 2D materials like graphene and transition metal dichalcogenides (TMDs)<sup>47,48</sup>, along with hybrid organic-inorganic solar cells such as mixed-halide perovskites and organic-inorganic hybrids<sup>44</sup>, represent thriving and promising fields of study focused on advancing photovoltaic technology.

In addition to novel materials, green advancements in solar technology encompass various techniques and innovations. Green solvents<sup>36,40,49</sup> such as triethyl phosphate (TEP), along with

green antisolvents like isopropanol (IPA) and isobutanol, are increasingly used to reduce the toxicity and environmental impact of solar cell manufacturing. While not entirely green, vacuum-assisted solution processing and spin coating<sup>36,41,49</sup> promote sustainability by enhancing material use and reducing waste. Vacuum-assisted solution processing improves thin-film deposition efficiency and reduces defects, leading to less material waste. Spin coating uses solvents efficiently, applies thin films precisely, and reduces overall solvent consumption.

A significant challenge in photovoltaic technology is the high operational temperature of PV cells, which can adversely affect performance and power output<sup>32</sup>. To address this, various cooling strategies have been developed to improve efficiency across different geographical locations. These strategies aim to mitigate the effects of high temperatures and enhance the overall performance of solar energy systems<sup>46</sup>.

### 1.2.3.3 Photocatalysis

Photocatalysis is a catalytic process that utilizes light energy to initiate chemical reactions. It involves the activation of a catalyst by light, leading to the generation of reactive species that can drive various chemical transformations<sup>50</sup>. Photocatalysis can be categorized into two main types: homogeneous and heterogeneous. In homogeneous photocatalysis, the catalyst and reactants are in the same phase, typically in solution, which enables efficient light absorption and reaction initiation. Conversely, heterogeneous photocatalysis involves a catalyst that is in a different phase from the reactants, often as a solid material or surface, which facilitates the separation and recovery of the catalyst for reuse. The process generally involves several key steps and mechanisms, as displayed in Fig.1.6. First, the photocatalyst absorbs light, creating electron ( $e^-$ ) - hole ( $h^+$ ) pairs with electrons in the conduction band (CB) and holes in the valence band (VB). Next, the charges

separate and migrate to the catalyst's surface, where they drive surface reactions, resulting in chemical transformations<sup>51</sup>.

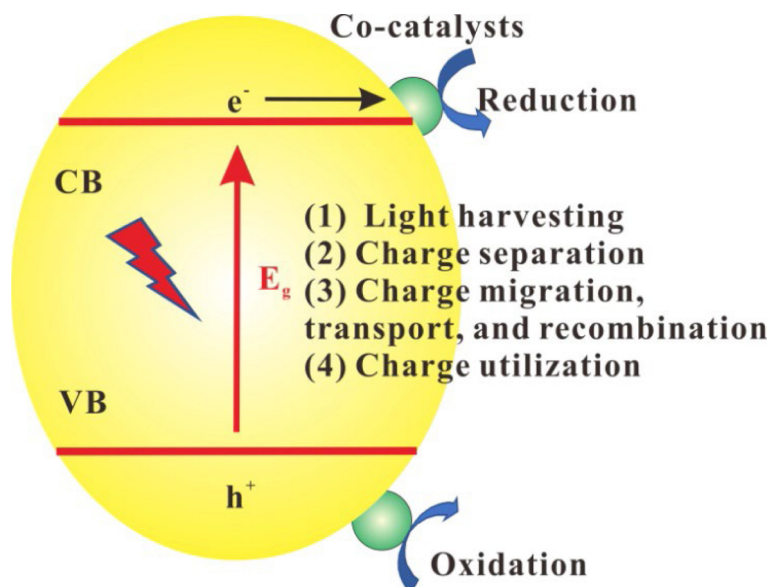


Figure 1.6: The four main steps in photocatalysis process. The figure is reproduced from Liao et al.<sup>51</sup>

As a rapidly expanding field of research, photocatalysis offers vast potential for applications such as water splitting, air cleaning, and pollutant degradation, thereby contributing to environmental sustainability. This process provides an eco-friendly alternative for various industrial applications, with the catalysts accelerating reactions without being consumed or altered, distinguishing them from thermal catalysts that rely on heat rather than light.

Traditional photocatalysts, such as  $TiO_2$  and zinc oxide ( $ZnO$ ), have been extensively used due to their stability, low cost, and effectiveness in generating electron-hole pairs under UV light<sup>52</sup>. Nonetheless, these metal oxides limit visible light absorption and relatively slow down the charge carrier separation, reducing efficiency. Recent developments in photocatalysis have focused on overcoming these limitations by exploring novel materials. Non-toxic metal-free photocatalytic materials, such as carbon-based nanomaterials (e.g., graphene oxide, graphitic carbon nitride

g-C<sub>3</sub>N<sub>4</sub>)<sup>53,54</sup>, COFs and MOFs<sup>55,56</sup>, as well as earth-abundant semiconductors (e.g., Fe<sub>2</sub>O<sub>3</sub>)<sup>57</sup> aim to enhance photocatalytic performance under visible light, improve the sustainability of the processes, and reduce the reliance on rare or toxic elements, promoting more eco-friendly and efficient photocatalytic applications. On top of that, coordination compounds (e.g., polypyridine complex [Ru(bpy)<sub>3</sub>]<sup>2+</sup>, multicarboxylate ligands), dyes and pigments (anthraquinones, thiazines, natural dyes, azo dyes)<sup>50</sup> with non-toxic metals are also used. These materials, especially with light-sensitive properties and the photoredox characteristics of coordination compounds, are shown to excel in photocatalytic applications such as organic pollutant degradation, CO<sub>2</sub> reduction, and Cr(VI) reduction. Furthermore, recent advancements in photocatalyst design include strategies like doping, dye sensitization, heterostructure formation, and modifications to  $\pi$ -conjugated architectures<sup>50</sup>, all aimed at improving performance under visible light.

Despite its potential for sustainable chemistry, photocatalysis faces several challenges. Key issues include optimizing photocatalytic systems for improved activity and selectivity, ensuring scalability and cost-effectiveness, and understanding the mechanistic aspects of photocatalytic reactions. Addressing these challenges is essential for integrating photocatalysis into green technologies and realizing its full potential in industrial applications.

## 1.3 Computational Methods for Green Chemistry Applications

### 1.3.1 Computational Chemistry Introduction

Computational chemistry is a multidisciplinary field that utilizes computer simulations and theoretical models to study, predict, and solve chemical problems, providing insights into the

properties and behaviors of chemical systems<sup>58</sup>. The methods and techniques in computational chemistry serve as tools for exploring a wide range of chemical phenomena. Key approaches include molecular mechanics, ab initio methods, semi-empirical approaches, and density functional theory (DFT). This diverse array of computational methods is especially valuable in the field of green chemistry, where the focus is on designing chemical processes that are both environmentally friendly and efficient. These methods allow for the accurate prediction of chemical outcomes before laboratory experiments are conducted, helping to identify the most sustainable and effective approaches to chemical synthesis. Within the broad spectrum of computational techniques, DFT is a powerful tool in green chemistry, balancing efficiency and accuracy. It effectively models and optimizes environmentally friendly chemical processes, predicting reaction pathways, catalysts, and material properties. DFT is especially impactful in carbon capture, photovoltaics, and photocatalysis, guiding the development of efficient, and eco-friendly technologies.

Given the extensive applications of DFT across numerous fields, and its longstanding role as a powerful computational tool, this thesis introduction highlights only a few examples to illustrate its significance and utility, particularly in the context of green chemistry.

## **1.3.2 Computational Chemistry Utility**

### **1.3.2.1 Carbon Capture**

In carbon capture applications, DFT first facilitates a detailed examination of interactions between CO<sub>2</sub> and various porous materials, offering critical insights into the binding mechanisms. This includes information about binding energies, bond strengths, and the electronic structures at adsorption sites. For materials with complex or poorly understood microscopic behaviors, traditional

experimental approaches often struggle to elucidate the precise mechanisms of CO<sub>2</sub> adsorption. In such cases, DFT offers a deeper understanding of the molecular and electronic processes that govern adsorption, which are challenging to discern experimentally. The CO<sub>2</sub> adsorption with alkyldiamine-grafted Mg<sub>2</sub>(dobpdc) MOFs serves as an example. While experiments confirm that CO<sub>2</sub> capture by ethylenediamine (en)-appended Mg<sub>2</sub>(dobpdc) forms an ammonium carbamate, the underlying mechanism remains intricate. Zhang et al.<sup>59</sup> utilized DFT modeling to address this challenge by calculating binding energies and CO<sub>2</sub> adsorption energies through geometry optimization. Additionally, they employed the climbing-image nudged elastic band (CI-NEB) method to trace the minimum-energy path of the reaction and studied the transition states along with the proton transfer between CO<sub>2</sub> and en-Mg<sub>2</sub>(dobpdc), thus providing a comprehensive understanding of the binding mechanisms and pathways for CO<sub>2</sub> capture in these amine - grafted MOFs. Similarly, through DFT calculations, investigations of the carbon adsorption sites in different MOF materials shed light on how CO<sub>2</sub> interacts with these MOFs at the molecular level<sup>60-63</sup>.

Secondly, DFT enables the evaluation of diverse functional groups and structural modifications to enhance adsorption performance. Novel materials synthesized through green techniques, as discussed in section 1.2.3, can be easily examined with DFT given a valid geometric electronic structure. Ha et al.<sup>64</sup> employed DFT to investigate the effects of alkali-metal doping in one of the most extensively studied MOFs, MOF-5. By introducing an alkali-metal atom (Li, Na, or K) above the central benzene ring, the study rapidly generated four test models and determined that K-doping was the most thermodynamically favorable, resulting in the lowest adsorption energy. Similarly, nitrogen doping in mesoporous carbon has been shown to significantly enhance CO<sub>2</sub> adsorption and improve selectivity between CO<sub>2</sub> and N<sub>2</sub>, attributed to the stronger interactions between CO<sub>2</sub> and the nitrogen-doped framework. Furthermore, research on surface functionalization of porous carbons

has demonstrated increased selectivity for both CO<sub>2</sub>/CH<sub>4</sub> and CO<sub>2</sub>/N<sub>2</sub> mixtures, underscoring the importance of functional group modifications in optimizing separation efficiency. These examples underscore DFT's critical role in guiding the development of more effective materials for carbon capture.<sup>65</sup>

Finally, the vast diversity of potential MOFs, arising from different combinations of linkers, nodes, and topologies, has resulted in extensive databases such as CoRE MOFs and CSD MOFs, which contain thousands of structures. DFT efficiently screens these materials for carbon capture applications and greatly reduces reliance on time-consuming and costly experimental testing. For example, a multi-scale modeling approach utilized DFT to screen the CoRE-MOF-2019 database for carbon capture under wet flue gas conditions, revealing MOFs with high CO<sub>2</sub> uptake capacity and selectivity in the presence of water vapor.<sup>66</sup> Similarly, DFT screening identified M-elements as selective CO<sub>2</sub> attractors, with elements possessing empty d orbitals demonstrating potential for selective CO<sub>2</sub> capture from flue gases at low pressures.<sup>67</sup> Additionally, DFT has been applied to investigate over 30,000 MOFs, showcasing its ability to manage extensive theoretical datasets and advance material discovery for carbon capture.<sup>68</sup>

### 1.3.2.2 Photovoltaics

The application of DFT in PV encompasses several critical aspects, including exciton dynamics, charge transfer, and interfacial interactions. These elements are interconnected and collectively influence the efficiency and reliability of PV devices. By employing DFT to investigate these components, researchers can optimize material properties and device architectures, ultimately enhancing energy conversion processes.

Upon photon absorption, excitons—bound states consisting of an excited electron and a cor-

responding hole—are generated and diffuse toward the interface between donor and acceptor materials, initiating the charge separation process. The dissociation of excitons plays a critical role in determining the overall efficiency of photovoltaic devices, as the dynamics of excitons, including their formation, migration, and dissociation, directly impact energy conversion efficiency<sup>69</sup>. DFT, often combined with time-dependent DFT (TDDFT) or molecular dynamics (MD), can investigate exciton dynamics by computing key excitonic properties, such as electron-hole binding energies and exciton diffusion lengths, as well as by examining the effects of material morphology on exciton transport<sup>70–74</sup>. For instance, DFT-1/2 was employed to optimize the crystal structures of lead-free, quasi-2D perovskites  $\text{Cs}_2\text{ZnX}$  ( $\text{X} = \text{Cl}_4, \text{Br}_2\text{Cl}_2, \text{I}_2\text{Cl}_2$ ), followed by band gap corrections to address the typical bandgap underestimation in standard DFT.<sup>74</sup> Additionally, DFT provided the basis for constructing the tight-binding Hamiltonian used in the Bethe-Salpeter Equation to calculate exciton binding energies and optical properties. The study found that the exciton binding energy of  $\text{Cs}_2\text{PbI}_2\text{Cl}_2$  matched experimental data, and DFT calculations helped identify excitonic effects, which are crucial for improving the optoelectronic properties and photovoltaic performance of the perovskite materials.

The separation of charges, where an exciton dissociates into a free electron and a free hole within a solar cell constitutes charge transfer (CT). In OPVs, this typically involves the dissociation of excitons at the donor-acceptor interface, while in inorganic PV, free charge carriers are generated directly from the semiconductor's band structure. The efficiency of CT is crucial for the overall performance of PV devices, as it affects energy conversion efficiency, device architecture, and long-term stability. Optimizing CT processes enhances free carrier generation and minimizes recombination losses, thereby advancing the efficiency and reliability of solar energy technologies. DFT facilitates the calculation of energy levels, molecular orbital distributions, and the alignment of energy levels at

interfaces. This allows for the simulation of interactions between donor and acceptor materials, helping to identify optimal combinations and configurations that enhance effective charge transfer. Specifically, Majeed et al.<sup>75</sup> apply DFT to explore the electronic, optical, and CT properties of seven newly designed molecules based on the indacenodithiophene core (IDTV-ThIC) to enhance the photovoltaic performance of organic solar cells (OSCs). DFT was used to calculate the energy levels of frontier orbitals (HOMO and LUMO), assess charge transfer efficiency through reorganization energy, and predict optical properties such as absorption spectra and exciton binding energies. These DFT calculations helped identify molecular modifications that improve charge mobility, enhance charge separation, and lower energy gaps, thereby optimizing the electronic and optical properties of the new IDTV-ThIC-based molecules for better photovoltaic performance in OSCs. The designed molecules, particularly DT1 (1-dicyanomethylene-2-methylene-3-oxo-indan-5,6-dicarbonitrile), DT4 (2-(6-Methylene-7-oxo-6,7- dihydro-1-thia-s-indacen-5-ylidene)-malononitrile), and DT5 (2-(1-Methylsulfanyl-6-oxo-5,6- dihydro-cyclopenta[c]thiophen-4-ylidene)-malononitrile), showed improved charge mobility, lower exciton binding energy, and enhanced open-circuit voltage compared to the reference IDTV-ThIC molecule.

Interfacial interactions are crucial for processes like charge transfer and exciton dissociation in photovoltaic devices. These interactions at the electronic and chemical interfaces directly influence charge separation and transfer, impacting the power conversion efficiency. DFT facilitates this analysis by modeling the electronic structure of heterojunctions and assessing interfacial interactions<sup>76–78</sup>. As an example, the study conducted by Ayoub and Lagowski<sup>76</sup> have employed DFT with the dispersion-corrected B97D3 to investigate the interfacial properties of polymer/fullerene heterojunctions in OSCs. DFT was used to optimize the geometries of the polymer and fullerene pairs, calculate their binding energies, and determine the electronic properties at the interface, such

as LUMO and HOMO offsets. The results showed that optimal interfacial interactions, characterized by a low LUMO offset and a high binding energy, enhance charge transfer and stability, which are crucial for improving the performance and power conversion efficiency of OSCs. These findings demonstrate that DFT calculations are effective in studying interfacial interactions, offering insights that can guide the design of more efficient photovoltaic materials.

Through the integrated application of DFT across these three aspects- exciton dynamics, charge transfer, and interface analysis- researchers can develop more efficient and durable photovoltaic devices, paving the way for advancements in solar energy conversion.

### 1.3.2.3 Photocatalysis

In photocatalysis, DFT plays a critical role in examining the electronic structure of materials (band structure) and in exploring how reactions occur on the surface of photocatalysts (surface reaction mechanisms).

Band structure analysis focuses on the conduction and valence bands, which determine their ability to absorb light and generate charge carriers (electrons and holes) essential for photocatalytic reactions. By analyzing the band structure and electronic density of states, DFT helps optimize photocatalysts of interest for enhanced photocatalytic performance in reactions such as water splitting<sup>79–82</sup> and organic pollutant degradation<sup>83–86</sup>. As an example, DFT has been applied to study the electronic properties of novel metal-free photocatalysts like g-C<sub>3</sub>N<sub>4</sub><sup>87,88</sup>. In particular, Lin et al. applied DFT to conduct band gap analysis, density of states (DOS), partial density of states (PDOS), charge density difference, and work function calculations to investigate the photocatalytic performance of C and B doped g-C<sub>3</sub>N<sub>4</sub>/TiO<sub>2</sub> heterostructures<sup>80</sup>. The band gap, DOS and PDOS analysis of g-C<sub>3</sub>N<sub>4</sub>/TiO<sub>2</sub> heterostructures revealed that doping with C on the TiO<sub>2</sub> (101) surface

and B on the g-C<sub>3</sub>N<sub>4</sub> monolayer effectively reduced the bandgap, enhancing light absorption and making the material more suitable for visible-light-driven photocatalysis. The charge density difference calculation demonstrated effective charge separation across the interface, with electrons accumulating on TiO<sub>2</sub> and holes on g-C<sub>3</sub>N<sub>4</sub>, preventing recombination. Finally, the work function results indicated that the difference between the two materials generated an internal electric field, further driving charge transfer and boosting photocatalytic efficiency.

Surface reaction mechanisms, which involve the adsorption, reaction, and desorption of reactants on a photocatalyst's surface, are critical for optimizing catalytic efficiency. DFT is applied to model the adsorption energies and reaction pathways of reactants, offering insights into activation energy barriers and identifying the most favorable reaction sites.<sup>84,89,90</sup> For instance, DFT has been employed to explore the electronic structures of TiO<sub>2</sub>-based, g-C<sub>3</sub>N<sub>4</sub>-based, and MOF/COF-based photocatalysts to improve the photocatalytic reduction of CO<sub>2</sub> to valuable products, such as methane (CH<sub>4</sub>) and carbon monoxide (CO)<sup>90</sup>. Through DFT calculations, the adsorption energies of CO<sub>2</sub> on these photocatalysts were analyzed, revealing stronger adsorption at specific active sites, which facilitates the capture and activation of CO<sub>2</sub>, key to initiate the reduction process. DFT also calculated the reaction energy barriers for key intermediates, showing that doping and surface modifications lowered these barriers, enhancing the conversion of CO<sub>2</sub> into CH<sub>4</sub> and CO. Furthermore, DFT provided crucial insights into charge transfer mechanisms, demonstrating efficient electron movement from the photocatalyst to the adsorbed CO<sub>2</sub>. This charge transfer is essential for reducing electron-hole recombination, which typically hampers photocatalytic efficiency. The DOS analysis further revealed how the electronic structure influenced reaction dynamics. Collectively, DFT results highlighted strong CO<sub>2</sub> adsorption, efficient charge transfer, and lower energy barriers, leading to improved photocatalytic performance.

These findings demonstrated that DFT effectively models surface reaction mechanisms, providing crucial insights into optimizing catalyst surfaces for improved photocatalytic CO<sub>2</sub> reduction.

## 1.4 Theoretical Methods for Green Chemistry Applications

### 1.4.1 DFT Overview

DFT is a quantum mechanical method used in physics and chemistry to investigate the electronic structure of many-body systems, particularly atoms, molecules, and condensed phases. Instead of directly solving the many-body Schrödinger equation, DFT simplifies the problem by focusing on the electron density, a function of only three spatial coordinates, rather than the wavefunction with  $3N$  coordinates needed for  $N$  electrons. This approach makes DFT computationally efficient while providing accurate predictions of properties such as energy, structure, and reactivity. Widely used in chemistry, materials science, and physics, DFT has become a fundamental tool for studying complex systems and designing new materials.

#### 1.4.1.1 Electronic Hamiltonian Derivation

The time-dependent Schrödinger equation (TDSE) is a fundamental equation in quantum mechanics that describes how the quantum state of a system evolves over time. It accounts for both spatial and temporal variations in the wavefunction (WF)  $\Phi$ , providing a complete picture of a system's dynamics:

$$i\hbar\frac{\partial}{\partial t}\Phi(\mathbf{R},\mathbf{r},t) = \hat{H}(\mathbf{R},\mathbf{r})\Phi(\mathbf{R},\mathbf{r},t) \quad (1.1)$$

where  $\Phi$  depends on the spatial coordinates of the electrons  $\mathbf{r}$ , the spatial coordinates of the nuclei  $\mathbf{R}$ , and time  $t$ . TDSE states that a tiny change in the state of the system with time can be obtained

by applying Hamiltonian  $\hat{H}$ , the operator that represents the total energy, to the state.  $\hat{H}$ , which includes both electronic and nuclear contributions, is given as the sum of  $\hat{T}_n$ ,  $\hat{T}_e$ , and  $\hat{U}(\mathbf{R}, \mathbf{r})$  as the kinetic energy of nuclei and electrons, and the potential energy of their Coulomb interactions, respectively. This Coulomb interaction term is further expressed as the electron-nuclei interaction  $\hat{U}_{ne}$ , the electron-electron repulsion  $\hat{U}_{ee}$ , and the nuclei-nuclei repulsion  $\hat{U}_{nn}$

$$\begin{aligned}\hat{H} &= \hat{T}_n + \hat{T}_e + \hat{U}(\mathbf{R}, \mathbf{r}) \\ &= \hat{T}_n + \hat{T}_e + \hat{U}_{ne} + \hat{U}_{ee} + \hat{U}_{nn} \\ &= - \sum_{a=1}^M \frac{\hbar^2}{2M_a} \nabla_a^2 - \sum_{i=1}^N \frac{\hbar^2}{2} \nabla_i^2 - \sum_{i=1}^N \sum_{a=1}^M \frac{Z_a}{|\mathbf{R}_a - \mathbf{r}_i|} + \frac{1}{2} \sum_{i,j=1}^N \frac{1}{|\mathbf{r}_i - \mathbf{r}_j|} + \frac{1}{2} \sum_{a,b=1}^M \frac{Z_a Z_b}{|\mathbf{R}_a - \mathbf{R}_b|}\end{aligned}\tag{1.2}$$

where  $N$  is the number of electrons,  $M$  is the number of nuclei,  $Z_a$  and  $M_a$  are the charge and mass of nucleus  $a$ . The solution to TDSE is the WF  $\Phi(\mathbf{R}, \mathbf{r}, t)$ , which describes how a quantum system evolves over time.  $\Phi(\mathbf{R}, \mathbf{r}, t)$  is essential for understanding time-dependent processes, such as chemical reactions and quantum interactions, and allows for the analysis of systems under time-varying conditions.

An effective strategy for addressing the TDSE is to decouple the spatial variables corresponding to electronic and nuclear motions. This approach is based on the observation that electrons, being much lighter and moving at much higher velocities, operate on a different timescale than the heavier, more slowly moving nuclei. This allows us to treat the nuclei as stationary and simplifies the TDSE into a time-independent Schrödinger equation (TISE) for the electrons, given by:

$$\begin{aligned}\hat{H}_e &\equiv \hat{T}_e + \hat{U}(\mathbf{R}, \mathbf{r}) \\ \hat{H}_e \phi(\mathbf{r}; \mathbf{R}) &= V_n(\mathbf{R}) \phi(\mathbf{r}; \mathbf{R})\end{aligned}\tag{1.3}$$

where  $\hat{H}_e$  is the electronic Hamiltonian that describes the behavior of electrons in the field of frozen nuclei. The electronic Hamiltonian plays a critical role in the foundation of DFT because it defines

the quantum mechanical interactions among electrons and nuclei. The main task of DFT is to find the eigenstates and eigenvalues of this Hamiltonian that determine the system's energy levels and electronic properties. As seen from Eq.(1.3),  $\hat{H}_e$  still depends on the position of the nuclei but not on their momenta, and electronic eigenvalues  $V_n(\mathbf{R})$ , also known as potential energy surfaces (PES), are dependent on the fixed nuclear coordinates  $\mathbf{R}$ . With these electronic eigenstates determined, the Born-Huang expansion<sup>91</sup> is then introduced to account for the interaction between nuclear and electronic motions, which time-dependent WF  $\Phi(\mathbf{R}, \mathbf{r}, t)$  can be written exactly in terms of the time-independent electronic WF  $\phi_m(\mathbf{r}; \mathbf{R})$  as:

$$\Phi(\mathbf{R}, \mathbf{r}, t) = \sum_m^{\infty} \phi_m(\mathbf{r}; \mathbf{R}) \chi_m(\mathbf{R}, t) \quad (1.4)$$

Here,  $\chi_m(\mathbf{R}, t)$  denotes the expansion coefficients representing the nuclear WF, which encapsulate information about how the nuclear positions change over time. Replacing the Born-Huang expansion in the initial the TDSE allows for the electronic degrees of freedom to be eliminated, resulting in only the nuclear wave functions being considered. This gives us the exact form of the TDSE for the nuclear wave functions:

$$\begin{aligned} i\hbar \frac{\partial}{\partial t} \chi_m(\mathbf{R}, t) &= \hat{H} \chi_m(\mathbf{R}, t) \\ &= \left[ \sum_a \frac{-\hbar^2}{2M_a} \nabla_a^2 + V_m(\mathbf{R}) \right] \chi_m(\mathbf{R}) + \\ &+ \sum_n \left[ \sum_a \frac{-\hbar^2}{2M_a} \left( \langle \phi_m | \nabla_a^2 | \phi_n \rangle + 2 \langle \phi_m | \nabla_a | \phi_n \rangle \nabla_a \right) \right] \chi_n(\mathbf{R}, t) \end{aligned} \quad (1.5)$$

In this equation, each nuclear component  $\chi_m(\mathbf{R}, t)$  changes in time under the influence of all other components on different PES. The second term is called nonadiabatic term, couples different electronic states and reflects how nuclear dynamics can involve transitions between electronic states during time evolution. This nonadiabatic behavior indicates that the system may not remain in a single electronic state but could transition to other states as it evolves.

To further simplify the TDSE, Born-Oppenheimer approximation is applied. It assumes that electrons adjust instantaneously to the positions of the moving nuclei, allowing for the nuclei to be treated as moving in a fixed potential. This greatly reduces the complexity of the problem by focusing on the nuclear dynamics and neglecting nonadiabatic coupling terms that would otherwise account for transitions between different electronic states:

$$i\hbar \frac{\partial}{\partial t} \chi_m(\mathbf{R}, \mathbf{t}) = \left[ \sum_a \frac{-\hbar^2}{2M_I} \nabla_a^2 + V_m(\mathbf{R}) \right] \chi_m(\mathbf{R}, \mathbf{t}) \quad (1.6)$$

The Born-Oppenheimer approximation is valid when electronic states are well-separated energetically and the electronic Hamiltonian changes only slightly with nuclear positions. If electronic states approach each other or if the Hamiltonian varies significantly, nonadiabatic effects become important, requiring a more complex treatment beyond the Born-Oppenheimer approximation.

#### 1.4.1.2 Hohenberg-Kohn Theorems

Formulated by Pierre Hohenberg and Walter Kohn in 1964, Hohenberg-Kohn (HK) theorems<sup>92</sup> are pivotal in DFT. HK theorems offers a way to simplify this problem by showing that all the ground-state properties of a many-electron system can be determined from its electron density  $\rho(\mathbf{r})$  alone, rather than from the many-body WFs.  $\rho(\mathbf{r})$  describes the probability of finding electrons at a particular point in space. It is computed by integrating over the spatial coordinates of all other electrons and considering their spin:

$$\rho(\mathbf{r}) = N \int \cdots \int |\phi_{GS}(\mathbf{r}, s_1, \mathbf{r}_2, s_2, \dots, \mathbf{r}_N, s_N)|^2 ds_1, d\mathbf{r}_2 \dots d\mathbf{r}_N, ds_N \quad (1.7)$$

where  $N$  is the number of electrons, which can also be calculated from the electron density via  $N = \int d\mathbf{r} \rho(\mathbf{r})$  and  $\phi_{GS}(\mathbf{r})$  is the ground-state electronic WF.

The first HK theorem states that the ground-state energy of a many-electron system is a unique functional of the electron density. This implies that  $\rho(\mathbf{r})$  completely determines the ground-state properties of the system, including the external potential  $v_{ext}(\mathbf{r})$ , the total number of electrons  $N$ , and the total energy. Consequently, the ground-state energy can be expressed as a functional of the electron density:

$$\begin{aligned} V_{GS} \equiv E_{GS} = E[\rho(\mathbf{r})] &= T[\rho] + V_{ee}[\rho] + V_{ne}[\rho] \\ &= T[\rho] + V_{ee}[\rho] + \int \rho(\mathbf{r}) v_{ext}(\mathbf{r}) d\mathbf{r} \\ &= F_{HK}[\rho] + \int \rho(\mathbf{r}) v_{ext}(\mathbf{r}) d\mathbf{r} \end{aligned} \quad (1.8)$$

where  $T[\rho]$  represents the electronic kinetic energy functional,  $V_{ee}[\rho]$  denotes the electron-electron interaction energy, and  $V_{ne}[\rho]$  is the electron-nuclear attraction term. After separating  $E[\rho(\mathbf{r})]$  into the dependent system parts, i.e., the potential energy due to the nuclei-electron attraction, and the universally system independent parts (independent from  $N$ ,  $R_a$  and  $Z_a$ ), Eq.(1.8) groups the system independent parts into a new quantity, the Hohenberg-Kohn functional  $F_{HK}[\rho]$ . This universal functional  $F_{HK}[\rho]$  is central to DFT because if it were known exactly, it would solve the Schrödinger equation exactly<sup>93</sup>. Even though the explicit forms of  $T[\rho]$  and  $V_{ee}[\rho]$  functionals are not known, we can at least determine the classical Coulomb interaction  $J[\rho]$ , and the non-classical term that contains all the effects of self-interaction correction, exchange and Coulomb correlation (Eq.(1.9)). The challenge of determining these functionals is a major focus of DFT research.

$$F_{HK}[\rho] = T[\rho] + V_{ee}[\rho] = T[\rho] + J[\rho] + \text{non-classical term} \quad (1.9)$$

The second HK theorem extends the variational principle to the electron density. It states that the ground-state energy can be obtained by minimizing the energy functional with respect to the electron density. Specifically, there exists an energy functional  $E[\tilde{\rho}]$  such that the exact ground-state

density corresponds to the minimum of this functional. Thus, minimizing the energy functional with respect to the electron density provides the ground-state energy and density of the system. Mathematically, for a trial density  $\tilde{\rho}(\mathbf{r})$ , such that  $\tilde{\rho}(\mathbf{r}) \geq 0$  and  $\int \tilde{\rho}(\mathbf{r})d\mathbf{r} = N$ ,  $E_{GS} \leq E[\tilde{\rho}]$ .

These theorems lay the groundwork for the practical implementation of DFT, as they guarantee that the problem of finding the ground-state energy and density can be framed as an optimization problem where the density is varied to minimize the energy functional.

### 1.4.1.3 Kohn-Sham Density Functional Theory (KS-DFT)

While the Hohenberg-Kohn theorems establish the theoretical basis for density functional theory (DFT), they do not provide a practical method for computing the energy functional due to the complexity of the unknown functionals,  $T[\rho]$  and  $V_{ee}[\rho]$ , which makes accurate computation difficult in practice. To overcome this, Walter Kohn and Lu Jeu Sham introduced the Kohn-Sham (KS) approach in 1965<sup>94</sup>.

KS-DFT simplifies the problem by replacing the many-body system with an equivalent system of non-interacting electrons through an effective potential  $V_{KS}(\mathbf{r})$ . This effective potential, which includes the external potential and the contributions from the exchange-correlation functional, is derived from the original electronic Hamiltonian and ensures that the resulting electron density is consistent with the true interacting system. The resulting total energy functional is referred to as the well-known orbital functional because it is expressed directly in terms of the Kohn-Sham orbitals,  $\phi_i^*(\mathbf{r})$ . The electron density is obtained from these orbitals and used to compute the energy components:

$$E_{KS}[\rho] = 2 \sum_{i=1}^{N/2} \int \phi_i^*(\mathbf{r}) \left[ -\frac{\hbar^2}{2} \nabla_i^2 \right] \phi_i(\mathbf{r}) d\mathbf{r} + E_{ext}[\rho] + J[\rho] + E_{XC}[\rho] \quad (1.10)$$

Although the kinetic energy obtained from the KS orbitals does not exactly match the true kinetic energy of the interacting system, the discrepancy is much smaller than in orbital-free methods. In the KS framework, any error in the kinetic energy is compensated by the non-classical part of the exchange-correlation function.

The Euler-Lagrange method of variations is used in KS-DFT to minimize the ground-state energy functional under the orthonormality constraint for KS orbitals. By introducing Lagrange multipliers to enforce this constraint, the minimization process leads to the well-known one-electron KS equations

$$\left[ -\frac{\hbar^2}{2}\nabla_i^2 + V_{KS}(\mathbf{r}) \right] \psi_j(\mathbf{r}) = \epsilon_j \psi_j(\mathbf{r}) \quad (1.11)$$

$$V_{KS}(\mathbf{r}) = \int \frac{\rho(\mathbf{r}')}{|\mathbf{r}-\mathbf{r}'|} d\mathbf{r}' + v_{ext}(\mathbf{r}) + \frac{\delta E_{XC}}{\delta \rho}$$

For a given approximation of the explicit density functional  $E_{XC}[\rho]$ , the XC potential  $v_{xc}(\mathbf{r}) = \frac{\delta E_{XC}}{\delta \rho}$  can be computed analytically. This potential is a key component in the KS equations, governing the interaction among electrons within the system. To find the ground-state electron density, the KS equations are solved using a self-consistent field (SCF) procedure. This iterative process involves starting with an initial guess for the electron density, calculating the effective potential, solving the resulting KS equations for the orbitals, and then updating the electron density. The cycle is repeated until the electron density converges to a self-consistent solution, providing an accurate description of the system's ground-state properties.

## 1.4.2 Exchange-Correlation (XC) Functionals

The last key component in DFT is the exchange-correlation (XC) functional,  $v_{xc}(\mathbf{r})$ , introduced in Eq.(1.11). Defined as the functional derivative of  $E_{XC}[\rho]$  with respect to  $\rho(\mathbf{r})$ , XC functionals

include the exchange energy due to the Pauli exclusion principle and the correlation energy arising from the dynamic, non-mean-field interactions among electrons. An accurate  $v_{xc}(\mathbf{r})$  ensures that the computed electron density closely resembles the true density of the interacting system, leading to reliable predictions of molecular and material properties. Since the exact form of the XC functional is unknown, various approximations, such as the local density approximation (LDA), generalized gradient approximation (GGA), and hybrid functionals, are employed to approximate it. Generally, the XC energy functional is the sum of the exchange energy  $E_X[\rho]$  and the correlation energy  $E_C[\rho]$ :

$$E_{XC}[\rho] = E_X[\rho] + E_C[\rho] = \int \rho(\mathbf{r})\varepsilon_X(\mathbf{r})d\mathbf{r} + \int \rho(\mathbf{r})\varepsilon_C(\mathbf{r})d\mathbf{r} \quad (1.12)$$

where  $\varepsilon$  is the energy density corresponding to the exchange and correlation energies.

### 1.4.2.1 Local Density Approximation (LDA)

The LDA originates from early studies by Thomas, Fermi, and Dirac on the homogeneous electron gas in the 1920s<sup>95</sup>. In LDA, the XC energy at each point in space is assumed to depend solely on the local electron density. Hence, in an inhomogeneous system, the functional could be approximated as an integral over a local function of the charge density, with the exchange energy being:

$$E_X[\rho]^{LDA} = -C_X \int \rho^{4/3}(\mathbf{r}) \quad (1.13)$$

where  $C_X = \frac{3}{4} \left( \frac{3}{\pi} \right)^{1/3}$ . The correlation energy,  $E_C[\rho]^{LDA}$ , is generally derived from quantum Monte Carlo simulations<sup>96–99</sup> of the homogeneous electron gas and is parameterized as a function of the local density. The simplicity and computational efficiency of LDA make it effective for systems with slowly varying densities, like bulk metals. Yet, its assumption of a uniform electron gas can

lead to inaccuracies for systems with significant density inhomogeneities, such as molecules or surfaces, leading to an overestimation of binding energies and bond strengths.

### 1.4.2.2 Generalized Gradient Approximation (GGA)

Beyond LDA, GGA functionals enhance accuracy by including the gradient of the electron density,  $\nabla\rho(\mathbf{r})$  which allows for a more precise treatment of systems with spatially varying densities. The exchange component of a GGA functional is generally expressed as a refinement to the LDA XC energy:

$$E_X^{GGA}[\rho] = \int \rho(\mathbf{r}) \epsilon_X^{LDA}(\mathbf{r}) F_X^{GGA}(\rho, \nabla\rho) d\mathbf{r} \quad (1.14)$$

where  $F_X^{GGA}(\rho, \nabla\rho)$  is generalized function that depends on both the local density and its gradient.

Two widely used GGA functionals are the PBE (Perdew-Burke-Ernzerhof)<sup>100,101</sup> and BLYP (Becke-Lee-Yang-Parr)<sup>102,103</sup>, both of which are applied in this thesis. PBE is a non-empirical functional, derived from first principles, and is known for delivering reliable results across a wide range of systems, including bulk materials, surfaces, and molecular complexes. It addresses the overbinding issues characteristic of LDA, making it particularly effective for predicting bond lengths, vibrational frequencies, and reaction energies. PBE refines the XC energy by incorporating both the electron density and its gradient, which is typically expressed as:

$$E_X^{PBE}[\rho] = \int \rho(\mathbf{r}) \epsilon_X^{LDA}(\mathbf{r}) F_X^{PBE}(s) d\mathbf{r} \quad (1.15)$$

with the enhancement factor  $F_X^{PBE}(s)$  depends on the dimensionless reduced density gradient

$s = \frac{|\nabla\rho(\mathbf{r})|}{2(3\pi^2)^{1/3}\rho^{4/3}(\mathbf{r})}$ . The PBE correlation energy includes a gradient correction accounts for the

density gradient contributions to the correlation energy.

On the other hand, the BLYP functional combines Becke's exchange functional with the Lee-Yang-Parr correlation functional. The Becke exchange introduces a gradient correction, while the LYP correlation improves electron correlation treatment. Unlike PBE, BLYP is semi-empirical, with parameters adjusted to fit experimental data. The BLYP XC energy is expressed as:

$$E_{XC}^{BLYP}[\rho] = E_X^{Becke}[\rho] + E_C^{LYP}[\rho] \quad (1.16)$$

This functional is particularly effective for molecular systems, offering enhancements in the calculation of molecular geometries, dipole moments, and energy barriers. However, it may encounter limitations in capturing significant dispersion interactions, which are not fully addressed by the GGA approach. While GGAs generally offer enhanced precision over LDA for molecular systems and chemical reactions, they can still face challenges with certain properties, particularly long-range van der Waals interactions.

To enhance the accuracy of the GGA approach, one can incorporate additional elements such as the second derivative of the density, as seen in meta-GGA functionals<sup>104</sup>. Another improvement comes from hybrid-GGA functionals<sup>105,106</sup>, which include exact exchange terms from Hartree-Fock (HF) theory. Additionally, Generalized RPA methods<sup>107-109</sup> use data from both occupied and virtual orbitals to achieve greater precision.

### 1.4.2.3 Hybrid Functionals

To improve the description of electronic interactions, hybrid functionals, also called adiabatic connection method (ACM) functionals, blend a portion of exact HF exchange energy  $E_{XC}^{HF}$  with the XC energy derived from a GGA or meta-GGA functional,  $E_{XC}^{DFT}[\rho]$ . This approach often yields improved accuracy for a wide range of systems, including molecules and solids. The general form

of a hybrid functional can be expressed as:

$$\begin{aligned}
 E_{XC}^{hybrid}[\rho] &= (1 - \alpha)E_{XC}^{DFT}[\rho] + \alpha E_{XC}^{HF} \\
 &= (1 - \alpha)E_{XC}^{DFT}[\rho] - \alpha \sum_{i=1}^{N/2} \sum_{j=1}^{N/2} \int \int \frac{\psi_i^*(\mathbf{r})\psi_j(\mathbf{r})\psi_j^*(\mathbf{r}')\psi_i(\mathbf{r}')}{|\mathbf{r} - \mathbf{r}'|} d\mathbf{r}d\mathbf{r}'
 \end{aligned}
 \tag{1.17}$$

where  $\alpha$  represents the fraction of exact exchange included.

Among the hybrid functionals, the Heyd-Scuseria-Ernzerhof (HSE) family<sup>105,106</sup>, used in this thesis, stands out for its ability to balance accuracy with computational efficiency. HSE functionals improve upon conventional GGAs by incorporating a range-separated Coulomb potential that divides the exchange interaction into short-range and long-range components. Exact exchange (25%) is applied only to the short-range part, while the long-range interactions are managed by a GGA exchange functional. This separation enhances the accuracy of long-range electron-electron interactions while controlling computational costs. Particularly, the HSE06 functional is a variant of the original HSE functional, with specific adjustments to improve its performance. The HSE06 functional offers improved results for electronic properties, including band gaps and transition energies, compared to both the original HSE and standard GGAs. It is particularly noted for its enhanced ability to accurately predict the electronic structure of systems with moderate to large band gaps. HSE06 is widely used in the study of semiconductors, insulators, and complex materials where precise electronic properties are crucial.

### 1.4.3 SCF Methods

The core of KS DFT is the self-consistent field (SCF) procedure, which aims to find the electronic density by minimizing the total energy functional  $E[\rho]$  with respect to variations in the one-electron orbitals  $\psi_i$ . Traditionally, this optimization enforces the orthogonality of one-electron

orbitals, which is essential for maintaining the Pauli exclusion principle.

### 1.4.3.1 Diagonalization of the Hermitian Matrix

The most common approach to maintaining orthogonality during SCF optimization involves the diagonalization of the KS matrix, known as the Roothaan-Hall equation. This method solves the generalized eigenvalue problem:

$$\mathbf{H}_{\text{KS}}\mathbf{C} = \mathbf{S}\mathbf{C}\boldsymbol{\varepsilon} \quad (1.18)$$

where  $\mathbf{S}$  is the overlap matrix,  $\mathbf{C}$  is the matrix of molecular orbital (MO) coefficients (eigenvectors), and  $\boldsymbol{\varepsilon}$  is the diagonal matrix of orbital energies (eigenvalues). This approach ensures orthogonality of the orbitals by construction, as the eigenvectors of the Hermitian Kohn-Sham (KS) matrix are inherently orthogonal. However, diagonalizing the KS matrix is computationally intensive, particularly for systems with a large number of basis functions, due to its cubic scaling with the size of the basis set ( $\mathcal{O}(N^3)$ ). For very large systems, iterative diagonalization techniques, such as the Davidson<sup>110</sup> or Lanczos methods<sup>111,112</sup>, density matrix methods<sup>113</sup>, sparse matrix techniques<sup>114</sup>, and linear scaling methods<sup>115</sup> are often employed to mitigate the computational burden by focusing on the calculation of only the lowest eigenstates. Convergence issues can still arise with this approach, but the rate of convergence may be enhanced by limiting the number of previous Fock matrices used to calculate the DIIS coefficients in the DIIS schemes<sup>116–118</sup>. For systems with nearly degenerate frontier orbitals<sup>119,120</sup>, the use of relaxed constraint algorithms<sup>121,122</sup> in conjunction with energy-based DIIS methods<sup>123–125</sup> can alleviate the strict idempotency constraint within DIIS, thereby improving SCF convergence.

### 1.4.3.2 Unitary Transformation

Alternatively, unitary transformations are employed to vary orbitals while maintaining orthogonality. The procedure begins by orthogonalizing the initial orbitals using methods such as Loewdin<sup>126</sup> or Gram-Schmidt orthogonalization<sup>127</sup>. After this, the orbitals are updated in each iteration using unitary transformations that inherently preserve orthogonality during the energy minimization process. A unitary matrix  $U$ , satisfying  $U^\dagger U = I$ , ensuring that the transformation preserves the inner products between vectors, thereby maintaining orthogonality and normalization. While this approach allows for diagonalization-free Roothaan–Hall SCF optimization and direct energy minimization with metric preservation, it is crucial to carefully parameterize the unitary transformation matrix  $U$ . The success and stability of the SCF process are largely determined by the specific parameterization method employed. Several methods for parameterizing unitary transformations in the SCF procedure include exponential parameterization, trigonometric parameterization, and Cayley Parameterization.

In the exponential parameterization, Helgaker method<sup>128</sup> is a well-known representative. Developed by Thomas Helgaker and his colleagues, the technique expresses the rotation of the MOs in terms of an anti-Hermitian matrix  $X$ . The exponential of this anti-Hermitian matrix, is then used to transform the orbitals, ensuring that they remain orthogonal by construction. Since the exponential of an anti-Hermitian matrix is unitary,  $U = \exp(-X)$ , the transformation preserves the orthogonality of the orbitals. This is a key advantage, as it eliminates the need for explicit orthogonalization steps that are typically required in other methods. Similarly, geometric direct minimization (GDM)<sup>129</sup> also employs the exponential parameterization of a unitary matrix  $U = \exp(-X)$ , where the anti-Hermitian matrix  $X$  can be optimized independently to minimize the energy functional directly with

respect to  $X$ . This approach facilitates smooth, differentiable optimization, making it suitable for refining orbital configurations while maintaining orthogonality.

Trigonometric Parameterization is utilized in methods like orbital transformation (OT), where the unitary matrix  $U$  is implicitly parameterized using sine and cosine functions of an update matrix<sup>130</sup>. Specifically,  $U$  is defined as:

$$U = (x^T S x)^{1/2} \quad (1.19)$$

and the orbital coefficients  $C(x)$  are given by  $C(x) = C_0 \cos(U) + x U^{-1} \sin(U)$ . Here,  $S$  is the overlap matrix,  $x$  is a vector of coefficients related to the orbital coefficients  $C$ , and  $c_0$  is the constant initial vector fulfilling. The transformation ensures that  $C_0^T S C_0 = I$  for all choices of  $x$ , confirming that the unitary transformation maintains the orthogonality of the orbitals. By using this parameterization and transformation, OT facilitates the optimization of orbitals while preserving orthogonality through the proper handling of the overlap matrix  $S$  and the introduction of new variables  $x$  and  $U$ .

The Cayley parameterization reformulates the unitary matrix as  $U = (I - X)(I + X)^{-1}$  where  $X$  is a skew-Hermitian matrix. This formulation simplifies the diagonalization of the KH Hamiltonian<sup>131</sup> and is noted for its numerical stability and straightforward implementation. These attributes make it particularly useful for iterative methods that require reliable convergence.

Despite these advancements, unitary transformation methods can introduce complexities in gradient computations and additional constraints that complicate the minimization process<sup>129,130</sup>. The parameterization can also make the minimization algorithm excessively complicated by introducing additional constraints<sup>130</sup> or by limiting the method to the energy minimization with a fixed KS Hamiltonian<sup>131</sup>. Moreover, methods that relax orthogonality constraints to optimize localized

orbitals have been explored. While promising, these methods face challenges such as slower SCF convergence and practical implementation issues<sup>132,133</sup>. These difficulties underscore the need for continued development of SCF optimization techniques to effectively balance orthogonality and locality constraints.

#### 1.4.4 DFT for Excited States

Excited states are crucial in green chemistry, particularly for optimizing processes like photocatalysis and light-driven reactions, where electronic transitions are vital. These states are key to designing efficient photocatalysts and improving light absorption in technologies related to spectroscopy, chemical reactions, and material properties such as conductivity and luminescence<sup>134</sup>. Since traditional DFT focuses on ground-state calculations, various extensions have been developed to handle excited-state processes. This section reviews a selection of these methods.

##### 1.4.4.1 TDDFT

One of the most widely used extensions of DFT for describing excited states is linear-response time-dependent (TD) DFT. TDDFT builds on the foundation of KS-DFT to describe time-dependent electronic excitations, offering a computationally efficient alternative to wave function-based methods, particularly for larger systems with hundreds of atoms<sup>135</sup>.

TDDFT extends traditional DFT to dynamic systems by focusing on the time-dependent electron density, which uniquely determines the external time-dependent potential and the governing Hamiltonian, as established by the Runge-Gross theorem<sup>136</sup>. Using KS formalism with a time-dependent XC potential, TDDFT computes electron density and predicts dynamic properties such as excitation energies and responses to external fields. It further employs time-dependent perturbation and

linear response theories<sup>137</sup> to model interactions and transitions between electronic states, offering insights into dynamic behaviors and experimental observables like absorption and emission spectra.

TDDFT calculates excited state properties by analyzing the response of a ground-state density functional to time-dependent perturbations, such as an external electric field<sup>138</sup>. While the method has been successful in predicting electronic excitation energies and properties, it does have limitations. A major challenge in TDDFT lies in selecting appropriate XC functionals, as the accuracy of TDDFT results heavily depends on this choice. Although TDDFT is, in principle, an exact method<sup>136</sup>, it tends to neglect double and higher excitations when used with approximate functionals. This limitation arises from its reliance on the adiabatic LDA approximation, which assumes that nuclear positions remain fixed during the excitation process. Consequently, adiabatic LDA is restricted to modeling single excitations and struggles with systems involving significant changes in electron density distribution, such as long-range charge transfer, Rydberg states, and core excitations<sup>135,138</sup>.

For long-range charge transfer excitations, where an electron is excited from a donor to a spatially distant acceptor, TDDFT frequently underperforms due to the incorrect asymptotic behavior of widely used XC functionals. Although hybrid functionals, which incorporate a fraction of exact HF exchange, offer some improvement, they still struggle to fully capture the long-range nature of these excitations.

A similar issue arises with Rydberg states, which involve excitations to highly diffuse orbitals far from the nucleus. Standard XC functionals often underestimate the excitation energies of these states because they fail to accurately describe the necessary long-range potential for diffuse electron density.

Core excitations, which involve promoting electrons from tightly bound core orbitals to higher-

energy virtual states, present additional challenges. Standard functionals are generally not suited to model the localized, short-range nature of core orbitals, resulting in significant inaccuracies when predicting core excitation energies. While approaches such as range-separated hybrid functionals and the Tamm-Dancoff approximation (TDA)<sup>139</sup> have been developed to mitigate these issues, they often come with increased computational complexity, limiting their practicality in large systems.

#### 1.4.4.2 $\Delta$ SCF

The  $\Delta$ SCF method<sup>140–144</sup> is a widely used approach to address some of the limitations associated with TDDFT. It is an orbital-optimized (OO) DFT method that extends the ground-state formalism to excited states by variationally optimizing orbitals, not only for the ground state but also for excited states.

$\Delta$ SCF treats the excited state as a single Slater determinant by solving KS equations for the excited configuration. Excited states are constructed by promoting one or more electrons from occupied orbitals to unoccupied (virtual) orbitals, thereby generating a new electron configuration. The method then performs the SCF calculation on this new configuration to optimize the orbitals for the excited state. Excitation energies are determined by computing the energy difference between the ground and excited states, both obtained through separate SCF calculations. To ensure that the system reaches self-consistency in the excited state, the occupations of higher-lying KS orbitals are fixed during the optimization process. This variational treatment of both ground and excited states allows  $\Delta$ SCF to provide better description of various electronic excitations, particularly for long-range charge transfer processes, compared to TDDFT.

However,  $\Delta$ SCF is not without challenges. One major issue is the problem of variational collapse, where the optimization process may converge to the ground state instead of the desired

excited state. This problem is particularly pronounced in systems with multiple close-lying excited states, where the method struggles to maintain the desired excitation. This occurs because  $\Delta$ SCF is an unconstrained optimization that lacks safeguards against collapsing back to the lowest energy solution. Additionally, spin contamination can occur in excited states arising from closed-shell ground states, resulting in mixtures of singlet, triplet, and higher-order spin states. Correcting for this contamination is often necessary to obtain accurate excitation energies.

#### 1.4.4.3 Orthogonality Constrained DFT (OCDFT)

Orthogonality constrained (OC) DFT is an alternative method developed to address the problem of variational collapse in excited-state calculations<sup>145</sup>. This method prevents variational collapse by enforcing orthogonality between the ground and excited state WF during optimization. The process begins by generating an initial excited state guess, where electrons are promoted from an occupied orbital (the "hole") to an virtual orbital. The orthogonality constraint is then introduced by applying a projection operator that removes any overlap between the excited state and the ground state occupied orbitals. After this orthogonality is established, the excited state orbitals are allowed to relax and minimize their energy while maintaining this constraint. This approach ensures the excited state remains accurate and does not collapse into the ground state during the optimization. Additionally, spin-adaptation procedures are employed to correct errors in excitation energies, enhancing the method's accuracy for excited state calculations. Nevertheless, a notable limitation of OCDFT is that the iterative solution of the modified eigenvector equations does not always guarantee convergence, which can affect the reliability of the method. Furthermore, the projector-based formalism, while effective for single excited states, becomes cumbersome when extended to multiple excited states, limiting its scalability and practicality for larger systems with

many excited states.

#### 1.4.4.4 Maximum Overlap Method (MOM)

Another popular approaches designed to prevent variational collapse in  $\Delta$ SCF calculations are The Maximum Overlap Method (MOM)<sup>146</sup> and its modified version, the Initial Maximum Overlap Method (IMOM)<sup>147,148</sup>. These methods are commonly used in conjunction with Fock matrix diagonalization techniques like DIIS to maintain convergence toward excited states rather than defaulting to the ground state.

Instead of following the aufbau principle, where orbitals are filled in order of increasing energy, MOM selects occupied orbitals at each SCF iteration by maximizing their overlap with those from the previous cycle. This keeps the calculation focused on higher-energy excited states, avoiding a collapse to the ground state. While the SCF algorithm remains mostly unchanged, MOM prioritizes stationary points over energy minima to find excited-state solutions. Drawback of MOM, however, is that it can sometimes converges to unintended solutions, particularly in systems with near-degenerate orbitals. Besides, MOM does not always succeed in preventing the collapse to the ground state, particularly in challenging systems. Two notable examples where MOM fails are the  $2p \rightarrow 3p$  excitation in the boron atom and a Rydberg-like excitation in formaldehyde, where an electron is promoted from the highest-energy oxygen lone-pair to a carbon  $4p_y$  orbital<sup>149</sup>. In such cases, MOM collapses back to the ground state, making it necessary to explore alternative solvers for more robust performance.

On the other hand, IMOM improves upon MOM by preventing orbital drifting over successive SCF iterations. Rather than maximizing overlap with the previous SCF cycle, IMOM maximizes the overlap with the initial excited-state guess, ensuring the SCF process remains focused on the

target state. This modification makes IMOM more reliable in complex systems, especially those with near-degenerate orbitals where MOM may fail. Despite this enhancement, IMOM can exhibit oscillatory behavior and fail to converge, particularly when small changes in orbital overlap cause discontinuous ranking shifts. An example is the  $\pi$  to  $\pi^*$  excitation in nitrobenzene, where IMOM failed to converge even after 500 iterations<sup>149</sup>, likely due to its sensitivity to fluctuations in orbital overlaps.

#### 1.4.4.5 Square Gradient Minimization (SGM)

The square gradient minimization (SGM)<sup>149</sup> method is a direct orbital optimization technique designed to address the challenge of variational collapse, ensuring that the optimized excited state is a true minimum rather than saddle points. SGM reformulates the problem by minimizing the square of the energy gradient,  $\Delta = |\nabla_{\vec{\theta}} E|^2$ , with respect to the orbital degree of freedom  $\vec{\theta}$  (a mixture of occupied and virtual orbitals). This approach requires only the calculation of energy gradients, making it more computationally feasible than methods that rely on higher-order derivatives. By transforming the saddle-point search into a minimization problem, SGM achieves stable convergence for challenging excited states, such as doubly excited or charge-transfer states, which are often difficult to capture using conventional methods like TDDFT. SGM can be applied to various quantum chemistry methods, including DFT, Møller-Plesset perturbation theory (MP2), or coupled cluster doubles (CCD), making it a versatile approach.

Yet, the main disadvantage of SGM is that it is less well-conditioned than energy minimization, requiring more iterations even with a preconditioner compared to ground-state optimizations—typically costing three times as much—due to its reliance on finite difference approximations<sup>149,150</sup>. Another shortcoming is that it may get “stuck” in local minima of  $\Delta$  that are not

stationary points in  $E$  ( $\Delta \neq 0$ ). Although practical solutions involve converging to the correct state with a different functional and using the resulting orbitals as an improved initial guess for  $\Delta$  minimization, these challenges have not hindered the successful optimization of desired states. They are unlikely to cause significant issues in practical applications.

Overall, the review underscores the need for a method that addresses key challenges in excited state calculations. It is crucial to develop a method that not only prevents the collapse of excited states to the ground state but also imposes minimal constraints to streamline the algorithm and enhance its accuracy compared to TDDFT. In response to these needs, we present the method introduced in Chapter 4, which aims to achieve these goals by offering a more robust and accurate approach for excited state optimization.

As mentioned earlier, the methodological developments in this thesis are unified by their focus on green chemistry, particularly in the computational modeling of electrons and atoms. In pursuit of these objectives, this thesis adopts a multidisciplinary approach, integrating theoretical foundations with computational innovations. The studies are presented across the next three distinct chapters. Chapter 2 focuses on the development of carbon capture materials, specifically exploring the  $\text{CO}_2$  adsorption mechanisms in cyclodextrin-derived MOF through DFT modeling and analysis of experimental data. Chapter 3 introduces a simple approach to direct unconstrained optimization of molecular orbital coefficients in DFT ground-state calculations, emphasizing the removal of orbital orthogonality constraints. Chapter 4 extends this method to optimize excited states directly using a self-consistent field approach in DFT. Together, these chapters illustrate how innovative computational strategies can address several challenges in electronic structure modeling of excited states, which of paramount importance in green photocatalytic and photochemistry processes. Finally, the concluding chapter discusses the broader implications, challenges, and future directions derived

from this work.

## 1.5 References

- [1] Anastas, P.; Eghbali, N. Green Chemistry: Principles and Practice. *Chem. Soc. Rev.* **2009**, *39*, 301–312.
- [2] Anastas, P. T.; Kirchoff, M. M. Origins, Current Status, and Future Challenges of Green Chemistry †. *Acc. Chem. Res.* **2002**, *35*, 686–694.
- [3] Kate, M. et al. Green chemistry as just chemistry. *Nat. Sustain.* **2023**, *6*, 502–512.
- [4] Ivanković, A. Review of 12 Principles of Green Chemistry in Practice. *Int. J. Sustain. Energy Dev.* **2017**, *6*, 39–48.
- [5] Abdussalam-Mohammeda, W.; Alia, A. Q.; Errayesb, A. O. Green Chemistry: Principles, Applications, and Disadvantages. *Chem. Methodol.* **2020**, *4*, 408–423.
- [6] Ameta, S. C.; Ameta, R. *GREEN CHEMISTRY : fundamentals and applications.*; APPLE ACADEMIC PRESS, 2021.
- [7] Harrison, E.; Smith, H.; Dekker, I. *Designing & Facilitating a Bioeconomy in the Capital Regional District Learning Through the Lenses of Biomimicry, Industrial Symbiosis, and Green Chemistry*; 2021.
- [8] Goren, A. Y.; Erdemir, D.; Dincer, I. Comprehensive review and assessment of carbon capturing methods and technologies: An environmental research. *Environ. Res.* **2024**, *240*, 117503.
- [9] Wu, C.; Huang, Q.; Xu, Z.; Sipra, A. T.; Gao, N.; de Souza Vandenberghe, L. P.; Vieira, S.; Soccol, C. R.; Zhao, R.; Deng, S.; et. al A comprehensive review of carbon capture science and technologies. *Carbon Capture Sci. Technol.* **2024**, *11*, 100178.
- [10] Hekmatmehr, H.; Esmaeili, A.; Pourmahdi, M.; Atashrouz, S.; Abedi, A.; Abuswer, M. A.; Nedeljkovic, D.; Latifi, M.; Farag, S.; Mohaddespour, A. Carbon capture technologies: A review on technology readiness level. *Fuel* **2024**, *363*, 130898.
- [11] Allangawi, A.; Alzaimoor, E. F.; Shanaah, H. H.; Mohammed, H. A.; Saqer, H.; El-Fattah, A. A.; Kamel, A. H. Carbon Capture Materials in Post-Combustion: Adsorption and Absorption-Based Processes. *C-J. Carbon Res.* **2023**, *9*, 17.
- [12] Zhang, G.; Liu, J.; Qian, J.; Zhang, X.; Liu, Z. Review of research progress and stability studies of amine-based biphasic absorbents for CO<sub>2</sub> capture. *J. Ind. Eng. Chem.* **2024**, *134*, 28–50.
- [13] Dziejarski, B.; Serafin, J.; Andersson, K.; Krzyżyńska, R. CO<sub>2</sub> capture materials: a review of current trends and future challenges. *Mater. Today Sustain.* **2023**, *24*, 100483.
- [14] Khedary, N. H.; Alayyar, A. S.; Alsarhan, L. M.; Alshihri, S.; Mokhtar, M. Metal Oxides as Catalyst/Supporter for CO<sub>2</sub> Capture and Conversion, Review. *Catal.* **2022**, *12*, 300.
- [15] Bhatta, L. K. G.; Bhatta, U. M.; Venkatesh, K. *Metal Oxides for Carbon Dioxide Capture*; Springer, Cham, 2019.
- [16] Oh, H.; Patel, R. Recent Development in Metal Oxides for Carbon Dioxide Capture and Storage. *Membr. J.* **2020**, *30*, 97–110.
- [17] Gao, Z.; Li, C.; Yuan, Y.; Hu, X.; Ma, J.; Ma, C.; Guo, T.; Zhang, J.; Guo, Q. Utilizing metal oxide enhancement for efficient CO<sub>2</sub> capture and conversion in calcium-based dual-function materials. *J. Energy Inst.* **2024**, *114*, 101630.

- [18] Lu, B.; Fan, Y.; Zhi, X.; Han, Z.; Wu, F.; Li, X.; Luo, C.; Zhang, L. Material design and prospect of dual-functional materials for integrated carbon dioxide capture and conversion. *Carbon Capture Sci. Technol.* **2024**, *12*, 100207.
- [19] Chen, J.; Xu, Y.; Liao, P.; Wang, H.; Zhou, H. Recent Progress in Integrated CO<sub>2</sub> Capture and Conversion Process Using Dual Function Materials: A State-of-the-Art Review. *Carbon Capture Sci. Technol.* **2022**, *4*, 100052.
- [20] Rashid, H.; Rafey, A. Solid adsorbents for carbon dioxide capture: a review. *Chemistry and Ecology* **2023**, *39*, 1–11.
- [21] Kong, M.; Song, L.; Liao, H.; Zhang, S.; Wang, Y.; Deng, X.; Feng, W. A review on development of post-combustion CO<sub>2</sub> capture technologies: Performance of carbon-based, zeolites and MOFs adsorbents. *Fuel* **2024**, *371*, 132103.
- [22] Liu, W.; Ji, Y.; Huang, Y.; Zhang, X. J.; Wang, T.; Fang, M. X.; Jiang, L. Adsorption-based post-combustion carbon capture assisted by synergetic heating and cooling. *Renew. Sustain. Energy Rev.* **2024**, *191*, 114141.
- [23] Gao, S.; Peng, H.; Song, B.; Zhang, J.; Wu, W.; Vaughan, J.; Zardo, P.; Vogrin, J.; Tulloch, S.; Zhu, Z. Synthesis of zeolites from low-cost feeds and its sustainable environmental applications. *J. Environ. Chem. Eng.* **2023**, *11*, 108995.
- [24] Tao, Z.; Tian, Y.; Wu, W.; Liu, Z.; Fu, W.; Kung, C.-W.; Shang, J. Development of zeolite adsorbents for CO<sub>2</sub> separation in achieving carbon neutrality. *npj Materials Sustainability* **2024**, *2*, 20.
- [25] Li, W.-L.; Shuai, Q.; Yu, J. Recent Advances of Carbon Capture in Metal–Organic Frameworks: A Comprehensive Review. *Small* **2024**, *n/a*, 2402783.
- [26] Li, S.; Zhang, H.; Li, S.; Wang, J.; Wang, Q.; Cheng, Z. Advances in hierarchically porous materials: Fundamentals, preparation and applications. *Renew. Sustain. Energy Rev.* **2024**, *202*, 114641.
- [27] Das, A.; Peu, S. D.; Hossain, M. S.; Nahid, M. M. A.; Karim, F. R. B.; Chowdhury, H.; Porag, M. H.; Argha, D. B. P.; Saha, S.; Islam, A. R. M. T.; Salah, M. M.; Shaker, A. Advancements in adsorption based carbon dioxide capture technologies- A comprehensive review. *Heliyon* **2023**, *9*, e22341.
- [28] Cui, B.; Ju, X.; Ma, H.; Meng, S.; Liu, Y.; Wang, J.; Wang, D.; Yang, Z. Aerogel-based carbon capture materials: Research progress and application prospects. *Sep. Purif. Technol.* **2024**, *354*, 128794.
- [29] Wen, B.; Li, Y.; Liang, C.; Chen, Y.; Zhao, Y.; Wang, Q. Recent Progress on Porous Carbons for Carbon Capture. *Langmuir* **2024**, *40*, 8327–8351.
- [30] Soo, X. Y. D.; Lee, J. J. C.; Wu, W. Y.; Tao, L.; Wang, C.; Zhu, Q.; Bu, J. Advancements in CO<sub>2</sub> capture by absorption and adsorption: A comprehensive review. *J. CO<sub>2</sub> Util.* **2024**, *81*, 102727.
- [31] Ren, J.; Zhao, D. Recent Advances in Reticular Chemistry for Clean Energy, Global Warming, and Water Shortage Solutions. *Adv. Funct. Mater.* **2023**,
- [32] Saxena, A.; Kumar, R.; Sagade, A. A.; Singh, D. B.; Tyagi, V. V.; Cuce, E.; Goel, V. A state-of-art review on photovoltaic systems: Design, performance, and progress. *Process. Saf. Environ. Prot.* **2024**, *190*, 1324–1354.
- [33] Green, M. A. Photovoltaics: Technology overview. *Energy Policy* **2000**, *28*, 989–998.

- [34] Donev, J.; et. al. Energy Education. <https://energyeducation.ca>, 2024.
- [35] Susilawati, S.; Doyan, A.; Purwoko, A. A.; Ibrahim, I.; Ahzan, S.; Gummah, S.; Bahtiar, B.; Muhammad, I.; Hakim, S.; Mulyadi, L.; Haris, M. A Systematic Review of the Trends Thin Film Characteristics Research as Electronic Device (2015-2024). *Jur. Penelit. Pendidik. IPA* **2024**, *10*, 313–322.
- [36] Li, M.; Zhu, Z.; Wang, Z.; Pan, W.; Cao, X.; Wu, G.; Chen, R. High-Quality Hybrid Perovskite Thin Films by Post-Treatment Technologies in Photovoltaic Applications. *Adv. Mater.* **2024**, *36*.
- [37] Park, N.-G. Towards Stable, 30
- [38] Jena, A. K.; Kulkarni, A.; Miyasaka, T. Halide Perovskite Photovoltaics: Background, Status, and Future Prospects. *Chem. Rev.* **2019**, *119*, 3036–3103.
- [39] Pecunia, V.; Occhipinti, L. G.; Chakraborty, A.; Pan, Y.; Peng, Y. Lead-free halide perovskite photovoltaics: Challenges, open questions, and opportunities. *APL Mater.* **2020**, *8*, 100901.
- [40] Prince, K. J.; Mirletz, H. M.; Gaulding, E. A.; Wheeler, L. M.; Kerner, R. A.; Zheng, X.; Schelhas, L. T.; Tracy, P.; Wolden, C. A.; Berry, J. J.; Ovaitt, S.; Barnes, T. M.; Luther, J. M. Sustainability pathways for perovskite photovoltaics. *Nat. Mater.* **2024**,
- [41] Zhao, X.; Gao, W.; Dong, H.; Zhou, Y.; Huang, H.; Wu, Z.; Ran, C. Advanced technical strategies for upscaling perovskite photovoltaics from cells to modules. *Nano Energy* **2024**, *128*, 109933.
- [42] Machín, A.; Márquez, F. Advancements in Photovoltaic Cell Materials: Silicon, Organic, and Perovskite Solar Cells. *Mater.* **2024**, *17*, 1165.
- [43] Kumar, V.; Kathiravan, A.; Jhonsi, M. A. Beyond lead halide perovskites: Crystal structure, bandgaps, photovoltaic properties and future stance of lead-free halide double perovskites. *Nano Energy* **2024**, *125*, 109523.
- [44] Njema, G. G.; Kibet, J. K. A Review of the Technological Advances in the Design of Highly Efficient Perovskite Solar Cells. *Int. J. Photoenergy* **2023**, *2023*.
- [45] Martínez, M.; Barrueto, Y.; Jimenez, Y. P.; Vega-Garcia, D.; Jamett, I. Technological Advancement in Solar Photovoltaic Recycling: A Review. *Minerals* **2024**, *14*, 638.
- [46] Mariam, E.; Ramasubramanian, B.; Reddy, V. S.; Dalapati, G. K.; Ghosh, S.; PA, T. S.; Chakraborty, S.; Motapothula, M. R.; Kumar, A.; Ramakrishna, S.; Krishnamurthy, S. Emerging trends in cooling technologies for photovoltaic systems. *Renew. Sustain. Energy Rev.* **2024**, *192*.
- [47] Aftab, S.; Iqbal, M. Z.; Hussain, S.; Hegazy, H. H.; Saeed, M. A. Transition metal dichalcogenides solar cells and integration with perovskites. *Nano Energy* **2023**, *108*.
- [48] Zhou, Z.; Lv, J.; Tan, C.; Yang, L.; Wang, Z. Emerging Frontiers of 2D Transition Metal Dichalcogenides in Photovoltaics Solar Cell. *Adv. Funct. Mater.* **2024**, *34*.
- [49] Kwon, N.; Lee, J.; Ko, M. J.; Kim, Y. Y.; Seo, J. Recent progress of eco-friendly manufacturing process of efficient perovskite solar cells. *Nano Converg.* **2023**, *10*.
- [50] Mohamadpour, F.; Amani, A. M. Photocatalytic systems: reactions, mechanism, and applications. *RSC Adv.* **2024**, *14*, 20609–20645.

- [51] Liao, G.; Li, C.; Liu, S. Y.; Fang, B.; Yang, H. Z-scheme systems: From fundamental principles to characterization, synthesis, and photocatalytic fuel-conversion applications. *Phys. Rep.* **2022**, 983.
- [52] Ameta, R.; Solanki, M. S.; Benjamin, S.; Ameta, S. C. *Chapter 6 - Photocatalysis*; Academic Press, 2018.
- [53] Durgalakshmi, D.; Rakkesh, R. A.; Rajendran, S.; Naushad, M. *Principles and Mechanisms of Green Photocatalysis*; Springer Cham, 2020.
- [54] Deng, S.; Xiong, W.-P.; Zhang, G.-X.; Wang, G.-F.; Chen, Y.-X.; Xiao, W.-J.; Shi, Q.-K.; Chen, A.; Kang, H.-Y.; Cheng, M.; Liu, Y.; Wang, J. Metal-Free Modification Overcomes the Photocatalytic Limitations of Graphitic Carbon Nitride: Efficient Production and In Situ Application of Hydrogen Peroxide. *Adv. Energy Mater.* **2024**, *n/a*, 2401768.
- [55] Gharanli, S.; Malekshah, R. E.; Moharramnejad, M.; Ehsani, A.; Shahi, M.; Joshaghani, A. H.; hossein Amini, A.; Haribabu, J.; ISTIFLI, E. S.; Tehrani, F. K. Recent progress in designing heterogeneous COFs with the photocatalytic performance. *Mol. Catal.* **2024**, 560, 114127.
- [56] Lei, T.; Ragab, A. H.; AL-Mhyawi, S. R.; Dang, A.; Shafi, M.; Zada, A. A comprehensive review on the exceptional photocatalytic and electrocatalytic applications of MOFs and COFs in energy generation and organic synthesis. *Int. J. Hydrog. Energy* **2024**, 83, 1032–1059.
- [57] Morshedy, A. S.; El-Fawal, E. M.; Zaki, T.; El-Zahhar, A. A.; Alghamdi, M. M.; Naggar, A. M. E. A review on heterogeneous photocatalytic materials: Mechanism, perspectives, and environmental and energy sustainability applications. *Inorg. Chem. Commun.* **2024**, 163.
- [58] Lewars, E. G. *Computational chemistry: Introduction to the theory and applications of molecular and quantum mechanics*; Springer, 2011.
- [59] Zhang, H.; Shang, C.; Yang, L. M.; Ganz, E. Elucidation of the Underlying Mechanism of CO<sub>2</sub> Capture by Ethylenediamine-Functionalized M<sub>2</sub>(dobpdc) (M = Mg, Sc-Zn). *Inorg. Chem.* **2020**, 59, 16665–16671.
- [60] Li, L.; Jung, H. S.; Lee, J. W.; Kang, Y. T. Review on applications of metal–organic frameworks for CO<sub>2</sub> capture and the performance enhancement mechanisms. *Renew. Sustain. Energy Rev.* **2022**, 162, 112441.
- [61] Kuruppathparambil, R. R.; Robert, T. M.; Pillai, R. S.; Pillai, S. K. B.; Shankaranarayanan, S. K. K.; Kim, D.; Mathew, D. Nitrogen-rich dual linker MOF catalyst for room temperature fixation of CO<sub>2</sub> via cyclic carbonate synthesis: DFT assisted mechanistic study. *J. CO<sub>2</sub> Util.* **2022**, 59, 101951.
- [62] Soleimani, B.; Shahrak, M. N.; Walton, K. S. The influence of different functional groups on enhancing CO<sub>2</sub> capture in metal-organic framework adsorbents. *J. Taiwan Inst. Chem. Eng.* **2024**, 163, 105638.
- [63] Cai, J.; Liang, Q.; Tang, Y.; Yang, J.; Fang, M.; Yao, S. CO<sub>2</sub> capture properties of a multi-metals CaMgZr-MOF derived CaO-based sorbents with highly dispersed doped metal atoms and DFT study. *Fuel* **2024**, 374, 132466.
- [64] Ha, N. T. T.; Lefedova, O. V.; Ha, N. N. Theoretical study on the adsorption of carbon dioxide on individual and alkali-metal doped MOF-5s. *Russ. J. Phys. Chem. A* **2016**, 90, 220–225.
- [65] Sharma, A.; Huang, R.; Malani, A.; Babarao, R. Computational materials chemistry for carbon capture using porous materials. *J. Phys. D Appl. Phys.* **2017**, 50, 463002.

- [66] Kancharlapalli, S.; Snurr, R. Q. High-Throughput Screening of the CoRE-MOF-2019 Database for CO<sub>2</sub> Capture from Wet Flue Gas: A Multi-Scale Modeling Strategy. *ACS Appl. Mater. Interfaces*. **2023**, *15*, 28084–28092.
- [67] Lee, H.; Bae, H.; Park, M.; Jang, B.; Kang, Y.; Park, J.; Lee, H.; Chung, H.; Chung, C.; Hong, S.; Kwon, Y.; Yakobson, B. I. High-throughput screening of metal-porphyrin-like graphenes for selective capture of carbon dioxide. *Sci. Rep.* **2016**, *6*, 21788.
- [68] Lei, Q.; Li, L.; Chen, H.; Wang, X. Emerging Directions for Carbon Capture Technologies: A Synergy of High-Throughput Theoretical Calculations and Machine Learning. *Environ. Sci. Technol.* **2023**, *57*, 17189–17200.
- [69] Dimitriev, O. P. Dynamics of Excitons in Conjugated Molecules and Organic Semiconductor Systems. *Chem. Rev.* **2022**, *122*, 8487–8593.
- [70] Sun, J.; Lee, C. W.; Kononov, A.; Schleife, A.; Ullrich, C. A. Real-Time Exciton Dynamics with Time-Dependent Density-Functional Theory. *Phys. Rev. Lett.* **2021**, *127*, 077401.
- [71] Melissen, S.; Bahers, T. L.; Steinmann, S. N.; Sautet, P. Relationship between Carbon Nitride Structure and Exciton Binding Energies: A DFT Perspective. *J. Phys. Chem. C* **2015**, *119*, 25188–25196.
- [72] Woźniak, T.; e hani, U.; Junior, P. E. F.; Ramzan, M. S.; Kuc, A. B. Electronic and Excitonic Properties of MSi<sub>2</sub>Z<sub>4</sub> Monolayers. *Small* **2023**, *19*, 2206444.
- [73] Mishra, P.; Singh, D.; Sonvane, Y.; Ahuja, R. Excitonic effects in the optoelectronic properties of graphene-like BC monolayer. *Opt. Mater.* **2020**, *110*, 110476.
- [74] Silveira, D. N.; Dias, A. C.; de Araujo, L. O.; Queiroz, M. A. A.; Dalmedico, J. F.; de Oliveira Bastos, C. M.; Rêgo, C. R. C.; Piotrowski, M. J.; Guedes-Sobrinho, D. Excitonic properties and solar harvesting performance of Cs<sub>2</sub>ZnY<sub>2</sub>X<sub>2</sub> as quasi-2D mixed-halide perovskites. *J. Alloys Compd.* **2024**, *1007*, 176434.
- [75] Majeed, M.; Waqas, M.; Aloui, Z.; Essid, M.; Ibrahim, M. A.; Khera, R. A.; Shaban, M.; Ans, M. Exploring the Electronic, Optical, and Charge Transfer Properties of A-D-A-Type IDTV-ThIC-Based Molecules To Enhance Photovoltaic Performance of Organic Solar Cells. *ACS Omega* **2023**, *8*, 45384–45404.
- [76] Ayoub, S. A.; Lagowski, J. B. Optimizing the performance of the bulk heterojunction organic solar cells based on DFT simulations of their interfacial properties. *Mater. Des.* **2018**, *156*, 558–569.
- [77] Niu, T. et al. Interfacial Engineering at the 2D/3D Heterojunction for High-Performance Perovskite Solar Cells. *Nano Lett.* **2019**, *19*, 7181–7190.
- [78] Welch, E. W.; Jung, Y. K.; Walsh, A.; Scolfaro, L.; Zakhidov, A. A density functional theory study on the interface stability between CsPbBr<sub>3</sub> and CuI. *AIP Adv.* **2020**, *10*, 085023.
- [79] Kishore, M. R. A.; Larsson, K.; Ravindran, P. Two-dimensional CdX/C<sub>2</sub>N (X = S, Se) heterostructures as potential photocatalysts for water splitting: A DFT study. *ACS Omega* **2020**, *5*, 23762–23768.
- [80] Lin, Y.; Wang, Q.; Ma, M.; Li, P.; Maheskumar, V.; Jiang, Z.; Zhang, R. Enhanced optical absorption and photocatalytic water splitting of g-C<sub>3</sub>N<sub>4</sub>/TiO<sub>2</sub> heterostructure through CB codoping: A hybrid DFT study. *Int. J. Hydrog. Energy* **2021**, *46*, 9417–9432.
- [81] Chong, W. K.; Ng, B. J.; Er, C. C.; Tan, L. L.; Chai, S. P. Insights from density functional theory calculations on heteroatom P-doped ZnIn<sub>2</sub>S<sub>4</sub> bilayer nanosheets with atomic-level charge steering for photocatalytic water splitting. *Sci. Rep.* **2022**, *12*, 1927.

- [82] Lamhani, M.; Chchiyai, Z.; Elomrani, A.; Manoun, B.; Hasnaoui, A. Enhanced Photocatalytic Water Splitting of SrTiO<sub>3</sub> Perovskite through Cobalt Doping: Experimental and Theoretical DFT Understanding. *Inorg. Chem.* **2023**, *62*, 13405–13418.
- [83] Ma, Q.; Ming, J.; Sun, X.; Zhang, H.; An, G.; Kawazoe, N.; Chen, G.; Yang, Y. Photocatalytic degradation of multiple-organic-pollutant under visible light by graphene oxide modified composite: degradation pathway, DFT calculation and mechanism. *J. Environ. Manag.* **2023**, *347*, 119128.
- [84] Wang, Z.; Li, W.; Wang, J.; Li, Y.; Zhang, G. Novel Z-scheme AgI/Sb<sub>2</sub>WO<sub>6</sub> heterostructure for efficient photocatalytic degradation of organic pollutants under visible light: Interfacial electron transfer pathway, DFT calculation and mechanism unveiling. *Chemosphere* **2023**, *311*, 137000.
- [85] Geldasa, F. T.; Kebede, M. A.; Shura, M. W.; Hone, F. G. Experimental and computational study of metal oxide nanoparticles for the photocatalytic degradation of organic pollutants: a review. *RSC Adv.* **2023**, *13*, 18404–18442.
- [86] Khan, M. S.; Li, Y.; Li, D. S.; Qiu, J.; Xu, X.; Yang, H. Y. A review of metal-organic framework (MOF) materials as an effective photocatalyst for degradation of organic pollutants. *Nanoscale Adv.* **2023**, *5*, 6318–6348.
- [87] Welch, E. W.; Jung, Y. K.; Walsh, A.; Scolfaro, L.; Zakhidov, A. Nitrogen doped g-C<sub>3</sub>N<sub>4</sub> with the extremely narrow band gap for excellent photocatalytic activities under visible light. *Appl. Catal. B: Environ.* **2021**, *281*, 119474.
- [88] Yu, X.; Xie, J.; Liu, Q.; Dong, H.; Li, Y. The origin of enhanced photocatalytic activity in g-C<sub>3</sub>N<sub>4</sub>/TiO<sub>2</sub> heterostructure revealed by DFT calculations. *J. Colloid Interface Sci.* **2021**, *593*, 133–141.
- [89] Xie, X.; Ge, P.; Xue, R.; Lv, H.; Xue, W.; Liu, E. Enhanced photocatalytic H<sub>2</sub> evolution and anti-photocorrosion of sulfide photocatalyst by improving surface reaction: A review. *Int. J. Hydrogen Energy.* **2023**, *48*, 24264–24284.
- [90] Zhang, J.; Jiang, J.; Lei, Y.; Liu, H.; Tang, X.; Yi, H.; Huang, X.; Zhao, S.; Zhou, Y.; Gao, F. Photocatalytic CO<sub>2</sub> reduction reaction: Influencing factors, reaction pathways and dominant catalysts. *Sep. Purif. Technol.* **2024**, *328*, 125056.
- [91] Born, M.; Huang, K.; Lax, M. *Dynamical Theory of Crystal Lattices*, 1st ed.; Oxford University Press, 1955; Vol. 23.
- [92] Hohenberg, P.; Kohn, W. Density Functional Theory (DFT). *Phys. Rev.* **1964**, *136*, B864.
- [93] Koch, W.; Holthausen, M. C. *A Chemist's Guide to Density Functional Theory*; Wiley VCH, 2001.
- [94] Kohn, W.; Sham, L. J. Self-consistent equations including exchange and correlation effects. *Phys. Rev.* **1965**, *140*, A1133.
- [95] Dirac, P. A. Note on Exchange Phenomena in the Thomas Atom. *Math. Proc. Camb. Philos. Soc.* **1930**, *26*, 376–385.
- [96] Ceperley, D. M.; Alder, B. J. Ground state of the electron gas by a stochastic method. *Phys. Rev. Lett.* **1980**, *45*, 566.
- [97] Vosko, S. H.; Wilk, L.; Nusair, M. Accurate spin-dependent electron liquid correlation energies for local spin density calculations: a critical analysis. *Can. J. Phys.* **1980**, *58*, 1200–1211.

- [98] Perdew, J. P.; Zunger, A. Self-interaction correction to density-functional approximations for many-electron systems. *Phys. Rev. B* **1981**, *23*, 5048.
- [99] Perdew, J. P.; Wang, Y. Accurate and simple analytic representation of the electron-gas correlation energy. *Phys. Rev. B* **1992**, *45*, 13244.
- [100] Perdew, J. P.; Burke, K.; Ernzerhof, M. Generalized Gradient Approximation Made Simple. *Phys. Rev. Lett.* **1996**, *77*, 3865.
- [101] Perdew, J. P.; Burke, K.; Ernzerhof, M. ERRATA Generalized Gradient Approximation Made Simple [Phys. Rev. Lett. 77, 3865 (1996)]. *Phys. Rev. Lett.* **1997**, *78*.
- [102] Becke, A. D. Density-functional exchange-energy approximation with correct asymptotic behavior. *Phys. Rev. A* **1988**, *38*, 3098–3100.
- [103] Lee, C.; Yang, W.; Parr, R. G. Development of the Colle-Salvetti correlation-energy formula into a functional of the electron density. *Phys. Rev. B* **1988**, *37*, 785–789.
- [104] Tao, J.; Perdew, J. P.; Staroverov, V. N.; Scuseria, G. E. Climbing the density functional ladder: Nonempirical meta-generalized gradient approximation designed for molecules and solids. *Phys. Rev. Lett.* **2003**, *91*, 146401.
- [105] Heyd, J.; Scuseria, G. E.; Ernzerhof, M. Hybrid functionals based on a screened Coulomb potential. *J. Chem. Phys.* **2003**, *118*, 8207–8215.
- [106] Heyd, J.; Scuseria, G. E.; Ernzerhof, M. Erratum: “Hybrid functionals based on a screened Coulomb potential” [J. Chem. Phys. 118, 8207 (2003)]. *J. Chem. Phys.* **2006**, *124*, 219906.
- [107] Yan, Z.; Perdew, J. P.; Kurth, S. Density functional for short-range correlation: Accuracy of the random-phase approximation for isoelectronic energy changes. *Phys. Rev. B Condens. Matter* **2000**, *61*, 169902.
- [108] Yan, Z.; Perdew, J. P.; Kurth, S. Erratum: Density functional for short-range correlation: Accuracy of the random-phase approximation for isoelectronic energy changes (Phys. Rev. B Condens. Matter (2000) 61 (16430)). *Phys. Rev. B Condens. Matter* **2010**, *81*, 169902.
- [109] Dobson, J. F.; Wang, J.; Gould, T. Correlation energies of inhomogeneous many-electron systems. *Phys. Rev. B Condens. Matter* **2002**, *66*, 081108(R).
- [110] Davidson, E. R. The iterative calculation of a few of the lowest eigenvalues and corresponding eigenvectors of large real-symmetric matrices. *J. Comput. Phys.* **1975**, *17*, 87–94.
- [111] Cullum, J. K.; Willoughby, R. A. *Lanczos algorithms for large symmetric eigenvalue computations. Vol. I: Theory*; Siam, 2002; Vol. 41.
- [112] Ericsson, T.; Ruhe, A. The spectral transformation Lánczos method for the numerical solution of large sparse generalized symmetric eigenvalue problems. *Math. Comput.* **1980**, *35*, 1251–1268.
- [113] Wigner, E. P. Random Matrices in Physics. *Siam Rev.* **1967**, *9*, 1–23.
- [114] Rubensson, E. H.; Rudberg, E.; Sałek, P. Sparse matrix algebra for quantum modeling of large systems. Lecture Notes in Computer Science (including subseries Lecture Notes in Artificial Intelligence and Lecture Notes in Bioinformatics). 2007.
- [115] Sałek, P.; Høst, S.; Thøgersen, L.; Jørgensen, P.; Manninen, P.; Olsen, J.; Jansík, B.; Reine, S.; Pawłowski, F.; Tellgren, E.; Helgaker, T.; Coriani, S. Linear-scaling implementation of molecular electronic self-consistent field theory. *J. Chem. Phys.* **2007**, *126*, 114110.

- [116] Pulay, P. Convergence acceleration of iterative sequences. the case of scf iteration. *Chem. Phys. Lett.* **1980**, *73*, 393–398.
- [117] Pulay, P. Improved SCF convergence acceleration. *J. Comput. Chem.* **1982**, *3*, 556–560.
- [118] Shepard, R.; Minkoff, M. Some comments on the DIIS method. *Mol. Phys.* **2007**, *105*, 2839–2848.
- [119] Gryn'ova, G.; Coote, M. L.; Corminboeuf, C. Theory and practice of uncommon molecular electronic configurations. *Wiley Interdiscip. Rev. Comput. Mol. Sci.* **2015**, *5*, 440–459.
- [120] Nguyễn, T. A. *Frontier orbitals : a practical manual*; John Wiley & Sons, 2007; p 304.
- [121] Cancès, E.; Bris, C. L. Can we outperform the DIIS approach for electronic structure calculations? *Int. J. Quantum Chem.* **2000**, *79*, 82–90.
- [122] Cancès, E. Self-consistent field algorithms for Kohn-Sham models with fractional occupation numbers. *J. Chem. Phys.* **2001**, *114*, 10616–10622.
- [123] Kudin, K. N.; Scuseria, G. E.; Cancès, E. A black-box self-consistent field convergence algorithm: One step closer. *J. Chem. Phys.* **2002**, *116*, 8255–8261.
- [124] Ödön Farkas; Ödön Farkas; Ödön Farkas; Schlegel, H. B. Methods for optimizing large molecules. Part III. An improved algorithm for geometry optimization using direct inversion in the iterative subspace (GDIIS). *Phys. Chem. Chem. Phys.* **2002**, *4*, 11–15.
- [125] Kudin, K. N.; Scuseria, G. E. Converging self-consistent field equations in quantum chemistry - Recent achievements and remaining challenges. *Math. Model. Num. Anal.* **2007**, *41*, 281 – 296.
- [126] Kashiwagi, H.; Sasaki, F. A generalization of the löwdin orthogonalization. *Int. J. Quantum Chem.* **1973**, *7*, 515–520.
- [127] Å Björck Numerics of Gram-Schmidt orthogonalization. *Linear Algebra Appl.* **1994**, *197-198*, 297–316.
- [128] Helgaker, T.; Larsen, H.; Olsen, J.; Jørgensen, P. Direct optimization of the AO density matrix in Hartree-Fock and Kohn-Sham theories. *Chem. Phys. Lett.* **2000**, *327*, 397–403.
- [129] Voorhis, T. V.; Head-Gordon, M. A geometric approach to direct minimization. *Mol. Phys.* **2009**, *100*, 1713–1721.
- [130] VandeVondele, J.; Hutter, J. An efficient orbital transformation method for electronic structure calculations. *The J. Chem. Phys.* **2003**, *118*, 4365.
- [131] Liang, W.; Head-Gordon, M. An exact reformulation of the diagonalization step in electronic structure calculations as a set of second order nonlinear equations. *J. Chem. Phys.* **2004**, *120*, 10379.
- [132] Stoll, H.; Wagenblast, G.; Preuß, H. On the use of local basis sets for localized molecular orbitals. *Theor. Chem. Acc.* **1980**, *57*, 169–178.
- [133] Ordejón, P.; Drabold, D. A.; Martin, R. M.; Grumbach, M. P. Linear system-size scaling methods for electronic-structure calculations. *Phys. Rev. B* **1995**, *51*, 1456.
- [134] Lasorne, B.; Worth, G. A.; Robb, M. A. Excited-state dynamics. *WIREs Comput. Mol. Sci.* **2011**, *1*, 460–475.
- [135] Ullrich, C. A. *Time-Dependent Density-Functional Theory: Concepts and Applications*; Oxford University Press, 2011.

- [136] Runge, E.; Gross, E. K. Density-Functional Theory for Time-Dependent Systems. *Phys. Rev. Lett.* **1984**, *52*, 997.
- [137] Casida, M. E. *Time-Dependent Density Functional Response Theory for Molecules*; World Scientific, 1995; Vol. Volume 1; pp 155–192.
- [138] Hait, D.; Head-Gordon, M. Orbital Optimized Density Functional Theory for Electronic Excited States. *J. Phys. Chem. Lett.* **2021**, *12*, 4517–4529.
- [139] Hirata, S.; Head-Gordon, M. Time-dependent density functional theory within the Tamm-Dancoff approximation. *Chemical Physics Letters* **1999**, *314*, 291–299.
- [140] Cullen, J.; Krykunov, M.; Ziegler, T. The formulation of a self-consistent constricted variational density functional theory for the description of excited states. *Chem. Phys.* **2011**, *391*, 124107.
- [141] Ziegler, T.; Rauk, A.; Baerends, E. J. On the calculation of multiplet energies by the hartree-fock-slater method. *Theor. Chim. Acta* **1977**, *43*, 261–271.
- [142] Barth, U. V. Local-density theory of multiplet structure. *Phys. Rev. A* **1979**, *20*, 1693.
- [143] Gavnholt, J.; Olsen, T.; Engelund, M.; Schiøtz, J.  $\Delta$  self-consistent field method to obtain potential energy surfaces of excited molecules on surfaces. *Phys. Rev. B Condens. Matter* **2008**, *78*, 075441.
- [144] Kowalczyk, T.; Yost, S. R.; Voorhis, T. V. Assessment of the  $\Delta$ SCF density functional theory approach for electronic excitations in organic dyes. *J. Chem. Phys.* **2011**, *134*, 054128.
- [145] Evangelista, F. A.; Shushkov, P.; Tully, J. C. Orthogonality constrained density functional theory for electronic excited states. *J. Phys. Chem. A* **2013**, *117*, 7378–7392.
- [146] Gilbert, A. T.; Besley, N. A.; Gill, P. M. Self-consistent field calculations of excited states using the maximum overlap method (MOM). *J. Phys. Chem. A* **2008**, *112*, 13164–13171.
- [147] Barca, G. M.; Gilbert, A. T.; Gill, P. M. Simple Models for Difficult Electronic Excitations. *J. Chem. Theory Comput.* **2018**, *14*, 1501–1509.
- [148] Barca, G. M.; Gilbert, A. T.; Gill, P. M. Excitation Number: Characterizing Multiply Excited States. *J. Chem. Theory Comput.* **2018**, *14*, 9–13.
- [149] Hait, D.; Head-Gordon, M. Excited State Orbital Optimization via Minimizing the Square of the Gradient: General Approach and Application to Singly and Doubly Excited States via Density Functional Theory. *J. Chem. Theory Comput.* **2020**, *16*, 1699–1710.
- [150] Shea, J. A.; Gwin, E.; Neuscamman, E. A Generalized Variational Principle with Applications to Excited State Mean Field Theory. *J. Chem. Theory Comput.* **2020**, *16*, 1526–1540.

## Chapter 2

---

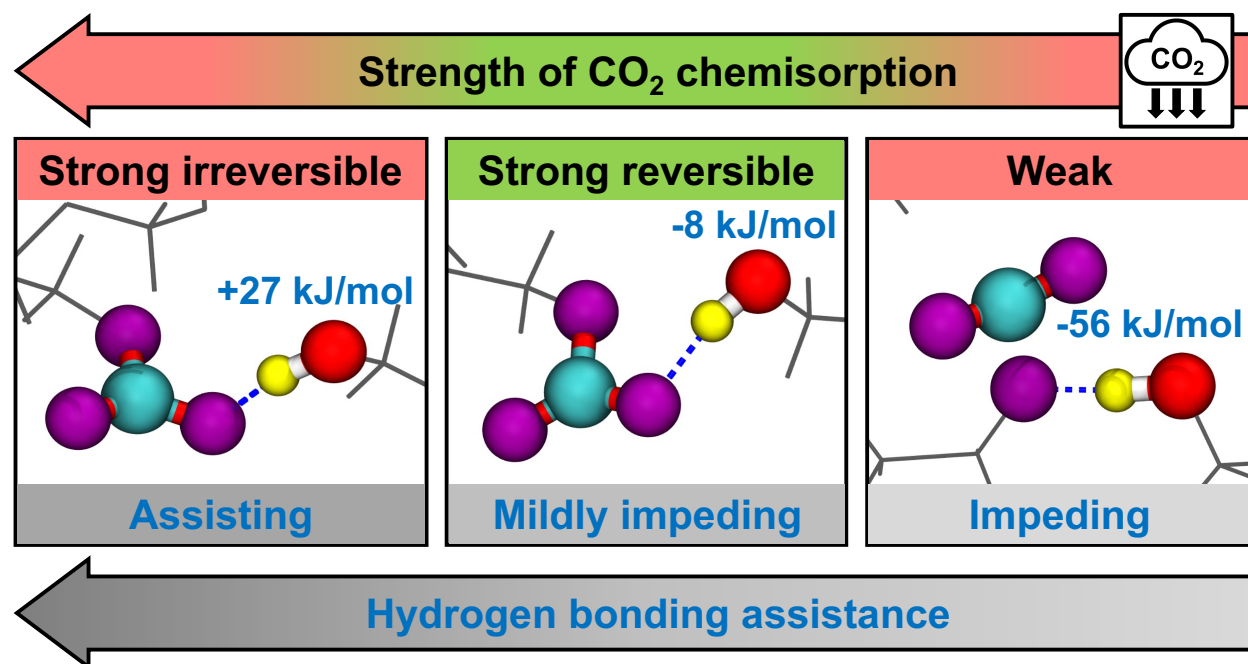
# Unraveling the origins of strong and reversible chemisorption of carbon dioxide in a green metal-organic framework

---

### 2.1 Preface

The integration of green chemistry and computational chemistry is vital for advancing carbon capture technologies. This chapter combines density functional theory modeling and experimental data analysis to explore the diverse CO<sub>2</sub> adsorption sites in CD-MOF-2, linking acid-base proton equilibrium and hydrogen bonding to the strength of CO<sub>2</sub> binding. These insights aim to guide the design of advanced materials for efficient CO<sub>2</sub> capture.

This chapter is reproduced from a published peer-reviewed article: **Pham, H. D. M.**, Khaliullin, R. Z. Unraveling the origins of strong and reversible chemisorption of carbon dioxide in a green metal-organic framework. *J. Phys. Chem. C* **2021**, 125 (44), 24719-24727.



## 2.2 Abstract

Cyclodextrin-derived metal-organic frameworks (MOFs) are remarkable not only because of their ability to absorb carbon dioxide strongly and reversibly but also because they can be readily obtained from inexpensive, renewable, and environmentally benign components. Despite the wealth of data on the carbon dioxide intake by CD-MOF-2, a representative of these MOFs, the nature and structural characteristics of its diverse adsorption sites, capable of binding CO<sub>2</sub> in the irreversible, reversible, and weak regimes, remains unclear. A comprehensive analysis of the results of the density functional theory modeling performed in this work in conjunction with experimental data shows that the hydroxyl counterions in CD-MOF-2 pull the protons away from the cyclodextrin alcohol groups, increasing their nucleophilic strength and turning them into strongly binding alkoxide chemisorption sites. At the same time, the diverse hydrogen bonding environments of the alkoxide sites reduce their nucleophilic character to a different extent, tuning their CO<sub>2</sub> binding to become irreversible, reversible or weak. By linking the acid-base proton equilibrium and hydrogen

bonding – two chemical concepts widely used for liquids – to the strength of the CO<sub>2</sub> binding in CD-MOF-2, this work suggests new strategies for advancing design of tunable solid materials for CO<sub>2</sub> capture or detection.

## 2.3 Introduction

Rising anthropogenic emission of carbon dioxide and the concomitant increase of the average global temperature<sup>1</sup> has created an urgent need to reduce the atmospheric levels of CO<sub>2</sub> or at least halt their rise<sup>2</sup>. Until long-term solutions to this challenge such as sunlight driven conversion of CO<sub>2</sub> into fuels reach maturity, carbon dioxide capture and storage (CCS) is envisioned as an important short-term strategy to lower atmospheric CO<sub>2</sub> concentration. During the capture step of CCS, carbon dioxide from flue gas must be separated from other gases to create a high purity CO<sub>2</sub> stream that is sequestered in the subsequent storage step. The adsorption of carbon dioxide followed by its release is proposed as one of the most reliable ways to capture CO<sub>2</sub> selectively. Therefore, low-cost environmentally benign materials capable of adsorbing large quantities of CO<sub>2</sub> fast, selectively and reversibly are being actively sought<sup>3</sup>.

Physisorption of carbon dioxide – that is, CO<sub>2</sub> binding through weak electrostatic, hydrophobic or Van der Waals forces – has been extensively studied experimentally and computationally as a promising carbon capture procedure<sup>4–8</sup>. Significant research effort has also been devoted to CO<sub>2</sub> chemisorption – binding of carbon dioxide through stronger chemical bonds such as covalent, ionic or metallic<sup>5,9–11</sup>. Because of the strong CO<sub>2</sub> binding, chemisorption is viewed as an important strategy to increase adsorption capacity of materials. However, carbon dioxide is often bound too strongly in the process of chemisorption making its release difficult and thus energetically costly.

High activation barriers of chemisorption reactions often make the absorption and release slow. Fortunately, there is a variety of chemisorption reactions, the thermodynamics and kinetics of which can be tuned to the desired range<sup>12-17</sup>.

Metal-organic frameworks (MOFs), long known for their ability to absorb large amount of gas efficiently<sup>5,18,19</sup>, have recently been gaining attention as promising carbon capture materials<sup>20-24</sup>. While most studies of carbon capture in MOFs have focused on CO<sub>2</sub> physisorption, it has been found that MOFs can bind carbon dioxide chemically. In this respect, a family of MOFs based on  $\gamma$ -cyclodextrin<sup>25</sup> are of particular interest not only because of their remarkable ability to absorb carbon dioxide strongly and reversibly<sup>26</sup> but also because they can be synthesized from green components<sup>27</sup>. It has been reported that MOFs with body-centered cubic structure can be crystallized at ambient temperature and pressure from the solution of  $\gamma$ -cyclodextrin (CD) and alkali halides in the mixture of water and ethanol<sup>25</sup> – substances that are inexpensive, renewable, environmentally benign and even edible. X-ray diffraction has shown<sup>25</sup> that the cubic unit cell of CD-MOF-2 – the  $\gamma$ -cyclodextrin MOF obtained using Rb(OH) instead of halides – contains six CD units linked by rubidium ions (Figure 2.1).

Initial gas-uptake experiments have indicated<sup>29,30</sup> that the activated dry form of CD-MOF-2 – with empirical formula of the unit cell<sup>25,29,30</sup> given by  $[(C_6H_{10}O_5)_8(RbOH)_2]_6$  – absorbs CO<sub>2</sub> with very high selectivity over CH<sub>4</sub><sup>26</sup> and C<sub>2</sub>H<sub>2</sub><sup>29</sup>. Because of the steep rise of the CO<sub>2</sub> adsorption isotherm it has been suggested that CO<sub>2</sub> forms strong covalent bonds with the adsorption sites in this MOF. At the same time, the color of methyl red pH indicator diffused into the pores of CD-MOF-2 has been found to change reversibly with the application and release of CO<sub>2</sub> pressure, indicating that the CO<sub>2</sub> binding is also reversible<sup>26,31</sup>.

Subsequent calorimetry experiments have been used to measure the enthalpy of the CO<sub>2</sub> adsorp-

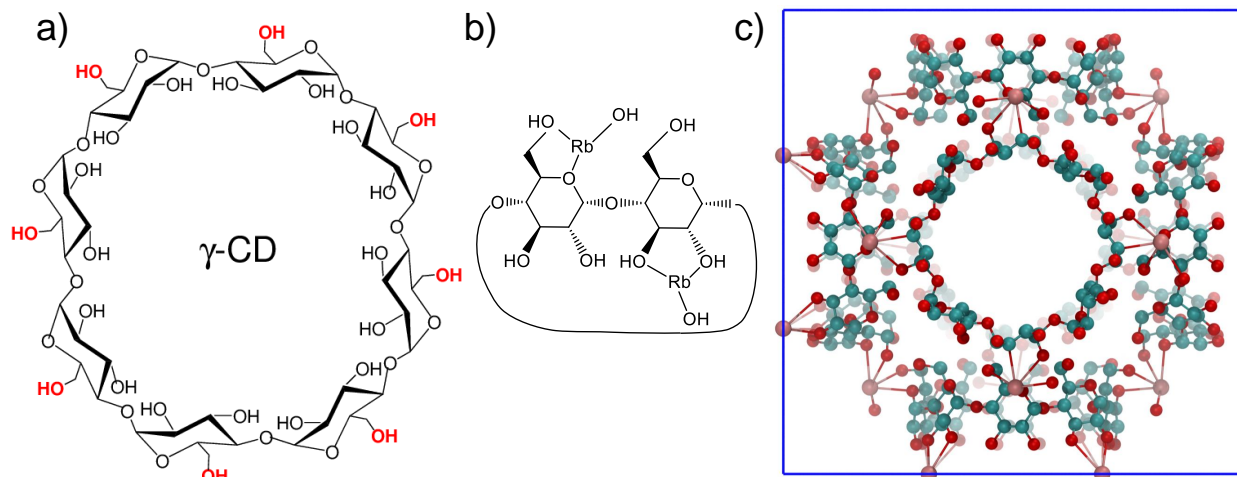


Figure 2.1: (a) Cyclic arrangement of  $\gamma$ -cyclodextrin (CD) showing eight  $\alpha$ -1,4-linked D-glucopyranosyl residues with the primary alcohol groups colored red. (b) Repeating maltosyl unit of CD with attached rubidium ions. (c) Cubic unit cell of CD-MOF-2 with carbon, oxygen, and rubidium atoms shown with cyan, red, and pink colors, respectively. The primary faces of the six CD tori point inward, whereas the secondary faces are oriented outward. The CD tori are connected via rubidium cations, forming an extended crystal structure<sup>25,26,28</sup>.

tion directly<sup>28</sup>. They have revealed that, at near-zero coverage, CO<sub>2</sub> is chemisorbed irreversibly with the enthalpy of -113.5 kJ/mol, whereas at higher coverage, the binding becomes reversible and the chemisorption enthalpy increases to -65.4 kJ/mol. At yet higher coverage, the weaker binding with the enthalpy of -40.1 kJ/mol has been observed and attributed to physisorbed CO<sub>2</sub>.

With the accumulation of experimental data, it has been hypothesized<sup>26</sup> that CO<sub>2</sub> is chemisorbed by reacting with weakly nucleophilic alcohol groups on the CD units and forming the alkylcarbonic adduct. This hypothesis has been supported by <sup>13</sup>C-NMR spectra of CD-MOF-2 that exhibit a new 158 ppm peak when exposed to CO<sub>2</sub><sup>26,32</sup>. The possibility of CO<sub>2</sub> reacting with hydroxyl counterions of CD-MOF-2 have been eliminated in control studies that use weakly basic fluoride counterions in CD-MOF-2 but still exhibit the 158 ppm peak upon exposure to CO<sub>2</sub>. The reversibility of CO<sub>2</sub> uptake has been suggested as further evidence that CO<sub>2</sub> does not react with hydroxyl counterions

since the latter process is known to be irreversible. It has also been speculated that more reactive primary alcohol groups chemisorb  $\text{CO}_2$  stronger than the secondary groups<sup>26,33</sup>.

Despite the wealth of experimental data, there are multiple unanswered questions about the microscopic mechanism of the  $\text{CO}_2$  binding in CD-MOF-2. One of the key questions is why alcohol groups, which are known to be inert to  $\text{CO}_2$  in simple alcohols<sup>32</sup>, react with carbon dioxide in CD-MOF-2. It is also unclear what is the atomistic structure of adsorption sites and, if  $\text{CO}_2$  binds exclusively to alcohol groups, why the adsorption enthalpy differs drastically for different sites. With the enormous practical importance of strong and reversible  $\text{CO}_2$  binding, answering these fundamental questions can help modify the chemistry of MOFs and help design better materials for CCS and multiple other applications such as gas separation<sup>29,34</sup>,  $\text{CO}_2$  detection in gas mixtures<sup>31</sup>, electrochemical sensing of  $\text{CO}_2$ <sup>35</sup>, and MOF-based memristors<sup>36,37</sup>.

In this work, atomistic modeling of  $\text{CO}_2$  binding in CD-MOF-2 was performed in order to answer these questions and advance the fundamental understanding of  $\text{CO}_2$  chemisorption. While computational methods has been widely used to design materials that utilize the physisorption process in MOFs for CCS applications<sup>38-44</sup>, computational studies of chemisorption have been limited<sup>16,17,45</sup>.

This is partially because the bond formation in chemisorption processes cannot be described with traditional force field methods and typically requires more computationally demanding electronic structure methods such as density functional theory (DFT).

## 2.4 Computational models and methods

All calculations were performed using the DFT module of the CP2K software package<sup>46</sup>. The dispersion corrected<sup>47</sup> generalized gradient approximation of Becke and Lee-Yang-Parr (BLYP)<sup>48,49</sup> was used as the exchange-correlation functional. In the dual Gaussian and plane-wave scheme implemented in CP2K<sup>50</sup>, double- $\zeta$  valence basis set with one set of polarization functions (DZVP)<sup>51</sup> and triple- $\zeta$  valence (TZV2P) with two set of polarization functions were used to represent atomic orbitals of Rb atoms and all other atoms, respectively. A plane-wave cutoff of 300 Ry was used to describe the electron density. Separable norm-conserving Goedecker-Teter-Hutter pseudopotentials were used to describe the interactions between the valence electrons and ionic cores<sup>52,53</sup>. The self-consistent field procedure was carried out using the direct minimization orbital transformation approach<sup>54</sup> with the kinetic preconditioner. For negatively charged unit cells, the calculations were done with the positive neutralizing uniform background. Atomic positions of all atoms were optimized using the limited-memory Broyden-Fletcher-Goldfarb-Shanno algorithm until the maximum force on atoms decreased below 0.00045 a.u.

A model of the unit cell of CD-MOF-2 was constructed using crystallographic data<sup>55</sup> obtained from the Cambridge Crystallographic Data Centre<sup>56</sup>. In order to reproduce partial site occupation, rubidium cations were placed randomly in a half of the available crystallographic sites. Hydroxyl counterions, the precise positions of which cannot be obtained in the X-ray diffraction experiments, were coordinated on rubidium ions. Water molecules were removed in order to obtain a unit cell with the stoichiometric formula  $[(C_6H_{10}O_5)_8(RbOH)_2]_6$  that is in agreement with the composition of the degassed CD-MOF-2 used in the CO<sub>2</sub> adsorption experiments<sup>25,28</sup>. Atomic positions were optimized with the lattice parameters fixed at their experimental values.

In addition to performing simple geometry relaxation of the experimentally determined crystal structure of CD-MOF-2, 2 ps constant volume constant temperature *ab initio* molecular dynamics (AIMD) simulations were carried out at  $T = 400$  K followed by the geometry optimization of the last AIMD snapshot. This was done to allow the thermal motion in AIMD simulations to re-arrange hydrogen bonds between the CD units of CD-MOF-2 and to produce more diverse adsorption environments.

Adsorption of carbon dioxide in CD-MOF-2 was modeled by attaching a single  $\text{CO}_2$  molecule to the oxygen atom of a pre-selected alcohol group in the unit cell. The initial position of the  $\text{CO}_2$  group was generated in the internal coordinates (i.e. Z-matrix) relative to the adsorption site. The oxygen binding site ( $\text{O}^*$ ) and its two preceding carbons ( $\text{C}^*$ ) from the oligosaccharide were used as the three reference atoms to specify the  $\text{CO}_2$  internal coordinates. The initial bond length between the carbon atom of  $\text{CO}_2$  and  $\text{O}^*$  was set to  $1.32 \text{ \AA}$ , whereas the  $\text{C}^*\text{O}^*\text{C}$  bond angle and  $\text{C}^*\text{C}^*\text{O}^*\text{C}$  dihedral angle were drawn randomly from the  $125 - 145^\circ$  and  $120 - 360^\circ$  ranges, respectively. In addition, the  $\text{O}^*\text{CO}$  angle was set to  $125^\circ$ , while the  $\text{OCO}$  angle of the  $\text{CO}_2$  molecule was set to  $110^\circ$ . These values were based on the structural experimental data for carbonic acid, which is expected to be similar to the alkylcarbonic adduct. Initial configurations with substantial interatomic overlap were rejected and the random structure generation was repeated until a chemically reasonable adduct structure without bad interatomic contacts was obtained.

Based on the arguments outlined in Supporting Information, the enthalpy of adsorption was approximated with the energy of adsorption.

## 2.5 Results and discussion

Since the precise location of the hydrogen atoms at the adsorption sites is not known from experiments<sup>25</sup>, different models for the location of the protons before and after CO<sub>2</sub> adsorption were examined. The results obtained for each model are discussed below.

### 2.5.1 Chemisorption on neutral alcohol groups

In the first model, CO<sub>2</sub> molecule reacts with a neutral alcohol group. Upon adsorption, the proton of the alcohol group is transferred to protonate the newly formed alkylcarbonic acid (Figure 2.2a).

The adsorption energies for several primary and secondary neutral alcohol groups are summarized in Figure 2.3. All adsorption energies were found to be positive, lying between 28 and 115 kJ/mol. Since the entropy decreases in the adsorption process, it is clear that the formation of alkylcarbonic acid via the neutral model reaction has positive free energy and, therefore, cannot proceed spontaneously contradicting experimental observations. The calculated values of the adsorption energies are also in dramatic disagreement with the experimentally measured enthalpies of adsorption lying between -114 and -40 kJ/mol.

Several attempts were made to search for alternative orientations of the alkylcarbonic group that could be stabilized by nearby functional groups and produce more favorable CO<sub>2</sub> binding. In one approach, the alkylcarbonic groups were manually rotated to bring them closer to either nearby alcohol groups or nearby counterions at rubidium atoms, with the expectation that newly formed hydrogen bonds can stabilize the system. In another approach, constant volume constant temperature AIMD simulations of the combined length of 2.5 ps were performed at T = 400 K in order to allow thermal fluctuation to overcome low-lying energy barriers between local minima

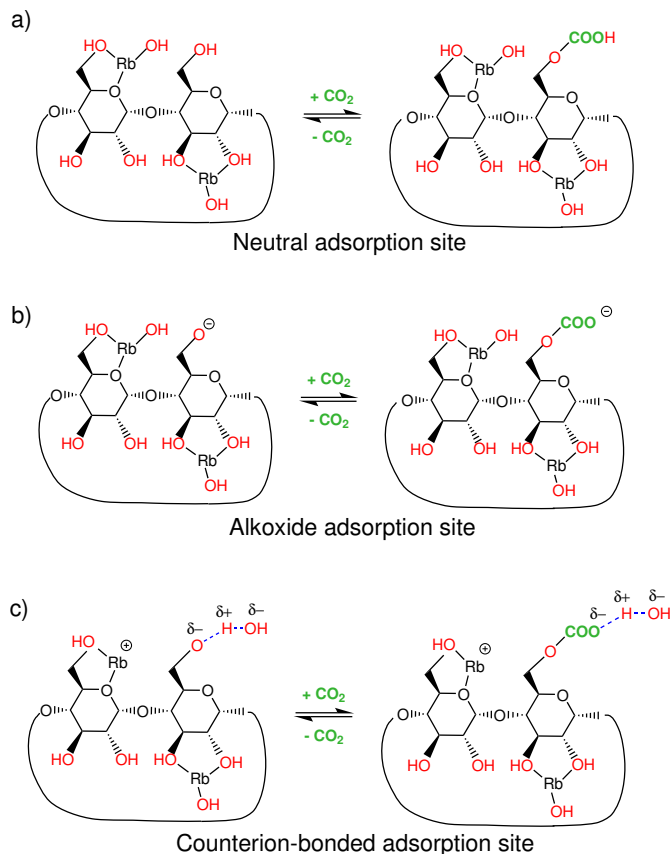


Figure 2.2: Model reactions for  $\text{CO}_2$  adsorption: (a) neutral alcohol groups, (b) alkoxide groups, (c) counterion-bonded groups. Only a single maltosyl unit of  $\gamma$ -cyclodextrin is shown for clarity. The proximity of the  $\text{CO}_2$  binding sites to the Rb ion in this simplified scheme might not correctly reflect the distance between them in the MOF crystal structure.

and to generate new stable configurations in an unbiased way. In both cases, the geometry of the newly generated structures was re-optimized and the adsorption energies were recomputed. Several structures of the alkylcarbonic adducts with lower energy were found but the reduction in the  $\text{CO}_2$  adsorption energy was 20.3 kJ/mol on average, bringing the lowest  $\text{CO}_2$  adsorption energy from 28.2 to 13.3 kJ/mol. This additional stabilization is not sufficient to explain the range of the experimentally measured adsorption enthalpies.

The positive adsorption energies calculated for neutral alcohol groups in CD-MOF-2 are not unexpected. They are in agreement with a body of previous studies of the interaction between

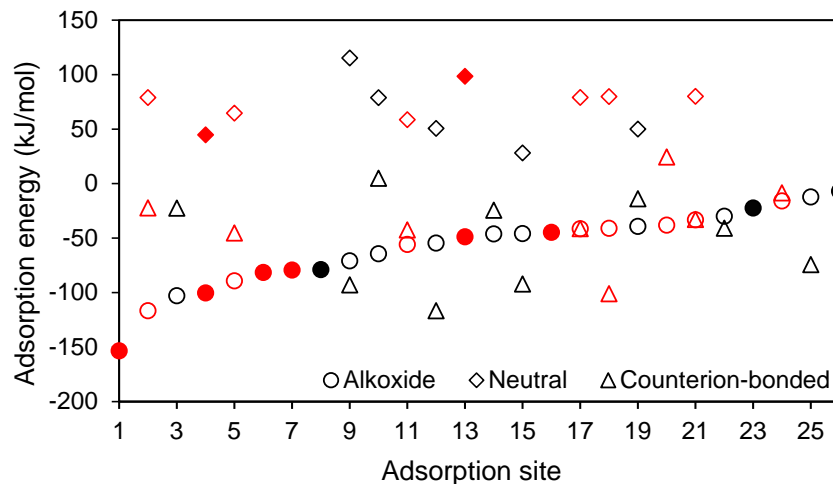


Figure 2.3: CO<sub>2</sub> adsorption energy calculated for different model reactions at primary (red) and secondary (black) binding sites. Filled shapes represent geometries generated using AIMD, whereas empty shapes represent geometries obtained from the straightforward geometry optimization. The corresponding numerical data is listed in Table 1.1 in Supporting Information.

CO<sub>2</sub> and simple alcohols<sup>32,57</sup>. For example, <sup>1</sup>H and <sup>13</sup>C NMR studies of pressurized CO<sub>2</sub> in pure anhydrous liquid methanol did not produce any evidence of the insertion of CO<sub>2</sub> into the O–H bond of methanol<sup>32</sup>. The accompanying gas-phase DFT calculations<sup>32</sup> showed that the standard free energy of the methylcarbonic acid formation from CO<sub>2</sub> and methanol is positive (41 kJ/mol) even if solvation effects are taken into account with explicitly included methanol molecules and a polarizable continuum model. Furthermore, the standard free energy of the methylcarbonic acid formation from CO<sub>2</sub> and methanol in the gas phase was measured to be 11 kJ/mol<sup>57</sup>. These measurements and calculations indicate the methylcarbonic acid is thermodynamically less stable than CO<sub>2</sub> and methanol. In addition to the thermodynamics considerations, high free energy barriers have been calculated for several pathways of the methylcarbonic acid formation from CO<sub>2</sub> and methanol<sup>32</sup>, suggesting that the process is expected to be very slow.

Despite a careful account of interactions between the chemisorbed CO<sub>2</sub> and its environment, the failure of neutral model to stabilize carbon dioxide in CD-MOF-2 implies that binding sites of

different nature must be considered.

### 2.5.2 Chemisorption on alkoxide sites

To explain the strong binding of CO<sub>2</sub>, the nucleophilic strength of a binding site was increased by removal of the proton of a selected alcohol group, producing an alkoxide site. Although it is unclear whether these negatively charged groups exist in the real CD-MOF-2 framework, the alkoxide adsorption model depicted in Figure 2.2b allows to estimate the maximum CO<sub>2</sub> binding ability of alcohol groups in CD-MOF-2. Furthermore, this simple model obviates the need of addressing a question of the proton location and thus enables quick exploratory calculations.

Figure 2.3 shows that adsorption energies for multiple randomly selected primary and secondary alkoxide sites are broadly distributed and negative. The strongest calculated binding energy (-153 kJ/mol) is stronger than the experimentally measured enthalpy for irreversible chemisorption (-114 kJ/mol), partially because of the known tendency of the employed exchange-correlation functional to overestimate binding strength (Table 1.2)<sup>58,59</sup>. There are also multiple model sites with the adsorption energy matching experimentally determined ranges for reversible chemisorption (-65 kJ/mol) and physisorption (-40 kJ/mol)<sup>28</sup>. It appears that simple alkoxide sites are capable of reproducing the range of the observed adsorption enthalpies and, therefore, can be considered as a more realistic model of CO<sub>2</sub> binding in CD-MOF-2 than neutral alcohol sites.

In addition to covering the range of experimentally measured interaction energies, the calculations imply that the weak CO<sub>2</sub> binding previously classified as physisorption can be attributed to weak chemisorption as well. Analysis of data in Figure 2.3 indicates that primary alkoxide sites bind CO<sub>2</sub> stronger (-67±38 kJ/mol) than secondary sites (-47±28 kJ/mol). However, the wide spread

of energies indicates that both primary and secondary sites can be occupied by CO<sub>2</sub> molecules, contrary to the previous suggestion that it is mostly primary alcohol groups that interact with carbon dioxide. It should be noted that the AIMD-generated structures of CD-MOF-2 exhibit the same ability to bind CO<sub>2</sub> as the structure obtained from the straightforward geometry optimization of the experimentally determined CD-MOF-2 crystal structure.

### 2.5.3 Effect of the environment on CO<sub>2</sub> adsorption

To understand the wide spread of the binding energies calculated using the alkoxide model, we examined the effect of environment on the CO<sub>2</sub> adsorption. It can be hypothesized that the nearby alcohol groups is the primary factor affecting CO<sub>2</sub> binding to the negatively charged sites. In order to verify this hypothesis, the alcohol groups located less than 3 Å from the alkoxide site were replaced by hydrogen atoms. The cutoff distance was chosen to eliminate moderate and strong hydrogen bonding interaction between the alcohol groups and the alkylcarbonyl adduct. As shown in Figure 2.4, the replacement of the alcohol groups with hydrogen atoms results in the substantial increase in the CO<sub>2</sub> binding strength for most of the adsorption sites. The average adsorption energy drops from -58.2 kJ/mol for sites with alcohol neighbors to -108.5 kJ/mol for sites with hydrogen neighbors. Moreover, the spread of adsorption energies decreased from 34.6 kJ/mol to 26.3 kJ/mol. It was verified in a control calculation that replacing a distant alcohol group 8 Å from an alkoxide site has a only small effect (5 kJ/mol) on the adsorption energy, as expected.

Further insight into the effect of alcohol groups on the CO<sub>2</sub> binding strength was obtained by replacing a single nearby alcohol group with a hydrogen atom. To quantify the effect of a nearby

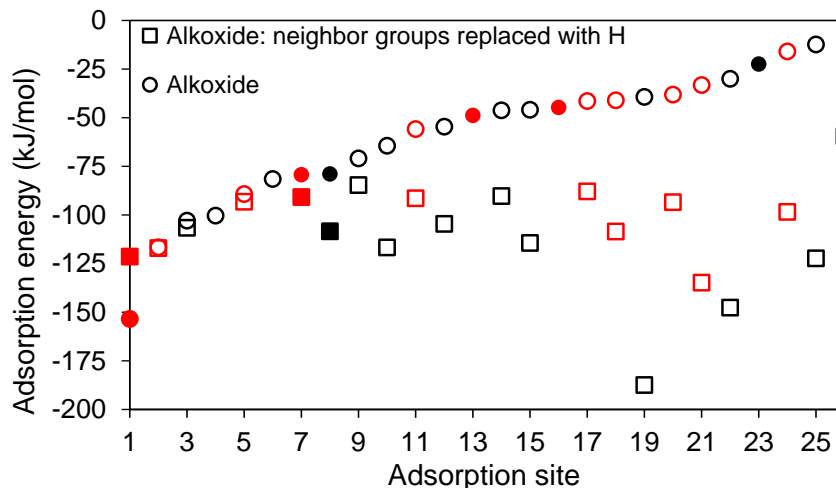


Figure 2.4: Effect of replacing neighbor alcohol groups with hydrogen atoms on  $\text{CO}_2$  adsorption energies at primary (red) and secondary (black) binding sites. Filled shapes represent models using AIMD before the adsorption procedure, while the unfilled ones did not. The corresponding numerical data is listed in Table 1.1

alcohol group ( $i$ ) on the  $\text{CO}_2$  adsorption energy at a given adsorption site, quantity  $\Delta\Delta E_{\text{ads}}^{(i)}$  is defined

$$\Delta\Delta E_{\text{ads}}^{(i)} = \Delta E_{\text{ads}}(\text{C}^{(i)}\text{-OH}) - \Delta E_{\text{ads}}(\text{C}^{(i)}\text{-H}) \quad (2.1)$$

as the difference between the initial adsorption energy  $\Delta E_{\text{ads}}(\text{C}^{(i)}\text{-OH})$  and the adsorption energy after the substitution  $\Delta E_{\text{ads}}(\text{C}^{(i)}\text{-H})$ . Positive values of  $\Delta\Delta E_{\text{ads}}^{(i)}$  indicate that neighbor ( $i$ ) weakens the  $\text{CO}_2$  binding because  $\text{CO}_2$  is bound more strongly after the replacement. In this case, the typically negative adsorption energy decreases upon the replacement. Conversely, negative value of  $\Delta\Delta E_{\text{ads}}^{(i)}$  indicate that neighbor ( $i$ ) strengthens the  $\text{CO}_2$  binding.

$\Delta\Delta E_{\text{ads}}^{(i)}$  values shown in Figure 2.5 for representative chemisorption sites indicate that nearby alcohol groups have dramatically different effect on the  $\text{CO}_2$  binding. The differences can be explained by analyzing hydrogen bonding patterns between the neighbors and the alkylcarbonic adduct (Figure 2.5, left panels) and also between the neighbors and the pre-adsorption site (Figure 2.5, right panels). According to the hydrogen bonds formed by the neighbors, they can be

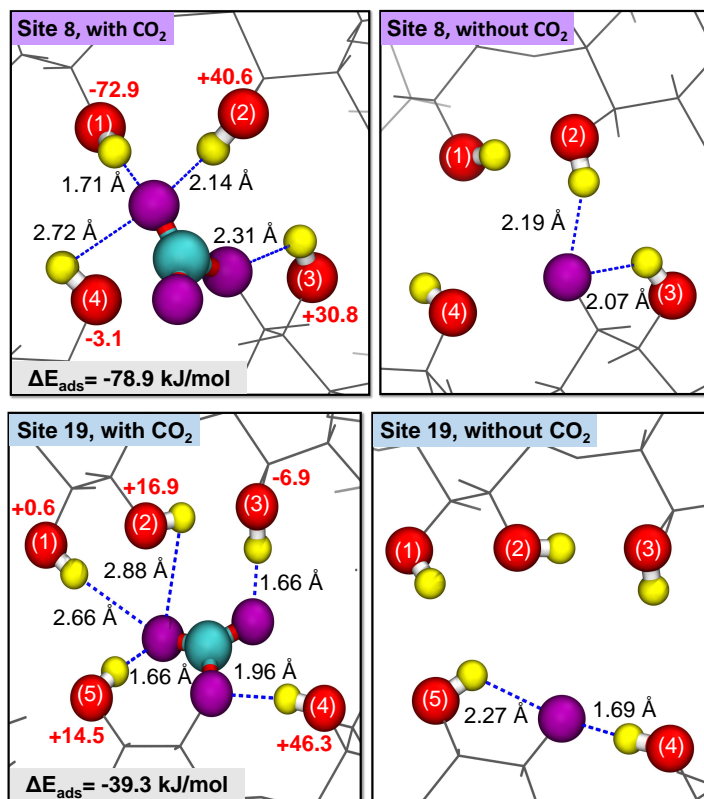


Figure 2.5: Effect of replacing neighbor alcohol groups with hydrogen atoms on the CO<sub>2</sub> binding strength. The adsorption site and nearby alcohol groups are shown as spheres in the wireframe MOF background. The CO<sub>2</sub> carbon atom is green and the hydrogen atoms are yellow. Oxygen atoms of the adsorption site and alkylcarbonyl group are shown in purple, whereas oxygen atoms of nearby alcohol groups are shown in red. Blue dash lines represent hydrogen bonds. Values of  $\Delta\Delta E_{\text{ads}}^{(i)}$ , defined in Eq. (2.1), are shown as red numbers. The CO<sub>2</sub> adsorption energies before the neighbor replacement are shown in grey fields.

logically divided into the following three categories.

In the first category, there are alcohol groups that form hydrogen bonds with the oxygen atom of the adsorption site before and after the CO<sub>2</sub> adsorption. Examples of these groups include neighbor (3) of site 8 and neighbor (4) of site 19 (Figure 2.5). Such neighbors tend to weaken the CO<sub>2</sub> binding because the hydrogen bond in the pre-adsorption site is stronger than that in the post-adsorption structure. The change in the strength of the hydrogen bond is due to the delocalization of the negative charge over the oxygen atoms in the alkylcarbonyl adduct. In other words, these

neighbors decrease the nucleophilic strength of the adsorption site, making its interaction with CO<sub>2</sub> weaker.

The second category includes alcohol groups that form hydrogen bonds with the oxygen atom of the adsorption site before the CO<sub>2</sub> adsorption and with the oxygen atom of CO<sub>2</sub> in the post-adsorption structure. Neighbor (2) of site 8 and neighbor (5) of site 19 in Figure 2.5 are representatives of this category. The positive values of  $\Delta\Delta E_{\text{ads}}^{(i)}$  for these neighbors indicate that the CO<sub>2</sub> insertion disrupts a stronger hydrogen bond than the hydrogen bond being formed. As a result, the neighbors in this category weaken the CO<sub>2</sub> binding.

Alcohol groups in the third category form a hydrogen bond with the oxygen atom of CO<sub>2</sub> exclusively in the post-adsorption alkylcarbonic structure. They make CO<sub>2</sub> binding stronger. The amount of the stabilization depends on the geometry of the hydrogen bond that is influenced by the relative position of the bonded atoms (e.g. compare neighbors (1) and (4) of site 8 in Figure 2.5) and the local configuration of the hydrogen bond network that extends to the next nearest neighbors.

It is interesting to note that the sum of individual neighbor effects (Figure 2.5) is not equal to the combined effect of all neighbors (Figure 2.4). For example, the sum of effects of individual neighbors on site 8 is 1.6 kJ/mol, while their combined effect is -29.5 kJ/mol. This non-additivity emphasizes that the insertion CO<sub>2</sub> disrupts a complex network of interacting hydrogen bonds in CD-MOF-2 and the CO<sub>2</sub> binding is determined to some extent by the cooperativity effects in this network.

The influence of single nearby alcohol groups can also be illustrated on the example of three sites that represent adsorption sites with strong (site 1), medium (site 7) and weak (site 26) CO<sub>2</sub> binding energies, each lying within the three ranges described in the calorimetric studies<sup>28</sup> (Figure 2.6). As expected, the strong CO<sub>2</sub> chemisorption at site 1 is accompanied by the strong stabilizing effect

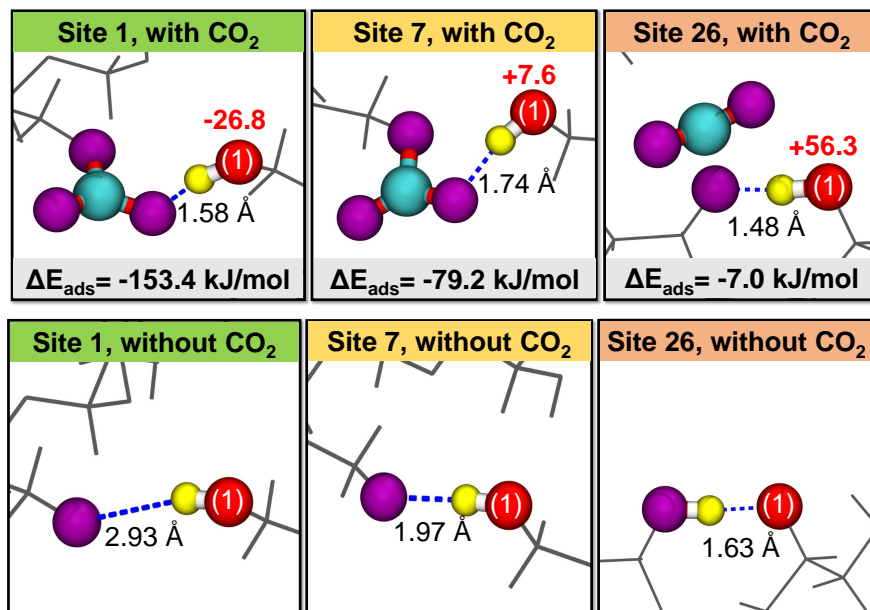


Figure 2.6: Effect of replacing neighbor alcohol groups with hydrogen atoms on the CO<sub>2</sub> binding strength for sites that bind CO<sub>2</sub> strongly (green), moderately (yellow) and weakly (red). Color coding and labels are explained in the caption of Figure 2.5.

of the neighbor from the third category. Meanwhile, the sole neighbor of the moderately binding site 7 belongs to the second category and exhibits only a minor destabilizing effect on the CO<sub>2</sub> adsorption. Finally, the neighbor at site 26 belongs to the first category and weakens the CO<sub>2</sub> adsorption dramatically. This case is a rather extreme example since the proton in the pre-adsorption site is completely transferred to the alkoxide site, significantly reducing its nucleophilic properties and CO<sub>2</sub> binding ability.

Data in Figure 2.6 shows that the spread in the adsorption energies at the three sites is significantly reduced upon the replacement of the neighbors – an example of the general “spread-reducing” effect of the neighbor substitution seen in Figure 2.4. This indicates that unique hydrogen bonding environments of adsorption sites are largely responsible for their ability to bind CO<sub>2</sub> and for the large spread in the experimentally measured binding enthalpies. Additionally, the quantitative analysis of the hydrogen bonding suggests that the influence of nearby alcohol groups can only

partially explain the spread in the binding strength. This is because the neighbor replacement does not produce equally strong adsorption sites. Besides immediate neighbors, there are apparently other factors that affect CO<sub>2</sub> adsorption. One example of such factors might include the electrostatic fields created by the MOF framework at the adsorption site.

The neighbor replacement experiment indicates that the CD-MOF-2 environment has the overall weakening effect on the CO<sub>2</sub> binding. The same effect can also be seen by comparing the strength of the CO<sub>2</sub> binding in CD-MOF-2 (Figure 2.3) and on the reference model sites with a minimal interaction between the alkoxide group and its environment (i.e. “environment-free” reference models): gas-phase methoxide (-169 kJ/mol), primary alkoxide sites on an amylose unit and a  $\gamma$ -cyclodextrin torus (-113 kJ/mol and -84 kJ/mol, respectively).

#### 2.5.4 Formation of active chemisorption sites

The success of the alkoxide model in reproducing the range of CO<sub>2</sub> binding energies requires an investigation of the mechanism of the formation of negatively charged alcohol groups.

One of many plausible pathways to form a negatively charged active site is to transfer the proton of an alcohol group to a hydroxyl counterion – a site with strong basic properties. A series of exploratory calculations reveals that proton transfer energies from an alcohol group to a counterion range from -103 to 232 kJ/mol (see Table 1.3). This wide spread indicates that the proton transfer is affected by the immediate surroundings of both the donor and acceptor sites, which is not surprising in light of the discussion of environment effects on the CO<sub>2</sub> adsorption energy. The presence of very low negative energies demonstrates that the formation of negatively charged alcohol groups is thermodynamically plausible if a proton is transferred to a hydroxyl counterion. At the same time,

the range of calculated energies suggests that a quantitative description of the thermodynamics of this long-range proton transfer and, therefore, the formation of adsorption sites requires extensive studies employing AIMD, which are beyond the scope of this work and perhaps at the limit of feasibility of modern high-cost AIMD methods.

An alternative to the long-range transfer of a proton is the local stabilization of the chemisorption site by a freely floating hydroxyl counterion, that is, a counterion not directly bonded to a rubidium cation (Figure 2.2c). Our calculations showed that some hydroxyl ions indeed detach from their rubidium sites during geometry optimization and AIMD simulations. Therefore, freely floating hydroxyls are expected to exist in CD-MOF-2 in noticeable concentrations. It was found that, in 13 out of 17 considered counterion-bonded absorption sites (Figure 2.2c), the proton transfers spontaneously from the alcohol group to the counterion with the formation of the alkoxide site hydrogen-bonded to the water molecule. Because of the strong nucleophilic character of the alkoxide group (see previous section), it is not surprising that the CO<sub>2</sub> adsorption energies calculated for these proton-transferred sites are negative and also cover the range of the experimental values (Figure 2.3). It is remarkable that 3 out of the 17 counterion-bonded sites (i.e. sites 3, 5, and 22 in Figure 2.3), which do not undergo any proton transfer, are still capable of binding CO<sub>2</sub> although weakly. This indicates that a mere presence of a hydrogen bond between the counterion and adsorption site can create a CO<sub>2</sub> binding site with sufficiently strong nucleophilic character. Another mechanism, through which a nearby counterion can stabilize the chemisorbed CO<sub>2</sub> molecule, is the proton transfer from the alkylcarbonic acid to a nearby counterion. This transfer was indeed observed in all 17 sites considered here.

Yet another possible mechanism of the formation of negatively charged adsorption sites is the self-ionization of the network of hydrogen-bonded alcohol groups, in which one neutral alcohol

group transfers its proton to another neutral alcohol group, creating an alkoxide site. The two-picosecond 400 K AIMD simulation and multiple geometry optimizations performed in this work did not produce such spontaneous self-ionization events. The only observed proton transfer occurred to hydroxyl counterions. While these limited calculations do not eliminate the possibility of self-ionization in the real CD-MOF-2 network, they imply that self-ionization is a less likely origin of the adsorption sites than the proton transfer to hydroxyl counterions with strong basic properties.

### 2.5.5 Analysis of computational and experimental data

The collected DFT data implies that hydroxyl counterions play an important role in the formation of alkoxide CO<sub>2</sub> adsorption sites as shown in the counterion-bonded model in Figure 2.2c. While the indirect participation of hydroxyl counterions has not been considered before, this hypothesis is in agreement with all experimental studies of CO<sub>2</sub> binding in CD-MOF-2.

First, calorimetry measurements<sup>28</sup> suggest that less than 4.63 CO<sub>2</sub> molecules are adsorbed per unit cell of CD-MOF-2 at the pressure when all sites binding CO<sub>2</sub> strongly and reversibly are occupied. (see Supporting Information for details). First, experimental measurements of the adsorbed CO<sub>2</sub> volume<sup>26</sup> and calorimetry measurements<sup>28</sup> suggest that between RZK and 1.4 of CO<sub>2</sub> molecules are adsorbed per unit cell of CD-MOF-2 at pressure under 1 torr and room temperature (see Supporting Information for details). Since the number of adsorbed CO<sub>2</sub> molecules is lower than the number of hydroxyl anions in the unit cell (12 hydroxyl ions), experimental data suggests that a sufficient number of hydroxyl anions is available to facilitate the adsorption of each CO<sub>2</sub> molecule. Hence, the indirect participation of hydroxyl anions is consistent with this experimental data.

Second, the indirect participation of hydroxyl counterions in the CO<sub>2</sub> binding is in agreement with the <sup>13</sup>C-NMR 158 ppm peak attributed to alkylcarbonic products<sup>26</sup>. It should also be mentioned here that the DFT calculations alone cannot eliminate the possibility of the direct CO<sub>2</sub> adsorption on hydroxyl counterions because the calculated adsorption energy for these sites is found to be around -94 kJ/mol, which is similar to the adsorption energies on alkoxide sites. The NMR data, however, favors the model of indirect hydroxyl participation over the direct chemisorption on hydroxyl anions.

Third, replacing hydroxyl counterions with weakly basic fluoride anions in computer models still produces weak CO<sub>2</sub> binding and therefore agrees with control experimental studies, in which the fluoride-substituted CD-MOF-2 exhibits the same 158 ppm peak upon its exposure to CO<sub>2</sub><sup>25</sup>. It is important to note that only 3 out of 8 fluoride-bonded adsorption sites (5, 12 and 18) have the negative CO<sub>2</sub> adsorption energy, ranging from -24 to -8 kJ/mol. The weak binding energy is not surprising because the nucleophilic strength of fluoride-bonded adsorption sites is expected to be much much lower than that of hydroxyl-bonded sites. However, even a few sites with chemisorbed CO<sub>2</sub> are sufficient to produce the NMR signature of alkylcarbonic structures.

## 2.6 Conclusions

DFT modeling was used to examine the nature of the CO<sub>2</sub> adsorption sites in CD-MOF-2 – a green MOF with a remarkable ability to chemisorb carbon dioxide strongly and reversibly. It was found that the interaction of CO<sub>2</sub> with neutral alcohol groups on  $\gamma$ -cyclodextrin units of CD-MOF-2 is thermodynamically prohibitive. In contrast, the CO<sub>2</sub> adsorption on negatively charged alkoxide groups was shown to occur spontaneously with the range of computed interaction energies matching

those measured experimentally.

A comprehensive analysis of environment effects revealed that the strength of the CO<sub>2</sub> binding is largely determined by the hydrogen bonds formed by both the adsorption sites and the alkylcarbonic adducts with the surrounding alcohol groups. It was demonstrated that the network of hydrogen bonds between alcohol groups in CD-MOF-2 tends to reduce the nucleophilic character of alkoxide adsorption sites, weakening the CO<sub>2</sub> binding and making it reversible. The diversity of the hydrogen bonding environments is also at the origins of the wide range of the adsorption energies measured for this unique MOF.

The calculations suggest that a negative alkoxide site can form readily through the proton transfer from an alcohol group to a freely-floating hydroxyl counterion. The formation of a strong hydrogen bond between an alcohol group and a nearby hydroxyl counterion appears to be sufficient to chemisorb CO<sub>2</sub> weakly. Such indirect participation of hydroxyl counterions in the chemisorption of CO<sub>2</sub> was shown to be consistent with the available experimental data.

Remarkably, the calculations suggests both primary and secondary sites bind CO<sub>2</sub> molecules, contrary to the previous suggestion that it is mostly primary alcohol groups that interact with carbon dioxide. The DFT data also suggests that the weak CO<sub>2</sub> binding previously classified as physisorption can also be attributed to weak chemisorption.

It should be noted that future computational studies aimed at a quantitative statistical description of the CO<sub>2</sub> binding in CD-MOF-2 should employ accelerated AIMD simulations in order to determine the most favorable locations of protons within the complex network of hydrogen bonds in this MOF. The utilization of hybrid density functionals can also improve the description of the energetics of the CO<sub>2</sub> binding. Unfortunately, such resource-demanding simulations are beyond the capabilities of most computing platforms today.

Several findings presented in this work have implications for advancing design of materials for carbon capture and storage. By quantifying the influence of hydrogen bonds on the energetics of the CO<sub>2</sub> binding, this work allows to estimate to which extent the carbon intake can be manipulated through hydrogen bonding. The importance of counterions for the CO<sub>2</sub> binding in CD-MOF-2 suggests a new strategy to tune the strength of the CO<sub>2</sub> chemisorption in similar “dual-agent” binding systems containing an adsorption site and activating counterion. In addition to modifying adsorption sites, changing the nature of activating agents can help to tune the CO<sub>2</sub> binding strength to the desired range.

## 2.7 Acknowledgements

The research was funded by the Natural Sciences and Engineering Research Council of Canada (NSERC) through Discovery Grant (RGPIN-2016-0505) and by Tri-agency Institutional Programs Secretariat through New Frontiers in Research Fund (NFRFE-2018-00852). The authors are grateful to Compute Canada for computer resources allocated under the CFI John R. Evans Leaders Fund program.

## 2.8 References

- [1] The Core Writing Team IPCC *Climate Change 2014: Synthesis Report. Contribution of Working Groups I, II and III to the Fifth Assessment Report of the Intergovernmental Panel on Climate Change*; 2015; p 151.
- [2] Friedlingstein, P.; Houghton, R. A.; Marland, G.; Hackler, J.; Boden, T. A.; Conway, T. J.; Canadell, J. G.; Raupach, M. R.; Ciais, P.; Le Quéré, C. Update on CO<sub>2</sub> Emissions. *Nat. Geosci.* **2010**, *3*, 811–812.
- [3] Patel, H. A.; Byun, J.; Yavuz, C. T. Carbon Dioxide Capture Adsorbents: Chemistry and Methods. *ChemSusChem* **2017**, *10*, 1303–1317.
- [4] Poloni, R.; Smit, B.; Neaton, J. B. CO<sub>2</sub> Capture by Metal–Organic Frameworks with Van Der Waals Density Functionals. *J. Phys. Chem. A* **2012**, *116*, 4957–4964.
- [5] Yu, C. H.; Huang, C. H.; Tan, C. S. A Review of CO<sub>2</sub> Capture by Absorption and Adsorption. *Aerosol Air Qual. Res.* **2012**, *12*, 745–769.
- [6] Herm, Z. R.; Swisher, J. A.; Smit, B.; Krishna, R.; Long, J. R. Metal-Organic Frameworks as Adsorbents for Hydrogen Purification and Precombustion Carbon Dioxide Capture. *J. Am. Chem. Soc.* **2011**, *133*, 5664–5667.
- [7] Abd, A. A.; Naji, S. Z.; Hashim, A. S.; Othman, M. R. Carbon Dioxide Removal through Physical Adsorption using Carbonaceous and Non-Carbonaceous Adsorbents: A Review. *J. Environ. Chem. Eng.* **2020**, *8*, 104142.
- [8] Müller, P.; Bucior, B.; Tuci, G.; Luconi, L.; Getzschmann, J.; Kaskel, S.; Snurr, R. Q.; Giambastiani, G.; Rossin, A. Computational Screening, Synthesis and Testing of Metal–Organic Frameworks with a Bithiazole Linker for Carbon Dioxide Capture and its Green Conversion into Cyclic Carbonates†. *Mol. Syst. Des. Eng.* **2019**, *4*, 1000–1013.
- [9] D’Alessandro, D. M.; Smit, B.; Long, J. R. Carbon Dioxide Capture: Prospects for New Materials. *Angew. Chem. Int. Ed.* **2010**, *49*, 6058–6082.
- [10] Fahlman, M.; Fabiano, S.; Gueskine, V.; Simon, D.; Berggren, M.; Crispin, X. Interfaces in Organic Electronics. *Nat. Rev. Mater.* **2019**, *4*, 627–650.
- [11] Younas, M.; Sohail, M.; Kong, L. L.; Bashir, M. J.; Sethupathi, S. Feasibility of CO<sub>2</sub> Adsorption by Solid Adsorbents: A Review on Low-Temperature Systems. *Int. J. Environ. Sci. Technol.* **2016**, *13*, 1839–1860.
- [12] Memon, M. Z.; Zhao, X.; Sikarwar, V. S.; Vuppaladadiyam, A. K.; Milne, S. J.; Brown, A. P.; Li, J.; Zhao, M. Alkali Metal CO<sub>2</sub> Sorbents and the Resulting Metal Carbonates: Potential for Process Intensification of Sorption-Enhanced Steam Reforming. *Environ. Sci. Technol.* **2016**, *51*, 12–27.
- [13] Zeng, S.; Zhang, X.; Bai, L.; Zhang, X.; Wang, H.; Wang, J.; Bao, D.; Li, M.; Liu, X.; Zhang, S. Ionic-Liquid-Based CO<sub>2</sub> Capture Systems: Structure, Interaction and Process. *Chem. Rev.* **2017**, *117*, 9625–9673.
- [14] Yang, X.; Rees, R. J.; Conway, W.; Puxty, G.; Yang, Q.; Winkler, D. A. Computational Modeling and Simulation of CO<sub>2</sub> Capture by Aqueous Amines. *Chem. Rev.* **2017**, *117*, 9524–9593.
- [15] Radovic, L. R. The Mechanism of CO<sub>2</sub> Chemisorption on Zigzag Carbon Active Sites: A Computational Chemistry Study. *Carbon N. Y.* **2005**, *43*, 907–915.

- [16] Yu, D.; Yazaydin, A. O.; Lane, J. R.; Dietzel, P. D. C.; Snurr, R. Q. A Combined Experimental and Quantum Chemical Study of CO<sub>2</sub> Adsorption in the Metal-Organic Framework CPO-27 with Different Metals †. *Chem. Sci.* **2013**, *4*, 3455–3556.
- [17] Vaidhyanathan, R.; Iremonger, S. S.; Shimizu, G. K. H.; Boyd, P. G.; Alavi, S.; Woo, T. K. Direct Observation and Quantification of CO<sub>2</sub> Binding within an Amine-Functionalized Nanoporous Solid. *Science* **2010**, *330*, 650–653.
- [18] Zhou, H.-C.; Long, J. R.; Yaghi, O. M. Introduction to Metal–Organic Frameworks. *Chem. Rev.* **2012**, *112*, 673–674.
- [19] Poloni, R.; Lee, K.; Berger, R. F.; Smit, B.; Neaton, J. B. Understanding Trends in CO<sub>2</sub> Adsorption in Metal-Organic Frameworks with Open-Metal Sites. *J. Phys. Chem. Lett.* **2014**, *5*, 861–865.
- [20] Rosen, A. S.; Notestein, J. M.; Snurr, R. Q. Realizing the Data-Driven, Computational Discovery of Metal-Organic Framework Catalysts. *arXiv e-prints* **2021**, arXiv:2108.06667.
- [21] Trickett, C. A.; Helal, A.; Al-Maythaly, B. A.; Yamani, Z. H.; Cordova, K. E.; Yaghi, O. M. The Chemistry of Metal–Organic Frameworks for CO<sub>2</sub> Capture, Regeneration and Conversion. *Nat. Rev. Mater.* **2017**, *2*, 1–16.
- [22] Ding, M.; Flaig, R. W.; Jiang, H. L.; Yaghi, O. M. Carbon Capture and Conversion using Metal-Organic Frameworks and MOF-Based Materials. *Chem. Soc. Rev.* **2019**, *48*, 2783–2828.
- [23] Sumida, K.; Rogow, D. L.; Mason, J. A.; McDonald, T. M.; Bloch, E. D.; Herm, Z. R.; Bae, T.-H.; Long, J. R. Carbon Dioxide Capture in Metal–Organic Frameworks. *Chem. Rev.* **2011**, *112*, 724–781.
- [24] Drisdell, W. S.; Poloni, R.; McDonald, T. M.; Long, J. R.; Smit, B.; Neaton, J. B.; Prendergast, D.; Kortright, J. B. Probing Adsorption Interactions in Metal–Organic Frameworks Using X-ray Spectroscopy. *J. Am. Chem. Soc.* **2013**, *135*, 18183–18190.
- [25] Smaldone, R. A.; Forgan, R. S.; Furukawa, H.; Gassensmith, J. J.; Slawin, A. M.; Yaghi, O. M.; Stoddart, J. F. Metalorganic Frameworks from Edible Natural Products. *Angew. Chem. Int. Ed.* **2010**, *49*, 8630–8634.
- [26] Gassensmith, J. J.; Furukawa, H.; Smaldone, R. A.; Forgan, R. S.; Botros, Y. Y.; Yaghi, O. M.; Stoddart, J. F. Strong and Reversible Binding of Carbon Dioxide in a Green Metal-Organic Framework. *J. Am. Chem. Soc.* **2011**, *133*, 15312–15315.
- [27] Rajkumar, T.; Kukkar, D.; Kim, K. H.; Sohn, J. R.; Deep, A. Cyclodextrin-Metal–Organic Framework (CD-MOF): From Synthesis to Applications. *J. Ind. Eng. Chem.* **2019**, *72*, 50–66.
- [28] Wu, D.; Gassensmith, J. J.; Gouveia, D.; Ushakov, S.; Stoddart, J. F.; Navrotsky, A. Direct Calorimetric Measurement of Enthalpy of Adsorption of Carbon Dioxide on CD-MOF-2, a Green Metal-Organic Framework. *J. Am. Chem. Soc.* **2013**, *135*, 6790–6793.
- [29] Li, L.; Wang, J.; Zhang, Z.; Yang, Q.; Yang, Y.; Su, B.; Bao, Z.; Ren, Q. Inverse Adsorption Separation of CO<sub>2</sub>/C<sub>2</sub>H<sub>2</sub> Mixture in Cyclodextrin-Based Metal-Organic Frameworks. *ACS Appl. Mater. Interfaces* **2019**, *11*, 2543–2550.
- [30] Forgan, R. S.; Smaldone, R. A.; Gassensmith, J. J.; Furukawa, H.; Cordes, D. B.; Li, Q.; Wilmer, C. E.; Botros, Y. Y.; Snurr, R. Q.; Slawin, A. M.; Stoddart, J. F. Nanoporous Carbohydrate Metal-Organic Frameworks. *J. Am. Chem. Soc.* **2012**, *134*, 406–417.
- [31] Yan, T. K.; Nagai, A.; Michida, W.; Kusakabe, K.; Yusup, S. B. Crystal Growth of Cyclodextrin-based Metal-organic Framework for Carbon Dioxide Capture and Separation. *Procedia Eng.* **2016**, *148*, 30–34.

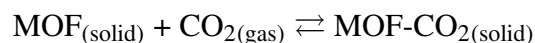
- [32] Dibenedetto, A.; Aresta, M.; Giannoccaro, P.; Pastore, C.; Pápai, I.; Schubert, G. On the Existence of the Elusive Monomethyl Ester of Carbonic Acid [CH<sub>3</sub>OC(O)OH] at 300 K: <sup>1</sup>H- and <sup>13</sup>C NMR Measurements and DFT Calculations. *Eur. J. Inorg. Chem.* **2006**, *2006*, 908–913.
- [33] Boger, J.; Corcoran, R. J.; Lehn, J. Cyclodextrin Chemistry. Selective Modification of All Primary Hydroxyl Groups of  $\alpha$ - and  $\beta$ -cyclodextrins. *Helv. Chim. Acta* **1978**, *61*, 2190–2218.
- [34] Liu, B.; Smit, B. Comparative Molecular Simulation Study of CO<sub>2</sub>/N<sub>2</sub> and CH<sub>4</sub>/N<sub>2</sub> Separation in Zeolites and Metal-Organic Frameworks. *Langmuir* **2009**, *25*, 5918–5926.
- [35] Gassensmith, J. J.; Kim, J. Y.; Holcroft, J. M.; Farha, O. K.; Fraser Stoddart, J.; Hupp, J. T.; Jeong, N. C. A Metal-Organic Framework-Based Material for Electrochemical Sensing of Carbon Dioxide. *J. Am. Chem. Soc.* **2014**, *136*, 8277–8282.
- [36] Liu, Z.; Stoddart, J. F. Extended Metal-Carbohydrate Frameworks. *J. Macromol. Sci. A* **2014**, *86*, 1323–1334.
- [37] Yoon, S. M.; Warren, S. C.; Grzybowski, B. A. Storage of Electrical Information in Metal-Organic-Framework Memristors. *Angew. Chem. Int. Ed.* **2014**, *53*, 4437–4441.
- [38] Boyd, P. G. et al. Data-Driven Design of Metal–Organic Frameworks for Wet Flue Gas CO<sub>2</sub> Capture. *Nature* **2019**, *576*, 253–256.
- [39] Güçlü, Y.; Erer, H.; Demiral, H.; Altintas, C.; Keskin, S.; Tumanov, N.; Su, B.-L.; Semerci, F. Oxalamide-Functionalized Metal Organic Frameworks for CO<sub>2</sub> Adsorption. *ACS Appl. Mater. Interfaces* **2021**, *13*, 33188–33198.
- [40] Burner, J.; Schwiedrzik, L.; Krykunov, M.; Luo, J.; Boyd, P. G.; Woo, T. K. High-Performing Deep Learning Regression Models for Predicting Low-Pressure CO<sub>2</sub> Adsorption Properties of Metal-Organic Frameworks. *J. Phys. Chem. C* **2020**, *124*, 27996–28005.
- [41] Vaidhyanathan, R.; Iremonger, S. S.; Shimizu, G. K. H.; Boyd, P. G.; Alavi, S.; Woo, T. K. Competition and Cooperativity in Carbon Dioxide Sorption by Amine-Functionalized Metal–Organic Frameworks. *Angew. Chem. Int. Ed.* **2012**, *51*, 1826–1829.
- [42] Queen, W. L. et al. Comprehensive Study of Carbon Dioxide Adsorption in the Metal–Organic Frameworks M<sub>2</sub>(dobdc) (M = Mg, Mn, Fe, Co, Ni, Cu, Zn). *Chem. Sci.* **2014**, *5*, 4569–4581.
- [43] McDonald, T. M. et al. Cooperative Insertion of CO<sub>2</sub> in Diamine-Appended Metal-Organic Frameworks. *Nature* **2015**, *519*, 303–308.
- [44] Yu, J.; Xie, L. H.; Li, J. R.; Ma, Y.; Seminario, J. M.; Balbuena, P. B. CO<sub>2</sub> Capture and Separations using MOFs: Computational and Experimental Studies. *Chem. Rev.* **2017**, *117*, 9674–9754.
- [45] Forse, A. C.; Milner, P. J.; Lee, J. H.; Redfearn, H. N.; Oktawiec, J.; Siegelman, R. L.; Martell, J. D.; Dinakar, B.; Porter-Zasada, L. B.; Gonzalez, M. I.; Neaton, J. B.; Long, J. R.; Reimer, J. A. Elucidating CO<sub>2</sub> Chemisorption in Diamine-Appended Metal-Organic Frameworks. *J. Am. Chem. Soc.* **2018**, *140*, 18016–18031.
- [46] Kühne, T. D. et al. CP2K: An Electronic Structure and Molecular Dynamics Software Package -Quickstep: Efficient and Accurate Electronic Structure Calculations. *J. Chem. Phys.* **2020**, *152*, 194103.
- [47] Grimme, S.; Antony, J.; Ehrlich, S.; Krieg, H. A Consistent and Accurate Ab Initio Parametrization of Density Functional Dispersion Correction (DFT-D) for the 94 Elements H-Pu. *J. Chem. Phys.* **2010**, *132*, 1–18.

- [48] Becke, A. D. Density-Functional Exchange-Energy Approximation with Correct Asymptotic Behavior. *Phys. Rev. A* **1988**, 38, 3098–3100.
- [49] Lee, C.; Yang, W.; Parr, R. G. Development of the Colle-Salvetti Correlation-Energy Formula into a Functional of the Electron Density. *Phys. Rev. B* **1988**, 37, 785–789.
- [50] Hutter, J.; Iannuzzi, M.; Schiffmann, F.; Vandevondele, J. Cp2k: Atomistic Simulations of Condensed Matter Systems. *Wiley Interdiscip. Rev. Comput. Mol. Sci.* **2014**, 4, 15–25.
- [51] VandeVondele, J.; Hutter, J. Gaussian Basis Sets for Accurate Calculations on Molecular Systems in Gas and Condensed Phases. *J. Chem. Phys.* **2007**, 127, 114105.
- [52] Goedecker, S.; Teter, M.; Hutter, J. Separable Dual-Space Gaussian Pseudopotentials. *Phys. Rev. B* **1996**, 54, 1703.
- [53] Krack, M. Pseudopotentials for H to Kr Optimized for Gradient-Corrected Exchange-Correlation Functionals. *Theor. Chem. Acc.* **2005**, 114, 145–152.
- [54] VandeVondele, J.; Hutter, J. An Efficient Orbital Transformation Method for Electronic Structure Calculations. *J. Chem. Phys.* **2003**, 118, 4365.
- [55] Smaldone, R.A.; Forgan, R.S.; Furukawa, H.; Gassensmith, J.J.; Slawin, A.M.Z.; Yaghi, O.M.; Stoddart, J.F. CCDC 773710: Experimental Crystal Structure Determination. 2011; [http://www.ccdc.cam.ac.uk/services/structure\\_request?id=doi:10.5517/cctz3d8&sid=DataCite](http://www.ccdc.cam.ac.uk/services/structure_request?id=doi:10.5517/cctz3d8&sid=DataCite).
- [56] Groom, C. R.; Bruno, I. J.; Lightfoot, M. P.; Ward, S. C. The Cambridge Structural Database. *Acta Crystallogr. Sect. B Struct. Sci. Cryst. Eng. Mater.* **2016**, 72, 171–179.
- [57] Hemmaplardh, B.; King, A. D. Solubility of Methanol in Compressed Nitrogen, Argon, Methane, Ethylene, Ethane, Carbon Dioxide, and Nitrous Oxide. Evidence for Association of Carbon Dioxide with Methanol in the Gas Phase. *J. Phys. Chem.* **1972**, 76, 2170–2175.
- [58] Dronskowski, R. *Computational Chemistry of Solid State Materials: A Guide for Materials Scientists, Chemists, Physicists and Others*; Wiley-VCH:Germany, 2005.
- [59] Sun, J.; Remsing, R. C.; Zhang, Y.; Sun, Z.; Ruzsinszky, A.; Peng, H.; Yang, Z.; Paul, A.; Waghmare, U.; Wu, X.; Klein, M. L.; Perdew, J. P. Accurate First-Principles Structures and Energies of Diversely Bonded Systems from an Efficient Density Functional. *Nat. Chem.* **2016**, 8, 831–836.

## 2.9 Supporting Information

### 2.9.1 Enthalpy of Adsorption

The adsorption of gas-phase CO<sub>2</sub> molecules in the solid-state MOF is described by the following reaction:



By definition, the enthalpy is equal to the sum of the internal energy and the  $pV$  term. In turn, the internal energy is a sum of the electronic, rotational, translational, and vibrational terms. For gas-phase molecules, the enthalpy is

$$H_{(\text{gas})} = E_{(\text{electronic})} + E_{(\text{rot})} + E_{(\text{tran})} + E_{(\text{vib})} + k_{\text{B}}T$$

For solid-state systems, the rotational and translational degrees of freedom can be omitted:

$$H_{(\text{solid})} = E_{(\text{electronic})} + E_{(\text{vib})} + pV$$

Subtracting the enthalpy of the reagents from that of the product, the adsorption enthalpy is

$$\Delta H_{(\text{ads})} = \Delta E_{(\text{electronic})} + \Delta E_{(\text{rot})} + \Delta E_{(\text{tran})} + \Delta E_{(\text{vib})} - k_{\text{B}}T$$

where the  $pV$  terms for the two solid-state systems can be assumed to be equal due to only minor differences in their bulk moduli. It can be further assumed that the change in the average vibrational energy is small,  $\Delta E_{(\text{vib})} = 0$ . Using the ideal-gas expressions for the enthalpy of CO<sub>2</sub>:

$$\Delta E_{(\text{rot})} = -E_{(\text{rot})}(\text{CO}_2) = -\frac{3}{2}k_{\text{B}}T$$

$$\Delta E_{(\text{tran})} = -E_{(\text{tran})}(\text{CO}_2) = -\frac{3}{2}k_{\text{B}}T$$

The final expression for the enthalpy of adsorption is

$$\Delta H_{(\text{ads})} = \Delta E_{(\text{electronic})} - 4k_{\text{B}}T$$

Since the adsorption experiments were performed at  $T = 298 \text{ K}^{1,2}$ , the  $4k_{\text{B}}T$  term is equal to 9.9 kJ/mol. This term is small compared to the adsorption energies reported in the experiments and simulations. Furthermore, this term is of the same order of magnitude with error in the employed exchange-correlation functional used to estimate adsorption energies. It is, therefore, neglected and the enthalpy is approximated with the electronic energy of adsorption.

Adsorption site	Adsorption energy for different adsorption models ( $\Delta E$ , kJ/mol)			
	Neutral	Alkoxide	Counterion-bonded	Alkoxide: neighbors replaced
1		-153.4		-121.4
2	79.0	-116.6	-22.3	-117.0
3		-102.9	-22.5	-106.6
4	44.8	-100.3		
5	64.7	-89.2	-45.3	-93.2
6		-85.1		
7		-79.3		-90.8
8		-78.9		-108.4
9	115.3	-70.9	-92.9	-84.6
10	78.9	-64.4	4.9	-116.7
11	58.7	-55.8	-42.5	-91.4
12	50.7	-54.6	-116.6	-104.6
13	98.5	-48.8		
14		-46.2	-24.4	-90.3
15	28.2	-45.9	-92.1	-114.4
16		-44.7		
17	79.1	-41.4	-41.3	-87.9
18	79.9	-41.0	-101.0	-108.5
19	50.1	-39.3	-13.9	-187.4
20		-38.1	24.5	-93.4
21	80.1	-33.2	-32.9	-134.8
22		-30.0	-40.9	-147.6
23		-22.4		
24		-15.9	-8.50	-98.4
25		-12.3	-74.3	-122.3
26		-7.0		-59.6

Table 2.1: CO<sub>2</sub> adsorption energy calculated for different model reactions (Figure 1.2)

## 2.9.2 Comparison of the CO<sub>2</sub> Binding Strength Obtained with BLYP and HSE06 Functionals

It is known that GGA exchange-correlation (XC) functionals, such as BLYP employed in our work, underestimate the electronic band gap. This, in turn, leads to artificially stronger donor-acceptor binding between two systems. Although hybrid functionals can improve the binding energies, they are too costly to apply to the large unit cell of CD-MOF-2 that contains more than 1,000 atoms. To demonstrate the extent of the overestimation, we performed hybrid DFT calculations (HSE06 XC functional) on several simplified models utilized in our work, namely, gas-phase methoxide, primary alkoxide sites on an amylose unit and a  $\gamma$ -cyclodextrin torus (Table 2.2).

	Methoxide	Primary alkoxide site	$\gamma$ -cyclodextrin torus
BLYP (GGA)	-169	-113	-84
HSE06 (Hybrid)	-140	-73	-46
$\Delta$	29	40	37

Table 2.2: Comparison of the CO<sub>2</sub> binding strength (kJ/mol) obtained with BLYP and HSE06 functionals.

Adsorption site	Proton transfer energy, kJ/mol
2	-21.9
5	152
9	18.1
10	-20.9
11	62.5
12	8.0
15	232
17	32.0
18	-25.0
19	-102.6
21	217

Table 2.3: Energy of the proton transfer from the specified adsorption site to a randomly selected hydroxyl counterion.

### 2.9.3 Number of CO<sub>2</sub> Molecules Adsorbed Per Unit Cell of CD-MOF-2

The number CO<sub>2</sub> adsorbed CD-MOF-2 per unit cell of CD-MOF-2 was calculated using data from gas-uptake measurements<sup>1,3</sup> and direct calorimetry measurements<sup>2</sup>. The [(C<sub>6</sub>H<sub>10</sub>O<sub>5</sub>)<sub>8</sub>(RbOH)<sub>2</sub>]<sub>6</sub><sup>4,5</sup> cubic unit cell of CD-MOF-2 has mass 9011.2 g/mol and size 31.079 Å.

**Direct calorimetry measurements.** The enthalpy of the CO<sub>2</sub> uptake as a function of surface coverage was directly measured in Ref.<sup>2</sup>. The CO<sub>2</sub> surface coverage for the strong chemisorption was reported to be approximately under 0.1 CO<sub>2</sub>/nm<sup>2</sup>. The surface area of CD-MOF-2 has been measured to be 1030 m<sup>2</sup>/g<sup>2</sup>. Using this data, the number of CO<sub>2</sub> molecules chemisorbed strongly per gram of CD-MOF-2 is under 1.03 × 10<sup>20</sup> CO<sub>2</sub>/g. Taking the mass of the unit cell into account, the number of unit cells in 1 g of CD-MOF-2 is 6.68 × 10<sup>19</sup> uc/g. The number of CO<sub>2</sub> molecules adsorbed irreversibly per one unit cell of CD-MOF-2 is under 1.54. The number of CO<sub>2</sub> molecules adsorbed strongly and reversibly per one unit cell of CD-MOF-2 is 3.09 (the corresponding coverage interval is from 0.1 to 0.4 CO<sub>2</sub>/nm<sup>2</sup>).

**Gas-uptake measurements.** The CO<sub>2</sub> adsorption isotherms measured at temperature of 298 K show that 60 cm<sup>3</sup> of CO<sub>2</sub> are adsorbed per 1 g of CD-MOF-2 at the saturation pressure of 800 Torr<sup>3</sup>. Assuming that CO<sub>2</sub> can be described by the ideal gas law, the number of CO<sub>2</sub> molecules per 1 g of CD-MOF-2 is 1.55 × 10<sup>21</sup> CO<sub>2</sub>/g. This yields 23.27 as the final number of CO<sub>2</sub> molecules adsorbed per unit cell of CD-MOF-2.

## 2.10 References

- [1] Gassensmith, J. J.; Kim, J. Y.; Holcroft, J. M.; Farha, O. K.; Fraser Stoddart, J.; Hupp, J. T.; Jeong, N. C. A Metal-Organic Framework-Based Material for Electrochemical Sensing of Carbon Dioxide. *J. Am. Chem. Soc.* **2014**, *136*, 8277–8282.
- [2] Wu, D.; Gassensmith, J. J.; Gouveia, D.; Ushakov, S.; Stoddart, J. F.; Navrotsky, A. Direct Calorimetric Measurement of Enthalpy of Adsorption of Carbon Dioxide on CD-MOF-2, a Green Metal-Organic Framework. *J. Am. Chem. Soc.* **2013**, *135*, 6790–6793.
- [3] Gassensmith, J. J.; Furukawa, H.; Smaldone, R. A.; Forgan, R. S.; Botros, Y. Y.; Yaghi, O. M.; Stoddart, J. F. Strong and Reversible Binding of Carbon Dioxide in a Green Metal-Organic Framework. *J. Am. Chem. Soc.* **2011**, *133*, 15312–15315.
- [4] Smaldone, R. A.; Forgan, R. S.; Furukawa, H.; Gassensmith, J. J.; Slawin, A. M.; Yaghi, O. M.; Stoddart, J. F. Metalorganic Frameworks from Edible Natural Products. *Angew. Chem. Int. Ed.* **2010**, *49*, 8630–8634.
- [5] Forgan, R. S.; Smaldone, R. A.; Gassensmith, J. J.; Furukawa, H.; Cordes, D. B.; Li, Q.; Wilmer, C. E.; Botros, Y. Y.; Snurr, R. Q.; Slawin, A. M.; Stoddart, J. F. Nanoporous Carbohydrate Metal-Organic Frameworks. *J. Am. Chem. Soc.* **2012**, *134*, 406–417.

## Chapter 3

---

# Direct unconstrained optimization of molecular orbital coefficients in density functional theory

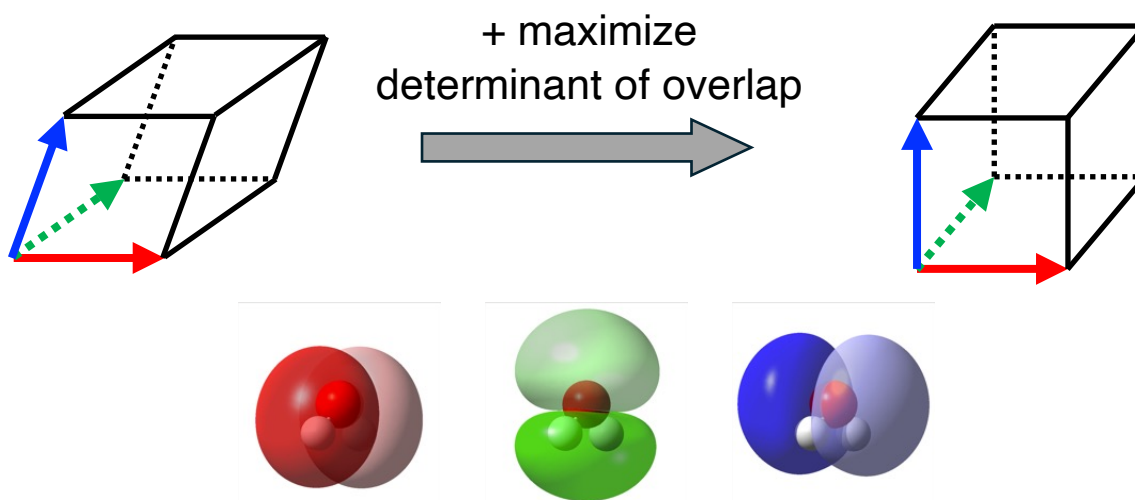
---

### 3.1 Preface

Kohn–Sham density functional theory (KS DFT) is popular for its balance of accuracy and computational efficiency. However, conventional SCF optimization is complicated by the need to enforce orbital orthogonality. This chapter presents a variable-metric (VM) SCF approach that removes this constraint, streamlining optimization and enabling more efficient, flexible solutions in electronic structure calculations.

This chapter is reproduced from a published peer-reviewed article: **Pham, H. D. M.**, Khaliullin, R. Z. Direct Unconstrained Optimization of Molecular Orbital Coefficients in Density Functional Theory. *J. Chem. Theory Comput.* **2024**, 20, 18, 7936–7947.

## Variational optimization



## 3.2 Abstract

One-electron orbitals in Kohn-Sham density functional theory (DFT) are typically constrained to be orthogonal during their variational optimization, leading to elaborate parameterization of the orbitals and complicated optimization algorithms. This work shows that orbital optimization can be performed with nonorthogonal orbitals if the DFT energy functional is augmented with a term that penalizes linearly dependent states. This approach, called variable metric self-consistent field (SCF) optimization, allows to use molecular orbital coefficients – natural descriptors of one-electron orbitals – as independent variables in a direct unconstrained minimization, leading to very simple closed-form expressions for the electronic gradient and Hessian. It is demonstrated that efficient convergence of the variable metric SCF procedure can be achieved with a basic preconditioned conjugate gradient algorithm for a variety of systems including challenging narrow gap systems and spin-pure two-determinant states of singlet diradicals. This simple reformulation of the variational procedure can be readily extended to electron correlation methods with multi-configuration states

and to the optimization of excited-state orbitals.

### 3.3 Introduction

Kohn–Sham density functional theory (KS DFT) is the most popular electronic structure method today because of its reasonably accurate description of electrons in molecules and materials at moderate computational cost<sup>1,2</sup>. In KS DFT, the electron distribution is calculated by minimizing the total energy functional with respect to variations of occupied one-electron orbitals.

Traditionally, the variational optimization of Kohn-Sham orbitals, known as the self-consistent field (SCF) procedure, is formulated to keep one-electron orbitals orthogonal during the optimization. The most common approach way to impose the orthogonality constraint is to recast the optimization problem as the diagonalization of the Hermitian KS matrix, whose eigenvectors – the desired one-electron orbitals – are then orthogonal by construction. Unfortunately, the iterative diagonalization-based SCF can be slow and is not guaranteed to converge especially for systems with nearly degenerate frontier orbitals<sup>3,4</sup> even with sophisticated extrapolations schemes such as DIIS<sup>5–7</sup>. For difficult cases, relaxed constrained algorithms<sup>8,9</sup> and energy DIIS<sup>10–12</sup> can be utilized to alleviate the idempotency constraint within DIIS, thereby improving the SCF convergence.

Another widely utilized approach is to start with orthogonal orbitals and vary them iteration-by-iteration using unitary transformations that preserve orbital orthogonality in the energy minimization procedure. Although the convergence is guaranteed in such a direct metric-preserving energy minimization, a special care must be taken to parameterize unitary transformations. For example, geometric direct minimization method employs the exponential parameterization of a unitary matrix  $U = \exp(-X)$ , where  $X$  is an anti-Hermitian matrix of parameters that can be optimized

independently<sup>13</sup>. In the orbital transformation (OT) method the unitary matrix is expressed implicitly as a sine and cosine function of an update matrix<sup>14</sup>. The diagonalization of the KS Hamiltonian has also been reformulated via the Cayley parameterization of a unitary matrix<sup>15</sup>. Unfortunately, the complicated parameterizations of unitary transformations make it difficult to write simple analytical expressions for the gradient of the KS energy with respect to variational parameters, especially in a closed form<sup>13,14</sup>. The parameterization can also make the minimization algorithm excessively complicated by introducing additional constraints<sup>14</sup> or by limiting the method to the energy minimization with a fixed KS Hamiltonian<sup>15</sup>.

Interestingly, the orbital orthogonality constraints have been relaxed altogether in a special class of KS DFT methods designed to variationally optimize *localized* orbitals<sup>16–25</sup>. In such methods, the orthogonality constraints are simply incompatible with the locality constraints<sup>16</sup>. Unfortunately, problems of sluggish SCF optimization of localized nonorthogonal orbitals prevent widespread adoption of these promising methods<sup>17,25–32</sup>. At the same time, the unconstrained optimization of general (that is, nonlocalized) nonorthogonal orbitals has not been considered because of a legitimate concern that the absence of locality constraints can result in linear dependencies between the occupied orbitals in the SCF optimization. Such a “collapse” of the occupied subspace would produce unphysical electronic states that violate the Pauli exclusion principle.

In this work, we introduce a simple SCF approach called variable-metric (VM) optimization that replaces the orthogonality constraint with a weaker linear independence constraint. The latter constraint is imposed on nonorthogonal orbitals via a single easy-to-compute penalty term added to the energy functional. This approach allows us to use orbital coefficients as independent variational parameters, to write simple mathematical expressions for the electronic energy gradient and second derivative in a closed form, to reformulate the SCF procedure as a direct unconstrained optimization

problem and, thus, to greatly expand the scope of algorithms that can be applied to the variational optimization.

## 3.4 Methodology

For the sake of clarity, the main text of the article describes the variable-metric SCF method for spin-restricted optimization of doubly-occupied orbitals of closed-shell systems. A generalized approach for spin-unrestricted optimization (UKS), restricted open-shell optimization (ROSO), as well as the ROKS optimization<sup>33,34</sup> for the singlet diradical states is described in detail in Supporting Information. The formalism presented here is currently limited to the  $\Gamma$ -point description of the electronic states of periodic systems, since our intent is to apply it to large simulation cells.

### 3.4.1 Theory

To perform an unconstrained SCF optimization of occupied Kohn-Sham orbitals, we minimize the loss functional  $\Omega$  that contains the DFT energy term  $E$  generalized for nonorthogonal orbitals and term  $\Omega_p$  that penalizes linearly dependent occupied orbitals

$$\begin{aligned}\Omega &\equiv E + \Omega_p \\ \Omega_p &\equiv -2C_p \ln \det(\sigma \sigma_d^{-1})\end{aligned}\tag{3.1}$$

where  $C_p > 0$  is the positive penalty strength,  $\sigma$  is the overlap matrix for the occupied orbitals,  $\sigma_d$  is the diagonal part of  $\sigma$ , and the factor of 2 accounts for the double occupation of orbitals in closed-shell systems (equations for open-shell systems can be found in Supporting Information).

The determinant of  $\sigma$  in the penalty term is equal to the square of the volume of the multidimensional parallelepiped spanned by the occupied orbitals. For non-zero orbitals, the determinant value

is equal to zero only when orbitals are linearly dependent.  $\sigma_d$  is the orbital normalization factor that ensures the determinant in the penalty functional does not exceed 1. With  $\det(\sigma\sigma_d^{-1})$  always in the  $(0, 1]$  interval, the logarithm function  $\Omega_p$  lies in  $(+\infty, 0]$ , making the states with linearly dependent orbitals (and with orbitals of zero length) inaccessible in the SCF procedure, if  $C_p > 0$ . A similar penalty term was used to prevent orbital ‘‘collapse’’ during the localization of nonorthogonal occupied and virtual orbitals<sup>35,36</sup>.

When written in terms of a finite number of basis set functions  $\chi_\mu(\mathbf{r})$ , the trial nonorthogonal Kohn-Sham orbitals  $\phi_i(\mathbf{r})$  When written in terms of a finite number of basis set functions  $\chi_\mu(\mathbf{r})$ , the trial nonorthogonal Kohn-Sham orbitals  $\phi_i(\mathbf{r})$

$$\phi_i(\mathbf{r}) = \sum_{\mu}^B \chi_{\mu}(\mathbf{r}) T_{\mu i} \quad (3.2)$$

are completely specified by their expansion coefficients  $T$ , where  $B$  is the number of basis set functions. The overlap matrix of occupied orbitals is a simple function of the expansion coefficients

$$\sigma_{ij} = \sum_{\mu\nu}^B T_{\mu i} S_{\mu\nu} T_{\nu j} \quad (3.3)$$

where  $S$  is the overlap matrix of basis set functions  $S_{\mu\nu} = \int \chi_{\mu}(\mathbf{r}) \chi_{\nu}(\mathbf{r}) d\mathbf{r}$ .

The VM approach allows, first, to formulate the SCF procedure using expansion coefficients as main independent variables and, second, to write the derivatives of the energy and penalty terms as simple analytical closed-form functions of these variables.

The energy term can be computed from the density matrix  $2P_{\mu\nu}$  using conventional DFT algorithms, as long as the density matrix is evaluated taking into account the nonorthogonality of the occupied orbitals

$$P_{\mu\nu} = \sum_{ij}^N T_{\mu i} (\sigma^{-1})_{ij} T_{\nu j} \quad (3.4)$$

where  $N$  is the number of doubly-occupied orbitals,  $P_{\mu\nu}$  is the projector onto the occupied subspace.

The KS DFT energy of a closed-shell system described within the  $\Gamma$ -point only approximation is

$$E = 2 \sum_{\mu\nu}^N F_{\mu\nu} P_{\nu\mu} - \frac{1}{2} \int \int \frac{\rho(\mathbf{r})\rho(\mathbf{r}')}{|\mathbf{r}-\mathbf{r}'|} d\mathbf{r}d\mathbf{r}' + E_{xc} - \int v_{XC}(\mathbf{r})\rho(\mathbf{r})d\mathbf{r} \quad (3.5)$$

where  $F$  is the Kohn-Sham Hamiltonian,  $E_{xc}$  is the exchange-correlation energy functional of the electron density

$$\begin{aligned} \rho(\mathbf{r}) &= 2 \sum_{ij=1}^N \phi_i^*(\mathbf{r})(\sigma^{-1})_{ij}\phi_j(\mathbf{r}) = \\ &= 2 \sum_{\mu\nu=1}^B \chi_\mu^*(\mathbf{r})P_{\mu\nu}\chi_\nu(\mathbf{r}) \end{aligned} \quad (3.6)$$

Eq. (4.16) shows that the Kohn-Sham energy is completely determined by the projector onto the occupied subspace  $P$ , which is invariant to any non-singular transformation of nonorthogonal orbitals *within* the occupied subspace. Therefore, the energy is also invariant to such transformations. This energy invariance is a generalization of the better known invariance to the unitary transformation of orthogonalized occupied orbitals.

The energy gradient with respect to  $T_{\mu i}$  can be evaluated using the chain rule (see Supporting Information):

$$\begin{aligned} G_{\mu i}^E &\equiv \frac{\partial E}{\partial T_{\mu i}} = \sum_{\lambda\nu}^B \frac{\partial E}{\partial P_{\lambda\nu}} \frac{\partial P_{\lambda\nu}}{\partial T_{\mu i}} = \\ &= 4[(I - SP)FT\sigma^{-1}]_{\mu i} \end{aligned} \quad (3.7)$$

It is easy to see that the derived energy gradient is simply the virtual-occupied block of the KS Hamiltonian, post-multiplied by the inverse of the orbital overlap matrix that keeps the equations tensorially consistent<sup>37</sup>.

The second derivative of the energy – the electronic Hessian – can also be evaluated analytically

$$\begin{aligned} \frac{\partial^2 E}{\partial T_{vj} \partial T_{\mu i}} &= \frac{\partial G_{\mu i}^E}{\partial T_{vj}} \\ &= 4 \left\{ [(I - SP)F(I - PS)]_{\mu\nu} (\sigma^{-1})_{ji} - (S - SPS)_{\mu\nu} (\sigma^{-1} T^\dagger F T \sigma^{-1})_{ji} \right\} - \\ &\quad - \left[ (ST \sigma^{-1})_{\mu j} G_{\nu i}^E - G_{\mu j}^E (ST \sigma^{-1})_{\nu i} \right] + 4 \sum_{\lambda\gamma}^N (I - SP)_{\mu\lambda} \frac{\partial F_{\lambda\gamma}}{\partial T_{vj}} (T \sigma^{-1})_{\gamma i} \end{aligned} \quad (3.8)$$

In this proof of concept work, we do not employ the exact Hessian and show instead that an efficient SCF algorithm can be designed based on an approximate Hessian that is much easier to invert (see below).

The first and second derivatives of the penalty term  $\Omega_p$  can also be evaluated analytically (see Supporting Information) and computed readily

$$G_{\mu i}^P \equiv \frac{\partial \Omega_p}{\partial T_{\mu i}} = -4C_p [ST(\sigma^{-1} - \sigma_d^{-1})]_{\mu i} \quad (3.9)$$

$$\begin{aligned} \frac{\partial^2 \Omega_p}{\partial T_{vj} \partial T_{\mu i}} &= \frac{\partial G_{\mu i}^P}{\partial T_{vj}} = -4C_p [(S - SPS)_{\mu\nu} (\sigma^{-1})_{ji} - \\ &\quad - (ST \sigma^{-1})_{\mu j} (ST \sigma^{-1})_{\nu i} - \delta_{ij} S_{\mu\nu} (\sigma_d^{-1})_{ii} + \\ &\quad + 2\delta_{ij} (ST \sigma_d^{-1})_{\mu i} (ST \sigma_d^{-1})_{\nu i}] \end{aligned} \quad (3.10)$$

where  $\delta_{ij}$  is the Kronecker delta.

### 3.4.2 Optimization Algorithm

The absence of the orthogonality constraints (and any other constraints) allows MO coefficients to be used as the main variable in a direct unconstrained optimization. Reformulating SCF as an unconstrained optimization problem is an advantage because there exist multiple general, simple and efficient algorithms to solve such problems<sup>38</sup>. Here, we demonstrate that the newly introduced VM

SCF approach is efficient even when the basic preconditioned conjugate gradient (PCG) algorithm for nonlinear problems<sup>39</sup> is employed.

The rate of convergence of a PCG algorithm can be significantly improved by utilizing a properly designed preconditioner that provides the information beyond the first order derivative. The preconditioners considered in this work are obtained from the first two terms of the electronic Hessian in Eq. (3.8), which remain dominant throughout SCF

$$\frac{\partial^2 E}{\partial T_{\nu j} \partial T_{\mu i}} \approx 4 \left[ (Q^\dagger F Q)_{\mu\nu} (\sigma^{-1})_{ji} - (Q^\dagger S Q)_{\mu\nu} (\sigma^{-1} T^\dagger F T \sigma^{-1})_{ji} \right] \quad (3.11)$$

where  $Q \equiv (I - PS)$  is the contravariant-covariant matrix of the projection operator onto the unoccupied (virtual) subspace. The two  $\mu\nu$  terms contain the virtual-virtual block of the Kohn-Sham Hamiltonian  $Q^\dagger F Q$  and the overlap of the basis set functions projected on the virtual subspace  $Q^\dagger S Q = S - SPS$ . The two  $ij$  terms contain the occupied-occupied block of the Kohn-Sham Hamiltonian  $\sigma^{-1} T^\dagger F T \sigma^{-1}$  and the overlap occupied orbitals  $\sigma^{-1}$ , both in the contravariant form, satisfying the tensor consistency rules<sup>37</sup>.

To obtain a simple easy-to-invert preconditioner, the occupied blocks of the approximate Hessian in Eq. (3.11) are replaced with diagonal matrices. The contravariant metric in the occupied space is replaced with the identity matrix  $\sigma^{-1} \approx I$ , which would be exact in case of orthogonal orbitals. The contravariant occupied-occupied block of the Hamiltonian would be equal to the diagonal  $N \times N$  matrix of occupied orbital energies in case of canonical orbitals, but it is simplified even further to  $\sigma^{-1} T^\dagger F T \sigma^{-1} \approx -|\epsilon_{\text{HOMO}}|I$ , where  $\epsilon_{\text{HOMO}}$  can be interpreted as the average energy of the occupied frontier orbitals or simply as the HOMO energy. The use of these two identity matrices for the occupied blocks allows to compute a common preconditioner for all occupied

orbitals, greatly reducing the computational cost of the procedure.

$$H_{\mu\nu} = 4 \left[ \left( Q^\dagger F Q \right)_{\mu\nu} + |\epsilon_{\text{HOMO}}| \left( Q^\dagger S Q \right)_{\mu\nu} \right] \quad (3.12)$$

We further explored the possibility of replacing the virtual projector  $Q$  with identity matrices. This approximation will produce positive definite preconditioners that can be inverted using the Cholesky decomposition that is more efficient than the more general diagonalization-based pseudo-inversion of positive semidefinite matrices. Finally, a regularization parameter  $0 < \kappa < 1$  is introduced into the preconditioner, so one is able to increase the weight of the overlap term and thus deal with ill-conditioned electronic structure problems. Taking into account all approximations and modifications of the Hessian, the family of preconditioners employed with the PCG algorithm in this work can be written as

$$\begin{aligned} H_{\mu\nu} &= 4 \left[ (1 - \kappa) \left( A^\dagger F A \right)_{\mu\nu} + \kappa |\epsilon_{\text{HOMO}}| \left( D^\dagger S D \right)_{\mu\nu} \right] = \\ &= 4 \left[ \left( 1 - \frac{\epsilon}{|\epsilon_{\text{HOMO}}|} \right) \left( A^\dagger F A \right)_{\mu\nu} + \epsilon \left( D^\dagger S D \right)_{\mu\nu} \right] \end{aligned} \quad (3.13)$$

where matrices  $A$  and  $D$  can be set to  $Q$ ,  $I$  or zero and where  $\epsilon \equiv \kappa |\epsilon_{\text{HOMO}}|$  is used as a combined regularization parameter expressed in the units of energy.

The preconditioner expression can be further simplified to gain additional insight into its physical meaning. If it is assumed that both occupied and virtual subspaces are spanned by canonical orbitals, which are orthogonal by definition, the approximate Hessian in Eq. (3.12) reduces to

$$\frac{\partial^2 E}{\partial T_{Vj} \partial T_{\mu i}} \approx 4 \left[ \epsilon_\mu \delta_{\mu\nu} \delta_{ji} - \delta_{\mu\nu} \delta_{ji} \epsilon_i \right] \quad (3.14)$$

where  $\epsilon_i$  and  $\epsilon_\mu$  are orbital energies of occupied and projected virtual orbitals (with  $N$  virtual energies being zero), respectively. The inverted Hessian for an occupied-virtual pair  $\mu i$  is then proportional to the inverted energy gap between the orbitals  $4^{-1}(\epsilon_\mu - \epsilon_i)^{-1}$ . Since the rate of SCF

convergence is determined by the energies of the frontier orbitals, the occupied and virtual energies can be replaced by the HOMO and LUMO energies, with the preconditioner reduced to the estimate of the HOMO-LUMO gap

$$H_{\mu\nu} \approx 4\delta_{\mu\nu} [\epsilon_{\text{LUMO}} - \epsilon_{\text{HOMO}}] = 4\delta_{\mu\nu} \epsilon_{\text{GAP}} \quad (3.15)$$

The representation of the virtual  $\mu\nu$  blocks in Eqs. (3.14) and (3.15) is oversimplified and they are not used in VM SCF. These equations are shown only to make the physical meaning of the preconditioner clearer.

For large systems, the computational cost of the variable-metric PCG algorithm is dominated by the inversion of the preconditioner  $H$  that has  $\mathcal{O}(B^3)$  computational complexity, where  $B$  is the number of basis set functions. Thus, the cost of the optimization is expected to be similar to the other orbital-based SCF algorithms such as orbital transformation<sup>14</sup>. In orbital-based direct optimization, the preconditioner inversion is performed only a few times (Figure 3.1). Only a single inversion is typically required in simple cases of closed-shell systems that do not contain elements beyond the third row of the periodic table. This makes orbital-based approaches more efficient for large systems compared to the methods based on the diagonalization or density matrices, in which the  $\mathcal{O}(B^3)$  operations are required on each SCF iteration. It should be noted in passing that  $\mathcal{O}(B^3)$  operations in all methods are performed with sparse matrices and, therefore, their cost can be reduced to  $\mathcal{O}(B)$  if appropriate sparse-matrix libraries are employed. We have not attempted to do so in this work.

Apart from the  $\mathcal{O}(B^3)$  inversion of the sparse preconditioner, the routine operations of the VM PCG algorithm have  $\mathcal{O}(B^2N)$  complexity, where  $N$  is the number of electrons (orbitals) that is typically an order of magnitude lower than  $B$ . The added cost of handling nonorthogonal MOs is

minor:  $\mathcal{O}(B^2N)$  to compute the orbital overlap  $\sigma$  in Eq. (3.3) and  $\mathcal{O}(N^3)$  to invert it.

The determinant of the overlap matrix  $\sigma$  can be computed via its LU decomposition at  $\mathcal{O}(N^3)$  cost. Alternatively, a linear scaling algorithm (with a higher prefactor) can be used if molecular orbitals are localized. In such a linear scaling algorithm, the logarithm of the determinant of the symmetric positive definite overlap matrix  $\sigma$  is computed using the trace of the matrix logarithm via Mercator series

$$\begin{aligned}\ln \det(\sigma) &= \ln [\det(s) \det(I + X) \det(s)], \\ \ln \det(I + X) &= \text{Tr} \ln [I + X], \\ \ln [I + X] &= X - \frac{1}{2}X^2 + \frac{1}{3}X^3 - \frac{1}{4}X^4 + \dots\end{aligned}\tag{3.16}$$

where  $s = [\text{diag}(\sigma)]^{1/2}$ . The series converges only if  $\|X\|_F < 1$ . If it is not the case, the square root of  $I + X$  is computed recursively until the norm requirement is satisfied. The advantage of this algorithm is that relies exclusively on matrix-matrix multiplication and can be readily implemented using any matrix library. Its computational cost grows linearly with  $N$  for sparse overlap matrices of localized orbitals and cubically for dense matrices.

### 3.4.3 Penalty Strength

Since the projector onto the occupied subspace and, consequently, the Kohn-Sham energy are invariant to the choice of the occupied orbitals that span the subspace, there exist many sets of occupied orbitals that correspond to the variationally optimal projector. The main goal of the SCF procedure is to determine this variationally optimal projector, whereas *any* set of occupied orbitals that span this optimal subspace are considered a proper solution to the SCF problem. The definition of the penalty term shows that, for the optimal projector, different sets of orbitals will have different

– not necessarily optimal – values of the penalty term. This means that the penalty term does not have to be fully minimized in the SCF procedure as long the energy is minimized and the occupied orbitals are linearly independent ( $\Omega_p < \infty$ ). Thus, the main goal of adding the penalty term to the energy functional is to steer the optimization away from the unphysical linearly dependent orbitals. This goal can be achieved with *any* finite penalty strength  $C_p > 0$ . In other words,  $C_p$  does not have to be determined precisely because it does not affect the final energy.

From the practical perspective, it is reasonable to impose the following conditions on  $C_p$ . First, its value has to be sufficiently large to keep the orbitals linearly independent and ensure the numerical stability of the algorithm, such as the  $\sigma$  inversion. Second,  $C_p$  should be sufficiently small so to not make the penalty term dominate the energy term. In a case of extremely large  $C_p$ , the optimization procedure will simply orthogonalize the orbitals without minimizing the energy functional. Multiple numerical tests described below confirm that there is a wide range of  $C_p$  values spanning many orders of magnitude in which the SCF optimization is both efficient and stable.

We implemented the following simple procedure to keep  $C_p$  in the practically acceptable range. We start with a very small  $C_p$  value and update it by adding the gradient of the loss functional with respect to  $C_p$ , in the spirit of a general method for finding stationary points of the Lagrangian<sup>40</sup>.

$$\begin{aligned} \frac{\partial \Omega}{\partial C_p} &= -2 \ln \det(\sigma \sigma_d^{-1}) > 0 \\ C_p &\leftarrow C_p + \frac{\partial \Omega}{\partial C_p} \end{aligned} \tag{3.17}$$

Unlike the general method in Ref.<sup>40</sup>, we do not update  $C_p$  in order to find the minimum of the loss functional with respect to  $C_p$ . Instead, we simply ensure that  $C_p$  is sufficiently large to ensure linear independence of the orbitals. Since the gradient in Eq. (3.17) is larger than or equal to zero, the value of  $C_p$  can only increase in this procedure. The increase will be very moderate if the orbitals

are already nearly orthogonal with the normalized determinant of their overlap –  $\det(\sigma\sigma_d^{-1})$  in Eq. (3.17) – only slightly smaller than 1. In contrast, the  $C_p$  increase will be significant if the deviation from the orthogonality is large. To avoid too large of an increase in  $C_p$  the update is limited to a trust-radius of 0.1 a.u.

We chose to implement the  $C_p$  adjustment as an outer loop to the PCG optimization of the orbital coefficients  $T$ , as shown in the pseudo-code in Figure 3.1. That is, the  $C_p$  value is kept fixed while the loss functional is minimized iteratively with respect to  $T$ . After the  $T$  optimization is converged, the  $C_p$  value is adjusted if necessary.

#### 3.4.4 Variable-metric Optimization for Open-shell Systems

In the unrestricted Kohn-Sham (UKS) method, molecular orbital coefficients for different spins are optimized independently and the generalization of the VM SCF is straightforward (see Supporting Information). In the (rarely-used) restricted open-shell formulation of DFT, some of molecular orbitals are doubly-occupied and some molecular orbitals are singly occupied. In our formulation, the singly occupied molecular orbitals can be occupied with spin-up and spin-down electrons, in contrast to the conventional formulation where only spin-up electrons are unpaired. This generalization is introduced to allow for the description of singlet diradicals (below) and to make this formulation suitable for excited state calculations that will be described in the upcoming work. We call this formulation restricted open-shell optimization (ROSO) to distinguish it from restricted open-shell Kohn-Sham DFT (ROKS).

Restricted open-shell KS DFT (ROKS) is a method designed to describe singlet diradicals<sup>33,34</sup>, that is, electronic states with a single unpaired spin-up electron, a single unpaired spin-down

---

```

1: Input  $\mathbf{T}$ 
2: Input  $C_p \leftarrow 10^{-5}$  a.u.
3: Input  $N > 0$ 
4: Input  $\varepsilon_1$ 
5: Input  $\varepsilon_0 > \varepsilon_1$ 
6: for  $k = 1, \dots, N$  do
7:   if  $N > 1$  then
8:      $\varepsilon_{\text{SCF}} \leftarrow \varepsilon_0 \left( \frac{\varepsilon_1}{\varepsilon_0} \right)^{\frac{k-1}{N-1}}$ 
9:   else
10:     $\varepsilon_{\text{SCF}} \leftarrow \varepsilon_1$ 
11:   end if
12:   StopSCF  $\leftarrow$  False
13:    $i_{\text{SCF}} \leftarrow 0$ 
14:   repeat
15:      $i_{\text{SCF}} \leftarrow i_{\text{SCF}} + 1$ 
16:      $\Omega_p \leftarrow -2C_p \ln \det(\sigma \sigma_d^{-1})$ 
17:      $\Omega \leftarrow E + \Omega_p$ 
18:      $\mathbf{G} \leftarrow \mathbf{G}^E + \mathbf{G}^P$ 
19:     if  $\|\mathbf{G}^E\|_{\text{RMS}} < \varepsilon_{\text{SCF}}$  then
20:       StopSCF  $\leftarrow$  True
21:     end if
22:     if not StopSCF then
23:       if  $i_{\text{SCF}} = 1$  then
24:          $\mathbf{K} \leftarrow \mathbf{H}^{-1}$ 
25:       else
26:          $\mathbf{G} \leftarrow \mathbf{G}$ 
27:          $\mathbf{O} \leftarrow \mathbf{D}$ 
28:       end if
29:        $\mathbf{D} \leftarrow -\mathbf{K}\mathbf{G}$ 
30:       if  $i_{\text{SCF}} > 1$  then
31:          $\beta \leftarrow \text{Tr}(\mathbf{G}^\dagger \mathbf{D}) / \text{Tr}(\mathbf{G}^\dagger \mathbf{O})$ 
32:          $\mathbf{D} \leftarrow \mathbf{D} + \beta \mathbf{O}$ 
33:       end if
34:        $\alpha \leftarrow \text{argmin}_\alpha \Omega(\mathbf{T} + \alpha \mathbf{D})$ 
35:        $\mathbf{T} \leftarrow \mathbf{T} + \alpha \mathbf{D}$ 
36:     end if
37:   until StopSCF
38:    $C_p \leftarrow C_p + \min\left(\frac{\Omega_p}{C_p}, 0.1 \text{ a.u.}\right)$ 
39: end for
40: return  $\mathbf{T}$ 

```

---

Figure 3.1: Variable-metric SCF based on the PCG algorithm.

electron, and with all other electrons paired (Figure 3.2). The major problem with applying KS DFT to such singlet diradicals is that a single electronic determinant in KS DFT cannot describe them. The best description offered by a single Slater determinant is the state representing a 50/50 mixture of the pure singlet and pure triplet states (Figure 3.2) – the so-called mixed state.

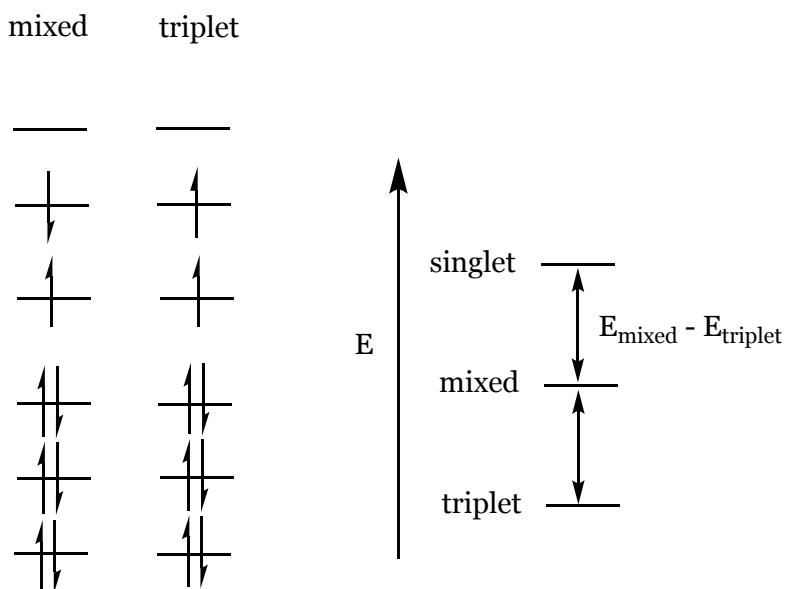


Figure 3.2: An illustrative example of the two Slater determinants that are used to describe a spin-pure singlet diradical state. The relation between the energies of the singlet, mixed, and triplet states is also shown.

ROKS has been proposed as a workaround solution to this problem. In ROKS, the energy functional for the singlet state is written as the energy of the mixed single-determinant state plus the energy difference between the mixed state and the triplet state

$$\begin{aligned}
 E_{\text{singlet}} &= E_{\text{mixed}} + (E_{\text{mixed}} - E_{\text{triplet}}) = \\
 &= 2E_{\text{mixed}} - E_{\text{triplet}}
 \end{aligned}
 \tag{3.18}$$

where  $(E_{\text{mixed}} - E_{\text{triplet}})$  accounts for the fact that the energy of the mixed state lies exactly half-way between those of the singlet and triplet states (Figure 3.2). Thus, a singlet diradical energy is described by mixed and triplet Slater determinants. To ensure the spin purity of the singlet state, the

electrons of the mixed and triplet Slater determinants should occupy the same orbitals. Therefore, the triplet state is not optimized independently; its orbitals are obtained by flipping the spin-down electron in the singly-occupied orbital to make it a spin-up electron (Figure 3.2).

The ROKS optimization can be easily performed using the variable-metric approach. In the VM ROKS, the penalty term is added only for the orbitals of the triplet state.

$$\Omega = E_{singlet} - C_p \sum_{\tau=\alpha}^{\beta} \ln \det \left[ \sigma_{triplet}^{\tau} \left( \sigma_{d,triplet}^{\tau} \right)^{-1} \right] \quad (3.19)$$

Since the orbitals of the mixed state are directly determined from the orbitals of the triplet state, they also remain linearly independent (see Supporting Information for caveats and implementation details).

### 3.4.5 Computational Details

Parameter	Notation	Default value	Described in
Initial penalty strength	$C_p$	$10^{-5}$ a.u.	Figure 3.1
Number of steps in the $C_p$ loop	$N$	4	Figure 3.1
SCF convergence threshold	$\epsilon_1$	$10^{-8}$ a.u.	Figure 3.1
Initial loose SCF threshold	$\epsilon_0$	$10^{-2}$ a.u.	Figure 3.1
Hamiltonian projector in the preconditioner	$A$	$Q$	Eq. (3.13)
Overlap projector in the preconditioner	$D$	$I$	Eq. (3.13)
Preconditioner regularization parameter	$\epsilon$	0.5 a.u.	Eq. (3.13)

Table 3.1: Key input parameters that control the PCG optimization of MO coefficients.

The variable-metric SCF algorithm was implemented in the electronic structure module of the CP2K software package<sup>41</sup>. In the current implementation, matrix operations were performed using the DBCSR<sup>42</sup> and ScaLAPACK<sup>43</sup> libraries.

A variety of atomistic systems were used to test accuracy, numerical stability and convergence rate of VM SCF. Fully optimized structures of supercells of hexagonal graphite ( $8 \times 8 \times 1$ , 256 atoms), cubic diamond ( $4 \times 4 \times 4$ , 512 atoms), and graphene ( $18 \times 18 \times 1$ , 648 atoms) were used.

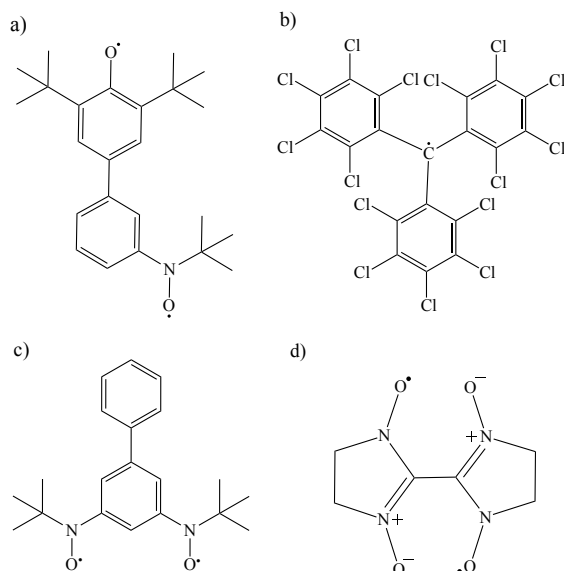


Figure 3.3: Organic radicals considered in this work: a) 3,5-ditert-butyl-3'-(N-tert-butyl-N-aminoxy)-4-oxybiphenyl (oxybiphenyl), b)  $\alpha H$ -undecachlorodiphenylmethyl (PTM), c) biphenyl-3,5-diyl-bis(N-t-butyl nitroxide) (biphenyl), and d) bis-nitronyl nitroxide (BNN).

Unit cells of zigzag (6,0) and armchair (5,5) single-walled carbon nanotubes (SWCNT) were multiplied in the axial direction 13 times and contained 312 atoms and 260 atoms, respectively. Such large supercells allowed us to test the efficiency of the optimization for wide- and narrow-gap systems. Large supercells were used to compensate for the absence of the  $k$ -point integration.

Other test systems, such as radical organic polymers, transition metal complexes, and singlet diradicals, were specifically chosen for their electronic and spin states<sup>44–46</sup> (Figure 3.3). Specifically, radical organic polymers (oxybiphenyl, PTM, biphenyl, BNN) contain unpaired electrons localized on specific sites within the polymer chain<sup>47,48</sup>. Transition metal complexes ( $[\text{Cr}(\text{CN})_6]^{4-}$ ,  $[\text{Cr}(\text{I})_6]^{4-}$ ) involve metal atoms with partially filled  $d$ -orbitals. They often exhibit intricate electronic structures and magnetic properties due to the interplay of ligand-field effects and electron correlation. Singlet diradicals, characterized by the presence of two unpaired electrons of the opposite spins<sup>46</sup>, are of particular interest due to the difficulties of describing them with conventional

KS DFT. Several small diradicals, namely  $\text{CH}_2$ ,  $\text{OH}^+$  and  $\text{NH}_2^+$ , were selected from the Slipchenko-Krylov test set<sup>49</sup>, whereas oxybiphenyl<sup>50</sup> and BNN<sup>51</sup> diradicals were chosen to represent larger diradical molecules.

Test calculations were carried out using the dispersion corrected<sup>52</sup> generalized gradient exchange-correlation functional of Perdew, Burke and Ernzerhof (PBE)<sup>53–55</sup>. In the dual Gaussian and plane-wave scheme implemented in CP2K<sup>56</sup>, double- $\zeta$  valence basis set with one set of polarization functions (DZVP)<sup>57</sup> were used to represent atomic orbitals. For singlet diradicals, triple- $\zeta$  valence basis sets with two set of polarization functions and one set of diffuse functions was used (aug-TZV2P). A plane-wave cutoff of 300 Ry was used to describe the electron density. Separable norm-conserving Goedecker-Teter-Hutter pseudopotentials were used to describe the interactions between the valence electrons and ionic cores<sup>58,59</sup>. The initial orbitals were obtained by superimposing atomic density matrices and then projecting randomly generated orbitals onto the total block-diagonal density matrix. The default values of the input parameters that control convergence of the PCG variable-metric optimization are shown in Table 3.1 and used unless specified otherwise.

### 3.5 Data Availability

Optimized atomic coordinates for all structures and lattice vectors for periodic structures are deposited in a Figshare database<sup>60</sup>.

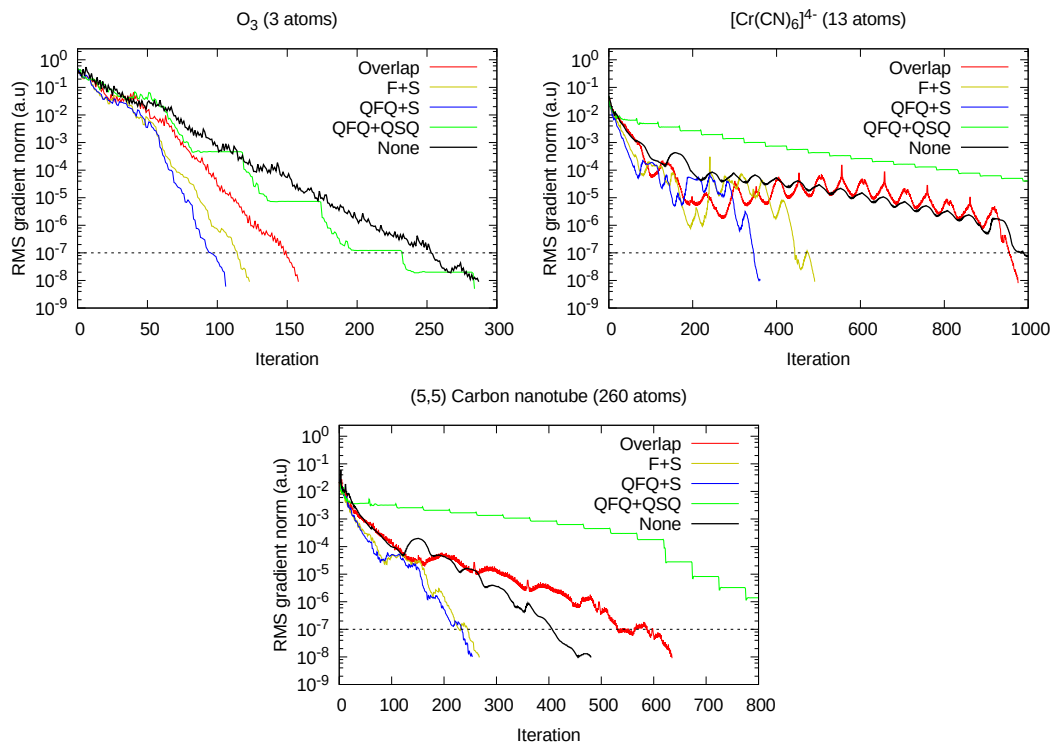


Figure 3.4: Influence of the preconditioner on the rate of convergence of the VM SCF optimization. The list of preconditioners includes: overlap ( $A = 0, D = I$ ),  $F + S$  ( $A = D = I$ ),  $QFQ + S$  ( $A = Q, D = I$ ),  $QFQ + QSQ$  ( $A = D = Q$ ). The dashed line refers to the level of the SCF accuracy typically required in *ab initio* molecular dynamics (AIMD) simulation. In all three tests,  $\epsilon$  was set to 0.85 a.u. for  $F + S$  preconditioner.

## 3.6 Numerical Results and Discussion

### 3.6.1 Preconditioner

The convergence rate of the PCG algorithm is strongly influenced by the choice of preconditioner (Figure 3.4). In the iterative SCF process, the preconditioner is constructed and inverted only at the start of each inner SCF cycle. Convergence of VM SCF for ozone molecule, triplet low-spin  $[\text{Cr}(\text{CN})_6]^{4-}$  complex, and (6,0) SWCNT shows that  $QFQ + QSQ$  preconditioner is the least efficient of all (Figure 3.4). This is because  $QHQ + QSQ$  preconditioner limits the update of the MO coefficients (see the algorithm in Figure 3.1) to the fixed virtual subspace  $Q$  of the Kohn-Sham

Hamiltonian evaluated once in the beginning of the inner SCF loop. MO updates limited to fixed  $Q$  would be accurate if the Hamiltonian were fixed in the inner loop. But the Hamiltonian depends on the orbitals and is updated on every SCF iteration. This leads to a stalled optimization that is manifested in plateaus in the gradient norm in Figure 3.4.  $QHQ + S$  preconditioner performs better because adding the  $S$  term outside the fixed virtual subspace leads to important (although imperfect) orbital updates outside  $Q$ .

Further comparison of preconditioners shows that incorporating information from both the overlap matrix and the Kohn-Sham Hamiltonian significantly improves convergence rates and enhances stability during optimization (Figure 3.4). Using the overlap preconditioner  $S$  alone is not efficient. Another advantage of using positive definite  $S$  instead of positive semidefinite  $QSQ$  allows to utilize fast Cholesky inversion, enhancing the efficiency of the preconditioner update.

Finally, it can be beneficial to change the default value of  $\epsilon$  in Eq. (3.13). High values of  $\epsilon$  reduce the contribution of the Hamiltonian term to the preconditioner and slow down convergence. For example, the overlap preconditioner performs worse than  $QFQ + S$  preconditioner (Figure 3.4). On the other hand, low values of  $\epsilon$  might can produce preconditioners with negative eigenvalues introduced by the Hamiltonian term, leading to the failure of the Cholesky inversion. For  $QFQ + S$  preconditioner, this is more likely to happen for systems with low lying unoccupied orbitals with negative energies. For  $F + S$  preconditioner, this happens more often even for wide-gap systems because the unprojected  $F$  contains negative orbital energies of the occupied space (see caption of Figure 3.4).

The default value of  $\epsilon = 0.5$  a.u. (Table 3.1) works well for most systems and, in our tests, we increased  $\epsilon$  only when the Cholesky factorization fails. For well-behaved systems with large band gaps, such as cubic diamond, tuning the value of  $\epsilon$  does not have significant impact on the

rate of convergence (Figure 3.5). For zero-gap graphene, increasing the weight of the Hamiltonian improves convergence noticeably until the preconditioner acquires negative eigenvalues and the Cholesky inversion fails (Figure 3.5).

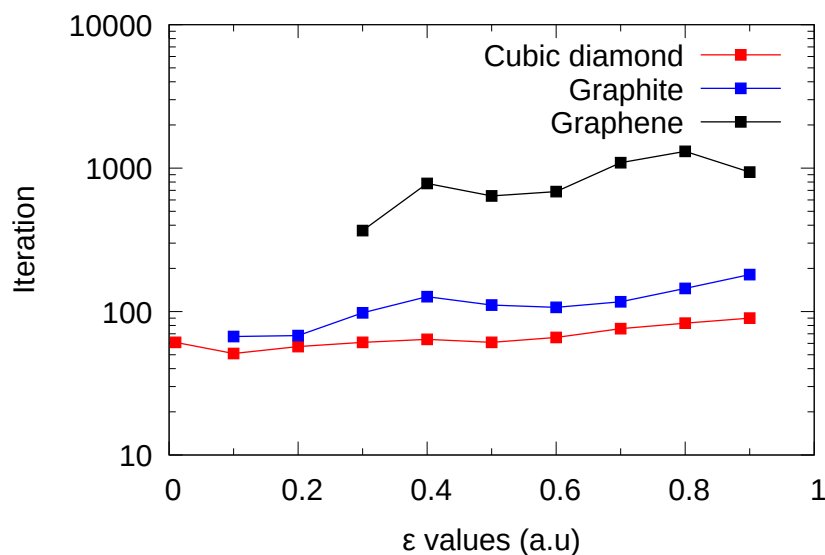


Figure 3.5: Influence of the value of  $\epsilon$  on the number of VM SCF steps required to reach convergence of  $10^{-8}$  a.u. Missing data points indicate the Cholesky inversion of the preconditioner failed. Default settings were used in all three tests.

### 3.6.2 Penalty Strength

A broad range of initial  $C_p$  values from  $10^{-9}$  to  $10^2$  a.u. was examined to evaluate the versatility of the variable-metric optimization algorithm. The initial  $C_p$  value was updated using Eq. (3.17) as described in Figure 3.1. It was found that the final  $C_p$  values did not differ significantly from their original values. For all systems, the difference between the initial and final values of  $C_p$  was within 10%. This confirms that the precise value of  $C_p$  is not crucial for maintaining the linear independence of the orbitals, at least with the currently implemented PCG algorithm.

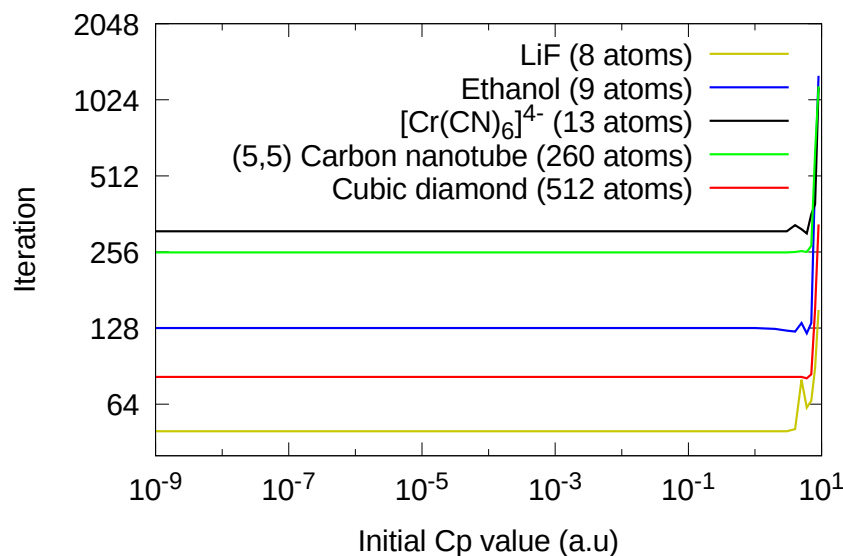


Figure 3.6: Convergence rate of VM approach corresponding to different scaling of penalty strength.

It should also be noted that the initial value of  $C_p$  does not have noticeable effect on the number of SCF iterations required to reach convergence (Figure 3.6). Only for very large  $C_p$  values the SCF procedure is negatively impacted, taking more iterations to converge (Figure 3.6). In such cases, the penalty term dominates over the energy term, causing the optimization procedure to focus primarily on orthogonalizing the orbitals instead of on minimizing the energy functional. The recommended default initial value for  $C_p$  for most systems is  $10^{-5}$  a.u. Figure 3.7 shows that the penalty term plays an important role restoring orthogonality of the orbitals in the SCF procedure.

### 3.6.3 SCF Convergence

The rate of convergence of the VM optimization was compared to that of the orbital transformation (OT) approach<sup>14</sup> – an efficient go-to SCF method implemented in CP2K. While OT uses the same PCG algorithm as VM, there are still substantial differences in their preconditioners, line search subroutines, and the structure of the inner and outer SCF loops, precluding exact compar-

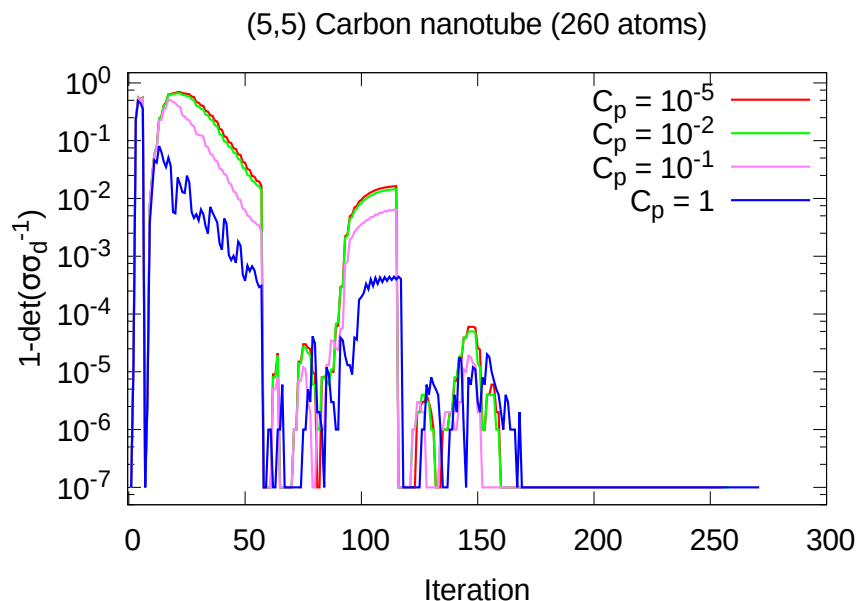


Figure 3.7: Deviation from the orthogonality for occupied MOs in the SCF optimization for armchair carbon nanotube for different initial values of the penalty strength  $C_p$ . Orbitals re-orthogonalized in the outer loop.

isons of the two theoretical approaches. For OT, we used the preconditioner based on the Cholesky inversion of the  $F + \lambda S$  matrix, where  $\lambda$  is the spectral shift applied to the Kohn-Sham matrix. This preconditioner resembles the  $QFQ + S$  preconditioner used for VM SCF, but is not the same.

The test systems included closed-shell electronic configurations described by restricted KS DFT (cubic diamond, hexagonal graphite, graphene, SWCNT), low-spin and high-spin open-shell configurations described by UKS ( $[\text{Cr}(\text{I})_6]^{4-}$ ,  $[\text{Cr}(\text{CN})_6]^{4-}$ , PTM<sup>61</sup>), and open-shell singlet diradicals described by ROSO (biphenyl<sup>62</sup>, oxybiphenyl<sup>50</sup>) and ROKS (BNN<sup>51</sup>, oxybiphenyl<sup>50</sup>,  $\text{OH}^+$ ,  $\text{CH}_2$ , and  $\text{NH}_2^+$  radicals). Default settings were applied to all test systems with a few exceptions (Table 1.3).

Figures 3.8 and 3.9 show that the VM approach exhibits the same rate of convergence as the OT method for all systems, including gas-phase molecules and periodic materials, systems with wide (diamond<sup>63</sup>), narrow (graphite<sup>64</sup>, armchair SWCNT<sup>65</sup>), and zero (zigzag SWCNT<sup>65</sup>, graphene<sup>66</sup>)

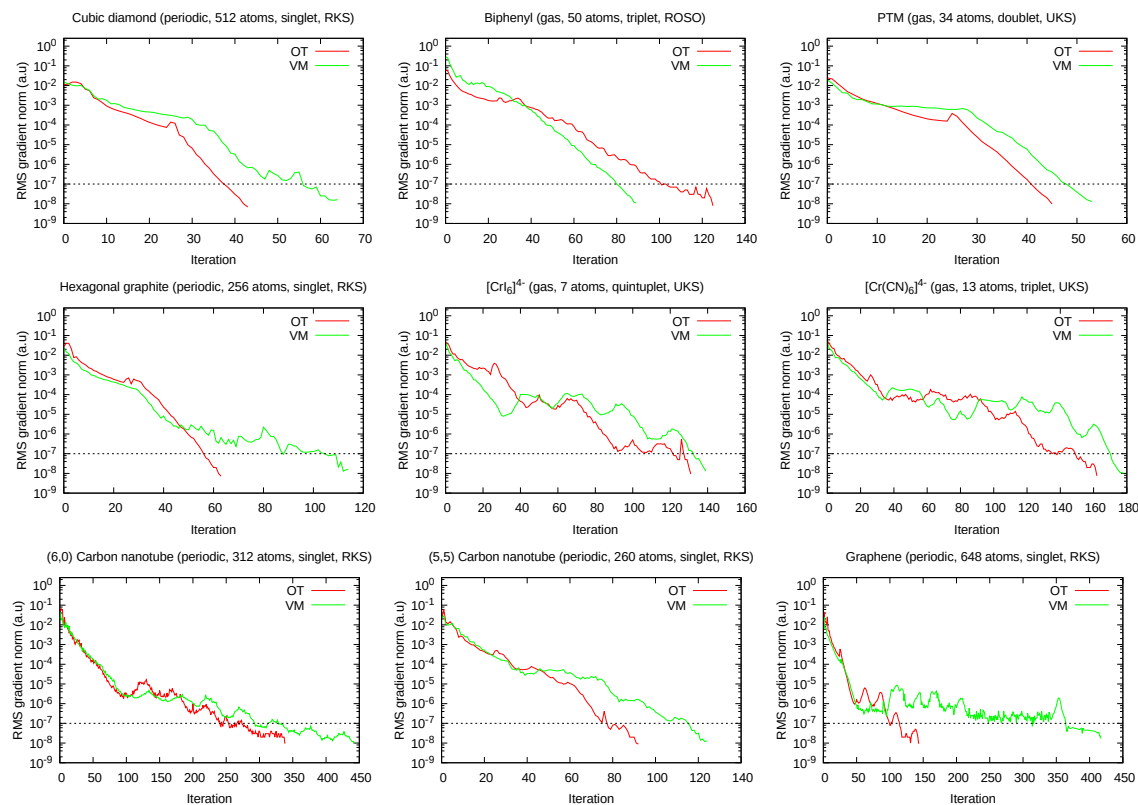


Figure 3.8: Comparison of the convergence rate for the VM and OT SCF procedures. Line search steps, one per PCG step, are not included in the iteration count. The dashed line refers to the level of accuracy typically required in *ab initio* molecular dynamics simulations.

band gaps. The latter two are particularly challenging tests for the SCF optimization.

It was verified that the final energies produced by OT and VM methods are the same within the allowed numerical threshold set at  $10^{-12}$  a.u.

### 3.6.4 Variable-metric ROKS SCF for Singlet Diradicals

The singlet-triplet energy gaps for typical singlet diradicals are severely underestimated in UKS calculations (Table 3.2)<sup>67</sup> because the UKS state lies approximately half way between the true triplet and singlet states in energy (Figure 3.9). That is why it is customary to double the UKS singlet-triplet energy gaps after the SCF procedure<sup>68</sup>. The ROKS approach is formulated to correct

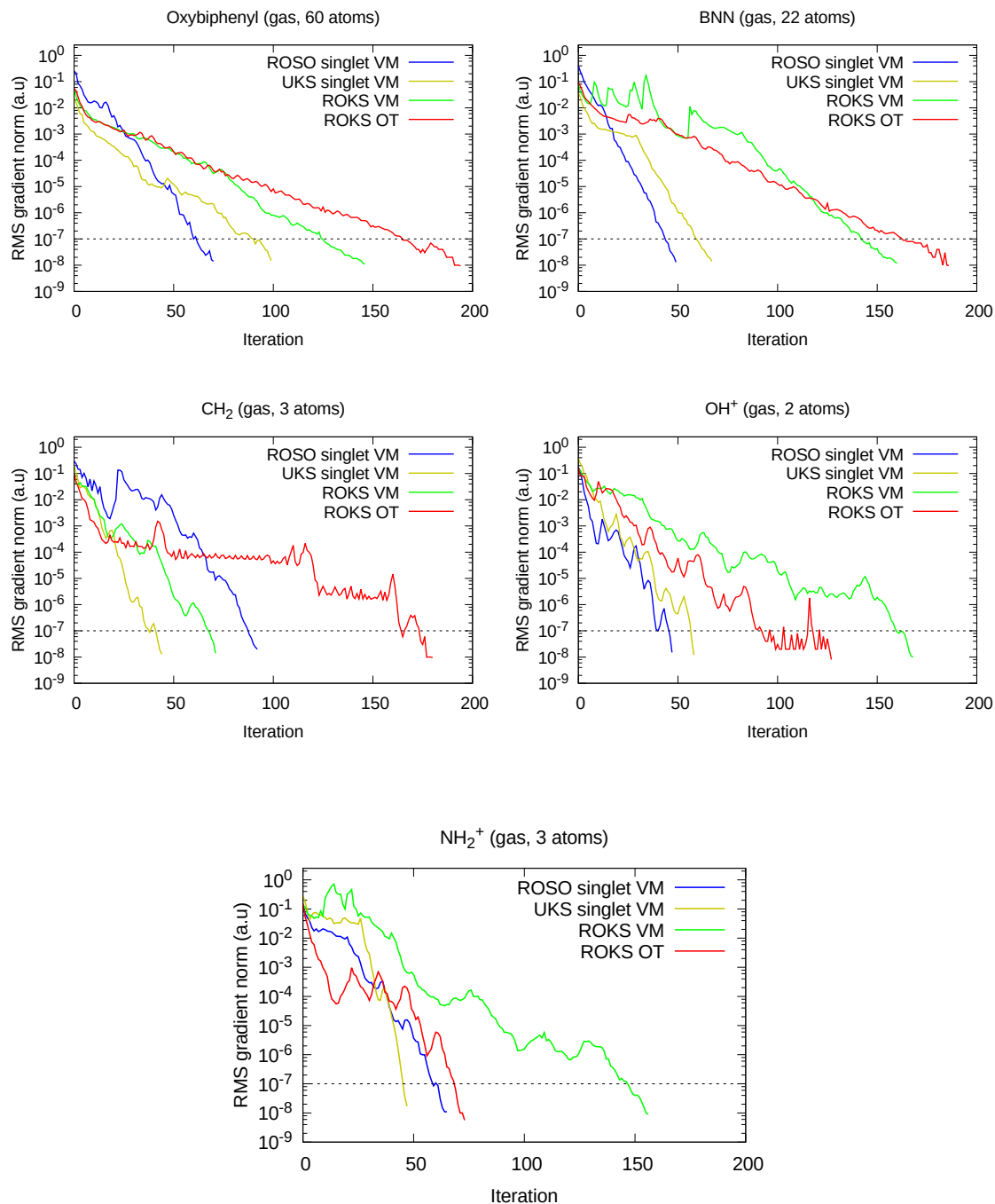


Figure 3.9: Comparison of the convergence rate of the VM and OT SCF procedures for singlet diradicals. Line search steps, one per PCG step, are not included in the iteration count. The dashed line refers to the level of accuracy typically required in *ab initio* molecular dynamics simulations.

this deficiency during, not after, the SCF procedure. Table 3.2 shows that the ROKS singlet-triplet gaps computed with the VM method are significantly better than the UKS gaps. At the same time, they are only slightly better than the doubled UKS gaps, suggesting that orbital relaxation effects play only minor role in correcting the diradical electronic states, at least for the systems considered here. The only example when the self-consistent ROKS treatment is better than the post-SCF correction is the case of bis-nitronyl nitroxide diradical. It is also worth mentioning that hybrid functionals are expected to improve ROKS prediction of the singlet-triplet gaps, whereas the opposite trend is expected for UKS calculations. This is because the spin contamination in UKS, known to be worse for hybrid than GGA functionals<sup>67,69,70</sup>, is eliminated in ROKS. Indeed, when HSE06<sup>71-73</sup> is used for BNN diradical, the singlet-triplet gap predicted with ROKS becomes slightly closer to the experimental value whereas UKS prediction becomes much worse (Table 3.2).

Molecules	$\Delta E_{ST}$ , kcal/mol			Exptl.
	UKS	UKS $\times 2$	ROKS	
OH <sup>+</sup>	18.0	36.1	36.9	50.5 <sup>67</sup>
CH <sub>2</sub>	10.2	20.4	23.8	32.9 <sup>67</sup>
NH <sub>2</sub> <sup>+</sup>	15.9	31.7	32.2	44.6 <sup>67</sup>
biphenyl	0.3	0.6	0.4	3.4 <sup>62</sup>
oxybiphenyl	1.0	2.1	1.2	3.1 <sup>50</sup>
BNN	-1.7	-3.3	0.007	0.89 <sup>51</sup>
BNN*	-5.7	-11.4	0.013	0.89 <sup>51</sup>

\* HSE06/aug-TZV2P singlet-triplet energy gaps.

Table 3.2: PBE/aug-TZV2P singlet-triplet energy gaps for singlet diradicals computed with the single-determinant UKS and two-determinant ROKS methods.

Figure 3.9 shows that ROKS optimization requires more iterations to converge than the single-determinant methods, such as UKS and ROSO, due to the complexities of the simultaneous optimization of two electronic states. As in the RKS and UKS cases, OT ROKS and VM ROKS converge with similar rates.

## 3.7 Conclusions

This work shows that the SCF optimization of molecular orbitals in KS DFT can be performed without imposing conventional orthonormality constraints on them. The optimization can instead be carried out with nonorthogonal orbitals if the DFT energy functional is augmented with a term that penalizes linearly dependent states. This generalization of the SCF procedure, called variable metric SCF, allows to use molecular orbital coefficients – arguably the most natural descriptors of one-electron wavefunctions – as independent variables in a direct unconstrained optimization procedure. In this ansatz, the expressions for the electronic energy gradient and Hessian can be written in a simple closed form. It is shown that a basic PCG algorithm can be used to converge the SCF procedure for a variety of systems including challenging narrow-gap systems and spin-pure two-determinant states for singlet diradicals.

Due to the simplicity of the unconstrained variable metric SCF, this approach can be easily implemented using other minimization techniques<sup>38</sup>, such as Broyden-Fletcher-Goldfarb-Shanno (BFGS) algorithm and trust region methods. Furthermore, variable metric optimization can be readily extended to the cases where linear dependencies present a problem, such as the optimization of strictly localized orbitals<sup>25</sup>, orbital-optimized excited states<sup>74</sup>, and multi-configurational wavefunctions.

## 3.8 Acknowledgements

The research was funded by the Natural Sciences and Engineering Research Council of Canada (NSERC) through Discovery Grant (RGPIN-2016-0505). The authors are grateful to Compute Canada for computer resources allocated under the CFI John R. Evans Leaders Fund program.

### 3.9 References

- [1] Kohn, W.; Sham, L. J. Self-consistent equations including exchange and correlation effects. *Phys. Rev.* **1965**, *140*, A1133.
- [2] Hohenberg, P.; Kohn, W. Inhomogeneous electron gas. *Phys. Rev.* **1964**, *136*, B864.
- [3] Gryn'ova, G.; Coote, M. L.; Corminboeuf, C. Theory and practice of uncommon molecular electronic configurations. *Wiley Interdiscip. Rev. Comput. Mol. Sci.* **2015**, *5*, 440–459.
- [4] Nguyễn, T. A. *Frontier orbitals : a practical manual*; John Wiley & Sons, 2007; p 304.
- [5] Pulay, P. Convergence acceleration of iterative sequences. the case of scf iteration. *Chem. Phys. Lett.* **1980**, *73*, 393–398.
- [6] Pulay, P. Improved SCF convergence acceleration. *J. Comput. Chem.* **1982**, *3*, 556–560.
- [7] Some comments on the DIIS method. *Mol. Phys.* **2007**, *105*, 2839–2848.
- [8] Cancès, E.; Bris, C. L. Can we outperform the DIIS approach for electronic structure calculations? *International Journal of Quantum Chemistry* **2000**, *79*.
- [9] Cancès, E. Self-consistent field algorithms for Kohn-Sham models with fractional occupation numbers. *Journal of Chemical Physics* **2001**, *114*.
- [10] Kudin, K. N.; Scuseria, G. E.; Cancès, E. A black-box self-consistent field convergence algorithm: One step closer. *Journal of Chemical Physics* **2002**, *116*.
- [11] Ödön Farkas; Ödön Farkas; Ödön Farkas; Schlegel, H. B. Methods for optimizing large molecules. Part III. An improved algorithm for geometry optimization using direct inversion in the iterative subspace (GDIIS). *Physical Chemistry Chemical Physics* **2002**, *4*.
- [12] Kudin, K. N.; Scuseria, G. E. Converging self-consistent field equations in quantum chemistry - Recent achievements and remaining challenges. *Mathematical Modelling and Numerical Analysis* **2007**, *41*.
- [13] Voorhis, T. V.; Head-Gordon, M. A geometric approach to direct minimization. *Mol. Phys.* **2009**, *100*, 1713–1721.
- [14] VandeVondele, J.; Hutter, J. An efficient orbital transformation method for electronic structure calculations. *J. Chem. Phys.* **2003**, *118*, 4365–4369.
- [15] Liang, W.; Head-Gordon, M. An exact reformulation of the diagonalization step in electronic structure calculations as a set of second order nonlinear equations. *J. Chem. Phys.* **2004**, *120*, 10379.
- [16] Stoll, H.; Wagenblast, G.; Preuß, H. On the use of local basis sets for localized molecular orbitals. *Theor. Chem. Acc.* **1980**, *57*, 169–178.
- [17] Ordejón, P.; Drabold, D. A.; Martin, R. M.; Grumbach, M. P. Linear system-size scaling methods for electronic-structure calculations. *Phys. Rev. B* **1995**, *51*, 1456.
- [18] Yang, W. Absolute-energy-minimum principles for linear-scaling electronic-structure calculations. *Phys. Rev. B* **1997**, *56*, 9294.
- [19] Skylaris, C.-K.; Haynes, P. D.; Mostofi, A. A.; Payne, M. C. Introducing ONETEP: Linear-scaling density functional simulations on parallel computers. *J. Chem. Phys.* **2005**, *122*, 084119.

- [20] Khaliullin, R. Z.; Head-Gordon, M.; Bell, A. T. An efficient self-consistent field method for large systems of weakly interacting components. *J. Chem. Phys.* **2006**, *124*, 204105.
- [21] Burger, S. K.; Yang, W. Linear-scaling quantum calculations using non-orthogonal localized molecular orbitals. *J. Phys.: Condens. Matter* **2008**, *20*, 294209.
- [22] Mo, Y. The Block-Localized Wavefunction (BLW) Perspective of Chemical Bonding. *The Chemical Bond: Fundamental Aspects of Chemical Bonding* **2014**, 199–232.
- [23] Nakata, A.; Bowler, D. R.; Miyazaki, T. Optimized multi-site local orbitals in the large-scale DFT program CONQUEST. *Phys. Chem. Chem. Phys.* **2015**, *17*, 31427–31433.
- [24] Staub, R.; Iannuzzi, M.; Khaliullin, R. Z.; Steinmann, S. N. Energy Decomposition Analysis for Metal Surface-Adsorbate Interactions by Block Localized Wave Functions. *J. Chem. Theory Comput.* **2019**, *15*, 265–275.
- [25] Shi, Y.; Karagunesian, J.; Khaliullin, R. Z. Robust linear-scaling optimization of compact localized orbitals in density functional theory. 2021; <https://arxiv.org/abs/2004.05901>.
- [26] Mauri, F.; Galli, G.; Car, R. Orbital formulation for electronic-structure calculations with linear system-size scaling. *Phys. Rev. B* **1993**, *47*, 9973.
- [27] Goedecker, S. Linear scaling electronic structure methods. *Rev. Mod. Phys.* **1999**, *71*, 1085.
- [28] Fattetbert, J.-L.; Gygi, F. Linear scaling first-principles molecular dynamics with controlled accuracy. *Comput. Phys. Commun.* **2004**, *162*, 24–36.
- [29] Feng, H.; Bian, J.; Li, L.; Yang, W. An efficient method for constructing nonorthogonal localized molecular orbitals. *J. Chem. Phys.* **2004**, *120*, 9458.
- [30] Tsuchida, E. Ab initio molecular dynamics simulations with linear scaling: application to liquid ethanol. *J. Phys.: Condens. Matter* **2008**, *20*, 294212.
- [31] Khaliullin, R. Z.; VandeVondele, J.; Hutter, J. Efficient linear-scaling density functional theory for molecular systems. *J. Chem. Theory Comput.* **2013**, *9*, 4421–4427.
- [32] Peng, L.; Gu, F. L.; Yang, W. Effective preconditioning for ab initio ground state energy minimization with non-orthogonal localized molecular orbitals. *Phys. Chem. Chem. Phys.* **2013**, *15*, 15518–15527.
- [33] Frank, I.; Hutter, J.; Marx, D.; Parrinello, M. Molecular dynamics in low-spin excited states. *J. Chem. Phys.* **1998**, *108*, 164101.
- [34] Filatov, M.; Shaik, S. Density-functional thermochemistry. III. The role of exact exchange. *J. Chem. Phys.* **1999**, *110*, 5648.
- [35] Luo, Z.; Khaliullin, R. Z. Direct Unconstrained Variable-Metric Localization of One-Electron Orbitals. *J. Chem. Theory Comput.* **2020**, *16*, 3558–3566.
- [36] Luo, Z.; Khaliullin, R. Z. Variable-Metric Localization of Occupied and Virtual Orbitals. *J. Chem. Theory Comput.* **2021**, *17*, 5581.
- [37] Head-Gordon, M.; Maslen, P. E.; White, C. A. A tensor formulation of many-electron theory in a nonorthogonal single-particle basis. *J. Chem. Phys.* **1998**, *108*, 616.
- [38] Nocedal, J.; Wright, S. *Numerical Optimization*; Springer Science & Business Media, 2006.
- [39] A Survey of Nonlinear Conjugate Gradient Methods. *Pac. J. Optim.* **2006**, *2*, 35–58.

- [40] Polyak, B. T. Iterative methods using lagrange multipliers for solving extremal problems with constraints of the equation type. *USSR Comput. Math. & Math. Phys.* **1970**, *10*, 42–52.
- [41] Kühne, T. D.; Iannuzzi, M.; Del Ben, M.; Rybkin, V. V.; Seewald, P.; Stein, F.; Laino, T.; Khaliullin, R. Z.; Schütt, O.; Schiffmann, F.; et al. CP2K: An Electronic Structure and Molecular Dynamics Software Package -Quickstep: Efficient and Accurate Electronic Structure Calculations. *J. Chem. Phys.* **2020**, *152*, 194103.
- [42] Borštnik, U.; VandeVondele, J.; Weber, V.; Hutter, J. Sparse matrix multiplication: The distributed block-compressed sparse row library. *Parallel Comp.* **2014**, *40*, 47–58.
- [43] Choi, J.; Demmel, J.; Dhillon, I.; Dongarra, J.; Ostrouchov, S.; Petitet, A.; Stanley, K.; Walker, D.; Whaley, R. ScaLAPACK: a portable linear algebra library for distributed memory computers — design issues and performance. *Comput. Phys. Commun.* **1996**, *97*, 1–15, High-Performance Computing in Science.
- [44] Denawi, H.; Abel, M.; Siri, O.; Hayn, R. Electronic and magnetic properties of metal–organic polymers with 4d and 5d-transition metal ions. *J. Magn. Magn. Mater.* **2021**, *537*, 168183.
- [45] Figgis, B. N. The magnetic properties of transition metal ions in asymmetric ligand fields. Part 2.—Cubic field 3T<sub>2</sub> terms. *Trans. Faraday Soc.* **1961**, *57*, 198–203.
- [46] Salem, L.; Rowland, C. The Electronic Properties of Diradicals. *Angew. Chem., Int. Ed. Engl.* **1972**, *11*, 92–111.
- [47] Mukherjee, S.; Boudouris, B. W. *Organic Radical Polymers: New Avenues in Organic Electronics*; Springer Int. Publ.: Cham, 2017; pp 1–15.
- [48] Zhang, K.; Monteiro, M. J.; Jia, Z. Stable organic radical polymers: synthesis and applications. *Polym. Chem.* **2016**, *7*, 5589.
- [49] Slipchenko, L. V.; Krylov, A. I. Singlet-triplet gaps in diradicals by the spin-flip approach: A benchmark study. *J. Chem. Phys.* **2002**, *117*, 4694–4708.
- [50] Liao, Y.; Xie, C.; Lahti, P. M.; Weber, R. T.; Jiang, J.; Barr, D. P. 3,5-Di-tert-butyl-3'-(N-tert-butyl-N-aminoxy)-4-oxybiphenyl: A Heterospin Diradical with Temperature Dependent Behavior. *Angew. Chem., Int. Ed. Engl.* **1950**, *77*, 5176–5182.
- [51] Kwon, O.; Chung, G. Density Functional and Multireference Perturbation Theory Calculations of Bis-nitronyl Nitroxide Biradical. *Bull. Korean Chem. Soc* **2008**, *29*.
- [52] Grimme, S.; Antony, J.; Ehrlich, S.; Krieg, H. A Consistent and Accurate Ab Initio Parametrization of Density Functional Dispersion Correction (DFT-D) for the 94 Elements H-Pu. *J. Chem. Phys.* **2010**, *132*, 1–18.
- [53] Zhang, Y.; Yang, W. Comment on "Generalized Gradient Approximation Made Simple". *Phys. Rev. Lett.* **1998**, *80*, 890–890.
- [54] Perdew, J. P.; Ruzsinszky, A.; Csonka, G. I.; Vydrov, O. A.; Scuseria, G. E.; Constantin, L. A.; Zhou, X.; Burke, K. Restoring the density-gradient expansion for exchange in solids and surfaces. *Phys. Rev. Lett.* **2008**, *100*, 136406.
- [55] Perdew, J. P.; Burke, K.; Ernzerhof, M. Generalized Gradient Approximation Made Simple. *Phys. Rev. Lett.* **1997**, *78*, 1396.
- [56] Hutter, J.; Iannuzzi, M.; Schiffmann, F.; Vandevondele, J. Cp2k: Atomistic Simulations of Condensed Matter Systems. *Wiley Interdiscip. Rev. Comput. Mol. Sci.* **2014**, *4*, 15–25.

- [57] VandeVondele, J.; Hutter, J. Gaussian basis sets for accurate calculations on molecular systems in gas and condensed phases. *J. Chem. Phys.* **2007**, *127*, 114105.
- [58] Goedecker, S.; Teter, M.; Hutter, J. Separable Dual-Space Gaussian Pseudopotentials. *Phys. Rev. B* **1996**, *54*, 1703.
- [59] Krack, M. Pseudopotentials for H to Kr Optimized for Gradient-Corrected Exchange-Correlation Functionals. *Theor. Chem. Acc.* **2005**, *114*, 145–152.
- [60] Pham, H. D. M.; Khaliullin, R. Z. Direct unconstrained optimization of molecular orbital coefficients in density functional theory dataset. **2024**, <https://doi.org/10.6084/m9.figshare.c.7360846>.
- [61] Ballester, M.; Riera-Figuera, J.; Castaner, J.; Badfa, C.; Monso, J. M. Inert carbon free radicals. I. Perchlorodiphenylmethyl and perchlorotriphenylmethyl radical series. *J. Am. Chem. Soc.* **2002**, *93*, 2215–2225.
- [62] Kurokawa, G.; Ishida, T.; Nogami, T. Remarkably strong intermolecular antiferromagnetic couplings in the crystal of biphenyl-3,5-diyl bis(tert-butyl nitroxide). *Chem. Phys. Lett.* **2004**, *392*, 74–79.
- [63] Yang, H.; Ma, Y.; Dai, Y. Progress of structural and electronic properties of diamond: a mini review. *Funct. Diamond* **2021**, *1*, 150–159.
- [64] Wallace, P. R. The Band Theory of Graphite. *Phys. Rev.* **1947**, *71*, 622.
- [65] Dass, D. Structural parameters, electronic properties, and band gaps of a single walled carbon nanotube: A pz orbital tight binding study. *Superlattices and Microstructures* **2018**, *120*, 108–126.
- [66] Bostwick, A.; Ohta, T.; McChesney, J. L.; Seyller, T.; Horn, K.; Rotenberg, E. Band structure and many body effects in graphene. *Eur. Phys. J. Spec. Top.* **2007**, *148*, 5–13.
- [67] Singlet-Triplet Energy Gaps for Diradicals from Fractional-Spin Density-Functional Theory. *J. Phys. Chem. A* **2010**, *115*, 76–83.
- [68] Ziegler, T.; Rauk, A.; Baerends, E. J. On the calculation of multiplet energies by the hartree-fock-slater method. *Theor. Chim. Acta* **1977**, *43*, 261–271.
- [69] Ess, D. H.; Cook, T. C. Unrestricted prescriptions for open-shell singlet diradicals: Using economical Ab initio and density functional theory to calculate singlet-triplet gaps and bond dissociation curves. *Journal of Physical Chemistry A* **2012**, *116*.
- [70] Saito, T.; Nishihara, S.; Yamanaka, S.; Kitagawa, Y.; Kawakami, T.; Yamada, S.; Isobe, H.; Okumura, M.; Yamaguchi, K. Singlet-triplet energy gap for trimethylenemethane, oxyallyl diradical, and related species: Single- and multireference computational results. *Theoretical Chemistry Accounts* **2011**, *130*.
- [71] Heyd, J.; Scuseria, G. E.; Ernzerhof, M. Hybrid functionals based on a screened Coulomb potential. *Journal of Chemical Physics* **2003**, *118*.
- [72] Heyd, J.; Scuseria, G. E. Efficient hybrid density functional calculations in solids: Assessment of the Heyd-Scuseria-Ernzerhof screened Coulomb hybrid functional. *Journal of Chemical Physics* **2004**, *121*.
- [73] Heyd, J.; Scuseria, G. E.; Ernzerhof, M. Erratum: “Hybrid functionals based on a screened Coulomb potential” [J. Chem. Phys.118, 8207 (2003)]. *J. Chem. Phys.* **2006**, *124*.
- [74] Hait, D.; Head-Gordon, M. Orbital Optimized Density Functional Theory for Electronic Excited States. *J. Phys. Chem. Lett.* **2021**, *12*, 4517–4529.

## 3.10 Supporting Information

### 3.10.1 Methodology

#### 3.10.1.1 Description of Unrestricted Kohn Sham (UKS)

In the unrestricted Kohn-Sham (UKS) method, molecular orbital coefficients for different spins are optimized independently. The equations below describe the UKS methods. Here, spin-up molecular orbitals are denoted with Greek letter  $\alpha$  and spin-down electron are denoted with Greek letter  $\beta$ . Greek letter  $\tau$  is used to denote a general spin index. Equation numbers for the UKS method below correspond to the analogous equations for the restricted closed-shell Kohn-Sham DFT described in the main text. No definitions are given here since all quantities are already defined in the main text.

$$\begin{aligned}\Omega &\equiv E + \Omega_p \\ \Omega_p &\equiv -C_p \sum_{\tau=\alpha}^{\beta} \text{ln det}[\sigma^\tau (\sigma_d^\tau)^{-1}]\end{aligned}\quad (3.20)$$

$$\phi_i^\tau(\mathbf{r}) = \sum_{\mu}^B \chi_{\mu}(\mathbf{r}) T_{\mu i}^\tau \quad (3.21)$$

$$\sigma_{ij}^\tau = \sum_{\mu\nu}^B T_{\mu i}^\tau S_{\mu\nu} T_{\nu j}^\tau \quad (3.22)$$

$$P_{\mu\nu}^\tau = \sum_{ij}^{N_\tau} T_{\mu i}^\tau [(\sigma^\tau)^{-1}]_{ij} T_{\nu j}^\tau \quad (3.23)$$

$$E = \sum_{\tau=\alpha}^{\beta} \sum_{\mu\nu}^N F_{\mu\nu}^\tau P_{\nu\mu}^\tau - \frac{1}{2} \int \int \frac{\rho(\mathbf{r})\rho(\mathbf{r}')}{|\mathbf{r}-\mathbf{r}'|} d\mathbf{r}d\mathbf{r}' + E_{xc} - \int v_{XC}(\mathbf{r})\rho(\mathbf{r})d\mathbf{r} \quad (3.24)$$

$$\begin{aligned}\rho(\mathbf{r}) &= \rho^\alpha(\mathbf{r}) + \rho^\beta(\mathbf{r}) \\ \rho^\tau(\mathbf{r}) &= \sum_{ij=1}^N \phi_i^{\tau*}(\mathbf{r}) [(\sigma^\tau)^{-1}]_{ij} \phi_j^\tau(\mathbf{r}) = \sum_{\mu\nu=1}^B \chi_{\mu}^*(\mathbf{r}) P_{\mu\nu}^\tau \chi_{\nu}(\mathbf{r})\end{aligned}\quad (3.25)$$

$$G_{\mu i}^{\tau E} \equiv \frac{\partial E}{\partial T_{\mu i}^{\tau}} = \sum_{\lambda \nu}^B \frac{\partial E}{\partial P_{\lambda \nu}^{\tau}} \frac{\partial P_{\lambda \nu}^{\tau}}{\partial T_{\mu i}^{\tau}} = 2 [(I - SP^{\tau})F^{\tau}T^{\tau}(\sigma^{\tau})^{-1}]_{\mu i} \quad (3.26)$$

$$\begin{aligned} \frac{\partial^2 E}{\partial T_{\nu j}^{\tau} \partial T_{\mu i}^{\tau}} &= \frac{\partial G_{\mu i}^{\tau E}}{\partial T_{\nu j}^{\tau}} = 2 \left\{ [(I - SP^{\tau})F^{\tau}(I - P^{\tau}S)]_{\mu \nu} [(\sigma^{\tau})^{-1}]_{ji} - (S - SP^{\tau}S)_{\mu \nu} [(\sigma^{\tau})^{-1}T^{\tau\dagger}F^{\tau}T^{\tau}(\sigma^{\tau})^{-1}]_{ji} \right\} - \\ &- \left\{ [ST^{\tau}(\sigma^{\tau})^{-1}]_{\mu j} G_{\nu i}^{\tau E} - G_{\mu j}^{\tau E} [ST^{\tau}(\sigma^{\tau})^{-1}]_{\nu i} \right\} + 2 \sum_{\lambda \gamma}^B (I - SP^{\tau})_{\mu \lambda} \frac{\partial F_{\lambda \gamma}^{\tau}}{\partial T_{\nu j}^{\tau}} [T^{\tau}(\sigma^{\tau})^{-1}]_{\gamma i} \end{aligned} \quad (3.27)$$

$$G_{\mu i}^{\tau P} \equiv \frac{\partial \Omega_p}{\partial T_{\mu i}^{\tau}} = -2C_p \{ ST^{\tau}[(\sigma^{\tau})^{-1} - (\sigma_d^{\tau})^{-1}] \}_{\mu i} \quad (3.28)$$

$$\begin{aligned} \frac{\partial^2 \Omega_p}{\partial T_{\nu j}^{\tau} \partial T_{\mu i}^{\tau}} &= \frac{\partial G_{\mu i}^{\tau P}}{\partial T_{\nu j}^{\tau}} = -2C_p \{ (S - SP^{\tau}S)_{\mu \nu} [(\sigma^{\tau})^{-1}]_{ji} - [ST^{\tau}(\sigma^{\tau})^{-1}]_{\mu j} [ST^{\tau}(\sigma^{\tau})^{-1}]_{\nu i} - \\ &- \delta_{ij} S_{\mu \nu} [(\sigma_d^{\tau})^{-1}]_{ii} + 2\delta_{ij} [ST^{\tau}(\sigma_d^{\tau})^{-1}]_{\mu i} [ST^{\tau}(\sigma_d^{\tau})^{-1}]_{\nu i} \} \end{aligned} \quad (3.29)$$

$$\frac{\partial^2 E}{\partial T_{\nu j}^{\tau} \partial T_{\mu i}^{\tau}} \approx 2 \left\{ (Q^{\tau\dagger}F^{\tau}Q^{\tau})_{\mu \nu} [(\sigma^{\tau})^{-1}]_{ji} - (Q^{\tau\dagger}SQ^{\tau})_{\mu \nu} [(\sigma^{\tau})^{-1}T^{\tau\dagger}F^{\tau}T^{\tau}(\sigma^{\tau})^{-1}]_{ji} \right\} \quad (3.30)$$

$$Q^{\tau} \equiv (I - P^{\tau}S)$$

$$H_{\mu \nu}^{\tau} = 2 \left[ \left( Q^{\tau\dagger}F^{\tau}Q^{\tau} \right)_{\mu \nu} + |\varepsilon_{\text{HOMO}}^{\tau}| \left( Q^{\tau\dagger}SQ^{\tau} \right)_{\mu \nu} \right] \quad (3.31)$$

$$H_{\mu \nu}^{\tau} = 2 \left[ (1 - \varepsilon/|\varepsilon_{\text{HOMO}}^{\tau}|) \left( A^{\tau\dagger}F^{\tau}A^{\tau} \right)_{\mu \nu} + \varepsilon \left( D^{\tau\dagger}SD^{\tau} \right)_{\mu \nu} \right] \quad (3.32)$$

### 3.10.1.2 Description of Restricted Open-Shell Optimization (ROSO)

To implement ROSO, the main variational parameters are organized as matrices  $\Theta^D$ ,  $\Theta^{\alpha}$ , and  $\Theta^{\beta}$  that represent expansion coefficients of doubly-occupied molecular orbitals,  $\alpha$  singly-occupied

orbitals, and  $\beta$  singly-occupied orbitals, respectively. Molecular orbital coefficients matrices are then obtained as a straightforward union of the parameter matrices:

$$\begin{aligned} T^\alpha &= \Theta^D \cup \Theta^\alpha \\ T^\beta &= \Theta^D \cup \Theta^\beta \end{aligned} \tag{3.33}$$

The optimization of the variational parameters  $\Theta^D$  proceeds using the restricted closed-shell expressions for the gradient and preconditioner (see main text) for the doubly-occupied orbitals. For the independent variables that describe singly-occupied orbitals ( $\Theta^\alpha$  and  $\Theta^\beta$ ), the UKS expressions shown in the preceding section are used for the gradient and preconditioner:

$$\begin{aligned} \frac{\partial \Omega}{\partial \Theta_{\mu i}^D} &= \frac{\partial \Omega}{\partial T_{\mu i}} \\ \frac{\partial \Omega}{\partial \Theta_{\mu i}^\tau} &= \frac{\partial \Omega}{\partial T_{\mu i}^\tau} \end{aligned} \tag{3.34}$$

### 3.10.1.3 Description of Restricted Open-Shell Kohn Sham (ROKS)

Independent electronic variables  $\Theta^D$ ,  $\Theta^\alpha$  and  $\Theta^\beta$  introduced above can also be used in the variable-metric ROKS optimization. However, there is an additional step necessary in the ROKS optimization, when the independent variables are converted to molecular orbital coefficients. In the VM ROKS optimization, the energy of the triplet state is invariant to the mixing of the two singly occupied orbitals (Figure 3.10). This is not true for the energy of the mixed state because the two singly-occupied orbitals belong to two different subspaces:  $\alpha$  and  $\beta$ . Because of this broken invariance, the singly-occupied orbitals will tend to pair up in the mixed state if the pairing process lowers  $E_{mix}$ , which is true for most systems. The accompanying energy lowering can be counterbalanced by the penalty term, but only for sufficiently large values of the penalty strength  $C_p$ . However, we prefer to preserve the convenient (but not strictly necessary) property of the

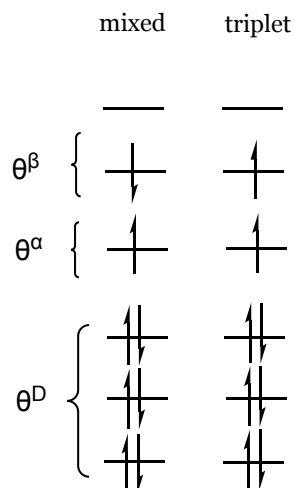


Figure 3.10: An illustrative example of the two Slater determinants that are used to describe a singlet diradical state.

independence between the energy and penalty minimization and, therefore, chose to solve the undesirable pairing of electrons by enforcing strict orthogonality between the two singly-occupied orbitals in the ROKS optimization. To this end, the  $\Theta^\alpha$  orbital is projected out from the  $\Theta^\beta$  orbital to obtain the projected  $\bar{\Theta}^\beta$  orbital

$$\bar{\Theta}^\beta = \Theta^\beta - P^\alpha S \Theta^\beta \quad (3.35)$$

where  $P^\alpha$  is the projector to the (one-dimensional) subspace of the singly-occupied  $\alpha$  orbital

$$P^\alpha = \Theta^\alpha (\Theta^{\alpha\dagger} S \Theta^\alpha)^{-1} \Theta^{\alpha\dagger} \quad (3.36)$$

It is the projected orbital  $\bar{\Theta}^\beta$  that is then used to construct the matrices of molecular orbital coefficients for the mixed Slater determinant (Figure 3.10)

$$\begin{aligned} T_{mix}^\alpha &= \Theta^D \cup \Theta^\alpha \\ T_{mix}^\beta &= \Theta^D \cup \bar{\Theta}^\beta \end{aligned} \quad (3.37)$$

The coefficient matrices  $T$  for the triplet state can be constructed by flipping the spin of the electron in the  $\Theta^\beta$  orbital. Since  $E_{triplet}$  is invariant to the mixing of singly-occupied orbitals, we chose to

use unprojected  $\Theta^\beta$  to represent molecular orbitals of the triplet state:

$$\begin{aligned} T_{triplet}^\alpha &= \Theta^D \cup \Theta^\alpha \cup \Theta^\beta \\ T_{triplet}^\beta &= \Theta^D \end{aligned} \quad (3.38)$$

The gradient expression for  $E_{mix}$  with respect to variational parameters  $\Theta^\alpha$  and  $\Theta^\beta$  must be modified to take into account the dependence of  $\bar{\Theta}^\beta$  on both of these parameters. This can be achieved applying the chain rule during the differentiation:

$$\begin{aligned} \frac{\partial E_{mix}}{\partial \Theta_{\mu i}^\alpha} &= \sum_{\lambda j} \frac{\partial E_{mix}}{\partial (T_{mix}^\alpha)_{\lambda j}} \frac{\partial (T_{mix}^\alpha)_{\lambda j}}{\partial \Theta_{\mu i}^\alpha} + \sum_{\lambda j} \frac{\partial E_{mix}}{\partial (T_{mix}^\beta)_{\lambda j}} \frac{\partial (T_{mix}^\beta)_{\lambda j}}{\partial \Theta_{\mu i}^\alpha} = \\ &= \sum_{\lambda j} \frac{\partial E_{mix}}{\partial (T_{mix}^\alpha)_{\lambda j}} \delta_{\lambda \mu} \delta_{i j} + \sum_{\lambda j} \frac{\partial E_{mix}}{\partial (T_{mix}^\beta)_{\lambda j}} \frac{\partial (T_{mix}^\beta)_{\lambda j}}{\partial \Theta_{\mu i}^\alpha} = \\ &= [G^{\alpha E_{mix}}]_{\mu i} + \left[ (I - SP^\alpha) \left( G^{\beta E_{mix}} \Theta^{\beta \dagger} S + S \Theta^\beta G^{\beta E_{mix} \dagger} \right) \Theta^\alpha (\sigma^\alpha)^{-1} \right]_{\mu i} \end{aligned} \quad (3.39)$$

$$\begin{aligned} \frac{\partial E_{mix}}{\partial \Theta_{\mu i}^\beta} &= \sum_{\lambda j} \frac{\partial E_{mix}}{\partial (T_{mix}^\alpha)_{\lambda j}} \frac{\partial (T_{mix}^\alpha)_{\lambda j}}{\partial \Theta_{\mu i}^\beta} + \sum_{\lambda j} \frac{\partial E_{mix}}{\partial (T_{mix}^\beta)_{\lambda j}} \frac{\partial (T_{mix}^\beta)_{\lambda j}}{\partial \Theta_{\mu i}^\beta} \\ &= \left[ (I - SP^\alpha) G^{\beta E_{mix}} \right]_{\mu i} \end{aligned} \quad (3.40)$$

where  $[G^{\tau E_{mix}}]_{\mu i} = \frac{\partial E_{mix}}{\partial T_{\mu i}^\tau}$  is the energy gradient expression derived for unprojected orbitals in Eq. (3.26).

Test systems	Default value	Non-default value
Graphite	$QFQ + S$	$F + S$
Armchair SWCNT	$QFQ + S$	$F + S$
Zigzag SWCNT	$\varepsilon = 0.5$ a.u.	$\varepsilon = 0.65$ a.u.
Graphene	$N = 4$	$N = 1$

Table 3.3: Non-default settings used for several test systems. Notation is defined in Table 1. Preconditioner  $QFQ + S$  is a shorthand for  $A = Q$  and  $D = I$ . Preconditioner  $F + S$  is a shorthand for  $A = D = I$ .

## 3.10.2 Derivation of the Equations for the Closed-Shell Case

### 3.10.2.1 Energy derivatives

The energy gradient equation for the closed-shell system was derived by differentiating the DFT energy functional with respect to orbital coefficients  $T_{\mu i}$  using the chain rule. The chain rule allows to re-write the derivative respect to orbital coefficients as the derivative with respect to the projector onto the occupied space and use the fact that the latter is equal to the Kohn-Sham Hamiltonian. Note that, in the summation limits,  $N$  denotes the number of doubly occupied molecular orbitals, whereas  $B$  indicates the number of the basis set functions.

$$\begin{aligned}
G_{\mu i}^E &\equiv \frac{\partial E}{\partial T_{\mu i}} = \sum_{\lambda \nu}^B \frac{\partial E}{\partial P_{\lambda \nu}} \frac{\partial P_{\lambda \nu}}{\partial T_{\mu i}} = \sum_{\lambda \nu}^B 2F_{\nu \lambda} \frac{\partial P_{\lambda \nu}}{\partial T_{\mu i}} = 2 \sum_{\lambda \nu}^B F_{\nu \lambda} \frac{\partial [\sum_{kj}^N T_{\lambda j}(\sigma^{-1})_{jk} T_{\nu k}]}{\partial T_{\mu i}} = \\
&= 2 \sum_{\lambda \nu}^B F_{\nu \lambda} \left\{ \sum_{kj}^N \frac{\partial T_{\lambda j}(\sigma^{-1})_{jk} T_{\nu k}}{\partial T_{\mu i}} + \sum_{kj}^N T_{\lambda j} \frac{\partial (\sigma^{-1})_{jk}}{\partial T_{\mu i}} T_{\nu k} + \sum_{kj}^N T_{\lambda j}(\sigma^{-1})_{jk} \frac{\partial T_{\nu k}}{\partial T_{\mu i}} \right\} = \\
&= 2 \sum_{\lambda \nu}^B F_{\nu \lambda} \left\{ \sum_{kj}^N \delta_{\lambda \mu} \delta_{ji} (\sigma^{-1})_{jk} T_{\nu k} - \sum_{kjl m}^N T_{\lambda j} [(\sigma^{-1})_{jl} \frac{\partial \sigma_{lm}}{\partial T_{\mu i}} (\sigma^{-1})_{mk}] T_{\nu k} + \sum_{kj}^N T_{\lambda j}(\sigma^{-1})_{jk} \delta_{\nu \mu} \delta_{ki} \right\} = \\
&= 2 \left\{ \sum_{\nu}^B \sum_k^N F_{\nu \mu} (\sigma^{-1})_{ik} T_{\nu k} - \sum_{\lambda \nu}^B \sum_{kjl m}^N F_{\nu \lambda} T_{\lambda j} (\sigma^{-1})_{jl} \sum_{\alpha \beta}^B \frac{\partial (T_{\alpha l} S_{\alpha \beta} T_{\beta m})}{\partial T_{\mu i}} (\sigma^{-1})_{mk} T_{\nu k} + \sum_{\lambda}^B \sum_j^N F_{\mu \lambda} T_{\lambda j} (\sigma^{-1})_{ji} \right\} = \\
&= 2 \left\{ (FT \sigma^{-1})_{\mu i} - \sum_{\nu \alpha \beta}^B \sum_{klm}^N (FT \sigma^{-1})_{\nu l} [\delta_{\alpha \mu} \delta_{li} S_{\alpha \beta} T_{\beta m} + T_{\alpha l} S_{\alpha \beta} \delta_{\beta \mu} \delta_{mi}] (\sigma^{-1})_{mk} T_{\nu k} + (FT \sigma^{-1})_{\mu i} \right\} = \\
&= 2 \left\{ (FT \sigma^{-1})_{\mu i} - \sum_{\nu \beta}^B \sum_{km}^N (FT \sigma^{-1})_{\nu i} S_{\mu \beta} T_{\beta m} (\sigma^{-1})_{mk} T_{\nu k} + \sum_{\nu \alpha}^B \sum_k^N (FT \sigma^{-1})_{\nu i} T_{\alpha i} S_{\alpha \mu} (\sigma^{-1})_{ik} T_{\nu k} + (FT \sigma^{-1})_{\mu i} \right\} = \\
&= 4 (FT \sigma^{-1})_{\mu i} - 2 \left\{ \sum_{\nu}^B (FT \sigma^{-1})_{\nu i} \left[ \sum_{\beta}^B S_{\mu \beta} P_{\beta \nu} + \sum_{\alpha}^B S_{\mu \alpha} P_{\alpha \nu} \right] \right\} = \\
&= 4 (FT \sigma^{-1})_{\mu i} - 2 \sum_{\nu}^B 2 (SP)_{\mu \nu} (FT \sigma^{-1})_{\nu i} = \\
&= 4 (FT \sigma^{-1})_{\mu i} - 4 [SP (FT \sigma^{-1})]_{\mu i} = \\
&= 4 [(I - SP) FT \sigma^{-1}]_{\mu i}
\end{aligned} \tag{3.41}$$

### 3.10.2.2 Penalty derivatives

The first derivative of the penalty term is evaluated as:

$$\begin{aligned}
G_{\mu i}^P &= \frac{\partial \Omega_p}{\partial T_{\mu i}} = -2C_p \frac{\partial \ln[\det(\sigma \sigma_d^{-1})]}{\partial T_{\mu i}} = \\
&= -2C_p \frac{1}{\det(\sigma \sigma_d^{-1})} \frac{\partial [\det(\sigma) \det(\sigma_d^{-1})]}{\partial T_{\mu i}} = \\
&= -2C_p \frac{1}{\det(\sigma \sigma_d^{-1})} \left[ \frac{\partial \det(\sigma)}{\partial T_{\mu i}} \det(\sigma_d^{-1}) + \det(\sigma) \frac{\partial [\det(\sigma_d)]^{-1}}{\partial \det(\sigma_d)} \frac{\partial \det(\sigma_d)}{\partial T_{\mu i}} \right] = \\
&= -2C_p \left[ \frac{1}{\det(\sigma)} \frac{\partial \det(\sigma)}{\partial T_{\mu i}} - \frac{1}{\det(\sigma_d)} \frac{\partial \det(\sigma_d)}{\partial T_{\mu i}} \right]
\end{aligned} \tag{3.42}$$

Find the derivative of the determinant of the orbital overlap

$$\begin{aligned}
\frac{\partial \det(\sigma)}{\partial T_{\mu i}} &= \det(\sigma) \sum_{jk} (\sigma^{-1})_{jk} \frac{\partial \sigma_{jk}}{\partial T_{\mu i}} = \\
&= \det(\sigma) \sum_{jk} (\sigma^{-1})_{jk} \frac{\partial (\sum_{\alpha\lambda} T_{\lambda j} S_{\lambda\alpha} T_{\alpha k})}{\partial T_{\mu i}} = \\
&= \det(\sigma) \sum_{jk} (\sigma^{-1})_{jk} \left( \sum_{\alpha\lambda} \frac{\partial T_{\lambda j}}{T_{\mu i}} S_{\lambda\alpha} T_{\alpha k} + \sum_{\alpha\lambda} T_{\lambda j} S_{\lambda\alpha} \frac{\partial T_{\alpha k}}{T_{\mu i}} \right) = \\
&= \det(\sigma) \sum_{jk} (\sigma^{-1})_{jk} \left( \sum_{\alpha\lambda} \delta_{\lambda\mu} \delta_{ji} S_{\lambda\alpha} T_{\alpha k} + \sum_{\alpha\lambda} T_{\lambda j} S_{\lambda\alpha} \delta_{\alpha\mu} \delta_{ki} \right) = \\
&= \det(\sigma) \left[ \sum_k (\sigma^{-1})_{ik} (ST)_{\mu k} + \sum_j (\sigma^{-1})_{ij} (T^\dagger S)_{j\mu} \right] = \\
&= \det(\sigma) [(ST\sigma^{-1})_{\mu i} + (\sigma^{-1}T^\dagger S)_{i\mu}] = \\
&= 2 \det(\sigma) (ST\sigma^{-1})_{\mu i}
\end{aligned} \tag{3.43}$$

The last equality uses the fact that  $(ST\sigma^{-1})_{\mu i} = (\sigma^{-1}T^\dagger S)_{i\mu}$ . The second term can be obtained using the result for the first term:

$$\frac{\partial \det(\sigma_d)}{\partial T_{\mu i}} = 2 \det(\sigma_d) (ST\sigma_d^{-1})_{\mu i} \tag{3.44}$$

Using these results the first derivative of the penalty term is

$$G_{\mu i}^P = -4C_p [ST(\sigma^{-1} - \sigma_d^{-1})]_{\mu i} \tag{3.45}$$

The second derivative of the penalty term can be obtained by the straightforward differentiation of the gradient

$$\begin{aligned}
\frac{\partial^2 \Omega_p}{\partial T_{\nu j} \partial T_{\mu i}} &= \frac{\partial G_{\mu i}^P}{\partial T_{\nu j}} = -4C_p \frac{\partial [ST(\sigma^{-1} - \sigma_d^{-1})]_{\mu i}}{\partial T_{\nu j}} = \\
&= -4C_p \left[ \frac{\partial (ST\sigma^{-1})_{\mu i}}{\partial T_{\nu j}} - \frac{\partial (ST\sigma_d^{-1})_{\mu i}}{\partial T_{\nu j}} \right]
\end{aligned} \tag{3.46}$$

Derivative the first term inside the bracket  $\frac{\partial (ST\sigma^{-1})_{\mu i}}{\partial T_{\nu j}}$  is:

$$\begin{aligned}
\frac{\partial(ST\sigma^{-1})_{\mu i}}{\partial T_{\nu j}} &= \frac{\partial \sum_{\lambda}^B \sum_k^N S_{\mu\lambda} T_{\lambda k} (\sigma^{-1})_{ki}}{\partial T_{\nu j}} = \\
&= \sum_{\lambda}^B \sum_k^N S_{\mu\lambda} \delta_{\lambda\nu} \delta_{kj} (\sigma^{-1})_{ki} + \sum_{\lambda}^B \sum_k^N S_{\mu\lambda} T_{\lambda k} \frac{\partial (\sigma^{-1})_{ki}}{\partial T_{\nu j}} = \\
&= S_{\mu\nu} (\sigma^{-1})_{ji} - \sum_{\lambda}^B \sum_{klm}^N S_{\mu\lambda} T_{\lambda k} (\sigma^{-1})_{kl} \frac{\partial \sigma_{lm}}{\partial T_{\nu j}} (\sigma^{-1})_{mi} = \\
&= S_{\mu\nu} (\sigma^{-1})_{ji} - \sum_{\varepsilon\omega}^B \sum_{lm}^N (ST\sigma^{-1})_{\mu l} \frac{\partial T_{\varepsilon l} S_{\varepsilon\omega} T_{\omega m}}{\partial T_{\nu j}} (\sigma^{-1})_{mi} = \\
&= S_{\mu\nu} (\sigma^{-1})_{ji} - \sum_{\varepsilon\omega}^B \sum_{lm}^N (ST\sigma^{-1})_{\mu l} [\delta_{\varepsilon\nu} \delta_{lj} S_{\varepsilon\omega} T_{\omega m} + T_{\varepsilon l} S_{\varepsilon\omega} \delta_{\omega\nu} \delta_{mj}] (\sigma^{-1})_{mi} = \\
&= S_{\mu\nu} (\sigma^{-1})_{ji} - (ST\sigma^{-1})_{\mu j} (ST\sigma^{-1})_{\nu i} - (ST\sigma^{-1} T^{\dagger} S)_{\mu\nu} (\sigma^{-1})_{ji} = \\
&= S_{\mu\nu} (\sigma^{-1})_{ji} - (ST\sigma^{-1})_{\mu j} (ST\sigma^{-1})_{\nu i} - (SPS)_{\mu\nu} (\sigma^{-1})_{ji} = \\
&= (S - SPS)_{\mu\nu} (\sigma^{-1})_{ji} - (ST\sigma^{-1})_{\mu j} (ST\sigma^{-1})_{\nu i}
\end{aligned} \tag{3.47}$$

The second term can be obtained in the same manner:

$$\begin{aligned}
\frac{\partial(ST\sigma_d^{-1})_{\mu i}}{\partial T_{\nu j}} &= \frac{\partial \sum_{\lambda} S_{\mu\lambda} T_{\lambda i} (\sigma_d^{-1})_{ii}}{\partial T_{\nu j}} = \\
&= \sum_{\lambda} S_{\mu\lambda} \delta_{\lambda\nu} \delta_{ij} (\sigma_d^{-1})_{ii} + (ST)_{\mu i} \frac{\partial (\sigma_d^{-1})_{ii}}{\partial T_{\nu j}} = \\
&= \delta_{ij} S_{\mu\nu} (\sigma_d^{-1})_{ii} - (ST)_{\mu i} (\sigma_d^{-2})_{ii} \frac{\partial (\sigma_d)_{ii}}{\partial T_{\nu j}} = \\
&= \delta_{ij} S_{\mu\nu} (\sigma_d^{-1})_{ii} - (ST)_{\mu i} (\sigma_d^{-2})_{ii} \frac{\partial \sum_{\varepsilon\gamma} T_{\varepsilon i} S_{\varepsilon\gamma} T_{\gamma i}}{\partial T_{\nu j}} = \\
&= \delta_{ij} S_{\mu\nu} (\sigma_d^{-1})_{ii} - (ST)_{\mu i} (\sigma_d^{-2})_{ii} \sum_{\varepsilon\gamma} [\delta_{\varepsilon\nu} \delta_{ij} S_{\varepsilon\gamma} T_{\gamma i} + T_{\varepsilon i} S_{\varepsilon\gamma} \delta_{\gamma\nu} \delta_{ij}] = \\
&= \delta_{ij} S_{\mu\nu} (\sigma_d^{-1})_{ii} - (ST)_{\mu i} (\sigma_d^{-2})_{ii} [\delta_{ij} (ST)_{\nu i} + (T^{\dagger} S)_{i\nu} \delta_{ij}] = \\
&= \delta_{ij} S_{\mu\nu} (\sigma_d^{-1})_{ii} - (ST)_{\mu i} (\sigma_d^{-2})_{ii} 2\delta_{ij} (ST)_{\nu i} = \\
&= \delta_{ij} S_{\mu\nu} (\sigma_d^{-1})_{ii} - 2\delta_{ij} (ST\sigma_d^{-1})_{\mu i} (ST\sigma_d^{-1})_{\nu i}
\end{aligned} \tag{3.48}$$

Combining the results for both terms, the final expression for the second derivative is obtained:

$$\begin{aligned}
\frac{\partial^2 \Omega_p}{\partial T_{vj} \partial T_{\mu i}} = & -4C_p [(S - SPS)_{\mu\nu} (\sigma^{-1})_{ji} - \\
& - (ST \sigma^{-1})_{\mu j} (ST \sigma^{-1})_{vi} - \\
& - \delta_{ij} S_{\mu\nu} (\sigma_d^{-1})_{ii} + 2\delta_{ij} (ST \sigma_d^{-1})_{\mu i} (ST \sigma_d^{-1})_{vi}]
\end{aligned} \tag{3.49}$$

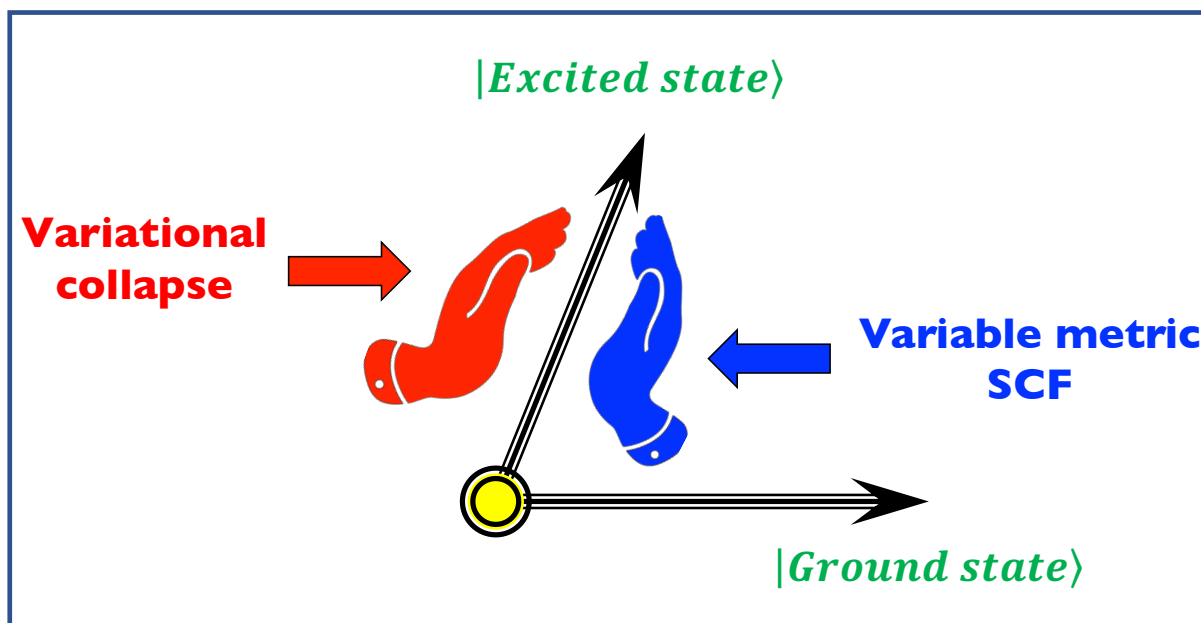
## Chapter 4

---

# Direct unconstrained optimization of excited states in density functional theory

---

### 4.1 Preface



Accurately understanding and describing excited electronic states is crucial for predicting the

properties of materials and molecular systems. Building on the direct unconstrained optimization approach for ground states discussed in Chapter 3, Chapter 4 introduces a variable-metric time-independent DFT (VM TIDFT) method to address the challenge of variational collapse in excited-state optimization.

This chapter is reproduced from a manuscript prepared for publication: **Pham, H. D. M., Khaliullin, R. Z.** Direct unconstrained optimization of excited states in density functional theory.

## 4.2 Abstract

Orbital-optimized density functional theory (DFT) has emerged as an alternative to time-dependent (TD) DFT capable of describing difficult excited states with significant electron density redistribution, such as charge-transfer, Rydberg, and double-electron excitations. Here, a simple method is developed to solve the main problem of the excited-state optimization – the variational collapse of the excited states onto the ground state. In this method, called variable-metric time-independent DFT (VM TIDFT), the electronic states are allowed to be nonorthogonal during the optimization but their orthogonality is gradually enforced with a continuous penalty function. With nonorthogonal electronic states, VM TIDFT can use molecular orbital coefficients as independent variables, which results in a closed-form analytical expression for the gradient and allows to employ any of the multiple unconstrained optimization algorithms that guarantees convergence of the excited-state optimization. Numerical tests on multiple molecular systems show that the variable-metric optimization of excited states performed with a preconditioned conjugate gradient algorithm is robust and produces accurate energies for well-behaved excitations and, unlike TDDFT, for more challenging charge-transfer and double-electron excitations.

### 4.3 Introduction

Excited electronic states play a crucial role in photophysics and photochemistry<sup>1-3</sup>. Theoretical and computational characterization of excited states is essential, not only from a fundamental science perspective but also for designing better photovoltaic, photocatalytic, and lighting materials. One of the most popular methods to describe excited states is time-dependent (TD) density functional theory (TDDFT), which is an extension of the ground-state Kohn-Sham (KS) density functional theory (DFT). TDDFT calculates excited state properties by analyzing the response of the ground-state density to time-dependent perturbations, such as an external electric field<sup>4</sup>. Although TDDFT is, in principle, exact<sup>5</sup>, it has multiple limitations that arise from its reliance on time-independent ground state XC functionals<sup>4</sup>. Consequently, TDDFT cannot describe double- and higher-electron excitations and struggles with excitations producing significant changes of the electron density distribution, such as long-range charge transfer states, Rydberg states, and core excitations<sup>6,7</sup>.

To address the limitations of TDDFT, a variety of orbital optimized (OO) DFT methods have been developed. In these methods, the ground-state DFT formalism is applied to optimize orbitals variationally not only for the ground state but also for the excited states. To contrast this approach to TDDFT, it has been referred to as time-independent DFT (TIDFT)<sup>8-11</sup>.  $\Delta$ SCF is another commonly used name for this approach<sup>12-17</sup> which emphasizes that the excitation energies are computed as the energy difference between self-consistent-field (SCF) calculations. The variational treatment of the excited states yields excellent results, comparable to those obtained with TDDFT for well-behaved excited states and superior for charge-transfer (CT) and multi-electron excitations<sup>18-24</sup>. Another advantage of using the ground-state formalism for excited states is that numerous techniques developed over several decades for KS DFT can be applied to excited states. For example, the

implicit solvation models employed in ground states calculations can be readily used for excited states<sup>25,26</sup>.

While the effort to establish a solid theoretical foundation for the excited-state OODFT methods is underway<sup>8-11,17</sup>, the most significant practical challenge in designing efficient OODFT methods is ensuring that the variational optimization converges to the correct excited state rather than collapsing back to the ground state<sup>24</sup>. There has been a number of methods proposed to avoid variational collapse of high-energy excited states to the states with lower energies<sup>27-44</sup>.

These methods have been recently reviewed<sup>6,30,45,46</sup> and only a brief description of some of them is presented here.

In the maximum overlap method (MOM)<sup>28</sup> and initial maximum overlap method (IMOM)<sup>47,48</sup>, the electrons are first promoted from the fully optimized ground-state occupied MOs to virtual MOs to generate the initial guess for an excited state. The newly selected occupied MOs are then optimized in the SCF procedure, in each step of which the list of occupied orbitals is updated using a non-aufbau population principle. In IMOM, the occupied orbitals are updated to maximize their overlap with the initial guess, whereas, in MOM, the orbitals are updated to produce maximum overlap with the orbitals in the previous SCF step. By maximizing the overlap with high-lying orbitals, MOM and IMOM prevent variational collapse to the ground state, guiding the SCF process toward the nearest excited state solution. Although both methods work well for multiple systems, MOM cannot always prevent variational collapse, as orbitals can drift to the ground state over multiple steps<sup>47-49</sup>. While this issue is addressed in IMOM, the latter exhibits its own convergence problems when multiple orbital selections have similar overlaps, which produces oscillatory non-convergent behavior<sup>37,38</sup>.

An alternative approach to prevent variational collapse is to constrain the KS determinant of

an excited state to be orthogonal to that of the ground state. In practice, orthogonality-constrained DFT (OCDFT)<sup>44</sup> recasts the optimization problem as a solution to modified eigenvector equations and imposes this constraint by projecting out a single “hole” orbital from the KS Hamiltonian. Unfortunately, the iterative solution of eigenvector problems is not guaranteed to converge. Furthermore, the projector-based formalism of OCDFT makes its extension to multiple excited states cumbersome.

To improve the rate of convergence, several direct minimization algorithms have been developed. For example, the ground-state geometric direct minimization (GDM) approach<sup>50</sup> has been extended to optimize excited states with the IMOM orbital-selection criterion applied on each GDM iteration to prevent the collapse<sup>34,35,40,43</sup>. While the combination of GDM and IMOM resolves some of the convergence issues of the original eigensolver-based MOM, the combined method still does not guarantee convergence because the application of the IMOM criterion is introduced as an *ad hoc* update, which can interfere with the GDM optimizer.

Another direct optimization approach is square gradient minimization (SGM)<sup>38</sup>. SGM minimizes the square of the Frobenius norm of the energy gradient instead of minimizing the energy and thereby converts the saddle-point excited-state optimization into the minimization problem, obviating the need in any collapse prevention measures. Despite being superior to MOM-based methods in terms of convergence for difficult problems, SGM has its own shortcomings, as the norm of the gradient is less well conditioned than the energy, typically requiring more iterations to converge for simple cases<sup>38,51</sup>. Furthermore, SGM can become trapped in local minima that are not stationary points of the energy functional<sup>38</sup>.

This work presents a new approach to the variational optimization of excited electronic states, called variable-metric (VM) TIDFT. Like OCDFT, VM TIDFT prevents the variational collapse by

imposing orthogonality constraints between electronic states. Unlike OCDFT, VM TIDFT allows nonorthogonal electronic states in the optimization process but pushes them towards orthogonality with a single continuous penalty function. The key advantage of VM TIDFT is the simplicity of its formalism that allows to relax multiple excited states using molecular orbital coefficients as independent variables in a direct unconstrained minimization that guarantees convergence of the SCF procedure. VM optimization has been designed specifically to prevent collapse of non-orthogonal wavefunctions and has been previously applied to improve localization of occupied and virtual orbitals<sup>52,53</sup> and to simplify the ground-state SCF procedure<sup>54</sup>.

## 4.4 Methodology

### 4.4.1 Theory

In our notation, capital Latin letters ( $I, J, K, \dots$ ) denote electronic states, lowercase Latin letters ( $i, j, k, \dots$ ) denote occupied molecular orbitals, and lowercase Greek letters ( $\mu, \nu, \gamma, \lambda, \dots$ ) represent basis set functions. Additionally, Greek letters  $\alpha$  and  $\beta$  are reserved for spin-up and spin-down electrons, respectively, whereas the symbol  $\tau$  denotes a general spin state.

The unrestricted VM TIDFT formalism presented here optimizes  $\alpha$  and  $\beta$  orbitals independently to take into account the open-shell nature of excited states. However, restricted closed-shell (RKS), restricted-open shell (ROSO), and spin-purified restricted open-shell Kohn-Sham (ROKS)<sup>55,56</sup> optimization of excited states can also be performed as described previously for the ground state<sup>54</sup>.

The optimization of multiple excited states is performed state-by-state. The loss functional minimized in the VM TIDFT procedure for electronic state  $I$  is a sum of the *intrastate* term  $\mathcal{E}^I$  and

the *interstate* penalty term  $\Omega_P$

$$\Omega = \mathcal{E}^I + \Omega_P \quad (4.1)$$

The intrastate term includes  $E^I$  the energy of state  $I$  and the intrastate penalty that ensures linear independence of MOs of state  $I$

$$\mathcal{E}^I = E^I - c_p^I \sum_{\tau=\alpha,\beta} \ln \det(\sigma_{II\tau} \sigma_{II\tau d}^{-1}) \quad (4.2)$$

where  $\sigma_{II\tau}$  is the overlap matrix for the occupied orbitals of spin  $\tau$ , and  $\sigma_{II\tau d}$  is its diagonal part. The intrastate term was described in our previous treatment of the simple ground-state orbital optimization method<sup>54</sup>.

The interstate term is designed to keep different electronic states orthogonal to each other

$$\Omega_P = -C_P \sum_{\tau=\alpha,\beta} \ln \det(\Phi_\tau \Phi_{\tau d}^{-1}) \quad (4.3)$$

In the state-by-state optimization, the orthogonality penalty is imposed between the currently optimized state and all previously optimized states. The key element of the penalty is  $\Phi_\tau$  – the overlap matrix between electronic states.  $\Phi_{\tau d}$  is a diagonal matrix containing the elements of  $\Phi_\tau$ . Element  $(\Phi_\tau)_{IJ}$  of the state overlap matrix can be calculated as the determinant of the overlap of MOs that describe states  $I$  and  $J$

$$(\Phi_\tau)_{IJ} = \det(\sigma_{IJ\tau}) \quad (4.4)$$

where the MO overlap matrix of occupied orbitals

$$(\sigma_{IJ\tau})_{ij} = \sum_{\mu\nu}^B T_{\mu i}^{I\tau} S_{\mu\nu} T_{\nu j}^{J\tau} \quad (4.5)$$

is written using coefficients  $T_{\mu i}^{I\tau}$  that represent occupied MOs  $\phi_i^{I\tau}(\mathbf{r})$  in terms of  $B$  basis set functions  $\chi_{\mu}(\mathbf{r})$

$$\phi_i^{I\tau}(\mathbf{r}) = \sum_{\mu}^B \chi_{\mu}(\mathbf{r}) T_{\mu i}^{I\tau} \quad (4.6)$$

Here,  $S_{\mu\nu}$  is the overlap between basis set functions  $\mu$  and  $\nu$

$$S_{\mu\nu} = \int \chi_{\mu}(\mathbf{r}) \chi_{\nu}(\mathbf{r}) d\mathbf{r} \quad (4.7)$$

For non-zero orbitals, the positive determinant in the penalty term in Eq. (4.3) is equal to zero when there is linear dependency between electronic states.  $\Phi_{\tau d}$  is the normalization factor that ensures the determinant in the penalty functional does not exceed 1. The determinant achieves its highest value of 1 only when all electronic states are orthogonal. With  $\det(\Phi_{\tau} \Phi_{\tau d}^{-1})$  always kept in the  $(0, 1]$  interval, the logarithm function  $\Omega_P$  lies in the  $(+\infty, 0]$  interval, making the linearly dependent states and states with orbitals of zero norm inaccessible in the variational procedure, for any  $C_P > 0$ . A similar penalty term has proven effective to prevent orbital collapse during the SCF optimization of ground-state MOs<sup>54</sup> and during the localization of nonorthogonal occupied and virtual orbitals<sup>52,53</sup>.

The key benefit of introducing the interstate penalty term is that it allows to use molecular orbital coefficients – arguably the most natural descriptors of the electronic degrees of freedom – as independent variables in the optimization procedure. As shown below, the expressions for the analytical gradient of the loss functional wrt these variables are very simple and can be written in a closed form, making it easy to use a multitude of well-developed unconstrained optimization algorithms, including conjugate gradient algorithms, quasi-Newton algorithms, or trust-region algorithms<sup>57</sup>.

The gradient of the intrastate term with respect to orbital coefficients is described in our previous work:

$$G_{\mu i}^{I\tau\mathcal{E}} \equiv \frac{\partial \mathcal{E}^I}{\partial T_{\mu i}^{I\tau}} = 2[(I - SP^{I\tau})F^{I\tau}T^{I\tau}(\sigma_{II\tau}^{-1})]_{\mu i} - 2c_p^I[ST^{I\tau}(\sigma_{II\tau}^{-1} - \sigma_{II\tau d}^{-1})]_{\mu i} \quad (4.8)$$

where  $F^{I\tau}$  and  $P^{I\tau}$  are the Kohn-Sham Hamiltonian and density matrices, respectively, for state  $I$  and spin  $\tau$ . The density matrix is evaluated taking into account nonorthogonality of occupied orbitals:

$$P_{\mu\nu}^{I\tau} = \sum_{ij}^{N_\tau} T_{\mu i}^{I\tau}(\sigma_{II\tau}^{-1})_{ij}T_{\nu j}^{I\tau} \quad (4.9)$$

The first derivatives of the interstate penalty term  $\Omega_P$  can also be evaluated analytically and computed readily

$$G_{\mu i}^{I\tau P} \equiv \frac{\partial \Omega_P}{\partial T_{\mu i}^{I\tau}} = -2C_P \left[ \sum_J (\Phi_\tau)_{IJ}^{-1} [ST^{J\tau} \text{adj}(\sigma_{IJ\tau})]_{\mu i} - (ST^{I\tau} \sigma_{II\tau}^{-1})_{\mu i} \right] \quad (4.10)$$

where  $\text{adj}(\sigma_{IJ\tau})$  is the adjugate of the singular or nearly-singular (i.e. ill-conditioned) overlap matrix between orbitals of states  $I$  and  $J$ . This adjugate matrix emerges from differentiating the determinant of the overlap matrix.

## 4.4.2 Optimization Algorithm

In this work, VM TIDFT methods is implemented using the basic preconditioned conjugate gradient (PCG) algorithm for nonlinear problems<sup>58</sup>. To minimize a function, PCG needs only its first derivative (i.e. gradient). Computation of the exact second derivative is not required, but approximate second derivative has been found useful for the construction of accurate preconditioners, which increase the rate of convergence of the PCG algorithm and making it practical.

The analytical gradient of the intrastate term in Eq. (4.8) can be computed efficiently as done in our previous work. However, the analytical gradient of the interstate term requires the evaluation of the lesser known adjugate matrix of  $\sigma_{IJ\tau}$  – the overlap between MOs of two electronic states. Fortunately, the adjugate of a matrix is well-conditioned even if the matrix itself is ill-conditioned<sup>59</sup>. This property is very important in our case because nearly orthogonal electronic states, which are often encountered during the optimization, produce ill-conditioned  $\sigma_{IJ\tau}$ .

Our algorithm for computing the adjugate is designed to avoid ill-conditioned intermediates<sup>59</sup>. It relies on computing the singular value decomposition of the overlap

$$\begin{aligned} \text{adj}(\sigma) &= \text{adj}(UdV^\dagger) = \text{adj}(V^\dagger)\text{adj}(d)\text{adj}(U) = \\ &= \det(V)\det(U)V\text{adj}(d)U^\dagger \end{aligned} \quad (4.11)$$

and then evaluating the adjugate of the diagonal matrix  $d$  using the relation between the co-factor of a matrix and its adjugate

$$[\text{adj}(d)]_{ii} = [C^\dagger]_{ii} = \left[ \prod_{j \neq i} d_{jj} \right]_{ii} \quad (4.12)$$

where  $C$  is the diagonal cofactor matrix of  $d$ . Note that the inversion of singular values is not required in this algorithm, making the algorithm stable for the often encountered ill conditioned matrices.

The preconditioner is constructed by simplifying the second derivative of the loss functional: the interstate term is neglected and the remaining intrastate term is approximated as described in the VM SCF optimization of a single electronic state<sup>54</sup>.

$$H_{\mu\nu}^{I\tau} = 4 \left[ (1 - \kappa) \left( A^{I\tau\dagger} F^{I\tau} A^{I\tau} \right)_{\mu\nu} + \kappa |\epsilon_{\text{HOMO}}| \left( D^{I\tau\dagger} S D^{I\tau} \right)_{\mu\nu} \right] \quad (4.13)$$

where  $\kappa$  is a dimensionless regularization parameter that allows a user to increase the weight of the overlap in case of poor convergence<sup>54</sup>. Matrices  $A^{I\tau}$  and  $D^{I\tau}$  can be set to the projector onto the

unoccupied subspace  $Q^{I\tau} \equiv (I - P^{I\tau}S)$ , identity matrix  $I$  or zero. This preconditioner is the same for all MOs of an electronic state and can be inverted independently for each state. The numerical tests described in the next section show that this preconditioner allows to optimize excited state MOs efficiently.

The computational cost of the PCG algorithm presented here is determined by both the number of the electronic states  $S$  and by the size of the system, that is, by the number electrons  $N$ , which is proportional to the number of basis set functions  $B$ . The cost of treating all  $S$  intrastate terms is dominated by the cost of inverting  $S$  preconditioners, which has  $\mathcal{O}(SB^3)$  computational complexity<sup>54,60</sup>. It should be noted that the preconditioners are inverted only in the beginning of the PCG procedure, making the direct optimization more efficient compared to the diagonalization-based methods, in which such costly operations are required on each iteration. It should also be noted that the intrastate cost of handling nonorthogonal MOs is lower –  $\mathcal{O}(SB^2N)$  to compute orbital overlaps  $\sigma_{II}$  and  $\mathcal{O}(SN^3)$  to invert them – because the number of electrons  $N$  is typically an order of magnitude lower than  $B$ . The determinants of the intrastate overlap matrices can also be computed relatively fast via their LU decomposition at  $\mathcal{O}(SN^3)$  cost.

Handling the interstate term and its derivative requires  $\mathcal{O}(S^2B^2N)$  time to build the  $S(S-1)/2$  overlap matrices for all pairs of electronic states,  $\mathcal{O}(S^2N^3)$  time to evaluate their adjugates and determinants (the latter being the elements of matrix  $\Phi$ ), and  $\mathcal{O}(S^3)$  time to compute the determinant of  $\Phi$ . Since the number of electronic states of interest is small compared to  $B^2N \gg S$  for most systems, building the overlap matrices will dominate the interstate computations.

To summarize, the intrastate and interstate terms are dominated by the  $\mathcal{O}(SB^3)$  and  $\mathcal{O}(S^2B^2N)$ , respectively. Therefore, the interstate term will represent the computational bottleneck for a large number of excited state, but does not consume significant computational time for most practical

problems with  $S < 100$ .

Initial excited state orbitals are generated using fully optimized canonical ground-state orbitals. The guess is obtained by systematically generating all possible excitations involving a fixed number electrons, typically two, and then retaining only the lowest (unoptimized) energy excitations for further optimization.

### 4.4.3 Penalty Strength Adjustment

The interstate penalty term plays a critical role in preventing the collapse of high-energy states onto lower-energy states. Increasing the strength of this term by increasing  $C_P$  pushes the electronic states to become closer to being orthogonal. If electronic states are not completely orthogonal, the optimized excited states can contain noticeable undesirable admixtures of the lower-lying states of the same symmetry. To produce orthogonal electronic states without strictly enforcing the orthogonality constraint, the interstate penalty strength is gradually increased using a fixed multiplicative update factor  $f_{upd} > 1$

$$C_P^{(n+1)} = C_P^{(n)} \times f_{upd} \quad (4.14)$$

until the electronic states become orthogonal, that is, until the deviation from the orthogonality (DFO) measured by the max norm of the off-diagonal elements of the interstate overlap matrix drops below a user-specified threshold  $\mathcal{E}_0$ :

$$\text{DFO} \equiv \|\Phi_{\tau d}^{-1/2} \Phi_{\tau} \Phi_{\tau d}^{-1/2} - I\|_{\max} < \mathcal{E}_0 \quad (4.15)$$

$C_P$  is adjusted in the outer loop, each iteration of which runs the PCG optimizer with a fixed penalty strength. This procedure guarantees that the optimization does not only produces accurate fully optimized MOs for each state, but also enforces orthogonality between the electronic states.

#### 4.4.4 Computational Details

The VM TIDFT procedure was implemented in the electronic structure module of the CP2K software package<sup>61</sup>. In the current implementation, matrix operations were performed using the DBCSR<sup>62</sup> library for sparse matrices and ScaLAPACK<sup>63</sup> library for dense matrices. The default values for the input parameters that control convergence of the PCG VM optimization are shown in Table 4.1 and used unless specified otherwise.

Parameter	Notation	Default value	Described in
Initial interstate penalty strength	$C_P^{(0)}$	10 Ha	Eq. (4.14)
SCF convergence threshold	$\ \frac{\partial \Omega}{\partial T}\ _{\text{RMS}}$	$10^{-6}$ Ha	
Final allowed DFO	$\epsilon_0$	$10^{-3}$	Eq. (4.15)
Interstate update factor	$f_{\text{upd}}$	2	Eq. (4.14)
Hamiltonian term in the preconditioner	$A$	0	Eq. (4.13) and Ref. <sup>54</sup>
Overlap term in the preconditioner	$D$	$I$	Eq. (4.13) and Ref. <sup>54</sup>

Table 4.1: Input parameters that control the PCG optimization of MO coefficients.

The efficiency and accuracy of the VM TIDFT method was tested on systems including gas-phase atoms (He, Be, B, Li) and small molecules (azulene, benzene, butadiene, ethene, formaldehyde, hydrogen chloride, hydrogen fluoride, nitrobenzene, N-phenylpyrrole, pyrrole, pyrazine, and naphthalene). We also calculated excitations in molecular complexes  $\text{C}_2\text{H}_4 \dots \text{C}_2\text{F}_4$ ,  $\text{NH}_3\text{-BF}_3$ ,  $\text{NH}_3 \dots \text{F}_2$ , and  $\pi$ -stacked dimer of pyrrole and pyrazine molecules. The organic molecules, particularly azulene, benzene, butadiene, nitrobenzene, and N-phenylpyrrole, are of special interest due to their distinct excited-state behavior driven by CT and bonding-antibonding interactions. These conjugated systems, with near-degenerate core and delocalized  $\pi$ -orbitals, are prone to root-flipping issues<sup>64,65</sup> during excited-state calculations, complicating the identification of states and making them excellent benchmarks. Moreover, the availability of extensive experimental and computational data for these systems enables meaningful comparisons, ensuring the reliability and accuracy of the tested method.

Unrestricted Kohn-Sham formalism (UKS) was used to describe spin-orbitals in this study unless indicated otherwise. Test calculations were carried out using the generalized gradient exchange-correlation functional of Perdew, Burke and Ernzerhof (PBE)<sup>66-68</sup>. In the dual Gaussian and plane-wave scheme implemented in CP2K<sup>69</sup>, double- $\zeta$  valence basis set with one set of polarization functions (DZVP)<sup>70</sup> were used to represent atomic orbitals. A plane-wave cutoff of 300 Ry was established to adequately describe the electron density, whereas a higher cutoff of 1500 Ry was used to produce smooth dissociation curves for the hydrogen  $H_2$  and the  $HeH^+$  molecules. Separable norm-conserving Goedecker-Teter-Hutter pseudopotentials were used to describe the interactions between the valence electrons and ionic cores<sup>71,72</sup>. All calculations were performed using a cubic simulation cell with dimensions of  $15 \times 15 \times 15$  for  $H_2$  and  $30 \times 30 \times 30$  for the rest of the systems. Electrostatic interactions between the periodic cell was eliminated using wavelet approach<sup>73,74</sup>.

## 4.5 Results and Discussion

### 4.5.1 Penalty Strength Effect

Fig. 4.1 shows the impact of the residual nonorthogonality between electronic states on the excitation energies. With higher penalty strength  $C_P$ , the electronic states are pushed to become orthogonal decreasing DFO and recovering the true excitation energies. When the allowed DFO is too large, only a fraction of the true excitation energies is recovered, signalling the admixture of lower-lying states due to insufficient orthogonality enforcement. This data highlights the importance of the interstate penalty term and suggests that  $\epsilon_0 = 10^{-4}$  is an acceptable DFO that recovers a large fraction of excitation energies. For HF, the bonding interaction arises from the overlap between the

hydrogen 1s orbital and the fluorine 2p<sub>z</sub> orbital, while the 1π orbitals are non-bonding as they have wrong symmetry to interact with the H 1s orbital and are localized primarily on the fluorine atom.

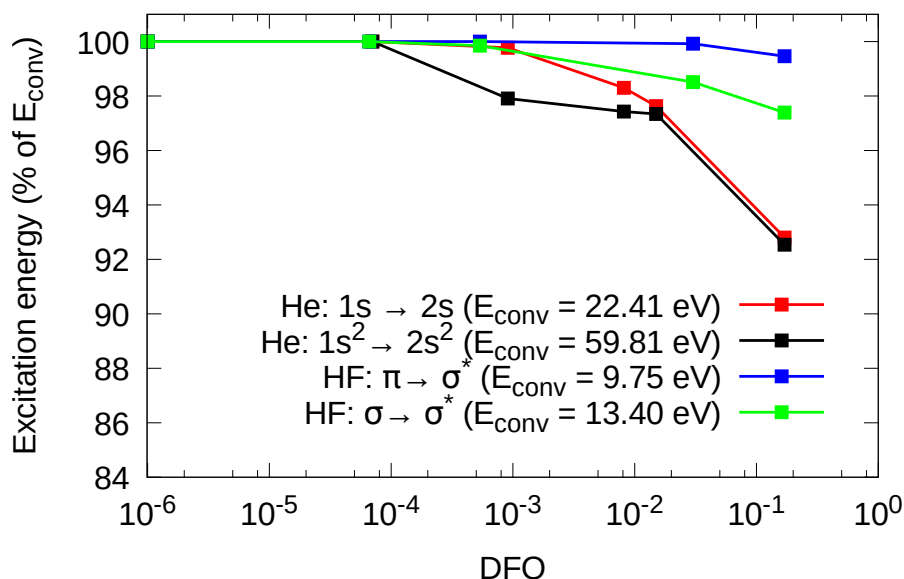


Figure 4.1: Excitation energy for the first two excitations of He atom (PBE/TZVP) and HF molecule (PBE/DZVP) computed with VM TIDFT optimization procedure for the DFO values measured after convergence is reached. The recovered excitation energy is a fraction of the converged excitation energy  $E_{\text{conv}}$  obtained with very tight requirement for the orthogonality criterion ( $\mathcal{E}_0 = 10^{-5}$ ).

## 4.5.2 Accuracy

Table 4.3 compares experimentally measured first singlet excitation energies with those computed using VM TIDFT, TDDFT in Tamm-Dancoff approximation, OCDFT, and wavefunction-based correlation methods (MP2 or CCSD).

Despite different optimization paradigms, VM TIDFT utilizes the same orthogonality constraint as OCDFT. Therefore, the fully optimized states in VM TIDFT and OCDFT are expected to be the same if computed using the same model chemistry (i.e. the same exchange-correlation functional and basis set). Table 4.3 shows that VM TIDFT excitation energies are indeed close to

those computed with OCDFT but not the same. This is due to the OCDFT results being partially spin-purified in the post-SCF procedure<sup>44</sup>, whereas spin-purification was not used in VM TIDFT optimization. The results are also different due to the different basis sets employed to represent occupied states: def2-TZVP in OCDFT is a larger more flexible basis set than DZVP in VM TIDFT.

For the six systems with complete experimental and computational data (first six rows in Table 4.3), VM TIDFT results are in reasonable agreement with experimental data (MAD = 1.02 eV). For comparison, the partially spin-purified OCDFT results are in slightly better agreement with experimental data than VM TIDFT (MAD = 0.89 eV), whereas TDDFT agreement is significantly worse (MAD = 1.71 eV).

When all test systems with available experimental excitation energies, are compared (not just the first six of them), the accuracy of VM TIDFT (MAD = 0.88 eV) remains noticeably better than that of TDDFT (MAD = 1.36 eV). Comparison between VM TIDFT and TDDFT shows that TDDFT tends to slightly underestimate excitation energies for the test systems (Fig. 4.2). On the other hand, VM TIDFT energies are underestimated compared to OCDFT, MP2, and CCSD energies (Fig. 4.2). OCDFT data suggests that using spin-purified VM TIDFT wavefunctions, described with larger basis set can substantially improve the excitation energies. Spin-purified VM TIDFT calculations will be performed using the ROKS optimizer in the future.

It is worth noting the magnitude of the residual norm of the energy gradient for the fully optimized excited states (Table 4.3). For most excited states, this norm is below the convergence threshold of  $10^{-6}$  Ha imposed on the loss (not the energy) functional, indicating that these excited states are true minima of the DFT functional. Once optimized, these states will not collapse to the lower-lying ground state even without the orthogonality constraint. There are, however, several excited systems with the energy gradient higher than the  $10^{-6}$  Ha threshold. These are He atom,

N-phenylpyrrole,  $\text{NH}_3 \dots \text{BF}_3$ , and pyrrole-pyrazine dimer. In these systems, the first excited states are not electronic minima and the non-zero energy gradient is fully compensated by the opposite non-zero gradient of the interstate penalty functional, producing the zero-gradient true minima of the loss functional. It is also important to note that such stationary points still correspond to physically meaningful excited states. For instance, VM TIDFT results for the He atom match closely with TDDFT results and experimental data for low-lying excitations while not being true electronic minima (Table 4.2). This confirms the validity of using orthogonality constraints in orbital-optimized excited-state DFT.

Excitation	TDDFT (eV)	VM TIDFT (eV)	RMS norm of the energy gradient (Ha)	Experiment (eV)
$1s^2 \rightarrow 1s2s$	20.24	20.91	$9.7 \times 10^{-2}$	20.62 <sup>75</sup>
$1s^2 \rightarrow 1s2p$	40.64	36.95	$3.2 \times 10^{-5}$	21.22 <sup>75</sup>
$1s^2 \rightarrow 1s3s$	37.47	39.10	$5.3 \times 10^{-2}$	22.93 <sup>75</sup>
$1s^2 \rightarrow 2s^2$	-	57.68	$3.5 \times 10^{-1}$	57.84 <sup>76</sup>
$1s^2 \rightarrow 2s2p$	-	67.63	$1.5 \times 10^{-1}$	60.15 <sup>77</sup>

Table 4.2: PBE/QZV3P excitation energies calculated using TDDFT and VM TIDFT.

### 4.5.3 Double-electron Excitations

Unlike TDDFT, VM TIDFT can trivially describe double-electron excitations. As an example, the energies calculated for the  $1s^2 \rightarrow 2s^2$  and  $1s^2 \rightarrow 2s^1 2p^1$  excitations in the helium atom are 57.68 eV and 67.63 eV, respectively, at the PBE/QZV3P level of theory. These values are close to the experimental values for these transitions, which are 57.84 eV<sup>76</sup> and 60.15 eV<sup>77</sup>, respectively. It should be noted that OCDFT with a single electron hole-particle pair cannot describe double-electron excitations<sup>44</sup>.

Molecules	RMS norm of the energy gradient  (Ha)	CP2K		Psi4	Gaussian	Experiment
		PBE/DZVP		PBE/def2-TZVP	MP2/6-31G*	
		TDDFT	VM TIDFT	OCDFT <sup>32</sup>	CCSD/aug-cc-pVTZ Best estimate <sup>78</sup>	
		(eV)	(eV)	(eV)	(eV)	(eV)
pyrazine	$6.0 \times 10^{-7}$	2.86	3.13	3.30	3.95 <sup>a</sup>	3.83 <sup>79</sup>
formaldehyde	$8.4 \times 10^{-7}$	3.12	3.42	3.33	3.88 <sup>a</sup>	4.28 <sup>80</sup>
benzene	$9.9 \times 10^{-7}$	4.11	5.13	5.11	5.08 <sup>a</sup>	4.79 <sup>81</sup>
pyrrole	$7.8 \times 10^{-7}$	4.31	5.21	5.97	6.37 <sup>a</sup>	5.22 <sup>82</sup>
butadiene	$7.3 \times 10^{-7}$	2.86	3.76	4.51	6.18 <sup>a</sup>	5.92 <sup>83</sup>
ethene	$4.9 \times 10^{-7}$	4.51	5.95	6.64	7.80 <sup>a</sup>	8.00 <sup>83</sup>
azulene	$8.9 \times 10^{-7}$	1.94	2.12	-	3.85 <sup>b</sup>	1.77 <sup>84</sup>
B atom	$5.9 \times 10^{-7}$	0.31	1.47	-	-	1.86 <sup>85</sup>
Be atom	$5.5 \times 10^{-7}$	3.08	3.98	-	-	2.73 <sup>86</sup>
Li atom	$7.2 \times 10^{-7}$	2.39	1.95	-	-	3.37 <sup>87</sup>
naphthalene	$9.1 \times 10^{-7}$	2.74	3.30	-	-	3.97 <sup>88</sup>
N-phenylpyrrole	$4.2 \times 10^{-3}$	3.36	3.96	-	5.32 <sup>b</sup>	4.35 <sup>89</sup>
nitrobenzene	$8.9 \times 10^{-7}$	2.81	3.12	-	5.41 <sup>b</sup>	4.38 <sup>90</sup>
HCl	$8.8 \times 10^{-7}$	8.10	8.83	-	-	9.56 <sup>91</sup>
HF	$6.2 \times 10^{-7}$	8.50	9.75	-	-	10.33 <sup>92</sup>
He atom	$1.9 \times 10^{-1}$	24.15	26.03	-	-	20.62 <sup>75</sup>
NH <sub>3</sub> . . . F <sub>2</sub>	$9.1 \times 10^{-7}$	1.90	2.50	-	-	-
pyrrole . . . pyrazine	$1.8 \times 10^{-6}$	2.52	3.10	-	-	-
C <sub>2</sub> H <sub>4</sub> . . . C <sub>2</sub> F <sub>4</sub>	$5.8 \times 10^{-7}$	4.39	5.46	-	-	-
NH <sub>3</sub> -BF <sub>3</sub>	$1.8 \times 10^{-4}$	7.29	8.81	-	-	-
MAE vs Experiment <sup>c</sup>		1.71	1.02	0.89	0.52	0.00
MAE vs Experiment <sup>d</sup>		1.36	0.88	-	-	0.00

<sup>a</sup> MP2/6-31G(d) results<sup>78</sup>

<sup>b</sup> CCSD/aug-cc-pVTZ results<sup>78</sup>

<sup>c</sup> Computed for the first six systems

<sup>d</sup> Computed for the systems with listed experimental values

Table 4.3: First singlet excitation energies calculated using TDDFT, VM TIDFT, OCDFT and high-level quantum mechanics calculations and shown alongside experimental data.

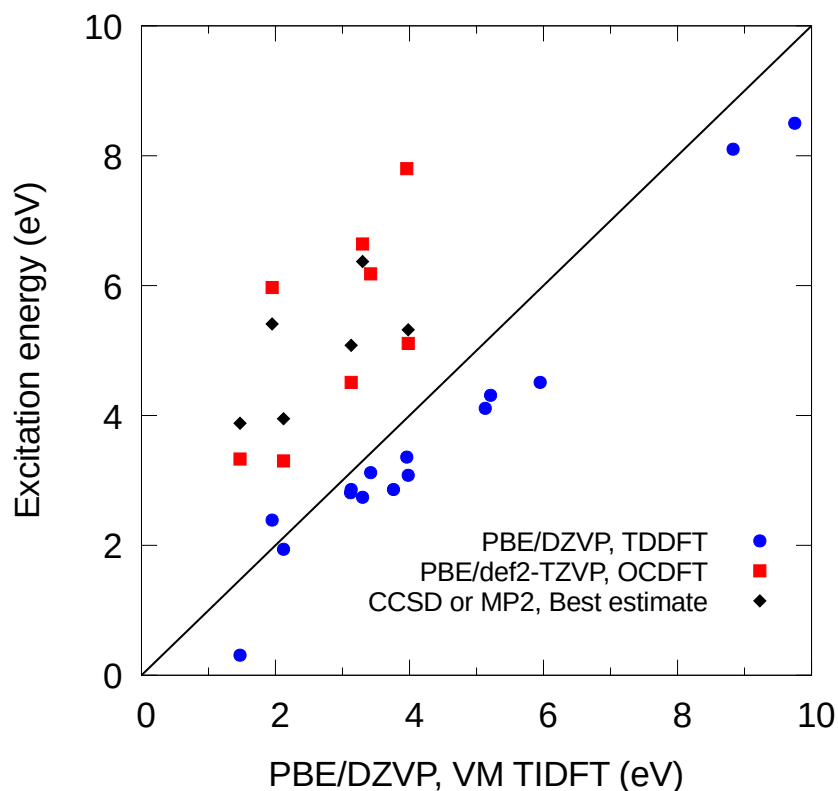


Figure 4.2: Comparison of VM TIDFT excitation energies with those calculated with TDDFT, OCDFT, and wavefunction correlation methods. TDDFT and VM TIDFT results were obtained in this work using CP2K, OCDFT energies were computed using Psi4 in Ref.<sup>44</sup>, and MP2/6-31G\* and CCSD/aug-cc-pVTZ results were computed using Gaussian in Ref.<sup>78</sup>.

#### 4.5.4 Charge-transfer Excitations

One of the most important advantages of OODFT methods over TDDFT is their ability to predict the energy of CT excitations accurately. Here, VM TIDFT is used to describe the CT excitation in a minimal-basis  $H_2$  molecule – a simple four-level test system previously employed to explain the success of OCDFT and failures of TDDFT<sup>44</sup>. Fig. 4.3 shows that VM TIDFT indeed correctly reproduces the long-range behavior of the CT excitation energy, matching the Coulomb potential of the interacting  $H^+$  and  $H^-$  ions perfectly. This behavior can be contrasted with the TDDFT CT energy of the excited states, which shows the attenuation of the Coulomb tail<sup>44</sup>, the degree of which

is determined by the fraction of the exact exchange in the employed exchange functional.

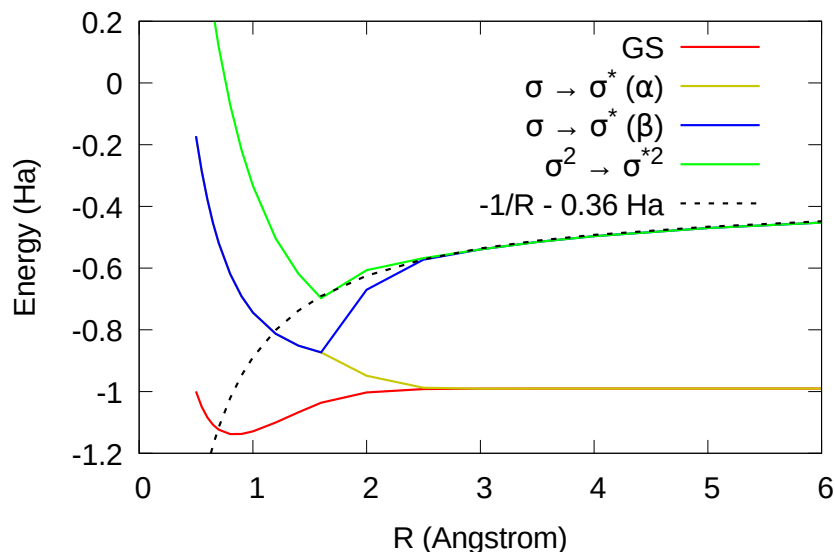


Figure 4.3: PBE/SZV ground-state and excited-state dissociation curves for  $\text{H}_2$  computed with VM TIDFT. The energy of the Coulomb interactions is down-shifted by 0.36 Ha to account for sum of the ionization potential (IP) and electron affinity (EA) of the isolated hydrogen atoms.

It is also instructive to demonstrate the correct behavior of the CT excitation energies in the  $[\text{He}\cdots\text{H}]^+$  ion. For large interatomic distances, the two electrons in the  $[\text{He}\cdots\text{H}]^+$  system are localized on the helium atom in the ground state. Upon excitation, one of the electrons transfers from helium to hydrogen, resulting in a  $\text{He}^+ \cdots \text{H}$  configuration. The energy of this excitation is the sum of the ionization potential (IP) of helium and the electron affinity (EA) of hydrogen. Crucially, this energy does not depend on the interatomic distance because the Coulomb interaction between the neutral and positive fragments is zero. VM TIDFT correctly reproduces the flat excitation energy in the large separation limit, in agreement with the spin-purified OCDFT excitation energy (Fig. 4.4). In contrast, TDDFT underestimates the excitation energy and fails to capture its asymptotic behavior (Fig. 4.4) because of the incomplete cancellation of the Coulomb and exchange interactions between electrons in the PBE and other exchange-correlation functionals.

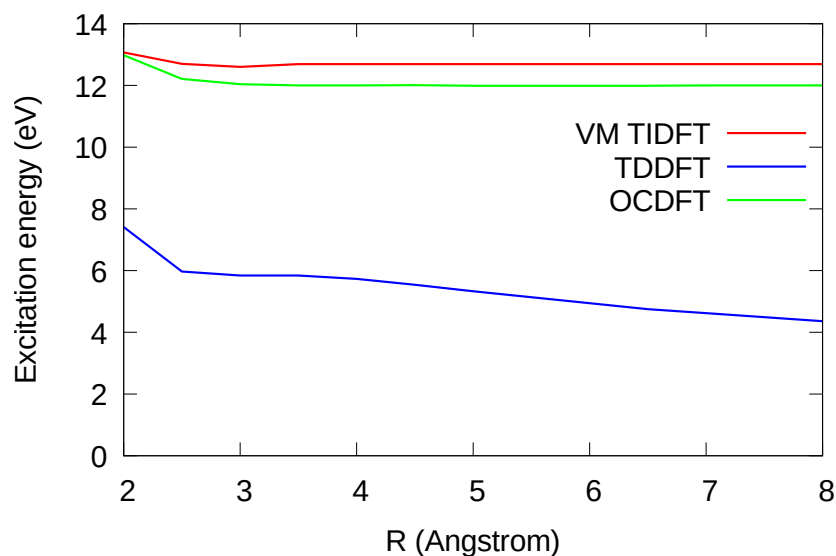


Figure 4.4: Excitation energy for the charge transfer state of  $\text{HeH}^+$  as a function of the He–H distance, computed using VM TIDFT and TDDFT at the PBE/DZVP level of theory. For comparison, OCDFT PBE/STO-3G results are also shown<sup>44</sup>.

### 4.5.5 SCF Convergence

Fig. 4.5 shows how the norm of the gradient of the loss functional changes during the PCG optimization of the ground and excited states. The default VM SCF optimization algorithm achieves stable convergence for the ground state<sup>54</sup>. The algorithm also works well for the optimization of excited-state orbitals, sometimes converging faster than the optimization of the ground state. This is because an excited-state optimization already starts with the well-converged canonical orbitals of the ground state. For some systems, however, the optimization of the excited states takes many more iterations to converge as the optimizer needs to find the right balance between maintaining orthogonality to the previously optimized states and minimizing the energy. Converging excited-state optimization also takes longer when the penalty strength update is necessary to enforce stricter orthogonality between the electronic states. These updates, performed in an outer loop of the main

PCG optimization, can be seen as sharp increases of the gradient norm from the convergence line in Fig. 4.5.

It should be noted that a large number of iterations is required to achieve convergence even for the ground state of simple systems. This suggests that the rate of convergence can be improved by replacing PCG – one of the simplest algorithm for unconstrained optimization – with quasi-Newton or trust-region optimizers that are known to work well for the ground-state KS DFT<sup>50</sup>. Additionally, faster optimization can be achieved by updating the penalty strength on each iteration, instead of updating it in the outer loop.

Finally, it is worth mentioning that VM TIDFT method does not guarantee to find the lowest-energy excitations. As with all other orbital-optimized DFT methods<sup>6</sup>, the result of the optimization will be a stationary point lying in the basin of the initial guess.

## 4.6 Conclusions

VM TIDFT is a simple DFT method designed to prevent collapse of excited states during their variational optimization. The main idea of VM TIDFT is to allow nonorthogonal electronic states in the optimization process but gradually push them towards orthogonality with a simple continuous penalty function. With nonorthogonal orbitals and electronic states, VM TIDFT can use molecular orbital coefficients as independent variables in the optimization procedure. This in turn leads to simple closed-form analytical expressions for the gradient and allows to employ any of the ubiquitous unconstrained optimization algorithms that guarantees convergence of the excited-state optimization. Numerical tests on multiple molecular systems show that VM TIDFT optimization performed with the PCG algorithm is robust and the method computes accurate energies for well-

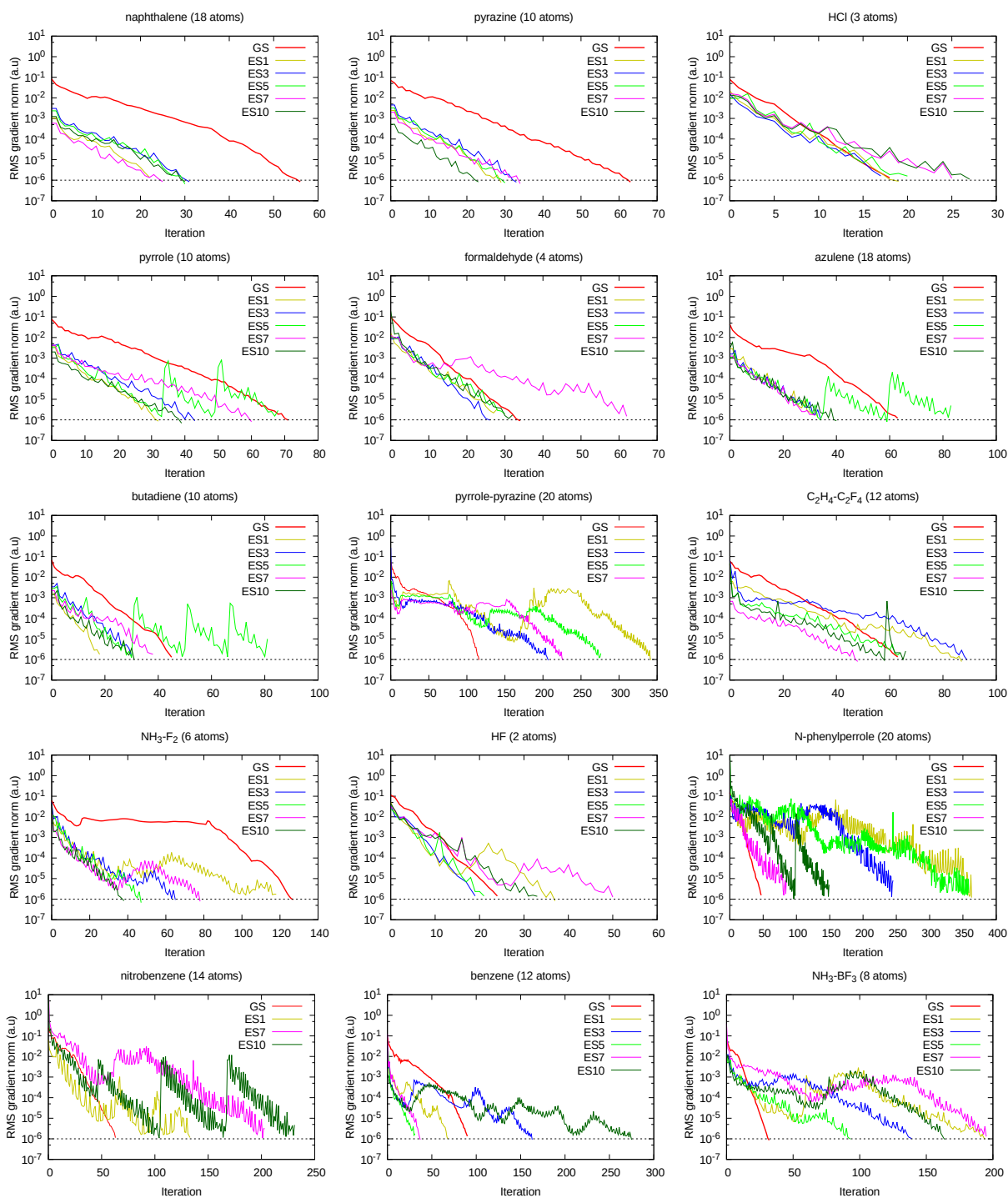


Figure 4.5: Convergence rate for the VM TIDFT procedure for the ground states (GS) and selected excited states (ES). Line search steps, one per PCG step, are not included in the iteration count. The dashed lines show the SCF convergence threshold.

behaved excitations and, unlike TDDFT, for more challenging CT and double-electron excitations.

Due to the simplicity of VM TIDFT, this approach can be implemented using other unconstrained minimization techniques, such as quasi-Newton or trust-region methods. This can improve the computational efficiency of VM DFT. VM TIDFT is also ideally suited to implement the full variational ROKS optimization of spin-purified open-shell singlet states<sup>54–56</sup>, which are necessary for more accurate description of many excited states. Additionally, unconstrained VM TIDFT optimization makes the computation of atomic forces in excited states straightforward, facilitating computation of emission spectra and dynamical photophysical and photochemical processes in excited states.

From a broader perspective, variable-metric optimization can be readily extended to electronic structure methods where the use of nonorthogonal wavefunctions is unavoidable (e.g. optimization of strictly localized orbitals<sup>79–82</sup>), or where linear dependencies present a serious problem during variational optimization (e.g. multi-configurational wavefunctions).

## 4.7 Acknowledgements

We would like to thank Zhenzhe Zhang for providing optimized structures for our tests. The research was funded by the Natural Sciences and Engineering Research Council of Canada (NSERC) through Discovery Grant. The authors are grateful to Compute Canada for computer resources allocated under the CFI John R. Evans Leaders Fund program.

## 4.8 References

- [1] Matsika, S.; Krylov, A. I. Introduction: Theoretical Modeling of Excited State Processes. *Chem. Rev* **2017**, *117*, 49.
- [2] Serrano-Andrés, L.; Merchán, M. Quantum chemistry of the excited state: 2005 overview. *J. Mol. Struct. Theochem.* **2005**, *729*, 99–108.
- [3] Schlag, E. W.; Schneider, S.; Fischer, S. F. Lifetimes in Excited States. *Annu. Rev. Phys. Chem.* **1971**, *22*, 465–526.
- [4] Dreuw, A.; Head-Gordon, M. Single-reference ab initio methods for the calculation of excited states of large molecules. *Chem. Rev.* **2005**, *105*, 4009–4037.
- [5] Runge, E.; Gross, E. K. Density-Functional Theory for Time-Dependent Systems. *Phys. Rev. Letters* **1984**, *52*, 997.
- [6] Hait, D.; Head-Gordon, M. Orbital Optimized Density Functional Theory for Electronic Excited States. *J. Phys. Chem. Lett.* **2021**, *12*, 4517–4529.
- [7] Ullrich, C. A. *Time-Dependent Density-Functional Theory: Concepts and Applications*; Oxford University Press, 2011.
- [8] Levy, M.; Ágnes Nagy Variational density-functional theory for an individual excited state. *Phys. Rev. Lett.* **1999**, *83*, 4361.
- [9] Nagy; Levy, M. Variational density-functional theory for degenerate excited states. *Phys. Rev. A: At. Mol. Opt. Phys.* **2001**, *63*, 052502.
- [10] Ayers, P. W.; Levy, M. Time-independent (static) density-functional theories for pure excited states: Extensions and unification. *Phys. Rev. A* **2009**, *80*, 012508.
- [11] Ayers, P. W.; Levy, M.; Nagy, A. Time-independent density-functional theory for excited states of Coulomb systems. *Phys. Rev. A* **2012**, *85*, 042518.
- [12] Cullen, J.; Krykunov, M.; Ziegler, T. The formulation of a self-consistent constricted variational density functional theory for the description of excited states. *Chem. Phys.* **2011**, *391*, 124107.
- [13] Ziegler, T.; Rauk, A.; Baerends, E. J. On the calculation of multiplet energies by the hartree-fock-slater method. *Theor. Chim. Acta.* **1977**, *43*, 261–271.
- [14] Barth, U. V. Local-density theory of multiplet structure. *Phys. Rev. A* **1979**, *20*, 1693–1703.
- [15] Gavnholt, J.; Olsen, T.; Engelund, M.; Schiøtz, J.  $\Delta$  self-consistent field method to obtain potential energy surfaces of excited molecules on surfaces. *Phys. Rev. B - Condens. Matter Phys* **2008**, *78*, 075441.
- [16] Kowalczyk, T.; Yost, S. R.; Voorhis, T. V. Assessment of the  $\Delta$ SCF Density Functional Theory Approach for Electronic Excitations in Organic Dyes. *J. Chem. Phys.* **2011**, *134*, 054128.
- [17] Yang, W.; Ayers, P. W. Foundation for the  $\Delta$ SCF Approach in Density Functional Theory. 2024; <https://arxiv.org/abs/2403.04604>.
- [18] Triguero, L.; Plashkevych, O.; Pettersson, L. G.; Ågren, H. Separate state vs. transition state Kohn-Sham calculations of X-ray photoelectron binding energies and chemical shifts. *J. Electron Spectros. Relat. Phenom.* **1999**, *104*, 195–207.

- [19] Cheng, C. L.; Wu, Q.; Voorhis, T. V. Rydberg energies using excited state density functional theory. *J. Chem. Phys.* **2008**, *129*, 124112.
- [20] Seidu, I.; Krykunov, M.; Ziegler, T. Applications of time-dependent and time-independent density functional theory to Rydberg transitions. *J. Phys. Chem. A* **2015**, *119*, 5107–5116.
- [21] Liu, J.; Zhang, Y.; Bao, P.; Yi, Y. Evaluating Electronic Couplings for Excited State Charge Transfer Based on Maximum Occupation Method  $\Delta$ SCF Quasi-Adiabatic States. *J. Chem. Theory Comput.* **2017**, *13*, 843–851.
- [22] Hait, D.; Head-Gordon, M. Highly Accurate Prediction of Core Spectra of Molecules at Density Functional Theory Cost: Attaining Sub-electronvolt Error from a Restricted Open-Shell Kohn-Sham Approach. *J. Phys. Chem. Lett.* **2020**, *11*, 775–786.
- [23] Kumar, C.; Luber, S. Robust  $\Delta$ SCF calculations with direct energy functional minimization methods and STEP for molecules and materials. *J. Chem. Phys.* **2022**, *156*, 154104.
- [24] Selenius, E.; Sigurdarson, A. E.; Schmerwitz, Y. L. A.; Levi, G. Orbital-Optimized Versus Time-Dependent Density Functional Calculations of Intramolecular Charge Transfer Excited States. *J. Chem. Theory Comput.* **2024**, *20*, 3809–3822.
- [25] Kunze, L.; Hansen, A.; Grimme, S.; Mewes, J. M. PCM-ROKS for the Description of Charge-Transfer States in Solution: Singlet-Triplet Gaps with Chemical Accuracy from Open-Shell Kohn-Sham Reaction-Field Calculations. *J. Phys. Chem. Lett.* **2021**, *12*, 8470–8480.
- [26] Nottoli, M.; Mazzeo, P.; Lipparini, F.; Cupellini, L.; Mennucci, B. A  $\Delta$ SCF model for excited states within a polarisable embedding. *Mol. Phys.* **2023**, *121*, e2089605.
- [27] Gross, E. K.; Oliveira, L. N.; Kohn, W. Density-functional theory for ensembles of fractionally occupied states. I. Basic formalism. *Phys. Rev. A* **1988**, *37*, 2821.
- [28] Gilbert, A. T.; Besley, N. A.; Gill, P. M. Self-consistent field calculations of excited states using the maximum overlap method (MOM). *J. Phys. Chem. A* **2008**, *112*, 13164–13171.
- [29] Baruah, T.; Pederson, M. R. DFT calculations on charge-transfer states of a carotenoid-porphyrin-C60 molecular triad. *J. Chem. Theory Comput.* **2009**, *5*, 834–843.
- [30] Kaduk, B.; Kowalczyk, T.; Voorhis, T. V. Constrained density functional theory. *Chem. Rev.* **2012**, *112*, 321–370.
- [31] Ziegler, T.; Krykunov, M.; Cullen, J. The implementation of a self-consistent constricted variational density functional theory for the description of excited states. *J. Chem. Phys.* **2012**, *136*, 124107.
- [32] Filatov, M. Spin-restricted ensemble-referenced Kohn-Sham method: Basic principles and application to strongly correlated ground and excited states of molecules. *Wiley Interdiscip. Rev. Comput. Mol. Sci.* **2015**, *5*, 146–167.
- [33] Ramos, P.; Pavanello, M. Low-lying excited states by constrained DFT. *J. Chem. Phys.* **2018**, *148*, 144103.
- [34] Levi, G.; Ivanov, A. V.; Jónsson, H. Variational Density Functional Calculations of Excited States via Direct Optimization. *J. Chem. Theory Comput.* **2020**, *16*, 6968–6982.
- [35] Levi, G.; Ivanov, A. V.; Jónsson, H. Variational Calculations of Excited States: Via Direct Optimization of the Orbitals in DFT. *Faraday Discuss.* **2020**, *224*, 448–466.
- [36] Zhao, L.; Neuscamman, E. Density Functional Extension to Excited-State Mean-Field Theory. *J. Chem. Theory Comput.* **2020**, *16*, 164–178.

- [37] Carter-Fenk, K.; Herbert, J. M. State-Targeted Energy Projection: A Simple and Robust Approach to Orbital Relaxation of Non-Aufbau Self-Consistent Field Solutions. *J. Chem. Theory Comput.* **2020**, *16*, 5067–5082.
- [38] Hait, D.; Head-Gordon, M. Excited State Orbital Optimization via Minimizing the Square of the Gradient: General Approach and Application to Singly and Doubly Excited States via Density Functional Theory. *J. Chem. Theory Comput.* **2020**, *16*, 1699–1710.
- [39] Roychoudhury, S.; Sanvito, S.; O'Regan, D. D. Neutral excitation density-functional theory: an efficient and variational first-principles method for simulating neutral excitations in molecules. *Sci. Rep.* **2020**, *10*, 8947.
- [40] Ivanov, A. V.; Levi, G.; Jónsson, E.; Jónsson, H. Method for Calculating Excited Electronic States Using Density Functionals and Direct Orbital Optimization with Real Space Grid or Plane-Wave Basis Set. *J. Chem. Theory Comput.* **2021**, *17*, 5034–5049.
- [41] MacEtti, G.; Genoni, A. Initial maximum overlap method for large systems by the quantum mechanics/extremely localized molecular orbital embedding technique. *J. Chem. Theory Comput.* **2021**, *17*, 4169–4182.
- [42] Zhang, J.; Tang, Z.; Zhang, X.; Zhu, H.; Zhao, R.; Lu, Y.; Gao, J. Target State Optimized Density Functional Theory for Electronic Excited and Diabatic States. *J. Chem. Theory Comput.* **2023**, *19*, 1777–1789.
- [43] Schmerwitz, Y. L. A.; Levi, G.; Jónsson, H. Calculations of Excited Electronic States by Converging on Saddle Points Using Generalized Mode Following. *J. Chem. Theory Comput.* **2023**, *19*, 3651.
- [44] Evangelista, F. A.; Shushkov, P.; Tully, J. C. Orthogonality Constrained Density Functional Theory for Electronic Excited States. *J. Phys. Chem. A* **2013**, *117*, 7378–7392.
- [45] Ziegler, T.; Krykunov, M.; Seidu, I.; Park, Y. C. In *Constricted variational density functional theory approach to the description of excited states*; Michael, Nicolas, H.-R. M. F., Filatov, Eds.; Springer International Publishing, 2015; Vol. 368; pp 61–95.
- [46] Cernatic, F.; Senjean, B.; Robert, V.; Fromager, E. Ensemble Density Functional Theory of Neutral and Charged Excitations: Exact Formulations, Standard Approximations, and Open Questions. *Top. Curr. Chem. (Z)* **2022**, *380*, 4.
- [47] Barca, G. M.; Gilbert, A. T.; Gill, P. M. Simple Models for Difficult Electronic Excitations. *J. Chem. Theory Comput.* **2018**, *14*, 1501–1509.
- [48] Barca, G. M.; Gilbert, A. T.; Gill, P. M. Excitation Number: Characterizing Multiply Excited States. *J. Chem. Theory Comput.* **2018**, *14*, 9–13.
- [49] Mewes, J. M.; Jovanović, V.; Marian, C. M.; Dreuw, A. On the molecular mechanism of non-radiative decay of nitrobenzene and the unforeseen challenges this simple molecule holds for electronic structure theory. *Phys. Chem. Chem. Phys.* **2014**, *16*, 12393–12406.
- [50] Voorhis, T. V.; Head-Gordon, M. A geometric approach to direct minimization. *Mol. Phys.* **2002**, *100*, 1713–1721.
- [51] Shea, J. A.; Gwin, E.; Neuscamman, E. A Generalized Variational Principle with Applications to Excited State Mean Field Theory. *J. Chem. Theory Comput.* **2020**, *16*, 1526–1540.
- [52] Luo, Z.; Khaliullin, R. Z. Direct Unconstrained Variable-Metric Localization of One-Electron Orbitals. *J. Chem. Theory Comput.* **2020**, *16*, 3558–3566.

- [53] Luo, Z.; Khaliullin, R. Z. Variable-Metric Localization of Occupied and Virtual Orbitals. *J. Chem. Theory Comput.* **2021**, *17*, 5581.
- [54] Pham, H. D. M.; Khaliullin, R. Z. Direct Unconstrained Optimization of Molecular Orbital Coefficients in Density Functional Theory. *J. Chem. Theory Comput.* **2024**, *20*, 7936–7947.
- [55] Frank, I.; Hutter, J.; Marx, D.; Parrinello, M. Molecular dynamics in low-spin excited states. *J. Chem. Phys.* **1998**, *108*, 164101.
- [56] Filatov, M.; Shaik, S. Density-functional thermochemistry. III. The role of exact exchange. *J. Chem. Phys.* **1999**, *110*, 5648.
- [57] Nocedal, J.; Wright, S. J. *Numerical Optimization*, 2nd ed.; Springer: New York, NY, USA, 2006.
- [58] A Survey of Nonlinear Conjugate Gradient Methods. *Pac. J. Optim.* **2006**, *2*, 35–58.
- [59] Stewart, G. W. On the adjugate matrix. *Linear Algebra Its Appl.* **1998**, *283*, 151–164.
- [60] VandeVondele, J.; Hutter, J. An efficient orbital transformation method for electronic structure calculations. *J. Chem. Phys.* **2003**, *118*, 4365.
- [61] Kühne, T. D. et al. CP2K: An Electronic Structure and Molecular Dynamics Software Package -Quickstep: Efficient and Accurate Electronic Structure Calculations. *J. Chem. Phys.* **2020**, *152*, 194103.
- [62] Borštnik, U.; VandeVondele, J.; Weber, V.; Hutter, J. Sparse matrix multiplication: The distributed block-compressed sparse row library. *Parallel Comp.* **2014**, *40*, 47–58.
- [63] Choi, J.; Demmel, J.; Dhillon, I.; Dongarra, J.; Ostrouchov, S.; Petitet, A.; Stanley, K.; Walker, D.; Whaley, R. ScaLAPACK: a portable linear algebra library for distributed memory computers — design issues and performance. *Comput. Phys. Commun.* **1996**, *97*, 1–15.
- [64] Marie, A.; Burton, H. G. Excited States, Symmetry Breaking, and Unphysical Solutions in State-Specific CASSCF Theory. *J. Phys. Chem. A* **2023**, *127*, 4538–4552.
- [65] Tran, L. N.; Shea, J. A.; Neuscammann, E. Tracking Excited States in Wave Function Optimization Using Density Matrices and Variational Principles. *J. Chem. Theory Comput.* **2019**, *15*, 4790–4803.
- [66] Zhang, Y.; Yang, W. Comment on “Generalized Gradient Approximation Made Simple”. *Phys. Rev. Lett.* **1998**, *80*, 890–890.
- [67] Perdew, J. P.; Ruzsinszky, A.; Csonka, G. I.; Vydrov, O. A.; Scuseria, G. E.; Constantin, L. A.; Zhou, X.; Burke, K. Restoring the density-gradient expansion for exchange in solids and surfaces. *Phys. Rev. Lett.* **2008**, *100*, 136406.
- [68] Perdew, J. P.; Burke, K.; Ernzerhof, M. Generalized Gradient Approximation Made Simple [Phys. Rev. Lett. 77, 3865 (1996)]. *Phys. Rev. Lett.* **1997**, *78*, 1396–1396.
- [69] Hutter, J.; Iannuzzi, M.; Schiffmann, F.; Vandevondele, J. Cp2k: Atomistic Simulations of Condensed Matter Systems. *Wiley Interdiscip. Rev. Comput. Mol. Sci.* **2014**, *4*, 15–25.
- [70] VandeVondele, J.; Hutter, J. Gaussian Basis Sets for Accurate Calculations on Molecular Systems in Gas and Condensed Phases. *J. Chem. Phys.* **2007**, *127*, 114105.
- [71] Goedecker, S.; Teter, M.; Hutter, J. Separable Dual-Space Gaussian Pseudopotentials. *Phys. Rev. B* **1996**, *54*, 1703.

- [72] Krack, M. Pseudopotentials for H to Kr Optimized for Gradient-Corrected Exchange-Correlation Functionals. *Theor. Chem. Acc.* **2005**, *114*, 145–152.
- [73] Genovese, L.; Deutsch, T.; Neelov, A.; Goedecker, S.; Beylkin, G. Efficient solution of Poisson’s equation with free boundary conditions. *J. Chem. Phys.* **2006**, *125*, 074105.
- [74] Genovese, L.; Deutsch, T.; Goedecker, S. Efficient and accurate three-dimensional Poisson solver for surface problems. *J. Chem. Phys.* **2007**, *127*, 054704.
- [75] Xie, B. P.; Zhu, L. F.; Yang, K.; Zhou, B.; Hiraoka, N.; Cai, Y. Q.; Yao, Y.; Wu, C. Q.; Wang, E. L.; Feng, D. L. Inelastic x-ray scattering study of the state-resolved differential cross section of Compton excitations in helium atoms. *Phys. Rev. A* **2010**, *82*, 032501.
- [76] Sekikawa, T.; Okamoto, T.; Haraguchi, E.; Yamashita, M.; Nakajima, T. Two-photon resonant excitation of a doubly excited state in He atoms by high-harmonic pulses. *Opt. Express* **2008**, *16*, 21922–21929.
- [77] Aufleger, L.; Friebel, P.; Rupprecht, P.; Magunia, A.; Ding, T.; Rebholz, M.; Hartmann, M.; Ott, C.; Pfeifer, T. Line-shape broadening of an autoionizing state in helium at high XUV intensity. *New J. Phys.* **2022**, *24*, 013014.
- [78] Schreiber, M.; Silva-Junior, M. R.; Sauer, S. P.; Thiel, W. Benchmarks for electronically excited states: CASPT2, CC2, CCSD, and CC3. *J. Chem. Phys.* **2008**, *128*, 134110.
- [79] Burger, S. K.; Yang, W. Linear-scaling quantum calculations using non-orthogonal localized molecular orbitals. *J. Phys.: Condens. Matter* **2008**, *20*, 294209.
- [80] Khaliullin, R. Z.; VandeVondele, J.; Hutter, J. Efficient Linear-Scaling Density Functional Theory for Molecular Systems. *J. Chem. Theory Comp.* **2013**, *9*, 4421–4427.
- [81] Peng, L.; Gu, F. L.; Yang, W. Effective preconditioning for ab initio ground state energy minimization with non-orthogonal localized molecular orbitals. *Phys. Chem. Chem. Phys.* **2013**, *15*, 15518–15527.
- [82] Shi, Y.; Karaguesian, J.; Khaliullin, R. Z. Robust linear-scaling optimization of compact localized orbitals in density functional theory. 2021; <https://arxiv.org/abs/2004.05901>.

## 4.9 Supporting Information

### 4.9.1 Unrestricted Kohn-Sham Equations for Variable Metric Time-Independent Optimization

In the unrestricted Kohn-Sham method (UKS), the molecular orbital coefficients for different spins are optimized independently. The notation and definitions are described in the main text. The Kohn-Sham energy functional and the electron density are given by

$$E^I = \sum_{\tau=\alpha}^{\beta} \sum_{\mu\nu}^B F_{\mu\nu}^{I\tau} P_{\nu\mu}^{I\tau} - \frac{1}{2} \int \int \frac{\rho^I(\mathbf{r})\rho^I(\mathbf{r}')}{|\mathbf{r}-\mathbf{r}'|} d\mathbf{r}d\mathbf{r}' + E_{xc}^I - \int v_{xc}^I(\mathbf{r})\rho^I(\mathbf{r})d\mathbf{r} \quad (4.16)$$

$$\rho^{I\tau}(\mathbf{r}) = \sum_{ij=1}^N \phi_i^{I\tau*}(\mathbf{r})(\sigma_{I\tau}^{-1})_{ij}\phi_j^{I\tau}(\mathbf{r}) = \sum_{\mu\nu=1}^B \chi_{\mu}^*(\mathbf{r})P_{\mu\nu}^{I\tau}\chi_{\nu}(\mathbf{r}) \quad (4.17)$$

### 4.9.2 First Derivative of the Intrastate Term

The derivation of the intrastate term is presented in the Supporting Information of our previous work<sup>2</sup>.

$$\begin{aligned} G_{\mu i}^{I\tau\varepsilon} &\equiv \frac{\partial \mathcal{E}^I}{\partial T_{\mu i}^{I\tau}} = \frac{\partial E^I}{\partial T_{\mu i}^{I\tau}} - \sum_{\tau=\alpha}^{\beta} \left[ c_p^I \frac{\partial \ln \det(\sigma_{II\tau} \sigma_{II\tau d}^{-1})}{\partial T_{\mu i}^{I\tau}} \right] = \\ &= 2[(I - SP^{I\tau})F^{I\tau}T^{I\tau}(\sigma_{II\tau}^{-1})]_{\mu i} - 2c_p^I [ST^{I\tau}(\sigma_{II\tau}^{-1} - \sigma_{II\tau d}^{-1})]_{\mu i} \end{aligned} \quad (4.18)$$

### 4.9.3 First Derivative of the Interstate Term

The first derivative of the interstate penalty term is

$$\begin{aligned}
G_{\mu i}^{I\tau P} &= \frac{\partial \Omega_P}{\partial T_{\mu i}^{I\tau}} = -C_P \sum_{\tau'=\alpha,\beta} \delta_{\tau\tau'} \frac{\partial \ln[\det(\Phi_{\tau'}\Phi_{\tau'd}^{-1})]}{\partial T_{\mu i}^{I\tau}} = \\
&= -C_P \frac{1}{\det(\Phi_{\tau}\Phi_{\tau d}^{-1})} \frac{\partial [\det(\Phi_{\tau})\det(\Phi_{\tau d}^{-1})]}{\partial T_{\mu i}^{I\tau}} = \\
&= -C_P \frac{1}{\det(\Phi_{\tau}\Phi_{\tau d}^{-1})} \left[ \frac{\partial \det(\Phi_{\tau})}{\partial T_{\mu i}^{I\tau}} \det(\Phi_{\tau d}^{-1}) + \det(\Phi_{\tau}) \frac{\partial [\det(\Phi_{\tau d})]^{-1}}{\partial \det(\Phi_{\tau d})} \frac{\partial \det(\Phi_{\tau d})}{\partial T_{\mu i}^{I\tau}} \right] = \\
&= -C_P \left[ \frac{1}{\det(\Phi_{\tau})} \frac{\partial \det(\Phi_{\tau})}{\partial T_{\mu i}^{I\tau}} - \frac{1}{\det(\Phi_{\tau d})} \frac{\partial \det(\Phi_{\tau d})}{\partial T_{\mu i}^{I\tau}} \right]
\end{aligned} \tag{4.19}$$

The derivative in the first term is evaluated using the fact that  $\Phi$  is an invertible matrix, but matrices

$\sigma_{IJ\tau}$  are not necessarily invertible

$$\begin{aligned}
\frac{\partial \det(\Phi_{\tau})}{\partial T_{\mu i}^{I\tau}} &= \det(\Phi_{\tau}) \sum_{KJ} (\Phi_{\tau}^{-1})_{KJ} \frac{\partial \Phi_{\tau JK}}{\partial T_{\mu i}^{I\tau}} = \det(\Phi_{\tau}) \sum_{KJ} (\Phi_{\tau}^{-1})_{KJ} \frac{\partial \det(\sigma_{JK\tau})}{\partial T_{\mu i}^{I\tau}} = \\
&= \det(\Phi_{\tau}) \sum_{KJ} (\Phi_{\tau}^{-1})_{KJ} \sum_{jk} \text{adj}(\sigma_{JK\tau})_{kj} \frac{\partial (\sum_{\alpha\lambda} T_{\lambda j}^{J\tau} S_{\lambda\alpha} T_{\alpha k}^{K\tau})}{\partial T_{\mu i}^{I\tau}} = \\
&= \det(\Phi_{\tau}) \sum_{KJ} (\Phi_{\tau}^{-1})_{KJ} \sum_{jk} \text{adj}(\sigma_{JK\tau})_{kj} \left( \sum_{\alpha\lambda} \frac{\partial T_{\lambda j}^{J\tau}}{\partial T_{\mu i}^{I\tau}} S_{\lambda\alpha} T_{\alpha k}^{K\tau} + \sum_{\alpha\lambda} T_{\lambda j}^{J\tau} S_{\lambda\alpha} \frac{\partial T_{\alpha k}^{K\tau}}{\partial T_{\mu i}^{I\tau}} \right) = \\
&= \det(\Phi_{\tau}) \sum_{KJ} (\Phi_{\tau}^{-1})_{KJ} \sum_{jk} \text{adj}(\sigma_{JK\tau})_{kj} \left( \sum_{\alpha\lambda} \delta_{JI} \delta_{\lambda\mu} \delta_{ji} S_{\lambda\alpha} T_{\alpha k}^{K\tau} + \sum_{\alpha\lambda} T_{\lambda j}^{J\tau} S_{\lambda\alpha} \delta_{KI} \delta_{\alpha\mu} \delta_{ki} \right) = \\
&= \det(\Phi_{\tau}) \sum_{KJ} (\Phi_{\tau}^{-1})_{KJ} \sum_{jk} \text{adj}(\sigma_{JK\tau})_{kj} [\delta_{JI} \delta_{ji} (ST^{K\tau})_{\mu k} + (T^{J\tau\dagger} S)_{j\mu} \delta_{KI} \delta_{ki}] = \\
&= \det(\Phi_{\tau}) \left[ \sum_{Kk} (\Phi_{\tau}^{-1})_{KI} \text{adj}(\sigma_{IK\tau})_{ki} (ST^{K\tau})_{\mu k} + \sum_{Jj} (\Phi_{\tau}^{-1})_{IJ} \text{adj}(\sigma_{JI\tau})_{ij} (T^{J\tau\dagger} S)_{j\mu} \right] = \\
&= \det(\Phi_{\tau}) \left[ \sum_K (\Phi_{\tau}^{-1})_{KI} [ST^{K\tau} \text{adj}(\sigma_{IK\tau})]_{\mu i} + \sum_J (\Phi_{\tau}^{-1})_{IJ} [\text{adj}(\sigma_{JI\tau}) T^{J\tau\dagger} S]_{i\mu} \right] = \\
&= 2 \det(\Phi_{\tau}) \sum_K (\Phi_{\tau}^{-1})_{KI} [ST^{K\tau} \text{adj}(\sigma_{IK\tau})]_{\mu i}
\end{aligned} \tag{4.20}$$

The derivative in the second term can be obtained using the result for the first term, the fact that  $\Phi_{\tau d}$  is a diagonal matrix, and that  $\sigma_{II\tau}$  is invertible with  $\text{adj}(\sigma_{II\tau}) = \det(\sigma_{II\tau})(\sigma_{II\tau}^{-1})$  for an invertible

matrix:

$$\begin{aligned}
\frac{\partial \det(\Phi_{\tau d})}{\partial T_{\mu i}^{I\tau}} &= 2 \det(\Phi_{\tau d}) \sum_K (\Phi_{\tau d}^{-1})_{KI} [ST^{K\tau} \text{adj}(\sigma_{IK\tau d})]_{\mu i} = \\
&= 2 \det(\Phi_{\tau d}) (\Phi_{\tau d}^{-1})_{II} [ST^{I\tau} \text{adj}(\sigma_{II\tau})]_{\mu i} = \\
&= 2 \det(\Phi_{\tau d}) [\det(\sigma_{II\tau})]^{-1} [ST^{I\tau} \det(\sigma_{II\tau}) (\sigma_{II\tau}^{-1})]_{\mu i} = \\
&= 2 \det(\Phi_{\tau d}) [ST^{I\tau} (\sigma_{II\tau}^{-1})]_{\mu i}
\end{aligned} \tag{4.21}$$

Using these results, the first derivative of the interstate penalty term is

$$G_{\mu i}^{I\tau P} = -2C_P \left[ \sum_K (\Phi_{\tau})_{IK}^{-1} [ST^{K\tau} \text{adj}(\sigma_{IK\tau})]_{\mu i} - (ST^{I\tau} \sigma_{II\tau}^{-1})_{\mu i} \right] \tag{4.22}$$

## Chapter 5

---

# Comprehensive Overview

---

The comprehensive overview section describes the areas that were not fully explored in Chapters 2, 3, and 4. It highlights potential future work that can further refine and enhance the presented research, offering a roadmap for continued improvement.

### 5.1 Facilitate CO<sub>2</sub> Binding in CD-MOF-2

As discussed in Chapter 2, the reversible chemisorption of CO<sub>2</sub> in CD-MOF-2 requires the formation of the alkoxide binding sites from alcohol groups, while the absorption strength is greatly influenced by the neighboring alcohol groups. Greater control of the proton removal from the alcohol groups and structural arrangements of neighbors open new opportunities for improving the material performance and boosting the adsorption capacity of this environmentally benign material.

### 5.1.1 Determine Precise Proton Transfer Mechanism

Understanding the formation of alkoxide sites requires detailed insight into proton transfer processes. One way to precisely determine the location and dynamics of the proton transfer is to employ *ab initio* molecular dynamics (AIMD) simulations. AIMD can provide a detailed and quantitative description of the thermodynamics and kinetics involved in this long-range proton transfer. By operating on time scales of picoseconds or femtoseconds, AIMD enables precise observation of rapid atomic vibrations and rotational movements within the MOF structure. To enable accurate computations for the extremely light protons, AIMD must include nuclear quantum effects (NQEs) explicitly. Several widely used techniques that account for NQEs in AIMD simulations are path integral molecular dynamics (PIMD)<sup>1,2</sup>, *ab initio* PIMD (AI-PIMD)<sup>3-6</sup>, ring polymer molecular dynamics (RPMD)<sup>7,8</sup>, centroid molecular dynamics (CMD)<sup>9,10</sup>, quantum thermal bath (QTB)<sup>11,12</sup>, and adaptive QTB (adQTB)<sup>13</sup>.

Once the proton transfer sites are identified and the alkoxide sites are formed, AIMD is also instrumental in analyzing the dynamics of the interaction between CO<sub>2</sub> and CD-MOF-2. By allowing atoms to relax and move, AIMD offers a more accurate representation of CO<sub>2</sub> binding, surpassing the limitations of the simplified description based on the straightforward geometry optimization. This insight is valuable for designing and optimizing the material by strategically incorporating strong bases besides alcohol groups, which can deprotonate them, leading to the formation of the alkoxide CO<sub>2</sub> binding sites. The increased basicity enhances the material's capability to facilitate proton transfer, which is essential for optimizing binding sites for CO<sub>2</sub> adsorption.

### 5.1.2 Analyze the H-bond Network Environment of CO<sub>2</sub> Binding Sites

It has been demonstrated that the network of hydrogen bonds between alcohol groups in CD-MOF-2 significantly influences the stability and reactivity of alkoxide sites. To precisely control the adsorption strength for either reversible or irreversible CO<sub>2</sub> chemisorption, a deeper exploration of these interactions within the MOF is essential. ALMO-EDA calculations are well-suited for analyzing hydrogen-bonding interactions in complex systems, including periodic materials like MOFs<sup>14</sup>. ALMO-EDA analysis can elucidate the contribution of individual bonds and interactions to the overall stabilization of the alkoxide sites. By systematically scanning coordinates of the binding site with its neighbor alcohol groups, floating counterions, and rubidium ions, followed by applying ALMO EDA, it is possible to identify specific contributions of these components to the interaction with the alkoxide site and with CO<sub>2</sub>. This method will help enhance the stabilization of carbonic acid adduct via its interactions with the surrounding environment.

Further insights into the stabilization of the hydrogen-bond network around each alkoxide site can be obtained through radial distribution function (RDF) analysis, which offers a detailed view of how the hydrogen bonds are spatially distributed relative to the alkoxide groups. The RDF will quantify the frequency of finding a particular atom type at a given distance from the alkoxide site, thereby revealing the local structural arrangement and interaction patterns. This method can be efficiently implemented using TRAVIS, a tool that only requires coordinate files as input. By computing the RDF, we can evaluate the effectiveness of the hydrogen-bond network in stabilizing the alkoxide site and gaining a deeper understanding of how different components of the MOF contribute to the overall CO<sub>2</sub> stabilization mechanism.

The results obtained from these calculation can be helpful to create more “good-neighbor”

alcohol groups that will produce the alkoxide sites that are “perfectly stabilized” for CO<sub>2</sub> binding.

### 5.1.3 Design Water-Stable Engineering Strategies

The presence of water in MOFs poses several challenges for practical applications. It can degrade structural integrity, compete with target gases for adsorption sites, block pores, and alter properties such as porosity and surface area. Additionally, water can induce phase changes that affect functionality and stability. To overcome these issues, designing water-stable MOFs or modifying existing ones to manage water-related problems is essential.

Since it is the OH<sup>-</sup> counterions that facilitate the proton removal from the alcohol groups, the formation of CO<sub>2</sub> binding sites will be accompanied by the formation of water. If the MOF is unstable in water, it is necessary to explore other bases that are both environmentally friendly and effective at capturing H<sup>+</sup> without producing water. Potential alternatives include ammonia (NH<sub>3</sub>), amine groups (e.g., pyridine, triethylamine), or ionic liquids with basic anions such as imidazolium-based ionic liquids. Another strategy to consider is incorporating hydrophobic elements such as hydrophobic ligands, hydrophobic groups, and hybrid composites<sup>15</sup>.

This approach can be extended to other MOFs with similar binding mechanisms by synthesizing and characterizing CD-MOF-2 variants with tailored adsorption sites and functional groups to optimize CO<sub>2</sub> adsorption while ensuring reversibility. Future research should also consider the use of green, sustainable synthetic methods to enhance environmental and economic viability.

### 5.1.4 Utilize Hybrid Functionals for More Accurate Binding Energies

Comparison of CO<sub>2</sub> adsorption energies obtained using BLYP and HSE06 functionals suggests that using hybrid density functionals can enhance the accuracy of the CO<sub>2</sub> binding energy prediction in CD-MOF-2. To improve the quality of these calculations, further exploration and analysis of the computational cost associated with applying hybrid exchange-correlation functionals to large periodic systems should be conducted.

## 5.2 Improve Convergence Rate of VM SCF

### 5.2.1 Implement BFGS Algorithm

Given the inherent simplicity of the unconstrained VM SCF approach described in Chapter 3, it is well-suited for implementation with any unconstrained minimization technique that guarantees convergence<sup>16</sup>. An area worth exploring in the future is using the Broyden-Fletcher-Goldfarb-Shanno (BFGS)<sup>17–20</sup> algorithm in the VM SCF orbital optimization. As the most widely used *quasi*-Newton method, BFGS significantly enhances convergence by building better and better approximations of the Hessian matrix. Hessian approximations, denoted  $\mathbf{B}_k$  here, is iteratively updated to reflect new information gained from the changes in the gradients  $\mathbf{G}_k$  along the search directions  $\mathbf{d}_k$ .

By applying  $\mathbf{B}_k$ , BFGS is expected to achieve faster convergence compared to conjugate gradient (CG) methods, without the need to compute the exact Hessian. The updated search direction and

inverse of the updated approximate Hessian matrix at the next iterate  $\mathbf{x}_{k+1}$  are defined by

$$\begin{aligned}\mathbf{d}_{k+1} &= -\mathbf{B}_{k+1}^{-1} \mathbf{G}_{k+1} \\ \mathbf{B}_{k+1}^{-1} &= (\mathbf{I} - \rho_k \mathbf{s}_k \mathbf{y}_k^T) \mathbf{B}_k^{-1} (\mathbf{I} - \rho_k \mathbf{y}_k \mathbf{s}_k^T) + \rho_k \mathbf{s}_k \mathbf{s}_k^T \\ \rho_k &= \frac{1}{\text{Tr}(\mathbf{y}_k^T \mathbf{s}_k)}\end{aligned}\tag{5.1}$$

where  $\mathbf{y}_k = \mathbf{G}_{k+1} - \mathbf{G}_k$  and  $\mathbf{s}_k = \mathbf{x}_{k+1} - \mathbf{x}_k$ . Here, the inverse of  $\mathbf{B}_k$  is useful because it allows for the efficient computation of the search direction via simple matrix-vector multiplication. This approach reduces the need of storing the full Hessian, which is computationally advantageous, especially in large scale applications like VM SCF. In the quasi-Newton framework, rather than recalculating  $\mathbf{B}^{-1}$  from scratch at each iteration, BFGS updates the matrix by incorporating the most recent information about the objective function with the existing knowledge embedded in the current Hessian approximation. The choice of the initial Hessian approximation,  $\mathbf{B}_0$ , is flexible and can be set as the identity matrix or scaled to reflect the variable magnitudes, providing a practical starting point for the optimization process.

For large-scale optimization problems, a limited-memory variant of BFGS (L-BFGS) can also be employed. This method utilizes curvature information from only the most recent iterations to construct an approximation of the Hessian. By discarding information from earlier iterations, which are less relevant to the current behavior of the Hessian, L-BFGS significantly reduces storage requirements. Unlike the full BFGS method, L-BFGS does not explicitly compute the Hessian or its inverse. Instead, it estimates the inverse Hessian indirectly by recursively contracting it with the gradient. This approach is useful for solving large problems where computing or storing the full Hessian is computationally prohibitive or when the Hessian is not sparse. However, L-BFGS tends to converge more slowly on ill-conditioned problems, where the Hessian matrix

exhibits a wide distribution of eigenvalues. Furthermore, by integrating the search directions of the quasi-Newton BFGS and CG methods, the hybrid BFGS-CG<sup>21</sup> presents an interesting alternative to conventional BFGS, building upon the advantages of both algorithms. This approach, alongside other hybridizations of quasi-Newton and CG methods, might offer some improvements in computational efficiency and convergence behavior.

### 5.2.2 Implement Trust Region (TR) Algorithm

The trust region method is another robust iterative optimization approach to employ beside BFGS in forthcoming research on VM SCF convergence. The method *approximates* the loss function, denoted  $m_k$ , within a localized region around the current iterate, known as the "trust region". Within this region, the algorithm solves a so-called *subproblem* of determining both the optimal step direction and size. The subproblem is formulated as:

$$\min_{\mathbf{p}} m_k(\mathbf{p}) = \Omega(\mathbf{x}_k) + \text{Tr}(\mathbf{G}_k^T \mathbf{p}) + \frac{1}{2} \text{Tr}(\mathbf{p}^T \mathbf{B}_k \mathbf{p}) \quad \text{s.t. } \|\mathbf{p}\|^2 \leq \Delta_k^2 \quad (5.2)$$

where  $\Delta_k > 0$  is the trust radius. After  $\mathbf{p}_k$  is computed, the current set of variables  $\mathbf{x}_k$  are updated using the optimal step  $\mathbf{p}_k$ :

$$\mathbf{x}_{k+1} = \mathbf{x}_k + \mathbf{p}_k. \quad (5.3)$$

and the exact, not approximate, loss function is evaluated. If the predictions made using the approximate and exact loss functions are sufficiently close, the trust radius is deemed acceptable and can even be increased. If not,  $\mathbf{x}_{k+1}$  is discarded, the optimizer returns to  $\mathbf{x}_k$ , the trust radius  $\Delta_k$  is reduced, and the updated subproblem is solved anew in the next iteration.

There are several methods to solve the subproblem. The simplest will be to use the Cauchy point  $\mathbf{p}_k^C$  as the solution. The Cauchy point is the point along the gradient that lies within the trust-region

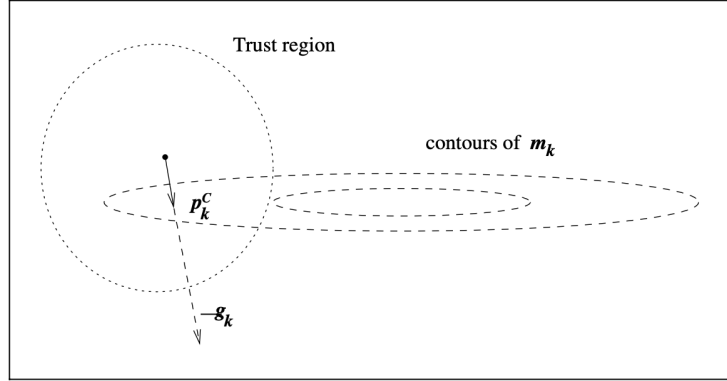


Figure 5.1: The Cauchy point. The figure is reproduced from Nocedal and Wright<sup>16</sup>

bounds  $\tau_k$  and guarantees to provide a sufficient reduction in  $m_k$  for the convergence of the TR procedure.

$$\mathbf{p}_k^C = -\tau_k \frac{\Delta_k}{\|\mathbf{G}_k\|} \mathbf{G}_k \quad (5.4)$$

where

$$\tau_k = \begin{cases} 1, & \text{if } \text{Tr}(\mathbf{G}_k^T \mathbf{B}_k \mathbf{G}_k) \leq 0 \\ \min(1, \frac{\|\mathbf{G}_k\|^3}{\Delta_k \text{Tr}(\mathbf{G}_k^T \mathbf{B}_k \mathbf{G}_k)}), & \text{otherwise.} \end{cases} \quad (5.5)$$

The last equation means that if the gradient is in a direction of negative curvature, the algorithm steps to the border of the trust region (Fig. 5.1). The Cauchy step  $\mathbf{p}_k^C$  is computationally efficient to calculate, as it avoids matrix factorizations, and plays a critical role in determining whether an approximate solution to the trust-region subproblem is acceptable. In TR, while finding the exact minimizer of the subproblem is ideal, achieving an approximate solution that is within the TR and provides a substantial reduction is often needed for global convergence. In this framework, the Cauchy point is pivotal in guiding the optimization process and enhancing overall efficiency.

Another approach to solve the subproblem would be to use the so-called “dogleg” method, schematically illustrated in Fig. 5.2. One of the advantages of the TR method over PCG is that

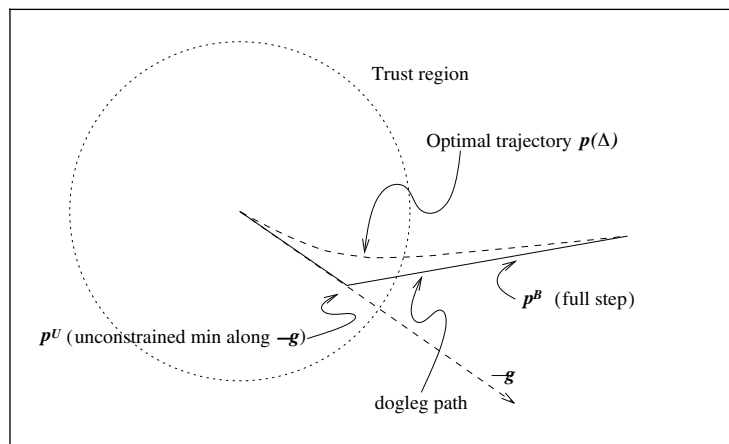


Figure 5.2: The dogleg method. The figure is reproduced from Nocedal and Wright<sup>16 16</sup>

it can handle ill-conditioned problems that could be encountered during orbital optimization by allowing adaptive adjustments to the trust region size. However, if the local model is not a good fit for the objective function, reducing the trust region can improve model accuracy and prevent excessively large steps that could lead to divergence or poor performance.

### 5.2.3 Reduce the Cost of the Preconditioner Inversion

In the current implementation, the inversion of the preconditioner is performed using Cholesky decomposition as implemented in ScaLAPACK library<sup>22</sup>, an operation of  $\mathcal{O}(B^3)$  computational complexity, where  $B$  is the number of basis set functions. While this approach is effective for small to moderately sized systems, it poses computational challenges for large molecular systems. For large systems, this step becomes the computational bottleneck and the cost of matrix inversion dominates the overall execution time of the algorithm.

Fortunately, the efficient preconditioner employed in the VM SCF PCG algorithm is a sparse matrix written in the basis set of localized atomic orbitals. One strategy to reduce the cost of inverting sparse matrices is to use sparse matrix libraries, designed specifically to take the sparsity

into account by focusing only on significant matrix elements and neglecting those close to zero. Utilizing sparse matrices can transform the  $\mathcal{O}(B^3)$  scaling of the preconditioner inversion to  $\mathcal{O}(B)$ , significantly improving the performance of the VM SCF algorithm for large systems. One of the sparse matrix libraries, DBCSR, is already used in our work (Chapters 3 and 4) for some of the computational steps and can be modified to handle Cholesky inversion. PETSc<sup>23,24</sup> and Trilinos<sup>25</sup> also offer advanced tools for sparse iterative solvers and preconditioning, including PCG and GMRES methods, and are designed for efficient parallel computing. Libkrylov<sup>26</sup> supports sparse matrix operations, complementing the capabilities of the other libraries. Together, these tools can enhance computational efficiency and scalability by leveraging matrix sparsity and distributing operations across multiple processors.

## 5.3 Improve Excited-State VM TIDFT Optimization

### 5.3.1 Design Better Loss Function

One of the key advantages of our VM TIDFT method (Chapter 4) is the ease of adding any necessary terms to the loss functional or redesigning it for specific optimization goals. For example, this flexibility will allow us to incorporate additional terms that ensure the optimizer remains close to any desired initial set of orbitals, as done in the MOM method<sup>27</sup>. By maximizing the overlap between the current occupied orbitals and those from the initial iteration, this term might help ensure that the optimized orbitals remain closely aligned with the initial excited-state configuration, offering better interpretation of the nature of VM TIDFT results.

Another strategy for redesigning the loss functional, inspired by the square gradient minimiza-

tion (SGM) approach<sup>28</sup>, will be to minimize the square of the energy gradient rather than the energy itself. The resulting loss functional for electronic state  $I$  will be

$$\Omega = \left| \frac{\partial \mathcal{E}^I}{\partial T_{\mu i}^{I\tau}} \right|^2 + \Omega_P \quad (5.6)$$

and the gradient of the loss function will be calculated as:

$$G_{vj}^{I\tau\epsilon} \equiv \frac{\partial}{\partial T_{vj}^{I\tau}} \left| \frac{\partial \mathcal{E}^I}{\partial T_{\mu i}^{I\tau}} \right|^2 = \frac{\partial}{\partial T_{vj}^{I\tau}} \sum_{\mu i} \frac{\partial \mathcal{E}^I}{\partial T_{\mu i}^{I\tau}} \cdot \frac{\partial \mathcal{E}^I}{\partial T_{\mu i}^{I\tau}} = 2 \sum_{\mu i} \frac{\partial^2 \mathcal{E}^I}{\partial T_{vj}^{I\tau} \partial T_{\mu i}^{I\tau}} \cdot \frac{\partial \mathcal{E}^I}{\partial T_{\mu i}^{I\tau}} \quad (5.7)$$

Minimizing the square of the energy gradient, as expressed in Eq. 5.7, prioritizes reducing fluctuations in energy, resulting in a more stable and accurate optimization. However, this approach introduces several computational challenges as it requires the calculation of not only the first but also the exact second derivatives of the energy. Moreover, the derivative of the adjugate matrix function in the penalty term is also needed, but it is presently unclear how it can be efficiently evaluated. One way to obviate the need for the adjugate derivative would be to utilize the BFGS method discussed in Section 5.2.1, which automatically constructs an approximate second derivative without the need for its analytical expression.

### 5.3.2 Implement ROKS Method for Spin-Pure States in VM TIDFT

In our work, we successfully used the ROKS method<sup>29,30</sup> to optimize spin-pure diradical ground states, as detailed in Chapter 3 and its Supporting Information. However, it would also be interesting to apply the same ROKS methodology in our VM TIDFT method for excited states, since most excited states of closed-shell systems are diradical in nature. Using ROKS in VM TIDFT is expected to improve the accuracy of describing such excited states by effectively managing spin contamination. This improvement is particularly important for a better direct comparison

with OCDFT, as OCDFT employs partial spin-purification in the post-SCF procedure<sup>31</sup>. Future work should prioritize the incorporation of ROKS into the VM TIDFT framework, enabling more accurate excited-state optimizations. This development would improve the general applicability of the method.

### 5.3.3 Perform Orbital Optimization with the Frozen Hamiltonian

We can approximate the excitation energy by performing our VM TIDFT optimization with a frozen Hamiltonian, which would significantly speed up the calculations. This is because constructing the Hamiltonian matrix is computationally expensive, particularly for practically important medium-sized systems containing hundreds of atoms. In CP2K, the Hamiltonian is built from scratch in each SCF step. By freezing the Hamiltonian after its initial construction, we can bypass this expensive process, making the method much more computationally efficient. This approach can provide a more affordable way to describe excitations while retaining a reasonable level of accuracy. The accuracy of this frozen Hamiltonian approach can be evaluated by comparing its results with those from the standard VM TIDFT optimization, where the Hamiltonian is recalculated at each step. Furthermore, benchmarking against other widely used methods, such as TDDFT and its Tamm-Dancoff linear response approximation<sup>32</sup>, will help evaluate the trade-offs between speed and accuracy.

## 5.4 References

- [1] Brown, L. M. *Feynman's thesis: A new approach to quantum theory*; World Sci., 2005; p 71–109.
- [2] Feynman, R. P. Space-time approach to non-relativistic quantum mechanics. *Rev. Mod. Phys.* **1948**, *20*, 367–387.
- [3] Berne, B. J.; Thirumalai, D. On the Simulation of Quantum Systems: Path Integral Methods. *Annu. Rev. Phys. Chem.* **1986**, *37*, 401–424.
- [4] Marx, D.; Parrinello, M. Ab initio path integral molecular dynamics: Basic ideas. *J. Chem. Phys.* **1996**, *104*, 4077–4082.
- [5] Chen, B.; Ivanov, I.; Klein, M. L.; Parrinello, M. Hydrogen bonding in water. *Phys. Rev. Lett.* **2003**, *91*, 215503.
- [6] Morrone, J. A.; Car, R. Nuclear quantum effects in water. *Phys. Rev. Lett.* **2008**, *101*, 017801.
- [7] Craig, I. R.; Manolopoulos, D. E. Quantum statistics and classical mechanics: Real time correlation functions from ring polymer molecular dynamics. *J. Chem. Phys.* **2004**, *121*, 3368–3373.
- [8] Habershon, S.; Manolopoulos, D. E.; Markland, T. E.; Miller, T. F. Ring-polymer molecular dynamics: Quantum effects in chemical dynamics from classical trajectories in an extended phase space. *Annu. Rev. Phys. Chem.* **2013**, *64*, 387–413.
- [9] Cao, J.; Voth, G. A. The formulation of quantum statistical mechanics based on the Feynman path centroid density. V. Quantum instantaneous normal mode theory of liquids. *J. Chem. Phys.* **1994**, *101*, 6184–6192.
- [10] Jang, S.; Voth, G. A. A derivation of centroid molecular dynamics and other approximate time evolution methods for path integral centroid variables. *J. Chem. Phys.* **1999**, *111*, 2371–2384.
- [11] Ceriotti, M.; Bussi, G.; Parrinello, M. Nuclear quantum effects in solids using a colored-noise thermostat. *Phys. Rev. Lett.* **2009**, *103*, 030603.
- [12] Dammak, H.; Chalopin, Y.; Laroche, M.; Hayoun, M.; Greffet, J. J. Quantum Thermal Bath for Molecular Dynamics Simulation. *Phys. Rev. Lett.* **2009**, *103*, 190601.
- [13] Mangaud, E.; Huppert, S.; Plé, T.; Depondt, P.; Bonella, S.; Finocchi, F. The Fluctuation-Dissipation Theorem as a Diagnosis and Cure for Zero-Point Energy Leakage in Quantum Thermal Bath Simulations. *J Chem Theory Comput.* **2019**, *15*, 2863–2880.
- [14] Khaliullin, R. Z.; Kühne, T. D. Microscopic properties of liquid water from combined ab initio molecular dynamics and energy decomposition studies. *Phys. Chem. Chem. Phys.* **2013**, *15*, 15746–15766.
- [15] Xiao, C.; Tian, J.; Chen, Q.; Hong, M. Water-stable metal-organic frameworks (MOFs): rational construction and carbon dioxide capture. *Chem. Sci.* **2024**, *15*, 1570–1610.
- [16] Nocedal, J.; Wright, S. J. *Numerical Optimization*, 2nd ed.; Springer: New York, NY, USA, 2006.
- [17] Broyden, C. G. The convergence of a class of double-rank minimization algorithms: 2. The new algorithm. *IMA J. Appl. Math.* **1970**, *6*, 222–231.
- [18] R, F. New approach to variable metric algorithms. *Comput. J.* **1970**, *13*, 317–322.

- [19] Goldfarb, D. A family of variable-metric methods derived by variational means. *Math. Comput.* **1970**, *24*, 23–26.
- [20] Shanno, D. F. Conditioning of quasi-Newton methods for function minimization. *Math. Comput.* **1970**, *24*, 647–656.
- [21] Stanimirović, P.; Ivanov, B.; Djordjević, S.; Brajević, I. New Hybrid Conjugate Gradient and Broyden–Fletcher–Goldfarb–Shanno Conjugate Gradient Methods. *J. Optim. Theory Appl.* **2018**, *178*, 860–884.
- [22] Choi, J.; Demmel, J.; Dhillon, I.; Dongarra, J.; Ostrouchov, S.; Petitet, A.; Stanley, K.; Walker, D.; Whaley, R. ScaLAPACK: a portable linear algebra library for distributed memory computers — design issues and performance. *Comput. Phys. Commun.* **1996**, *97*, 1–15.
- [23] Leasure, B.; Kuck, D. J.; Gorbach, S.; Cole, M.; Watson, G. R.; Darte, A.; Padua, D.; Banerjee, U.; Schenk, O.; Gärtner, K.; et al. *PETSc (Portable, Extensible Toolkit for Scientific Computation)*; Springer, Boston, MA, 2011.
- [24] Balay, S.; Abhyankar, S.; Adams, M. F.; Brown, J.; Brune, P.; Buschelman, K.; Dalcin, L.; Eijkhout, V.; Gropp, W.; Kaushik, D.; others *PETSc Users Manual*, Argonne National Laboratory, 2014.
- [25] Heroux, M. A.; Willenbring, J. M. A new overview of the Trilinos project. *Sci. Program.* **2012**, *20*, 397–423.
- [26] Rappoport, D.; Bekoe, S.; Mohanam, L. N.; Le, S.; George, N.; Shen, Z.; Furche, F. Libkrylov: A modular open-source software library for extremely large on-the-fly matrix computations. *J. Comput. Chem.* **2023**, *44*, 1105–1118.
- [27] Gilbert, A. T.; Besley, N. A.; Gill, P. M. Self-consistent field calculations of excited states using the maximum overlap method (MOM). *J. Phys. Chem. A* **2008**, *112*, 13164–13171.
- [28] Hait, D.; Head-Gordon, M. Excited State Orbital Optimization via Minimizing the Square of the Gradient: General Approach and Application to Singly and Doubly Excited States via Density Functional Theory. *J. Chem. Theory Comput.* **2020**, *16*, 1699–1710.
- [29] Frank, I.; Hutter, J.; Marx, D.; Parrinello, M. Molecular dynamics in low-spin excited states. *J. Chem. Phys.* **1998**, *108*, 164101.
- [30] Filatov, M.; Shaik, S. Density-functional thermochemistry. III. The role of exact exchange. *J. Chem. Phys.* **1999**, *110*, 5648.
- [31] Evangelista, F. A.; Shushkov, P.; Tully, J. C. Orthogonality Constrained Density Functional Theory for Electronic Excited States. *J. Phys. Chem. A* **2013**, *117*, 7378–7392.
- [32] Hirata, S.; Head-Gordon, M. Time-dependent density functional theory within the Tamm-Dancoff approximation. *Chemical Physics Letters* **1999**, *314*, 291–299.

## Chapter 6

---

# Conclusion

---

### 6.1 Summary

In Chapter 2, we explored the intricate nature of CO<sub>2</sub> adsorption sites in CD-MOF-2, derived from cyclodextrins and notable for its strong and reversible carbon dioxide chemisorption. DFT modeling and comprehensive analysis of experimental data reveal how the structural characteristics of adsorption sites are governed by complex interactions involving hydroxyl counterions and hydrogen bonding networks. The findings show that the nucleophilic character of alkoxide sites, generated via proton transfer from alcohol groups, plays a pivotal role in determining the strength and reversibility of CO<sub>2</sub> binding. Moreover, the diversity of hydrogen bonding environments within CD-MOF-2 is shown to modulate these binding sites, resulting in a range of CO<sub>2</sub> binding strengths from irreversible to weak chemisorption. The results of this research addressed our initial objectives, enhancing the fundamental understanding of CO<sub>2</sub> adsorption mechanisms in CD-MOF-2. By bridging traditional concepts of acid-base equilibrium and hydrogen bonding with solid-state CO<sub>2</sub> capture, we offer strategies for designing tunable materials for carbon capture and storage. The findings also open avenues for refining these materials using advanced computational methods,

such as AIMD simulations and hybrid exchange-correlation functionals, which could improve the accuracy of binding site characterization. These approaches provide a promising pathway toward developing more efficient and customizable CO<sub>2</sub> capture technologies.

Chapter 3 introduced a simple approach to orbital optimization in KS DFT by removing the conventional requirement of orbital orthogonality. By augmenting the DFT energy functional with a penalty term for linearly dependent states, the study demonstrates that orbital optimization can be effectively performed with nonorthogonal orbitals. This method, called variable-metric (VM) SCF optimization, allows MOs coefficients to serve as independent variables in a direct, unconstrained minimization process. The result is a significant simplification of the variational procedure, yielding closed-form expressions for both the electronic gradient and Hessian. The research further validates the efficacy of this approach through the implementation of a basic PCG algorithm, which achieves efficient convergence for a range of systems, including challenging narrow-gap systems and spin-pure two-determinant states of singlet diradicals. Due to its simplicity, VM SCF can be readily implemented using alternative unconstrained minimization techniques. The ability to optimize orbitals without the burden of orthogonality constraints represents a notable advancement in one of the most fundamental procedures in computational chemistry. Interestingly, the same variable-metric principles can be applied to optimize wavefunctions in more advanced quantum chemistry methods.

Chapter 4 builds on the developments of Chapter 3 by extending the VM SCF method to excited states. This extension offers a unified framework for describing ground and excited states with the same level of precision, significantly expanding the applicability of DFT to a broader range of electronic structure problems. Chapter 3 highlights the versatility of the approach, and the Comprehensive Overview describes potential future improvements.

The work presented across these chapters exemplifies the critical role of DFT in exploring and solving green chemistry challenges. In the context of carbon capture, DFT provides a detailed understanding of molecular interactions that can inform the design of more efficient and sustainable materials. Moreover, the simple SCF optimization methods presented here address some of the fundamental limitations of traditional DFT, enabling its application to more complex electronic structures and excited states. The ability to accurately model excited states will enhance our understanding of the photochemical and photophysical processes behind the energy transformation in materials, leading to more effective solutions for pressing environmental challenges. The continued development of computational techniques, such as variable metric SCF, will expand the boundaries of what can be achieved with DFT, driving further advancements in green chemistry and beyond.